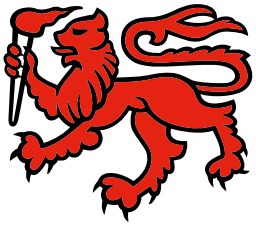

UNIVERSITY*of*
TASMANIA

The influence of nuclei content on tip vortex cavitation inception

Matthew Khoo, B.Eng (Hons), B.Sci
National Centre for Maritime Engineering and Hydrodynamics
Australian Maritime College

Submitted in fulfilment of the requirements
for the degree of Doctor of Philosophy,
University of Tasmania

November, 2021

Declarations

Declaration of Originality

This thesis contains no material which has been accepted for a degree or diploma by the University or any other institution, except by way of background information and as duly acknowledged in the text, and to best of my knowledge and belief no material previously published or written by another person except where due acknowledgement is made in the text of the thesis, nor does the thesis contain any material that infringes copyright.

Signed: _____ Date: 17 November 2021

Matthew Khoo

Statement Regarding Published Work

The papers comprising Chapters 2 to 5 and Appendices A to E in this thesis are author accepted manuscripts of published journal articles and conference papers, some of which have been modified following thesis examiners' feedback. Citations and hyperlinks to the final authenticated versions are provided in the introductory text at the start of each of these chapters and appendices. Due to the thesis chapters and appendices being in article form, there is unavoidable repetition of material within this thesis.

Signed: _____ Date: 17 November 2021

Matthew Khoo

Statement of Authority of Access

This thesis may be made available for loan and limited copying and communication in accordance with the Copyright Act 1968.

Signed: _____ Date: 17 November 2021

Matthew Khoo

Statement of Co-Authorship

The following people and institutions contributed to the publication of work undertaken as part of this thesis:

Candidate	Mr Matthew T. Khoo	University of Tasmania Defence Science and Technology Group
Author 1	Prof. Paul A. Brandner	University of Tasmania
Author 2	Dr Bryce W. Pearce	University of Tasmania
Author 3	Dr James A. Venning	University of Tasmania
Author 4	Dr Takayuki Mori	Acquisition, Technology & Logistics Agency
Author 5	Mr Kenshiro Takahashi	Acquisition, Technology & Logistics Agency
Author 6	Mr Yves Lecoffre	Hydeo France
Author 7	Dr Jun Arai	Acquisition, Technology & Logistics Agency
Author 8	Dr Dev Ranmuthugala	Defence Science and Technology Group

Contribution of work by co-authors for each paper:

Paper 1: Located in Chapter 2

M. Khoo, J. Venning, B. Pearce, K. Takahashi, T. Mori, and P. Brandner. Natural nuclei population dynamics in cavitation tunnels. Exp. Fluids, 61(2):34, 2020.

Author contributions:
Conceived experiment design: Candidate, Author 3, Author 1, Author 4, Author 5
Performed experiments: Candidate, Author 3, Author 5
Analysed data: Candidate, Author 3, Author 1
Prepared manuscript: Candidate, Author 3, Author 1, Author 2, Author 4, Author 5

Paper 2: Located in Chapter 3

M. Khoo, J. Venning, B. Pearce, and P. Brandner. Statistical aspects of tip vortex cavitation inception and desinence in a nuclei deplete flow. Exp. Fluids, 61(6):145, 2020.

Author contributions:
Conceived experiment design: Author 3, Candidate, Author 1
Performed experiments: Author 3
Analysed data: Candidate, Author 3
Prepared manuscript: Candidate, Author 3, Author 1, Author 2

Paper 3: Located in Chapter 4

M. Khoo, J. Venning, B. Pearce, and P. Brandner. Nucleation effects on hydrofoil tip vortex cavitation. In Proc. 21st Australasian Fluid Mech. Conf., 2018.

Author contributions:
Conceived experiment design: Candidate, Author 3, Author 1
Performed experiments: Candidate, Author 3
Analysed data: Candidate, Author 3
Prepared manuscript: Candidate, Author 3, Author 1, Author 2

Paper 4: Located in Chapter 5

M. Khoo, J. Venning, B. Pearce, and P. Brandner. Nucleation and cavitation number effects on tip vortex cavitation dynamics and noise. Exp. Fluids, 62(10):216, 2021.

Author contributions:
Conceived experiment design: Candidate, Author 3, Author 1
Performed experiments: Author 3, Candidate
Analysed data: Candidate, Author 3
Prepared manuscript: Candidate, Author 3, Author 1, Author 2

Paper 5: Located in Appendix A

M. Khoo, J. Venning, B. Pearce, P. Brandner, and Y. Lecoffre. Development of a cavitation susceptibility meter for nuclei size distribution measurements. In Proc. 20th Australasian Fluid Mech. Conf., 2016.

Author contributions:
Conceived experiment design: Candidate, Author 1, Author 6
Performed experiments: Candidate, Author 3
Analysed data: Candidate, Author 3, Author 1
Prepared manuscript: Candidate, Author 3, Author 1, Author 2, Author 6

Paper 6: Located in Appendix B

M. Khoo, J. Venning, K. Takahashi, J. Arai, T. Mori, B. Pearce, P. Brandner, and D. Ranmuthugala. Joint research between Australia and Japan on the cavitation inception of marine propellers and control surfaces. In MAST Asia 2017, pages 1–6, 2017.

Author contributions:
Conceived experiment design: Candidate, Author 3, Author 1, Author 4, Author 5
Performed experiments: Candidate, Author 3, Author 5, Author 7
Analysed data: Candidate, Author 3, Author 1
Prepared manuscript: Candidate, Author 3, Author 1, Author 2, Author 4, Author 5, Author 7, Author 8

Paper 7: Located in Appendix C

J. Venning, M. Khoo, B. Pearce, and P. Brandner. Background nuclei measurements and implications for cavitation inception in hydrodynamic test facilities. Exp. Fluids, 59(4):71, 2018.

Author contributions:
Conceived experiment design: Author 3, Candidate, Author 1
Performed experiments: Author 3
Analysed data: Author 3, Author 1, Author 2, Candidate
Prepared manuscript: Author 3, Author 1, Author 2, Candidate

Paper 8: Located in Appendix D

J. Venning, M. Khoo, B. Pearce, and P. Brandner. Observations on a cavitating trailing vortex behind a control surface. In MAST Asia 2019, pages 1–9, 2019.

Author contributions:
Conceived experiment design: Author 3, Candidate, Author 1
Performed experiments: Author 3, Candidate
Analysed data: Author 3
Prepared manuscript: Author 3, Candidate, Author 1, Author 2

Paper 9: Located in Appendix E

M. Khoo, J. Venning, B. Pearce, and P. Brandner. Nucleation effects on tip vortex cavitation inception location. In Proc. 22nd Australasian Fluid Mech. Conf. The University of Queensland, 2020.

Author contributions:
Conceived experiment design: Candidate, Author 3, Author 1
Performed experiments: Candidate, Author 3
Analysed data: Candidate, Author 3
Prepared manuscript: Candidate, Author 3, Author 1, Author 2

We, the undersigned, endorse the above stated contribution of work undertaken for each of the published (or submitted) peer-reviewed manuscripts contributing to this thesis:

Signed: _____ Date: 17 November 2021

Mr Matthew Khoo
Candidate
National Centre for Maritime Engineering and Hydrodynamics
Australian Maritime College, University of Tasmania

Signed: _____ Date: 17 November 2021

Prof Paul Brandner
Primary Supervisor
National Centre for Maritime Engineering and Hydrodynamics
Australian Maritime College, University of Tasmania

Signed: _____ Date: 17 November 2021

Dr Vikram Garaniya
Head of School
National Centre for Maritime Engineering and Hydrodynamics
Australian Maritime College, University of Tasmania

Acknowledgements

This research was supported by an Australian Government Research Training Program (RTP) Scholarship and the Australian Department of Defence. I thank the Australian Department of Defence for allowing me the opportunity, time and funding to pursue further study.

I thank my colleagues in the Hydroacoustics group and Acoustic Signature Management branch for their support during my candidature. I appreciate and value those that have engaged in stimulating technical and non-technical discussions, and the friendships that have developed. I thank Dr Chris Norwood, and more recently, Mr Andrew Tynan, for overseeing my journey within the branch. I thank Mr Brendon Anderson and Dr Dev Ranmuthugala for their continued support and active involvement in my career development, as well as for providing sage advice during times of stress.

I thank staff from the Australian Maritime College for their technical and personal contributions throughout my candidature, including Mr Robert Wrigley, Mr Steven Kent, Dr Patrick Russell, Mrs Elizabeth Russell, Dr Luka Barbaca, Dr Rhys Paul and Dr Zhi Leong.

I thank staff from Japan's Acquisition, Technology & Logistics Agency, particularly Dr Takayuki Mori, Mr Kenshiro Takahashi, Dr Jun Arai and Mr Kenji Naganuma for their technical contributions and hospitality during collaborative experiments and the preparation of joint publications.

I thank Mr Yves Lecoffre for sharing his passion for fluids engineering, patient explanations of various technical concepts and hospitality during the early stages of my candidature.

I appreciate the continued support of my supervisors during my candidature. Prof. Paul Brandner, thank you for showing faith in me from the beginning and for seeing the big picture. I am fortunate to have had access to a world-class test facility without which this research would not have been possible. Our Japanese dinners with Lou are always a highlight of my visits. Dr Bryce Pearce, thank you for contributing your knowledge of the literature and test facility operation, as well as your professionalism in reviewing papers. Dr James Venning, thank you for your generosity and the grace you showed in the face of

lengthy experimental campaigns, and for contributing ideas which never cease to challenge my thinking. Meals with your family really helped to foster a sense of home during my visits. Dr David Clarke, thank you for reminding me to prioritise the important things and to manage my expectations.

I thank my parents, Cheryl and Dennis Khoo, and sister, Carena Khoo, for their endless love, support and encouragement. I hope I have made you proud.

Lastly, and most importantly, I thank my wife, Michiyo Moriyama, and our daughter, Millie, for their unwavering love, support and encouragement. I have been a challenge to deal with at times, and you always respond with kindness and patience. I look forward to the next chapter of our life together. I love you.

Abstract

Tip vortex cavitation (TVC) is detrimental to the acoustic stealth performance of naval ship and submarine propellers and control surfaces. Nuclei, or microbubble, content can vary in environmental waters, having implications for TVC inception and acoustic signature. While it is commonly known that TVC inception occurs earlier in flows abundant with nuclei, further research is required to broaden understanding of nucleation effects on TVC behaviour and its associated physics. This includes research in the interrelated areas of natural nuclei population dynamics in test facilities, the statistical nature of TVC inception in nuclei deplete flows, and the influence of different nuclei populations on the physical characteristics of TVC inception and development. To address the lack of published information in these areas, a series of experiments were conducted in variable pressure water tunnels, also known as cavitation tunnels, which are typically used to study TVC and nucleation effects under controlled conditions.

The natural nuclei population behaviour in different test facilities was measured using a cavitation susceptibility meter (CSM). This informed the design of subsequent TVC experiments concerning nucleation effects on TVC about lifting surfaces. The statistical nature of TVC inception and desinence about an elliptical hydrofoil in flows deplete of nuclei was quantified using the optical detection of a large number of cavitation events. A nuclei abundant flow was then introduced to assess the effect of vastly different nuclei populations on TVC behaviour about an elliptical hydrofoil. High-resolution photographs and acoustic measurements were acquired at fixed Reynolds and cavitation numbers. The deplete and abundant nuclei populations were quantified using the CSM and Mie scattering imaging, respectively. The study was then extended to consider the effects of different artificially-generated nuclei populations on TVC inception location and cavity kinematics using synchronised video and acoustic measurements.

The natural nuclei population in the cavitation tunnel at the Australian Maritime College Cavitation Research Laboratory is found to follow a power law, and remains invariant at a baseline level over short timescales. The baseline level of the natural nuclei population in the Japanese Acquisition, Technology & Logistics Agency's Flow Noise Simulator is similar to that of the Australian tunnel. The test section pressure of the Japanese tunnel is a better indicator of whether the natural nuclei population has increased above the baseline, which is in contrast to the dissolved oxygen saturation

condition in the plenum for the Australian facility. It is discovered that for undersaturated conditions in the plenum of the Australian tunnel, the natural nuclei population remains constant around the tunnel circuit. Therefore, the population in the test section can measured by sampling water into the CSM from the lower-segment resorber, provided the water is undersaturated in the plenum. This is a convenient way to monitor the natural nuclei population during TVC experiments for which the presence of the CSM sampling probe in the test section would be prohibitive. In one such experiment, TVC inception is shown to be a stochastic process that requires a large number of repeated measurements for characterisation. At a given test condition, the probability of inception increases with waiting time. This is due to a larger volume of water, and thus higher number of susceptible nuclei, passing through the streamtube of opportunity. Meanwhile, TVC desinence exhibits much less statistical variation, suggesting it is less dependent on the natural nuclei population. Comparisons of TVC inception behaviour in nuclei deplete and abundant flows confirm that cavitation inception occurs at a higher incidence in a nuclei deplete flow due to a lack of weaker nuclei. In both flows tested, the sound pressure level reaches a local peak at or after inception, although the physics driving this behaviour are different between the seeding cases. In a nuclei abundant flow, intermittent activations occur before the formation of a continuous tip vortex cavity at higher tensions, which results in a higher overall sound level. It is also found that both the nuclei population and cavitation number have a significant impact on the inception location distribution along the trailing vortex of an elliptical hydrofoil, and in particular, on inception event rates. The cavitation number changes the flow volume subjected to tension, and hence the shape of the inception location distribution as well. It is found that once ingested nuclei are activated, cavity kinematic and acoustic properties are influenced by the local pressure (i.e. inception location and cavitation number) rather than the initial nucleus size, at least in the $\sim$50–100 µm diameter range activated in this study.

A greater understanding of the effects of nuclei content on TVC has been achieved. Natural nuclei population dynamics in test facilities should be factored into experimental design when testing in flows with low pressures. This was taken into account in the study of TVC in nuclei deplete flows, which quantitatively shows inception to be stochastic in nature and strongly dependent on the nuclei population, in contrast to desinence. The extent to which nuclei content affects TVC behaviour increases as the difference between the populations becomes greater. While the appearance and noise emissions of TVC differ markedly between nuclei deplete and abundant flows, the differences in these characteristics are less pronounced between flows with injected mono- and polydisperse nuclei populations which are more similar with respect to bubble size and concentration distributions. Nevertheless, variations in nuclei concentration between populations are clearly reflected by changes in inception event rate. To further understanding about nucleation effects on TVC, additional work is required on nuclei measurement and bubble generation techniques, TVC behaviour across a wider range of nuclei populations and validation of theoretical cavity dynamic and acoustic models using experimental data.

Contents

List of Figures

List of Tables

Nomenclature

Greek symbols

α	incidence
α_{d}	desinence angle
α_{i}	inception angle
ϵ_{f}	total uncertainty in variable of interest, f
η	contraction ratio
Γ	circulation
γ	ratio of DO concentration at a given pressure to saturation at atmospheric pressure
ν	fluid kinematic viscosity
ω_{c}	resonant frequency of a cylindrical bubble
ω_{s}	natural frequency of spherical bubble oscillation
ρ	fluid density
σ	cavitation number
σ_{d}	desinent cavitation number
σ_{gen}	generator cavitation number
σ_{min}	minimum cavitation number

Other symbols

A	constant of proportionality
A_2	contraction outlet area upstream of venturi
A_{VT}	venturi throat area
a_1	constant of proportionality of flow coefficient trendline
a_2	constant of proportionality of venturi $C_{\mathrm{p,min}}$ trendline
b	hydrofoil half-span
b_1	Re exponent of flow coefficient trendline
b_2	Re exponent of venturi $C_{\mathrm{p,min}}$ trendline

C	nuclei concentration
c	dissolved oxygen concentration, root chord length, nuclei concentration density
C_{L}	lift coefficient
C_{p}	pressure coefficient
$C_{\mathrm{p,min}}$	minimum pressure coefficient
C_{Q}	flow coefficient
c_{sat}	saturation level of DO in water at equilibrium conditions
D	diameter
D_∞	initial bubble diameter
D_0	initial bubble diameter
D_2	contraction outlet diameter upstream of venturi
d	diameter
d_0	initial bubble diameter
E	inception event rate
f	frequency, variable of interest
$f_{\mathrm{l}}^{(n)}$	lower frequency of the nth band
f_{peak}	peak frequency
$f_{\mathrm{u}}^{(n)}$	upper frequency of the nth band
G_{pp}	single-sided spectrum
g	acceleration due to gravity
H	height
h	height of the centreline upstream of the contraction relative to the test-section centerline
K_{H}	Henry's law constant
L	length, lift force
L_{max}	maximum cavity length
$\dot{L}$	cavity elongation rate
$\dot{L}_{\mathrm{max}}$	maximum elongation rate
M	molar mass
N	number of activations
n	power-law index, frequency band number
P	pressure
p	pressure
p_∞	freestream pressure
$p_{\infty 0}$	initial freestream pressure
p_0	initial pressure, test section pressure
p_1	pressure upstream of contraction located upstream of venturi
p_2	pressure downstream of contraction located upstream of venturi
p_{c}	critical pressure
p_{down}	generator outlet pressure

p_{g}	partial pressure of oxygen in air saturated with water vapour
p_{min}	minimum pressure
p_{ref}	reference pressure
p_{sat}	saturation pressure
p_{TS}	test section pressure
p_{up}	plenum pressure, pressure upstream of the generator orifice
p_{VT}	venturi throat static pressure
p_{v}	vapour pressure
p_{x}	pressure at location x in venturi throat
Q	volumetric flow rate
Q_{UT}	volumetric flow rate (ultrasonic flow meter)
q	dynamic pressure
R	radius, correlation coefficient
Re	Reynolds number
r	relative saturation level of oxygen in water
r_{TS}	relative saturation level of oxygen in water in test section
r_{up}	relative saturation level of oxygen in water in plenum
S	surface tension, hydrofoil planform area
s	distance along cavity trajectory downstream of hydrofoil tip
s_{i}	location of TVC inception downstream of hydrofoil tip
T	temperature, highest tension
T_{c}	critical tension
t	time
t'	non-dimensional time
U	mean flow velocity
U_{∞}	freestream velocity
U_2	mean flow velocity at contraction outlet upstream of venturi
U_{c}	cavity advection velocity
U_{c1}	main cavity body advection velocity
U_{c2}	remnant bubble advection velocity
U_{TS}	test section flow velocity
U_{VT}	mean flow velocity in venturi throat
V_{P}	voltage across a piezoceramic sensor
Vol	tank volume for flow meter calibration
W	width
x	location in venturi throat, streamwise coordinate
z	vertical coordinate

Abbreviations

AMC	Australian Maritime College
ATLA	Acquisition, Technology & Logistics Agency
CRL	Cavitation Research Laboratory
CSM	cavitation susceptibility meter
DO	dissolved oxygen
DST	Defence Science and Technology Group
FNS	Flow Noise Simulator
GTH	Grand Tunnel Hydrodynamique
IMI	interferometric Mie imaging
inc.	initial inception incidence
L.E.	leading-edge cavitation
LMS	long-range microscopic shadowgraphy
MSI	Mie scattering imaging
NACA	National Advisory Committee for Aeronautics
PSD	power spectral density
PDF	probability density function
SPL	sound pressure level
S.P.	single-phase
TVC	tip vortex cavitation
UM	University of Michigan
V.C.	trailing-vortex cavitation

Chapter 1

General introduction

Tip vortices are inherently generated from the tips of three-dimensional lifting surfaces operating at non-zero lift. Low pressures exist in these regions of concentrated vorticity, particularly in the vortex core, making the flow susceptible to tip vortex cavitation (TVC) inception when the local pressure falls below vapour pressure, see Fig 1.1.

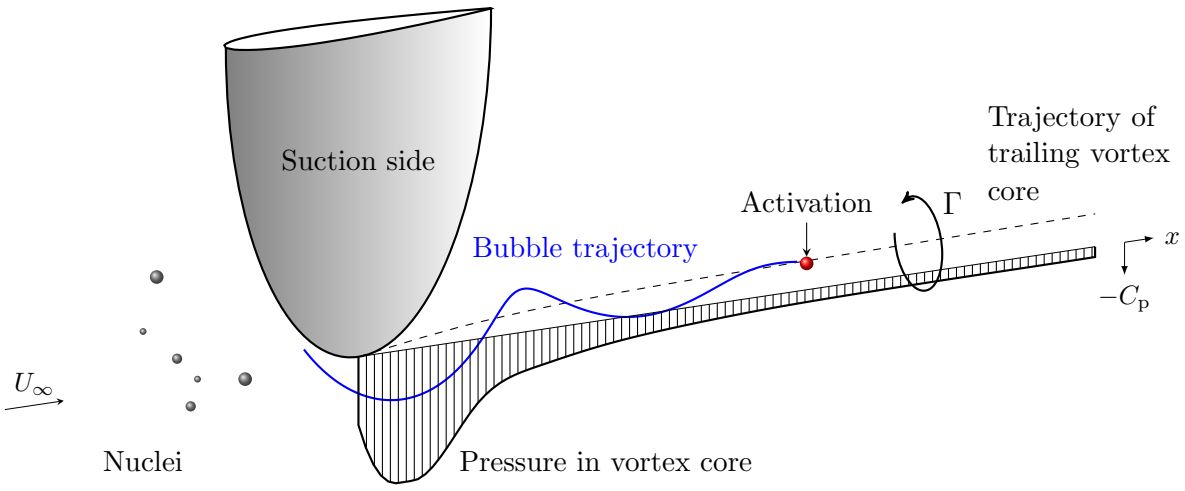

Figure 1.1: Notional capture of a nucleus (red sphere) into the vortex trailing from a lifting surface. The blue line denotes the nucleus trajectory. The freestream velocity is U_∞ and the circulation is Γ. The generic variation of the pressure coefficient, C_p, with streamwise location, x, similar to the trends observed for elliptical foils (Chen et al., 2019; Asnaghi et al., 2020), is also shown with the minimum pressure occurring close to the tip and pressure recovery downstream as the vortex diffuses.

TVC is often the first type of cavitation to occur about marine propellers, control surfaces and turbomachinery due to the low pressures generated in the core of tip vortices (Brennen, 1995; Franc and Michel, 2006). It happens when fluid changes from liquid to vapour phase due to pressure reduction. Cavitation nucleation in practical flows such as laboratory and environmental waters is invariably heterogeneous, and weaknesses called nuclei are activation sites for cavitation to occur. Cavitation nuclei can be free gas microbubbles, and potentially gas-containing biological organisms or solid particles with trapped gas (Lecoffre, 1999). When they are exposed to a size-dependent critical pressure, their equilibrium becomes unstable and they grow explosively, filling with vapour and forming macroscopic cavities, see Fig. 1.2 for an example of a cavitating trailing vortex.

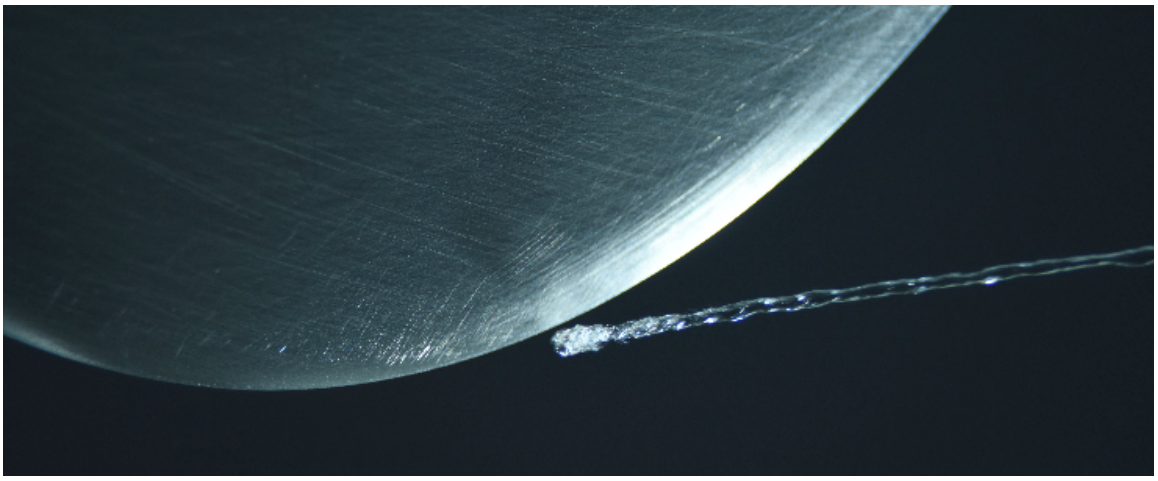

Figure 1.2: Photograph of the tip of a hydrofoil with an unattached cavitating trailing vortex.

The stability of a spherical microbubble nucleus can be described using single bubble equilibrium theory (Chahine and Shen, 1986; Franc and Michel, 2006). Assuming the mass of gas in the bubble is constant and that it grows isothermally, the behaviour of a bubble in equilibrium can be expressed by

$$p_\infty = \left(p_{\infty 0} - p_\mathrm{v} + \frac{4S}{D_0}\right)\left(\frac{D_0}{D}\right)^3 + p_\mathrm{v} - \frac{4S}{D}, \tag{1.1}$$

where p_∞ is the freestream pressure, p_v is the liquid vapour pressure, S is the surface tension, D is the diameter and the '0' subscript denotes initial conditions. The size variation of bubbles with four different initial sizes with changing pressure is shown in Fig. 1.3. The blue circles denote the critical pressure of each bubble, which is the lowest pressure it can withstand while remaining in equilibrium on the left of the dotted line. The equilibrium is unstable to the right of the dotted line. Nuclei with smaller initial diameters have lower critical pressures.

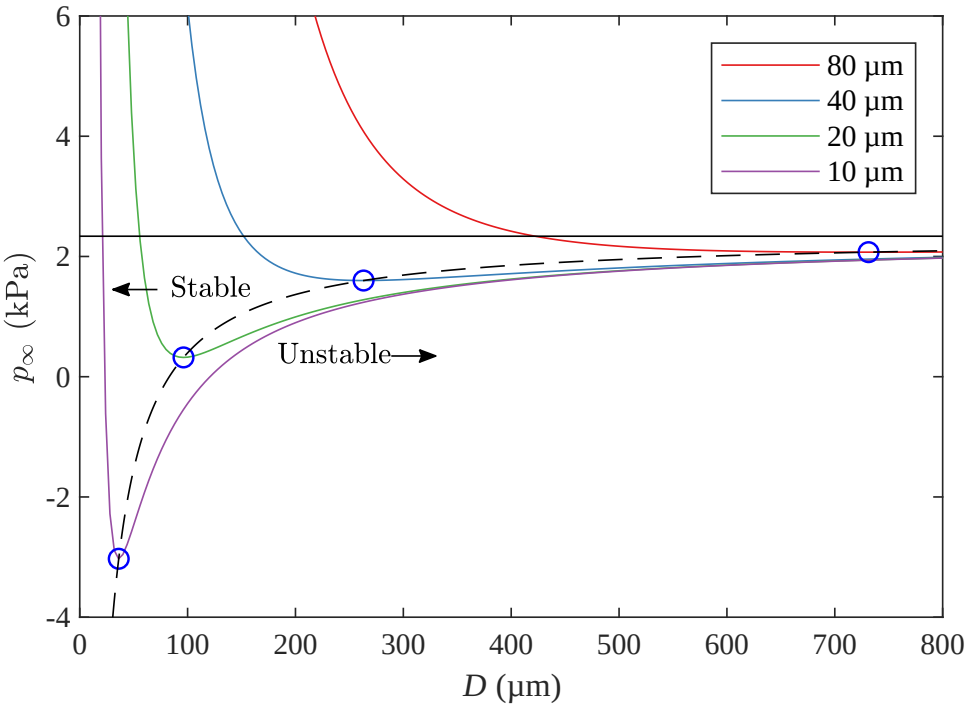

Figure 1.3: Spherical bubble equilibrium showing freestream pressure, p_∞, against bubble diameter, D, for four different initial diameters, D_0. A temperature of $T = 20°C$ and an initial freestream pressure of $p_{\infty 0} = 100$ kPa are used. The blue circles represent the critical pressures of each bubble. A dashed line is drawn between these critical pressures. Bubble equilibrium is stable to the left of the dashed line and unstable to the right. The horizontal line represents vapour pressure.

The streamwise pressure distribution in a tip vortex, and hence location of minimum pressure, is dependent on hydrofoil planform, cross-section and tip geometry (Astolfi et al., 1999). Cavitation inception may occur at streamwise locations along the vortex away from the location of minimum pressure, as long as the local pressure is sufficiently low to activate a captured nucleus. Nuclei can be captured into a vortex either axially or radially, the latter being due to buoyancy forces exerted by the radial pressure gradient. This capture is dependent on vortex strength, bubble size and the distance of the nucleus from the vortex (Ligneul and Latorre, 1989, 1993; Chen et al., 2019). Vorticity tends to decrease with increasing downstream distance due to viscous diffusion, causing a pressure recovery in the vortex core and subsequent cavity collapse.

The noise generated by TVC is detrimental to the acoustic stealth performance of naval platforms. Both TVC growth and collapse are known to generate noise due to complex transients (Choi and Ceccio, 2007), oscillatory modes (Pennings et al., 2015a) and large volumetric accelerations (Lamb, 1945; Fitzpatrick, 1958; Leighton, 2012). The following formula for the natural frequency of spherical bubble oscillation, ω_s, initially derived by Minnaert (1933), was extended to account for surface tension (Brennen, 1995). Assuming isothermal gas behaviour and zero damping, which is reasonable for larger bubbles, this is described as

$$\omega_\mathrm{s} = \sqrt{\frac{1}{\rho}\left(\frac{12(p_\infty - p_\mathrm{v})}{D^2} + \frac{32S}{D^3}\right)}, \tag{1.2}$$

where ρ is the fluid density. Larger bubble diameters and lower external pressures result in lower resonant frequencies, similarly to cylindrical cavities. The resonant frequency (i.e. breathing mode) of a cylindrical bubble, ω_c, is given by Neppiras (1980) as

$$\omega_\mathrm{c} = \sqrt{\frac{4p_\infty}{\rho D L}}, \tag{1.3}$$

where L is length. According to this theory, longer cavities resonate at lower frequencies.

Due to the very low critical pressures that stronger nuclei can sustain, water is capable of withstanding high tensions below vapour pressure without cavitating (Blake Jr, 1949). This property is also known as water tensile strength. According to single-bubble equilibrium theory, a 1 µm diameter bubble can sustain about 1 atm of tension prior to activation for standard temperature and pressure initial conditions. The present research (Appendix C) shows that given 'infinite' sampling times, the natural nuclei population of a body of water has no strength due to the presence of very low concentrations of large nuclei. However, tensile strength is observable in many practical flows. Tensile strength is probabilistic in nature, as nuclei spatial and temporal distributions can vary (Arndt and Keller, 1992; Briançon-Marjollet and Merle, 1996; Mørch, 2000). The consequence is that TVC inception is a complex probabilistic process.

It is widely accepted that nuclei content affects TVC inception behaviour, with the earlier onset of cavitation measured in flows with 'weak' water, as opposed to 'strong'

water devoid of nuclei (Arndt and Keller, 1992; Boulon et al., 1997; Gindroz and Billet, 1998). Numerical simulations have also shown that fewer nuclei activations occur for populations with smaller nuclei (Hsiao and Chahine, 2005). A range of different nuclei populations can exist in practical flows. Depending on the type of flow, these populations can vary over several orders of magnitude, thereby necessitating the use of a range of nuclei generation and measurement techniques for experimental modelling and quantification, as discussed below.

A number of these techniques have been developed in the Cavitation Research Laboratory (CRL) at the Australian Maritime College (AMC) (Brandner, 2018). Sample microbubble or nuclei population measurements in the AMC cavitation tunnel are shown in Fig. 1.4. The weakest population with the highest concentrations of larger microbubbles was measured using long-range microscopic shadowgraphy (LMS) and is typical of those found in cavitating wakes at relatively high cavitation numbers (Russell et al., 2018b). They have effectively no tensile strength and are the most susceptible to TVC inception. The inflows to ship propulsors may contain such nuclei populations.

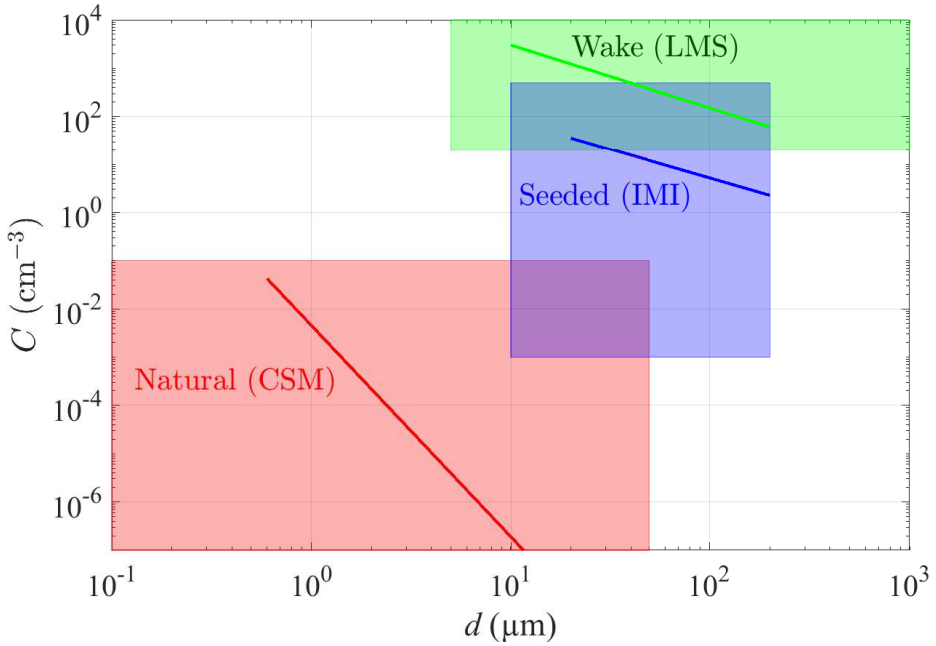

Figure 1.4: Nuclei distribution graph showing the bubble diameter, d, and concentration, C, ranges (shaded regions) for which practical measurements can be made using the Cavitation Susceptibility Meter (CSM), Interferometric Mie Imaging (IMI) and Long-range Microscopic Shadowgraphy (LMS). Optical methods (e.g. IMI and LMS) are more suitable for higher concentrations of larger bubbles, while the hydrodynamic method (CSM) is suitable for lower concentrations of smaller bubbles. The lines represent recent nuclei measurements at the AMC cavitation tunnel.

The intermediate population was measured using Mie scattering imaging (MSI) and is representative of a test flow artificially seeded with a relatively high concentration of microbubbles between 10 and 100 µm in diameter (Brandner, 2018; Russell et al., 2020a). Such populations may be used for the experimental modelling of cavitation inception. Only a limited number of test facilities currently exist which have depressurisation capabilities for cavitation studies as well as nuclei injection and dissolved gas management systems that allow for strict control over free and dissolved gas contents (Lecoffre et al., 1988; Brandner et al., 2007; Song et al., 2017). In other test facilities, nuclei, or free gas, content may only be controlled indirectly via manipulation of the dissolved air content (Arndt and Maines, 2000; Chang et al., 2011).

Finally, the strongest population with lower concentrations of stronger nuclei is representative of the natural nuclei population in the AMC cavitation tunnel under typical operating conditions. These nuclei may be activated at low pressures in vortical flows. This population was measured via mechanical activation using a cavitation susceptibility meter (CSM). This is necessary due to both the diffraction limit of optical techniques ($\mathcal{O}(0.1)$ µm) and the excessive number of images required to quantify low nuclei concentrations.

Numerous measurements of natural nuclei populations have been made in both laboratory and environmental waters since the mid-twentieth century using optical, acoustic and hydrodynamic techniques (Gavrilov, 1969; Shen et al., 1984; O'Hern et al., 1988; Gindroz, 1995; Randolph et al., 2014). In nature, these populations are known to vary with location and depth (Gindroz et al., 1995; Gowing and Shen, 2001), as well as sea state (Johnson, 1986) and potentially biological activity (O'Hern et al., 1986). A phenomenological model proposed by Franklin (1992) describes the relationship between nuclei size and concentration as a power law with an index of -4, which infers a universal characteristic of natural nuclei populations in water. The experimental measurements presented in this thesis (Chapter 2 and Appendix C) also show that the relationship between concentration and critical tension is a power law. Natural nuclei populations play a role in TVC inception and are therefore an important part of TVC testing in experimental facilities. While these populations have been measured in several test facilities, detailed characterisations of their dynamics are difficult to find in the literature. They are known to be influenced by hydrodynamic configuration and operating condition of the facility which affect the pressure history of the water (Gindroz et al., 1997; Atlar, 2002). Additional work is required to acquire a deeper understanding of natural nuclei population dynamics in cavitation tunnels to enable better-controlled TVC experiments. This is addressed in Chapter 2.

An understanding of natural nuclei population dynamics in test facilities allows nucleation effects on TVC to be studied with greater dependability through the modelling of both strong and weak flows. As mentioned earlier, TVC inception is known to occur earlier in weaker flows with higher nuclei populations, and this is supported by a number

of experimental studies of propeller and hydrofoil models (Briançon-Marjollet and Merle, 1996; Boulon et al., 1997; Gindroz and Billet, 1998; Song et al., 2017). Boulon et al. (1997) made the additional observation that the permanent attachment of the vapour core to a hydrofoil tip occurs at practically the same incidence regardless of nuclei content. Meanwhile, McCormick (1962) noted that free gas influences TVC behaviour more than dissolved gas. McCormick (1962) also observed lower repeatability of TVC inception measurements compared to desinence, and attributed it to the random distribution of nuclei in the flow. This makes TVC desinence easier to study, but inception is likely to be of greater relevance for practical applications. While some statistical approaches have been made in numerical studies of TVC (Messino et al., 1963; Hsiao and Chahine, 2005, 2008), the small sample sizes typically used in TVC experiments are insufficient to properly characterise the phenomenon. An event rate approach was taken by Schiebe (1969) for the study of travelling bubble cavitation about a headform, and it was concluded that larger statistical samples were required for comparisons with event rates calculated based on measured nuclei populations. This was achieved with greater success by Ceccio and Brennen (1991) who used a large sample size of several thousand measurements. It is evident that further studies are required to quantify TVC inception from a statistical perspective using sufficiently large sample sizes. One such study is provided in Chapter 3.

Once tip vortex cavitation inception occurs, the cavity grows and emits noise. Some observations of water quality effects on TVC dynamics and noise at inception have been made during previous studies. Higher tip vortex cavity elongation rates (Arndt and Maines, 2000) and higher acoustic pulses (Choi and Ceccio, 2007) have been measured in stronger flows. In a numerical study, these behaviours were associated with explosive growth at low pressures with the cavity overshooting its equilibrium diameter before oscillating and generating noise (Choi et al., 2009). Furthermore, the relatively low concentrations of nuclei activated in stronger flows produces fewer acoustic pressure pulses, as noted by Hsiao and Chahine (2005). As for noise emissions in weaker flows, nucleus activation at high pressures close to vapour pressure produces quasi-steady cavity growth and lower noise emissions (Choi et al., 2009). A study into the visual and acoustic characteristics of TVC behaviour in flows with different water quality is presented in Chapter 4.

TVC inception location is of interest because the streamwise pressure distribution may affect tip vortex cavity dynamics and acoustics. However, detailed quantitative data is scarce with anecdotal evidence suggesting that in weak water TVC usually incepts near the tip (Maines and Arndt, 1993; Arndt and Maines, 2000), but can occur between -0.05 and about 1.5 chord lengths downstream of the tip (Higuchi et al., 1989; Maines and Arndt, 1993). Meanwhile, in strong water TVC inception location has been observed to be between 0.05 and 1.0 chord lengths downstream of the tip with equal probability (Arndt and Maines, 2000), though quantitative distributions were not provided. Additionally, water quality was set by saturating the flow with air, rather than by independent control over both the free and dissolved gas contents.

While the effect of water quality on TVC dynamics and acoustics has been noted in previous studies, there exists an opportunity to gain further insight into the associated physics, through quantitative spatial and acoustic measurements of TVC inception and development in flows with strictly-controlled free and dissolved gas contents. Relating these measurements to TVC inception location would provide a holistic understanding of the phenomenon and greater knowledge of how cavity characteristics can vary along the tip vortex. This is addressed in Chapter 5.

There is little doubt that nuclei content and the vortical pressure field about a lifting surface control TVC inception. A review of the literature has revealed several areas for further investigation to improve understanding about water quality and its effect on TVC behaviour. The research questions are:

1. What are the natural nuclei population dynamics in different cavitation tunnels?

    - The natural, or pre-existing, nuclei population in hydrodynamic test facilities can play a role in TVC inception. As such, these populations and their dynamics must be measured and understood. Changes with tunnel operating conditions such as pressure, velocity and dissolved oxygen content, as well as temporal variations need to be quantified to achieve this. A study on this is presented in Chapter 2.

2. How do natural nuclei populations affect TVC inception and desinence behaviour?

    - As the natural nuclei population in test facilities may be activated in tip vortex flows, it is important to understand the characteristics of TVC behaviour in such flows deplete of nuclei. Large sample sizes are required to quantify the probabilistic nature of inception and desinence, which can be achieved via the use of automated cavity detection. This is addressed in Chapter 3.

3. How do natural and injected nuclei populations influence TVC inception behaviour?

    - Nuclei populations in environmental waters can be higher than the natural nuclei populations found in test facilities. Therefore, a comparison of TVC inception behaviour in flows with vastly different nuclei populations is necessary to properly assess nucleation effects on TVC. While it is generally agreed that TVC inception occurs earlier in weaker water, the visual and acoustic characteristics of TVC behaviour in flows deplete and abundant in nuclei need to be measured to deepen understanding in this area, as described in Chapter 4.

4. How do different injected nuclei populations influence TVC kinematics and acoustics?

    - To further understanding about nucleation effects on TVC behaviour, comparative measurements of tip vortex cavity kinematics and acoustics in flows with different nuclei populations are required. Synchronised high speed video

and acoustic measurements can be used to study the relationship between nuclei population, inception location, as well as cavity kinematics and acoustics. Large sample sizes are useful for characterising inception location distributions along the vortex. This research question is addressed in Chapter 5.

To address these research questions, a series of experiments were conducted at the cavitation tunnel in the AMC CRL, taking advantage of its ancillaries for artificial nuclei seeding and fast degassing. Experiments on nuclei population dynamics were also conducted in the Japanese Acquisition, Technology & Logistics Agency's Flow Noise Simulator as part of a collaborative research project with Australia's Defence Science and Technology Group. This enabled a comparison of natural nuclei population dynamics between test facilities with different architectures. A deeper understanding about nuclei and their effects on TVC behaviour will contribute to better TVC test, prediction and management capabilities for practical applications.

The main body of this thesis, contained in Chapters 2 to 5, comprises peer-reviewed journal and conference papers. Supplementary publications that support the main thesis are provided in the appendices. At the beginning of each of the main body chapters, publication details are provided, along with introductory text on the context of the work and its contribution to the research objectives, as well as links with other chapters and supplementary papers.

Chapter 2

Natural nuclei population dynamics in cavitation tunnels

There exists an ever-present natural nuclei population in all hydrodynamic test facilities. Prior to TVC testing, an understanding of the behaviour of this population is necessary. To this end, the natural nuclei population dynamics in the cavitation tunnel at the Australian Maritime College Cavitation Research Laboratory and in the Japanese Acquisition, Technology & Logistics Agency's Flow Noise Simulator were investigated using a cavitation susceptibility meter (CSM). This research builds upon previous work to develop and commission the CSM (Khoo et al. (2016) in Appendix A), preliminary measurements in each facility (Khoo et al. (2017) in Appendix B) and detailed measurements of the natural nuclei population at fixed operating conditions in the Australian test facility (Venning et al. (2018b) in Appendix C). Comparisons are also made with other test facilities and environmental waters to better understand how natural nuclei populations can vary with location and measurement technique. The results guide the design of the TVC experiments presented in Chapters 3 to 5.

This chapter is a post-peer-review, pre-copyedit version of an article published in *Experiments in Fluids*, modified following thesis examiners' feedback. The final authenticated version is available online at:

`https://doi.org/10.1007/s00348-019-2843-x`.

The citation for the paper is:

M. Khoo, J. Venning, B. Pearce, K. Takahashi, T. Mori, and P. Brandner. Natural nuclei population dynamics in cavitation tunnels. Exp. Fluids, 61(2):34, 2020.

2.1 Abstract

Nuclei, or microbubble, populations control the inception and dynamics of cavitation. It is therefore important to quantify distributions in cavitation test facilities to rigorously model nucleation dynamics. Measurements of natural nuclei population dynamics were made in two test facilities in Australia and Japan via mechanical activation using a Cavitation Susceptibility Meter (CSM). A range of tunnel operating parameters, including pressure, velocity and dissolved oxygen (DO) content, were investigated. The DO saturation condition upstream of the test section is found to provide a threshold as to whether the population is affected by DO in the Australian test facility. Historical trends in the population are quantified, indicating that regular monitoring is required. Variation of the population around the Australian cavitation tunnel circuit was studied by varying the water sampling location. Provided the water remains undersaturated, as defined above, the natural nuclei population in the test-section can be measured by sampling from the lower-limb resorber. Comparisons are made between test facilities in Australia, Japan and other countries, as well as environmental waters, using different measurement techniques. Optical and acoustic methods show microbubbles in the size range of 10 to 100 µm typical of those used to model cavitation nucleation. CSM measurements show varying distributions of nuclei with equivalent bubble diameters in the range of 0.5 to 5 µm but global trends suggest a universal characteristic.

2.2 Introduction

Microbubble disperse flows are intrinsic to surface oceanography and naval hydrodynamics as they control, or interact with, many phenomena and processes of interest including cavitation inception and dynamics, gaseous diffusion, noise generation, acoustic and shockwave propagation and turbulence. With regard to cavitation, microbubbles provide nuclei that control the inception and dynamics of unsteady cavitation; but cavitation itself is also a prolific source of microbubbles by its very nature. Modelling of these flows experimentally remains a challenge as microbubble concentrations and size ranges may vary over several orders of magnitude. To this end, several techniques for generating and measuring microbubbles have been developed in the Cavitation Research Laboratory (CRL) at the Australian Maritime College (AMC) (Brandner, 2018). Sample results from these techniques for measuring microbubbles or nuclei populations in the AMC cavitation tunnel are shown in Fig. 2.1. Overall concentrations and sizes range over 10 and 5 orders of magnitude respectively. The population with the largest concentrations and sizes is typical of that in the wake of a cavitating object at relatively high Reynolds numbers (Russell et al., 2018b). This population of relatively high concentration/larger microbubbles has been measured using Long-range Microscopic Shadowgraphy (LMS). The intermediate population is representative of a test flow artificially seeded with a relatively high concentration of microbubbles in the size range 10 to 100 µm for experimental modelling of cavitation inception. These were measured using Interferometric Mie Imaging (IMI)

(Brandner, 2018; Russell et al., 2020a). The most sparse population shown in Fig. 2.1 is typical of the background or naturally occurring nuclei population ever present in the AMC cavitation tunnel under normal operating conditions. Optical measurement of these nuclei is impractical due to the low concentrations, requiring an excessive number of images. Furthermore, there is a diffraction limit on these techniques which constrains the smallest measurable bubble diameter to $\mathcal{O}(1)$ µm. The natural nuclei population has been measured via mechanical activation using a Cavitation Susceptibility Meter (CSM) (Khoo et al., 2017). It is the dynamics of this population within cavitation tunnels that is the subject of the present work.

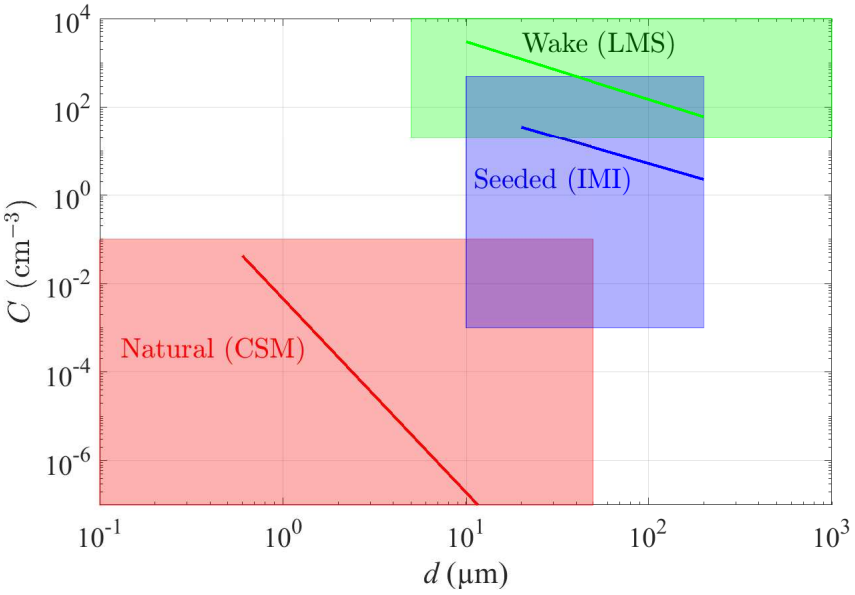

Figure 2.1: Nuclei distribution graph showing the bubble diameter, d, and concentration, C, ranges (shaded regions) for which practical measurements can be made using the Cavitation Susceptibility Meter (CSM), Interferometric Mie Imaging (IMI) and Long-range Microscopic Shadowgraphy (LMS). Optical methods (e.g. IMI and LMS) are more suitable for higher concentrations of larger bubbles, while the hydrodynamic method (CSM) is suitable for lower concentrations of smaller bubbles. The lines represent recent nuclei measurements at the AMC cavitation tunnel.

Cavitation nucleation in practical flows is invariably heterogeneous. Such practical flows in test facilities and oceans contain dissolved gas and gas free as microbubbles that typically provide nuclei for cavitation inception. The equilibrium of a microbubble is unstable below a size-dependent critical pressure, p_c. This can be expressed as a tension, $p_\mathrm{c} - p_\mathrm{v}$, where p_v is vapour pressure. The following equation gives this tension as a function of bubble diameter, d, and ambient pressure, p_∞:

$$p_\mathrm{c} - p_\mathrm{v} = \frac{-2}{3\sqrt{3}} \sqrt{\frac{(4S/d)^3}{p_\infty - p_\mathrm{v} + 4S/d}} \tag{2.1}$$

where S is the surface tension. This can be derived from consideration of the equilibrium of bubble internal and external pressures and the surface tension assuming isothermal internal gas behaviour and no mass transfer via phase change or diffusion (Franc and Michel, 2006).

A bubble undergoes explosive growth once exposed to the critical pressure subsequently filling with vapour leading to rapid development of macroscopic cavitation. For microbubbles smaller than 100 µm diameter, this critical pressure is well below vapour pressure, decreasing with decreasing size to several atmospheres of tension for micron-sized nuclei. That is, water may exist in a metastable state exposed to large tensions relative to vapour pressure before nucleation occurs. Vapour pressure represents a state of equilibrium, or more specifically dynamic equilibrium, between a liquid and its vapour and does not provide absolute limits on phase change.

Microbubble nucleation has been investigated extensively and remains a major area of research into the physics of cavitation inception and dynamics. Indeed, the literature is abundant with theoretical and experimental work on single bubble dynamics from which considerable insight has been gained and current understanding is largely based. However, there are other sources of cavitation nuclei in practical flows for which much less is known both in oceans, where there are organic and other impurities (Stramski et al., 2004), or test facilities where there may be less impurities. Venning et al. (2018b) showed that the water in the AMC cavitation tunnel, where no microbubbles generated by cavitation or artificial nuclei seeding were present, is susceptible to cavitation at all tensions given sufficiently long sampling time. It was also observed that the relationship between concentration and critical tension is a power law. This is in line with observations made in various laboratory tests and in environmental waters.

Ocean surface bubble populations ranging from millimetre to micrometre scales have been studied extensively. Arguments for observed power-law relationships between concentration and size have been based on dimensional considerations (Garrett et al., 2000; Deane and Stokes, 2002). These involve larger bubble turbulent breakup limited by surface tension as expressed through the Hinze scale giving an index of $-10/3$ and for sub-Hinze scales where the production mechanism is jet entrainment with an associated index of $-3/2$. These indices may then be modified by the competing effects of buoyancy and dissolution. In a review of oceanography data by Zhang (2001) for bubble sizes ranging from order 10 microns to millimetre diameters, indices ranged from -7 to -2 although it was noted that -4 fits most results reasonably well. However, more recent near surface measurements have been made in Arctic ice leads showing similar global microbubble distributions in the absence of waves demonstrating that other mechanisms also produce such typical populations (Norris et al., 2011).

Similar results have been found for microbubble or nuclei populations in test facilities and environmental waters in a review by Billet (1985) citing an index of -3. Gavrilov (1969) investigated microbubble populations in long standing tap water and reported an index of -3.5. Franklin (1992) argues that based on a power-law relationship between concentration and size and self similarity of the distribution that the index be -4 and further proposes a phenomenological theory for the concentration levels based on dissolved gas and molecular considerations that goes some way to explaining experimental results.

The gas within microbubbles will diffuse into the surrounding water if undersaturated with dissolved gas, resulting in complete dissolution of the bubbles. This is one of the mechanisms used in the AMC tunnel to continuously eliminate injected or cavitation generated microbubbles from the circuit. It has been postulated that nuclei may persist in cavitation tunnels due to gases trapped in crevices of hydrophobic particles (Harvey et al., 1944), bubbles being stabilised by a rigid permeable skin of organic impurities (Fox and Herzfeld, 1954) or surface contamination (Brennen, 1995) and from cosmic radiation (Brennen, 1995). Laboratory studies of ocean water by Johnson and Cooke (1981) show that bubbles created do dissolve but that there is a remnant population of stabilised microbubbles of sizes ranging from less than 1 to 13 microns. Observations have been made of nuclei distributions in cavitation test facilities, though detailed characterisations of the population dynamics are lacking in the literature. Nuclei content can be influenced by factors such as the hydrodynamic configuration and operating condition of the facility which affect the pressure history of the water (Gindroz et al., 1997; Atlar, 2002).

Natural nuclei concentrations and critical pressures have generally been observed to increase with decreasing pressure and test section velocity(since a reduction in velocity generally causes a reduction in static pressure throughout the rest of the tunnel circuit), as well as increasing relative saturation level of dissolved gas and tunnel operating history (Arndt and Keller, 1976; Liu et al., 1993; Brennen, 1994; Gindroz et al., 1997; Atlar, 2002; Nagaya et al., 2011). Other researchers have found that nuclei distributions do not change with pressure and velocity (Gates et al., 1979; Billet, 1984). However, this may be due to the limited range of test parameters investigated. For example, Billet (1984) mainly used relatively high test-section pressures and flow velocities. Although larger changes in nuclei content were observed with varying air content.

Due to the low concentration and low critical pressures of the natural nuclei population in the AMC tunnel they are not active in high cavitation number flows such as sheet and cloud cavitation (Venning et al., 2018b). However, for low cavitation number flows where cavitation occurs in vortices such as shear layers, structured turbulence or tip vortices, it is vital that the natural population be measured to investigate inception and dynamics. In the present work, the operating parameters of the AMC cavitation tunnel are systematically varied in order to quantify their influence on natural nuclei populations. Venning et al. (2018b) observed that the natural nuclei population in the AMC tunnel is invariant across normal operating conditions. In this study, the limits of this operating window are discussed, and further insights into the nature of the natural population are presented. Historical variations in the population are described. The natural nuclei population dynamics in the AMC tunnel are compared with those in the Japanese Acquisition, Technology & Logistics Agency (ATLA) Flow Noise Simulator (FNS), characterised using the same measurement equipment. Finally, natural nuclei distributions are compared across various test facilities and environmental waters using a range of nuclei measurement techniques.

2.3 Experimental setup

Nuclei measurements were acquired in the AMC cavitation tunnel and the ATLA FNS using the same AMC CSM. The main characteristics of each cavitation tunnel are provided in Tab. 2.1. Further details regarding the AMC and ATLA tunnel designs and operation are described in Brandner et al. (2007) and Mori et al. (2007) respectively. The experimental setup in each test facility is described below.

AMC tunnel	**ATLA tunnel**
Location	
Launceston, Tasmania, Australia	Nakameguro, Tokyo, Japan
Year established	
2011	2005
Material (wetted surfaces)	
Stainless steel	Stainless steel
Volume (m^3)	
365	2000
Working fluid	
Demineralised water	Filtered municipal water
Test-section dimensions, $H \times W \times L$ (m)	
$0.6 \times 0.6 \times 2.6$	$2 \times 2 \times 10$
Test-section absolute pressure range (centreline) (kPa)	
4–400	20–310
Nominal test-section flow velocity range (m/s)	
2–12	1.5–15
Test-section velocity profile uniformity	
<0.5% of mean velocity	<1% of mean velocity
Test-section turbulence intensity (%)	
<0.5	<0.5
Main motor capacity (kW)	
200	2800
Microbubble seeding control	
Direct/dilute minitube injector arrays with downstream tank and lower-limb resorber	Single-point injection of oversaturated water

Table 2.1: Specifications of the AMC and ATLA cavitation tunnels.

2.3.1 AMC cavitation tunnel

A schematic of the AMC cavitation tunnel is shown in Fig. 2.2. The variable-pressure, closed-circuit tunnel has a volume of 365 m^3, with demineralised water the working fluid. The test section has a 0.6×0.6 m cross section and is 2.6 m long. The test-section centreline absolute pressure can be varied between 4–400 kPa and the nominal flow velocity range is 2–12 m/s.

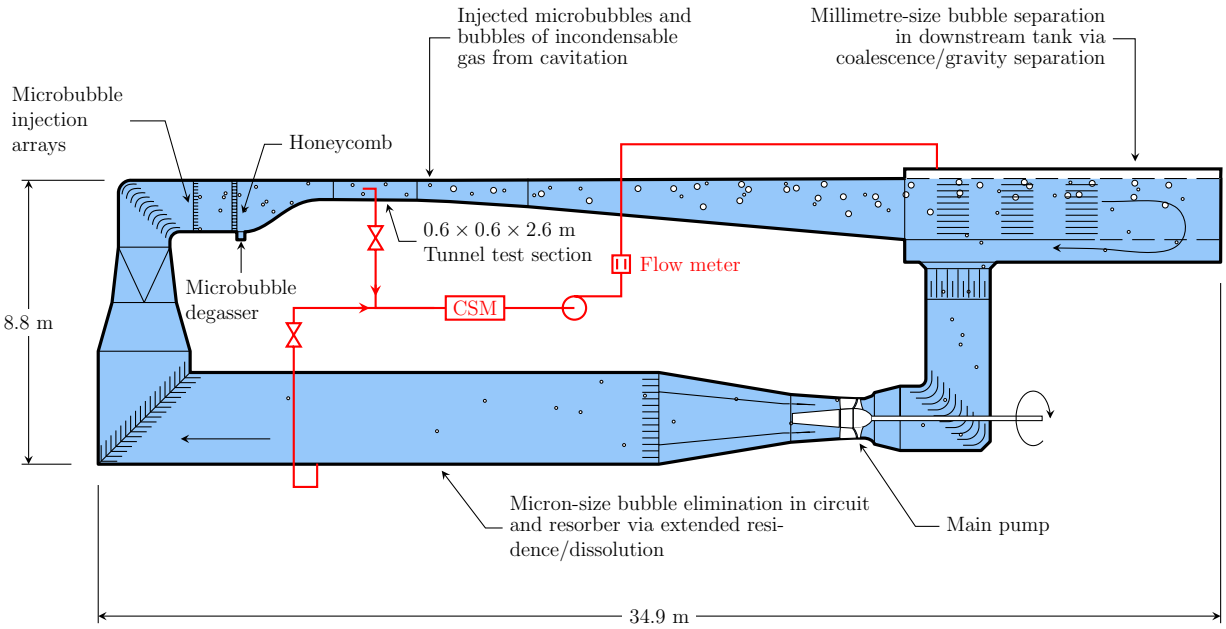

Figure 2.2: Schematic of the AMC cavitation tunnel showing circuit architecture and ancillaries for microbubble and dissolved gas control and CSM circuit integration. Test water for the CSM can be sampled from either the tunnel test section or lower limb resorber.

The tunnel has ancilliaries for fast degassing and nuclei injection that enable strict control of the dissolved gas and nuclei contents. Dissolved gas content is controlled by injecting millimetre-size bubbles into the test section under low pressure, so the water is oversaturated and dissolved gas molecules diffuse into the bubbles. A low test section velocity is also used which increases the residence time of the bubbles in the test section and therefore the opportunity for diffusion to occur. The bubbles are advected into the downstream tank where larger ones (> 100 µm in diameter) are removed from the circuit via gravity separation, thus reducing the dissolved gas content in the circuit. Smaller bubbles dissolve in the lower limb resorber due to extended residence under high static pressure. The tunnel water spends about 50% of the total circulation time in the lower limb (39 s out of 85 s for a test-section velocity of 12 m/s). These processes allow for continuous separation of bubbles that have been generated by cavitation or injected purposefully.

The tunnel is designed to operate at low dissolved oxygen (DO) levels of nominally 30% of saturation at atmospheric pressure, which promotes microbubble dissolution around the entire circuit. The natural nuclei population comprises any remaining nuclei. With the

exception of one test to assess the effectiveness of free gas removal in the tunnel (Fig. 2.8), the nuclei injection system was not used for the present study. Similarly, no cavitating models generating microbubbles were present in the test section.

The degassing procedure described above is typically carried out prior to cavitation measurements depending on the desired dissolved oxygen content. When cavitation testing is conducted at higher test section pressures, undersaturation conditions may occur, resulting in the dissolution of gas into the water and a gradual increase in the dissolved gas content. The degassing procedure is then repeated. In this way, the dissolved oxygen content is controlled within a range during experiments, such as 21–45% relative to saturation at atmospheric pressure, as stated in Chapter 5.

Dissolved oxygen content is used as a proxy for total dissolved gas content and is monitored using a sensor (Endress+Hauser Oxymax W COS41) installed in the lower-limb resorber. It is calibrated onsite as per the manufacturer's instructions (Endress+Hauser, 2004).

While the saturation conditions in the tunnel circuit are mostly undersaturated due to the extended residence and high static pressure in the lower limb, the water can be exposed to oversaturated conditions in the test section through which the typical transit time is $\mathcal{O}(100)$ ms. This is also possible in the upper limb plenum upstream of test section for which the transit time is $\mathcal{O}(1)$ s. It will be shown later that there is a threshold saturation value in this part of the circuit below which the natural nuclei population is no longer independent of operating conditions.

The tunnel main pump is designed to have available net positive suction head and is located in the high pressure lower-limb such that cavitation is minimised. No main pump cavitation has been heard during operation of the cavitation tunnel. Therefore, it is unlikely to have affected the free and dissolved gas contents during testing.

2.3.2 ATLA Flow Noise Simulator

Comparative natural nuclei population measurements were made in a larger cavitation tunnel in Japan as part of a collaborative research project between ATLA and Australia's Defence Science and Technology Group. The Japanese FNS is situated at ATLA's Naval Systems Research Center in Nakameguro, Tokyo, Japan (Fig. 2.3). The ATLA FNS test section has a 2×2 m cross section and is 10 m long which makes it possible to study scaling effects on cavitation behaviour at large physical scales. It contains 2000 m^3 of filtered municipal water and is operated over a range of DO contents, typically between 30% and 80% of saturation at atmospheric pressure. This is intended to reflect the varying conditions in which different marine vessels operate and to aid in the control of nuclei populations. The test-section centreline absolute pressure range is 20–310 kPa and the flow velocity can be varied between 1.5–15 m/s. Water may spend a significantly longer duration exposed to oversaturated conditions in the FNS test section (1 to 2.5 s) compared to that in the AMC tunnel. This suggests that the saturation conditions in the ATLA FNS test section, by virtue of its larger size, play a more significant role in controlling the natural nuclei population compared to the AMC facility. This observation is supported by the results presented later. The differences in operating conditions and circuit architecture between the AMC and ATLA tunnels represent alternative strategies for nuclei management and control. For the ATLA tunnel, nuclei control is principally achieved through variation of dissolved gas.

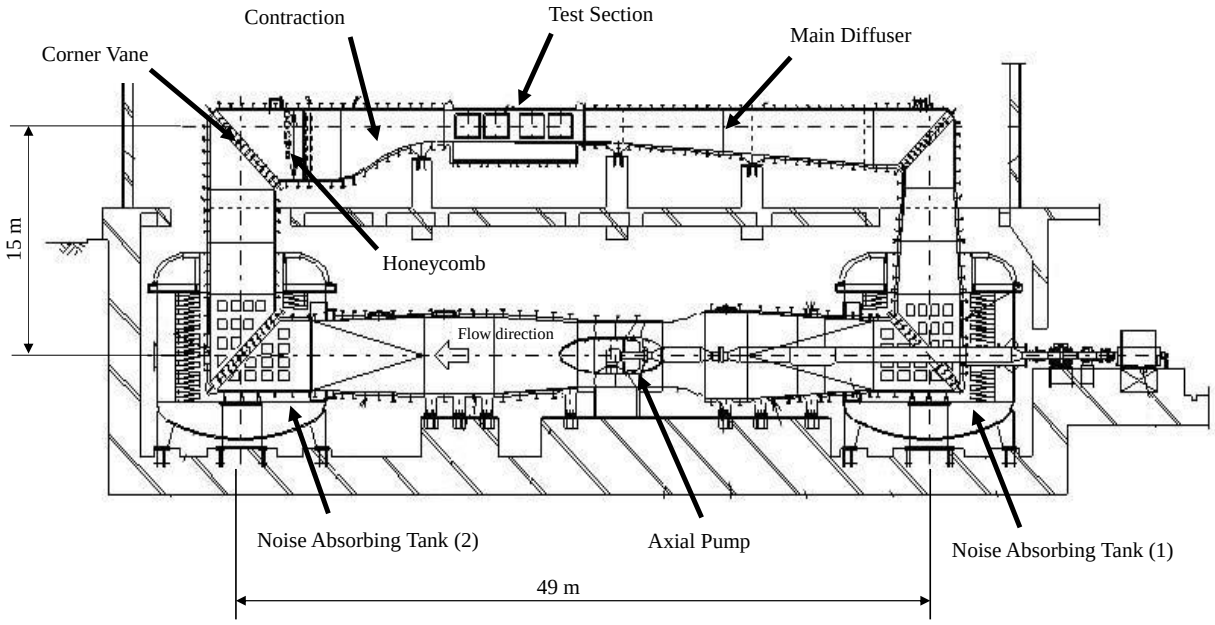

Figure 2.3: Schematic of the ATLA Flow Noise Simulator. Test water for the CSM is sampled from the test section (not shown).

2.3.3 AMC cavitation susceptibility meter

The AMC CSM (Fig. 2.4) was designed by YLec Consultants (Grenoble, France) and is also known as the '*Venturix*' (Pham et al., 1997). It is a hydrodynamic device that uses a centrebody venturi to reduce the pressure and thus activate nuclei in the flow. A piezoceramic sensor bonded to the external sleeve around the venturi is used to detect nuclei activations and ultrasonic flow meters are used to measure the flow rate. The combined measurement of activation rate and volumetric flow rate for a series of throat pressures provides a cumulative distribution of concentration against critical tension.

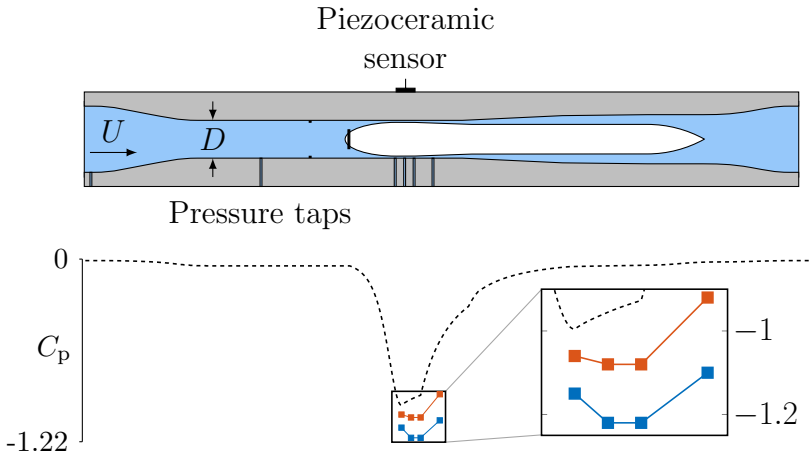

Figure 2.4: Schematic showing venturi arrangement and location of sensor and pressure taps. The centrebody is shown in white and outer sleeve in grey. Bottom plot is pressure coefficient, C_p, against location (scaled to the schematic) showing the measured pressure coefficient (squares) for the minimum (2.9×10^4, blue) and maximum (1.5×10^5, red) Reynolds numbers and the solution from one-dimensional inviscid theory in black dashes.

The tension applied to the water in the venturi is derived from a calibration based on the flow rate through the venturi and prior measurement of the pressure at four streamwise locations along the outer sleeve of the centrebody venturi. This tension represents the critical pressure of the strongest nucleus activated in the venturi. Sample calibration measurements are given in Fig. 2.4 for two Reynolds numbers ($Re = \frac{UD}{\nu}$, where U is the mean flow velocity, D is the pipe diameter and ν is the fluid kinematic viscosity). The data are represented as pressure coefficients ($C_p = \frac{p_x - p_1}{\frac{1}{2}\rho {U_{VT}}^2}$, where p_x is the pressure at location x in the throat, p_1 is the pressure at a reference location upstream of the venturi, ρ is the density of water and U_{VT} is the flow velocity in the venturi throat). At the higher Reynolds number, the boundary layers are thinner, increasing the effective cross-sectional area of the venturi, and thus the pressure drop is reduced. The solution for one-dimensional inviscid theory demonstrating the upper bound with Reynolds number is shown for reference. The calibration thus characterises how the pressure coefficient in the venturi changes with Reynolds number. More detailed information on the calibration of the CSM is described in Khoo et al. (2016).

A mirror polish was specified for the manufacture of a smooth centrebody. In order to assess the cavitation behaviour in the venturi, an acrylic sleeve was temporarily installed for cavitation observation. Photographs were taken of vapour cavities downstream of the venturi throat as the pressure was reduced. The location of inception was inferred from the angular locations of these vapour cavities with no obvious trend being observed. This suggests that parasitic cavitation was not occurring. Visual observations have been made of the centrebody condition during equipment assembly and disassembly. These observations were made several times over a couple of years, though no noticeable surface alteration has been detected.

Cavitation events are counted by measuring the voltage, V_{P}, across a piezoceramic sensor (1 MHz resonant frequency). The signal is sampled at 2 MHz using an NI USB-6366 data acquisition device. The analog input bandwidth of the device is 1 MHz (i.e. measured amplitude 3 dB less than actual at this frequency), so it essentially acts as an anti-aliasing filter. A four stage discriminator algorithm is implemented via digital filtering to count individual nuclei activations:

1. High-pass filter with 100 kHz cut-off (to remove low frequency structural resonance)
2. Rectification (to make all events the same sign)
3. Low-pass filter with 200 Hz cut-off (to smooth response to activations into single peaks)
4. Log function (to homogenise response amplitudes to improve peak discrimination, that is, a visual aid for threshold setting)

An example of raw and processed signals is shown in Fig. 2.5. The effect of discriminator threshold level on the total nuclei count is shown in Fig. 2.6, for the complete dataset from which the results shown in Fig. 2.5 were extracted. If the threshold is set too high, nuclei events are missed. Conversely, if the threshold level is set too low, additional peaks due to unfiltered structural response are counted, resulting in a higher nuclei concentration. The threshold has been set to discriminate all peaks on the time series which corresponds with a plateau shown in Fig. 2.6.

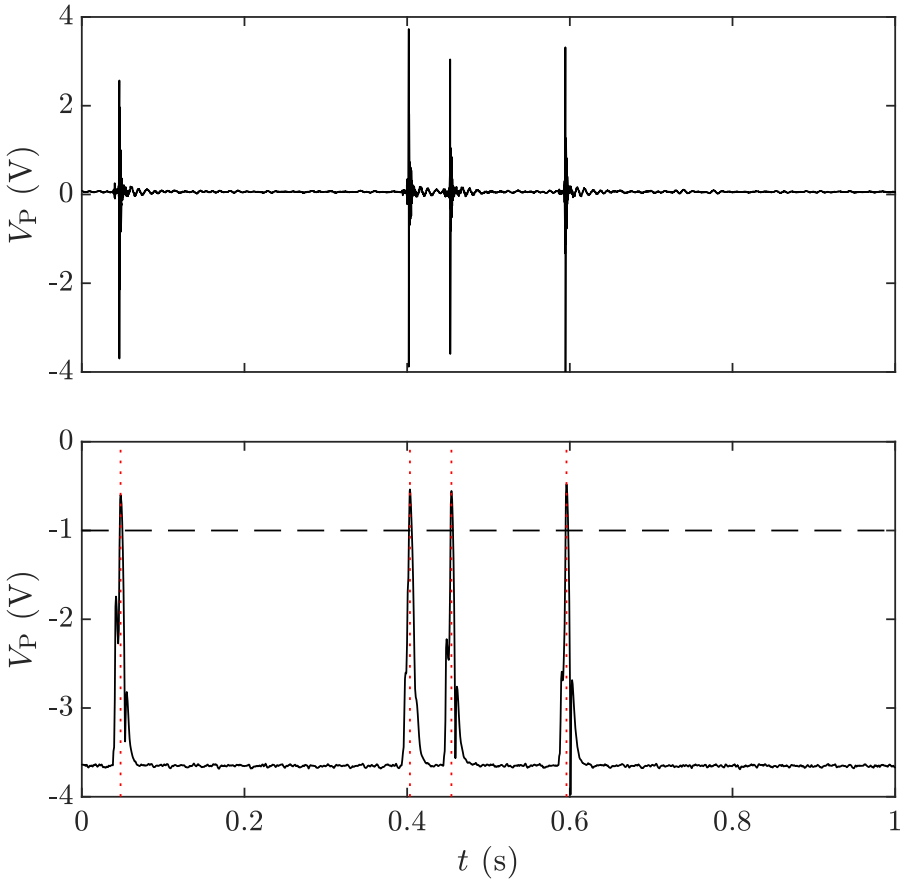

Figure 2.5: Voltage output, V_P, from CSM piezoceramic sensor: raw (top) and processed (bottom). A threshold level of -1 (horizontal, dashed line) gives a count of 4. Vertical, dotted lines indicate detections.

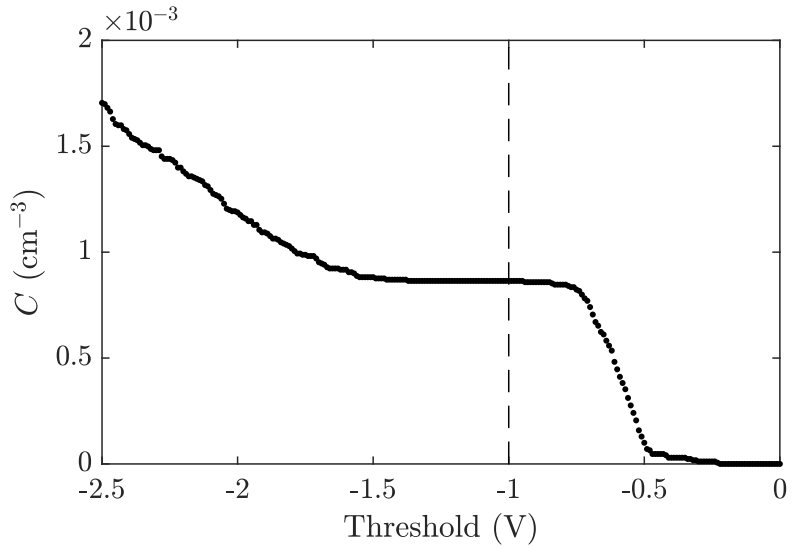

Figure 2.6: Effect of CSM discriminator threshold setting on measured nuclei concentration, C.

The CSM is suitable for measuring nuclei with critical pressures ranging to several atmospheres of tension corresponding to micro- and nanometre equivalent bubble sizes, in hydrodynamic test facilities. A particular advantage of the CSM for nuclei measurements is that critical pressures of all viable nuclei that would be active in a cavitating flow are directly measured. This is in contrast with optical techniques where all entities (e.g. microbubbles and particles) are measured whether they are viable nuclei or not. Although critical pressures can be estimated for microbubbles measured optically, this is not possible for active particles which can only be measured by mechanical activation. Optical techniques are also limited in minimum measurable sizes by the diffraction limit of the system.

A shortcoming of mechanical activation techniques is that although larger microbubbles greater than about 50 µm in diameter are counted, their size cannot be determined with high accuracy as critical pressures are all close to vapour pressure. As water must be sampled for this technique, it can be intrusive and has no spatial resolution which therefore makes it only suitable for measurements of natural nuclei populations. The maximum concentration measurable with the present AMC CSM is approximately 0.3 cm^{-3} before either the CSM venturi throat, or the discriminator algorithm, become saturated. Dilution of the sampled water may be used to reduce the cavitation event rate, but this may also alter the nuclei population.

In both test facilities, water was sampled from the test section through a streamlined sampling probe designed to avoid cavitation across the typical range of tunnel operating conditions. In the AMC cavitation tunnel, the probe was mounted to the test-section floor, nominally midway along the test section, with water sampled from the test section centreline. In the ATLA FNS, the probe was mounted to the test-section side wall, located about 8 m from the test-section entrance, 1 m from the ceiling, with water sampled 0.3 m

away from the wall. Water was passed through the venturi located approximately 5 m below the test section. The length of pipework between the sampling probe and venturi was about 7 m for the AMC cavitation tunnel and about 13 m for the ATLA FNS, resulting in about twice the transit time at the ATLA tunnel. In the AMC tunnel, water can alternatively be sampled from the resorber in the lower limb of the tunnel. This has implications for measurement of natural nuclei populations during cavitation testing, as discussed later in Sect. 2.4.5.

The natural nuclei population in the ATLA tunnel is known to be strongly dependent on tunnel operating history (Takahashi et al., 2019). Therefore, the same pre-pressurisation procedure was used prior to each nuclei distribution measurement to minimise these effects. The FNS test-section pressure was set to 200 kPa for at least 10 minutes (it has been observed that this combination of pressure and duration is effective at resetting the natural nuclei population in the FNS to the baseline level (Takahashi, 2021)), then reduced to the value specified for the nuclei measurement. After the test-section conditions were set in either facility (i.e. pressure, p_{TS}, flow velocity, U_{TS}, and DO concentration, c), the venturi throat pressure was set using a downstream pump to produce approximately one cavitation event every 10 s. The throat pressure was systematically decreased by incrementally increasing the pump speed and data were recorded at each pressure. This process was repeated until a flow rate was reached such that the throat pressure could no longer be reduced (choked condition) or the event rate saturates being too high for individual events to be discriminated (> 300 events per second).

2.3.4 Data reduction and presentation

The nuclei populations reported in this paper, with the exception of Fig. 2.23, are cumulative distributions representing the concentration of nuclei in the sampled volume of water that have a critical pressure, p_{c}, equal to or greater than the minimum venturi throat pressure at that measurement point. The critical pressure is typically expressed as a tension, $T_{\mathrm{c}} = p_{\mathrm{c}} - p_{\mathrm{v}}$, which represents how much the throat pressure, p_{c}, must be reduced below vapour pressure, p_{v}, for a nucleus to be activated.

The DO concentration is measured in units of mg/L and can be expressed as a percentage, γ, which describes the ratio of the DO concentration at a given pressure to saturation at atmospheric pressure (9.1 mg/L at 20°C). The saturation level of DO in water at equilibrium conditions, c_{sat}, at a given pressure and temperature can be calculated using the following equations (Warneck and Williams, 2012; Worch, 2015):

$$c_{\mathrm{sat}} = p_{\mathrm{g}} K_{\mathrm{H}} M \tag{2.2}$$

where $p_{\mathrm{g}} = 0.21(p_{\infty} - p_{\mathrm{v}})$ is the partial pressure of oxygen in air saturated with water vapour, p_{∞} is the ambient pressure of the water, K_{H} is the Henry's law constant and M is the molar mass (32 g/mol for O_2).

It is also useful to calculate the saturation pressure, p_{sat}, corresponding to a particular measured dissolved oxygen concentration, c:

$$p_{\text{sat}} = p_{\text{v}} + \frac{c}{0.21 K_{\text{H}} M} \tag{2.3}$$

The relative saturation level of oxygen in water, r, which describes the tendency for DO to either pass into solution, or come out of solution as free gas, is defined as the ratio of the measured DO concentration and the saturation level of DO at a reference pressure, p_∞:

$$r = \frac{c}{c_{\text{sat}}} \times 100\% \tag{2.4}$$

That is, ignoring surface tension, if $r > 100\%$ the water is oversaturated and dissolved gas will tend to be released and for $r < 100\%$ the water will be undersaturated and gas will tend to pass into solution. As an example, the saturated DO concentration in water at 20°C and an ambient pressure of 35 kPa is $c_{\text{sat}} = 3$ mg/L. If the measured DO concentration in the water is $c = 2.4$ mg/L, the relative saturation is $r = 80\%$ and therefore the water is undersaturated. Given an air-water interface, oxygen would dissolve in the water at this condition. Since the pressure varies throughout the circuit and changes with test-section conditions, the degree of saturation varies accordingly. For the AMC tunnel, a suitable reference pressure is that within the plenum upstream of the contraction, p_{up}. The reasoning for this is that the water spends about 20 times longer in the plenum ($\mathcal{O}(1)$ s) compared to the test section ($\mathcal{O}(100)$ ms), so the saturation conditions in this part of the circuit influence gas exchange or transport between liquid and free gas bubbles much more than the test-section conditions. The notation for the relative saturation is therefore r_{up} (r_{TS} is used when test-section pressure is the reference pressure). The pressure in the plenum is given by:

$$p_{\text{up}} = p_{\text{TS}} + \frac{1}{2}\rho {U_{\text{TS}}}^2 (1 - \eta^2) - \rho g h \tag{2.5}$$

where ρ is the density of water, and for the AMC cavitation tunnel, $\eta = \frac{9}{64}$ is the contraction ratio and $h = -0.5$ m is the height of the centreline upstream of the contraction relative to the test-section centreline. For the ATLA FNS, $\eta = \frac{1}{5.06}$ and $h = -1.25$ m. However, water spends $\mathcal{O}(1)$ s in the ATLA FNS test section and it is therefore expected to play a more significant role in controlling the natural nuclei population.

2.4 Results

2.4.1 Convergence study

A convergence study was undertaken at a number of venturi throat tensions to identify a suitable sampling duration. Typical tunnel operating conditions for cavitation studies were used ($p_{TS} = 50$ kPa, $U_{TS} = 7$ m/s and $\gamma = 38\%$). Figure 2.7 shows a comparison of data taken in 60 and 600 s blocks. The amount of scatter increases as the magnitude of the tension decreases due to the decreasing nuclei activation rate, and thus smaller sample sizes for a given sampling duration. This scatter could be reduced by using an event count criterion (rather than a fixed acquisition time) to increase the sample size for throat pressures closer to vapour pressure, as used by Venning et al. (2018b). However, the long acquisition durations required to capture large sample sizes at such throat tensions can become impractical when multiple measurements are required. Assuming that the data for the 10 minute runs have converged, 60 s blocks were deemed to be acceptable as they give sufficient convergence for the purposes of this study while minimising total data acquisition time. It should be noted that a more conservative sampling duration of 120 s was used at the ATLA FNS.

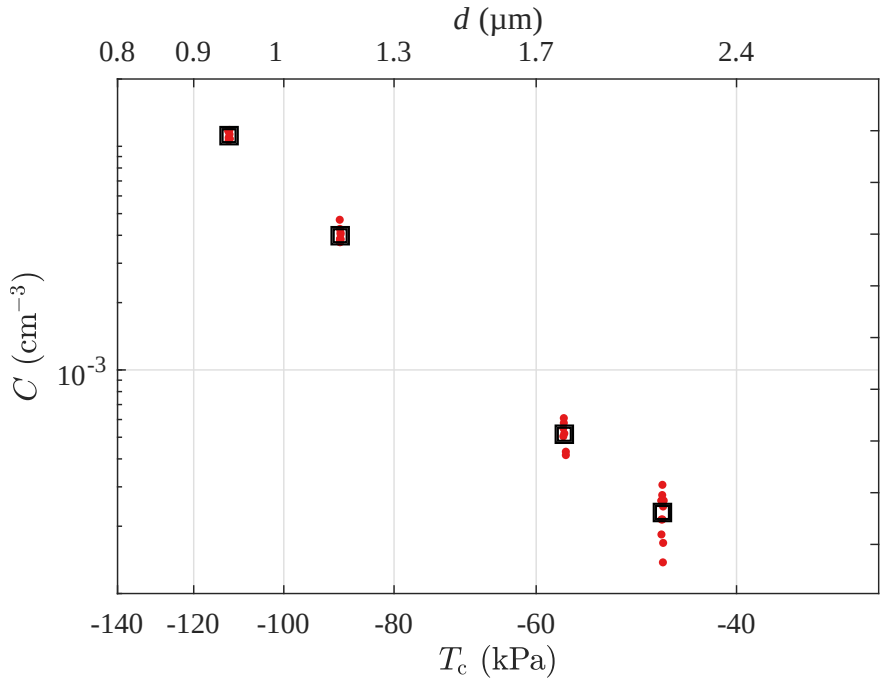

Figure 2.7: Cumulative nuclei distribution as nuclei concentration, C, against critical tension, T_c. The corresponding equivalent bubble diameters, d, are also provided. The squares and red points represent 600 and 60 second acquisition periods (or blocks), respectively. Tunnel conditions were $p_{TS} = 50$ kPa, $U_{TS} = 7$ m/s and $\gamma = 38\%$.

2.4.2 Effectiveness of free gas removal

A test was conducted to assess the effectiveness of free gas removal in the test facility. The measured nuclei concentration for a constant venturi throat pressure, $T_c = -14$ kPa, is shown in Fig. 2.8. The nuclei injection system was turned on at the first vertical line and off at the second then the time taken for the concentration to stabilise or return to its initial state was observed. The results show that the measured nuclei concentration increased within 10 s after nuclei injection was started and returned to its initial state within 20 s after injection was halted. As bubble dissolution in the CSM circuit is possible (Gowing et al., 1988), further microbubble measurements were made in the test section using IMI (Brandner et al., 2018). The results showed the same behaviour as for the CSM, confirming that free gas is effectively removed from the AMC tunnel and that injected nuclei do not recirculate and accumulate, at least for typical tunnel operating conditions.

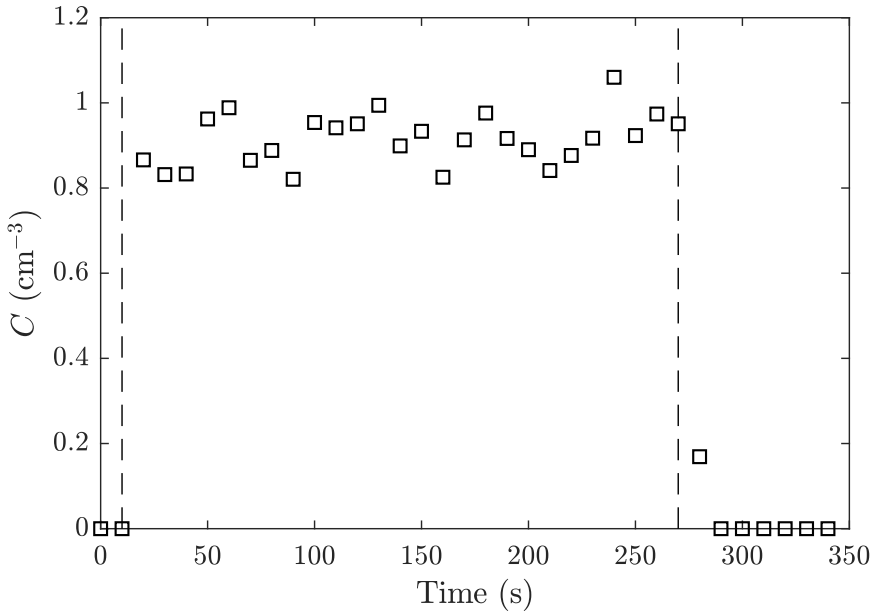

Figure 2.8: Effectiveness of free gas removal in the AMC cavitation tunnel. The nuclei concentration, C, is seen to increase immediately after start of injection (left, dashed line) then to return back to the initial level shortly after injection is ceased (right, dashed line). Tunnel conditions were $p_{TS} = 50$ kPa, $U_{TS} = 7$ m/s and $\gamma = 32\%$. Venturi throat pressure was $T_c = -14$ kPa (equivalent bubble diameter of d =5.8 µm).

2.4.3 Historical trends

Variations in the natural nuclei population over time in the AMC tunnel were recorded using continuous CSM measurements at a fixed throat tension ($T_c = -80$ kPa) and undersaturated test-section conditions over 35 hours with tunnel operating conditions of $p_{TS} = 50$ kPa and $U_{TS} = 7$ m/s. The nuclei concentration for this tension gradually decreases by approximately 1.8×10^{-3} cm^{-3} during this period, as shown in Fig. 2.9. The same y-axis range is used as for later graphs (e.g. Fig. 2.11) which allows the changes to be assessed relative to the other nuclei distribution measurements. Note that the DO content increased from 37% to 51% over the 35 hours due to equilibration, which includes air dissolution via the free surface in the upper part of the tunnel downstream tank. There are several possible explanations for the decrease in concentration, including depletion of nuclei due to activation and destruction during the CSM measurement process, long term exposure to undersaturated conditions and natural variations in the potential populations of gas-containing microorganisms.

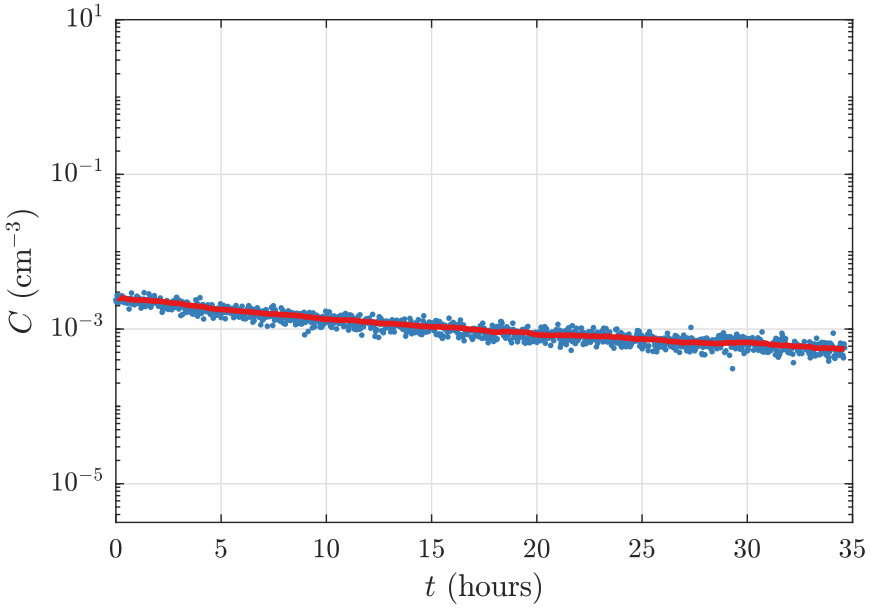

Figure 2.9: CSM measurements showing a reduction in natural nuclei concentration in water subjected to a tension of $T_c = -80$ kPa (equivalent bubble diameter of d =1.3 µm) over a 35 hour period. The blue data points represent sequential acquisitions in 100 s blocks. The red line is a moving average of these data. Tunnel conditions were $\gamma = 39\%$ ($t = 0$ h) $\rightarrow 53\%$ ($t = 35$ h), $p_{TS} = 50$ kPa and $U_{TS} = 7$ m/s.

Calculations were carried out to assess the viability of the depletion hypothesis. Knowing the nuclei activation rate in the CSM and flow rate through the device, the total number of activations over the 35-hour period is estimated as 1.6×10^5. If the overall population had decreased by this amount, the concentration would have reduced to 2.0×10^{-3} cm^{-3}, which is higher than the final measured concentration of about 0.57×10^{-3} cm^{-3}. That is, the number of activations would only account for about 23% of the observed reduction in concentration. This suggests that nuclei depletion due to CSM operation is not the major or sole contributor to the observed reduction in nuclei concentration with time.

Historical trends were further studied by taking daily measurements of the natural nuclei population at the same nominal tunnel conditions (undersaturated in the test section and plenum) during a one-week test campaign. These data presented in Fig. 2.10 show the population to shift to the lower left over the week. This corresponds to a reduction in cumulative concentration of about an order of magnitude for a fixed tension. It is difficult to ascertain whether it is the concentration or tension, or both, that is varying with time. After several weeks of other experiments, the undersaturated natural nuclei population was remeasured and observed to return to close to its initial position. Similar regeneration has also been observed after degassing using bubble injection. Furthermore, monitoring over a two-year period has shown the natural nuclei population to fluctuate within an order of magnitude, which indicates that although there is no single baseline population, there do appear to be upper and lower bounds.

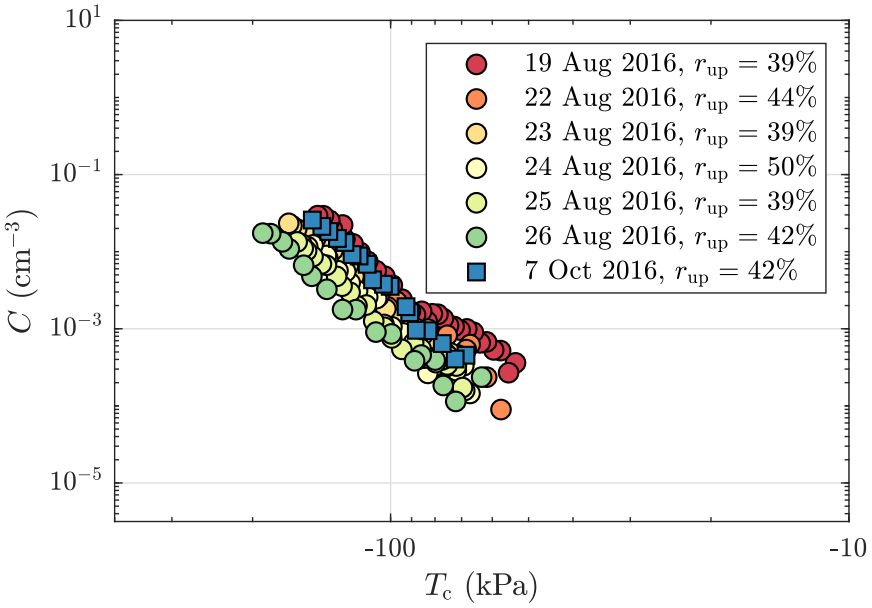

Figure 2.10: CSM measurements over a one-week test campaign (circles) showing a reduction in natural nuclei population, then regeneration after several weeks (squares). Note that the tunnel conditions were varied in between measurements, but each nuclei distribution was measured at the same nominal conditions of $\gamma = 30$–39%, $p_{TS} = 50$ kPa and $U_{TS} = 7$ m/s.

As noted above, the natural nuclei population is potentially affected by several properties of the water or processes within the tunnel including gaseous diffusion between tunnel water and the gas volume used to control the tunnel pressure, diffusion between nuclei and tunnel water around the circuit driven by pressure and residence variations, although the former has been developed to be a relatively slow process. Other possible influences are contaminants of various origins and even cosmic radiation. Given the complexity of such a system it is difficult to gain more understanding from the current investigation. Clearly, further insights must be gained from systematic elimination of these factors including testing with a much smaller isolated volume of water eliminating mass transfer, fixing the volume of dissolved gas, treatment to set or control contaminants including sterilisation to eliminate any biological entities, minimising pressure variations and shielding from radiation. In such a setup the natural nuclei population could be continuously measured with

a CSM providing the opportunity to assess its dynamic behaviour with greater control over the properties and processes which may affect natural nuclei over time.

Without an accurate measurement or prediction of the nuclei content, unexplained differences in cavitation inception results could occur from day to day. Ideally, the natural nuclei population could be predicted using a database or model based on tunnel conditions such as test-section pressure, velocity and DO content. However, the observed historical trends, which are not currently well-understood, preclude the use of a model-based approach. Until these factors are better understood, regular monitoring of the natural nuclei population is necessary when investigating cavitation phenomena that are influenced by nuclei content.

2.4.4 Effect of test-section conditions

The effect of test-section pressure on the natural nuclei population is presented in Fig. 2.11, for a low DO content and a mid-range test-section flow velocity. No significant differences between the measured distributions are evident over the range of pressures tested, with the exception of a slight reduction in concentration for the highest test-section pressure. The distributions in Fig. 2.11 appear to follow a power law, consistent with the findings of Venning et al. (2018b). Uncertainty bars are also provided in Fig. 2.11 for one of the data series. Further details on this uncertainty analysis can be found in Khoo et al. (2016).

The effects of test-section flow velocity and DO content on the natural nuclei population are shown in Figs. 2.12 and 2.13, respectively. Over this range of conditions, neither parameter has a measurable influence. This indicates that for typical operating conditions, the natural nuclei population is independent of the AMC cavitation tunnel conditions. The nuclei distributions presented thus far were measured under conditions for which the water in the plenum was undersaturated ($r_{\text{up}} < 100\%$). That is, the static pressure in the plenum was greater than the equilibrium saturation pressure, meaning that free oxygen will tend to dissolve in the water.

In contrast, at extreme operating conditions, higher concentrations of weaker nuclei were observed when the sampled water was exposed to oversaturated conditions in the plenum ($r_{\text{up}} > 100\%$), as shown in Fig. 2.14. This is not an unexpected result, as dissolved gas will tend to come out of solution when water is exposed to a pressure less than equilibrium saturation pressure.

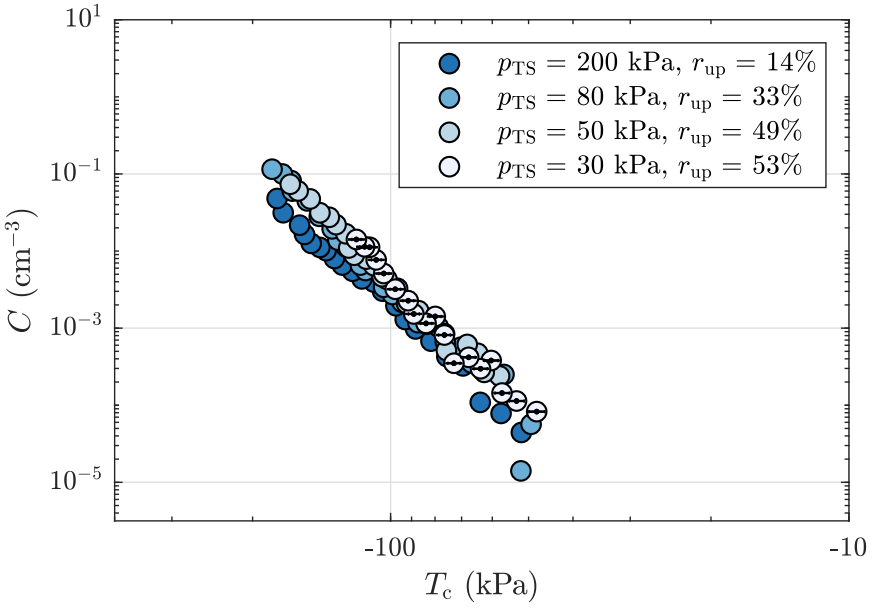

Figure 2.11: Effect of test-section pressure, p_{TS}, on the natural nuclei population. The relative saturation level of oxygen in the plenum, r_{up}, is also provided. Test-section pressure has little influence across this range of tunnel conditions. Uncertainty intervals for both tension and nuclei concentration are plotted for the 30 kPa data series. Tunnel conditions were $\gamma = 30$–38% and $U_{TS} = 7$ m/s.

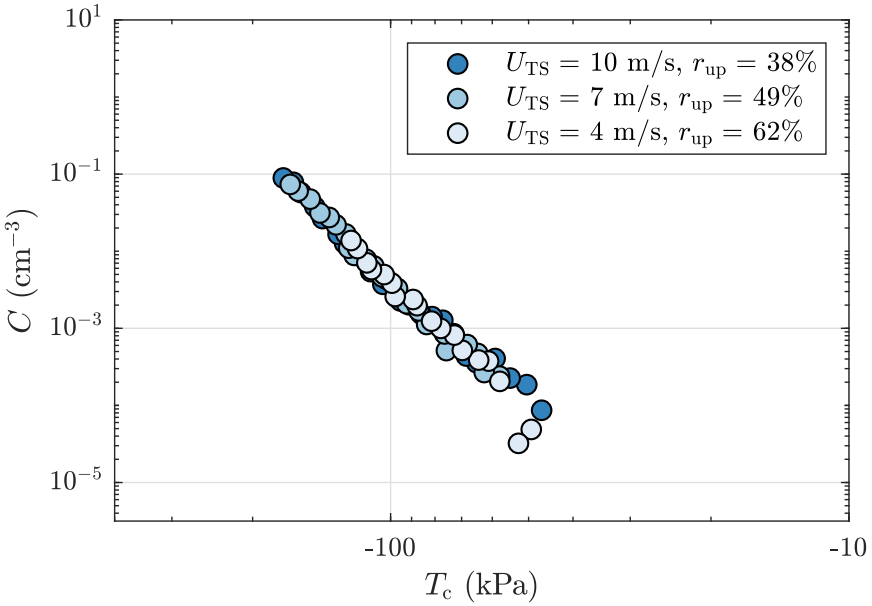

Figure 2.12: Effect of test-section velocity, U_{TS}, on the natural nuclei population. The relative saturation level of oxygen in the plenum, r_{up}, is also provided. There is little influence across a range of test conditions. Tunnel conditions were $\gamma = 38$–39% and $p_{TS} = 50$ kPa.

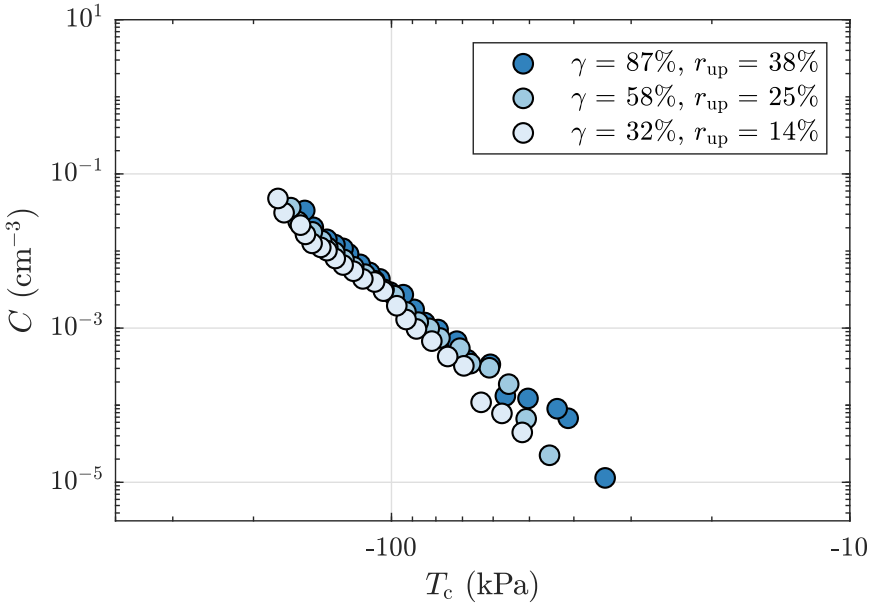

Figure 2.13: Effect of dissolved oxygen content, γ, on the natural nuclei population. The relative saturation level of oxygen in the plenum, r_{up}, is also provided. There is little influence across a range of test conditions. Tunnel conditions were $p_{\mathrm{TS}} = 200$ kPa and $U_{\mathrm{TS}} = 7$ m/s.

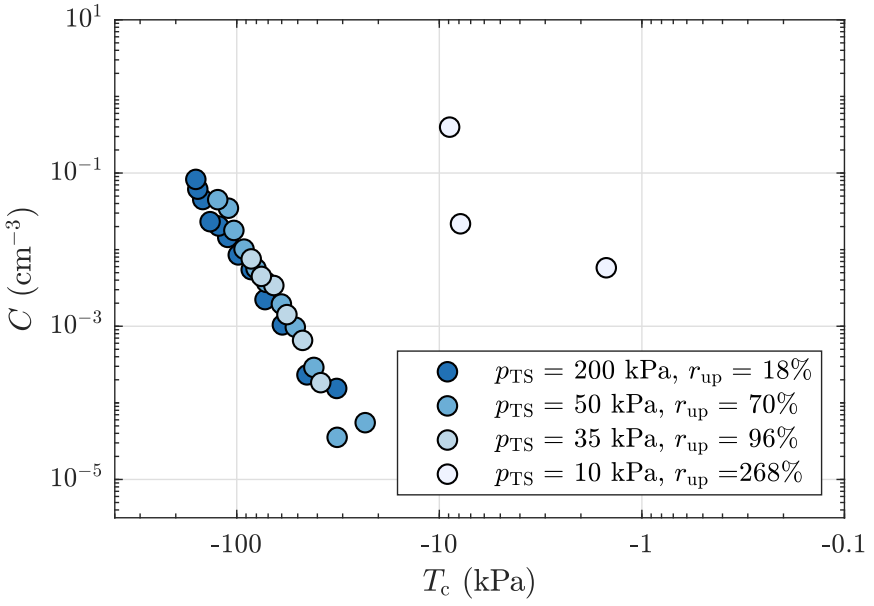

Figure 2.14: Effect of test-section pressure, p_{TS}, on the natural nuclei population at low test-section velocity. The relative saturation level of oxygen in the plenum, r_{up}, is also provided. The nuclei population increases noticeably when the test-section pressure is reduced to 10 kPa (oversaturated). Tunnel conditions were $\gamma = 38\%$ and $U_{\mathrm{TS}} = 2$ m/s.

A summary of nuclei distributions measured in the AMC tunnel presented as plenum static pressure against saturation pressure of water in the plenum is shown in Fig. 2.15. Each data point represents a measured nuclei distribution. It should be noted that while data in each of the Figs. 2.11 to 2.14 were taken over a maximum period of 12 hours to minimise historical effects, this was not practical for the large dataset captured in Fig. 2.15. Power-law trend lines were fitted to each nuclei distribution. Distributions that show a consistent power-law trend indicating no effect of increasing relative saturation are represented with hollow symbols. These indicate that the distributions were essentially unchanged from those presented in Figs. 2.11 to 2.13, hereafter termed the baseline. Distributions that depart from the power law as determined from the fitted parameters are represented with solid symbols. These signify that the nuclei distribution had increased above the baseline. The 10 kPa data series in Fig. 2.14, as indicated by the solid red symbol in Fig. 2.15, is an example of this behaviour.

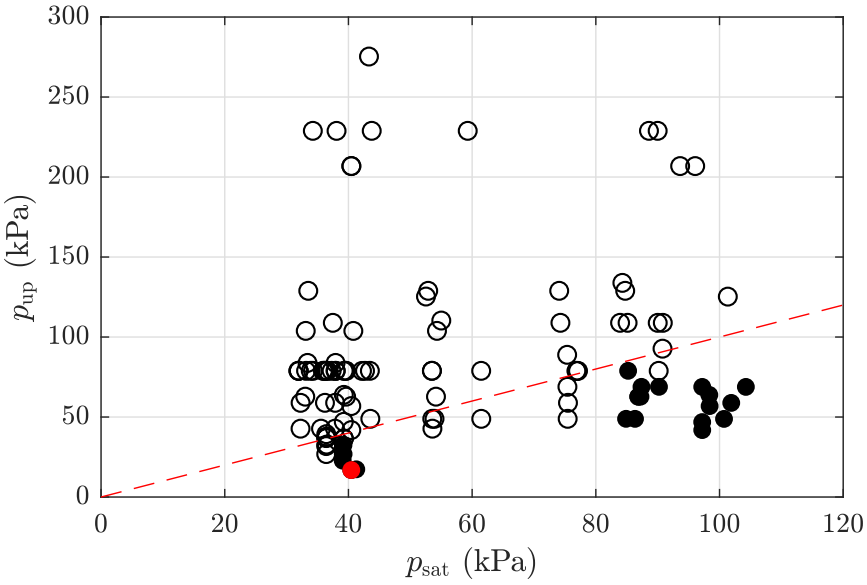

Figure 2.15: Baseline natural nuclei populations (hollow) and distributions above the baseline (solid) as a function of plenum pressure, p_{up}, and saturation pressure of the water, p_{sat}. The red line represents when these pressures are equal ($p_{up} = p_{sat}$, $r_{up} = 100\%$), i.e. the line represents a conservative delineation where populations remain at baseline if $r_{up} < 100\%$. The red dot represents the 10 kPa data in Fig. 2.14 which is above the baseline.

The red dashed line in Fig. 2.15 represents the conditions for which the water in the plenum is saturated with DO (i.e. $p_{up} = p_{sat}$, $r_{up} = 100\%$). The water upstream of the contraction is undersaturated for points above this line and oversaturated for points below. The natural nuclei population was observed to increase only for oversaturated conditions. Little information is available on the nature of the natural nuclei population, however, this similarity in behaviour to microbubbles indicates that gaseous diffusion plays a role in the population dynamics. Some nuclei distributions measured with oversaturated water remain at the baseline. In this sense, this behaviour could be attributed to the effect of surface tension delaying diffusion beyond equilibrium conditions, as occurs for microbubbles. An additional influence may stem from the dissolution of the free gas in the CSM circuit between the sampling probe and the venturi.

The increase in static pressure in the CSM circuit due to the decrease in dynamic pressure (relative to the test section) would make the water more undersaturated. This would result in the dissolution of free gas present, the extent of which is influenced by the residence time of the water in the CSM circuit as it transits between the sampling point and the centrebody venturi (approximately 5 s at the AMC tunnel). This effect could be reduced by moving the venturi closer to the test section and minimising the transit time at the expense of moving the range of measurable tensions towards higher tensions (i.e. more negative, according to the definition of tension in this paper).

2.4.5 Effect of sampling location

The historical trends discussed in the previous section necessitate regular monitoring of the natural nuclei population when carrying out low cavitation number testing in unseeded flows. Due to the relative size and positioning of the CSM sampling probe within the AMC tunnel test section, it is not ideal to sample water from the test section for CSM measurements while conducting cavitation testing. If the sampling probe was positioned upstream of a test component, it would affect the oncoming flow field. Additionally, it cannot always be positioned downstream due to the cavitating wake of the test model.

Tests were conducted to determine whether the natural nuclei population in the test-section water could be inferred from water sampled from the tunnel resorber. The CSM circuit can be configured to sample water from either the test section or the resorber in the lower limb of the tunnel (see Fig. 2.2). Measurements were repeated at the same nominal test-section conditions for both sampling locations. For undersaturated conditions in the plenum, no significant difference was observed regardless of whether the water was sampled from the test section or resorber, as shown in Fig. 2.16 . This indicates stability of the natural population around the circuit. However, for water sampled from the test section in oversaturated conditions, the natural nuclei population tends to increase above the baseline with the amount of oversaturation, consistent with Fig. 2.15. This is also the case for higher test-section velocities (not shown) for which the degree of oversaturation increases with decreasing test-section pressure. The natural nuclei populations of water sampled from the resorber, which had not been exposed to oversaturated conditions in the plenum, remained at the baseline even at extreme conditions (i.e. low p_{TS} and U_{TS}, high r_{up}). From these results it can be concluded that a baseline nuclei distribution in the test section can be inferred from CSM measurements of water sampled from the resorber for undersaturated conditions in the plenum (i.e. $p_{\mathrm{up}} > p_{\mathrm{sat}}$).

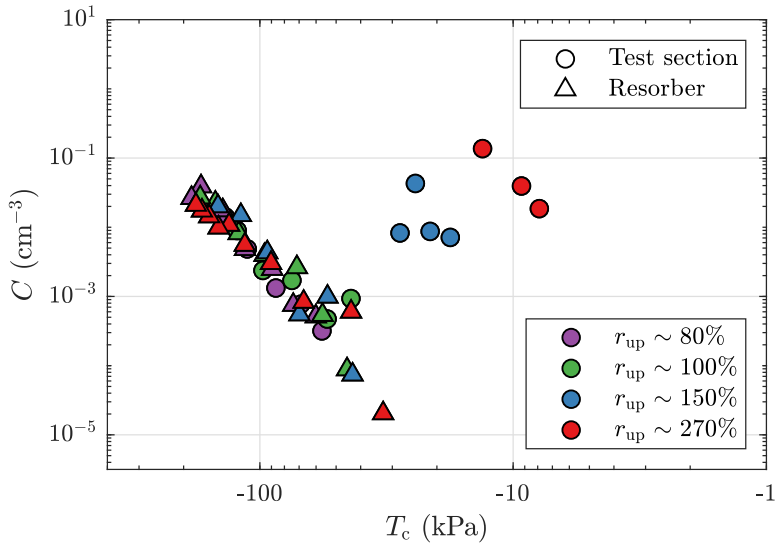

Figure 2.16: Effect of sampling location on natural nuclei population for a range of relative saturation levels. The sampling location is denoted by the symbol shape. Measurements are at the baseline level for each location except for the test section when $r_{up} > 100\%$. Tunnel conditions were $\gamma = 35$–42% and $U_{TS} = 2$ m/s.

2.4.6 Comparisons with the ATLA test facility

A comparison of measurements using the AMC CSM at the AMC and ATLA tunnels for similar operating conditions for a range of test-section velocities is shown in Fig. 2.17. The test-section pressure was approximately equal to the saturation pressure. The independence of the natural nuclei population from the test-section velocity at these conditions is consistent between the test facilities. The AMC tunnel data show a temporal variation of up to an order of magnitude as described above and the ATLA tunnel data lie within this range. For similar tunnel operating conditions, the AMC and ATLA tunnel data compare closely in magnitude which is somewhat coincidental. However, the close comparison of slope and independence of velocity indicate a universality of this water property.

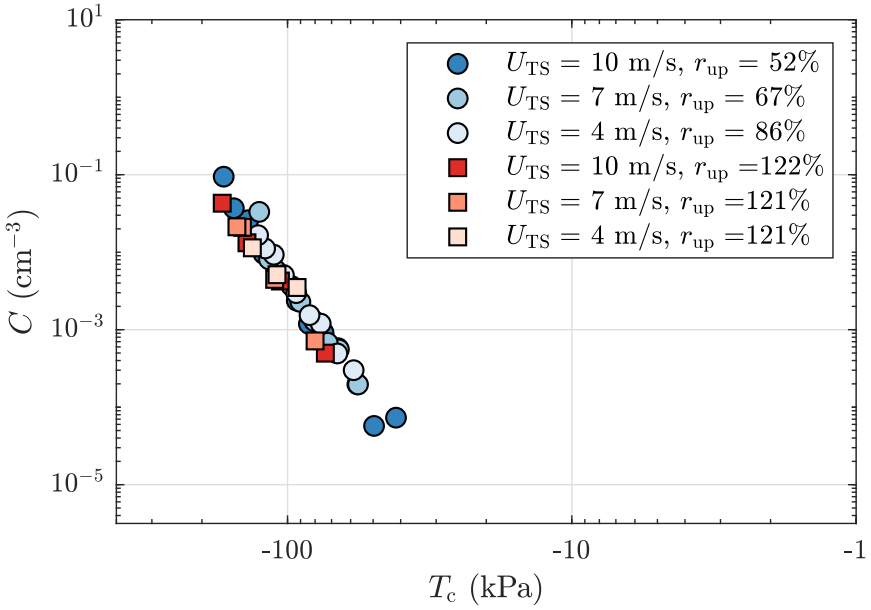

Figure 2.17: Comparison of natural nuclei populations at the same nominal test conditions (across a range of test-section velocities, U_{TS}, in the AMC (circles) and ATLA (squares) cavitation tunnels. The relative saturation levels of oxygen in the plenum, r_{up}, and the test section, r_{TS}, are provided for each tunnel respectively. Similar distributions are observed from the two facilities of significantly differing circuit architecture and dimensions. Tunnel conditions were γ =52–59% and p_{TS} = 50 kPa.

At certain oversaturated conditions, an initial increase in the natural nuclei population followed by a reduction with decreasing throat pressure was observed in the ATLA FNS (Fig. 2.18). Since CSM nuclei population measurements are inherently cumulative, these results raise questions about the CSM behaviour. Simultaneous CSM and optical measurements could be used to confirm how representative these CSM nuclei distribution measurements are of the test-section water, however this would only be possible for a limited range of microbubble sizes due to the diffraction limits of optical techniques, see Fig. 2.1. The fact that the measured distributions seem to return to the baseline level at higher tensions tends to indicate the influence of another factor. This discrepancy only occurs when the flow rate through the venturi is low, which could indicate Reynolds number effects such as laminar boundary layer separation and cavity detachment as observed in a venturi tube diffuser by d'Agostino and Acosta (1991a). The Reynolds numbers used for the venturi throat pressure calibration appear to be sufficiently high to ensure turbulent boundary layers (thus suppressing boundary layer separation in the diffuser section) in the single-phase flow (Khoo et al., 2016). However, it is more difficult to be sure of the boundary layer condition in two-phase flows in which instabilities may arise due to interactions between cavities and boundary layers. Furthermore, the venturi was operated at a slightly lower Reynolds number (4.8×10^4 for $p_{TS} = 30$ kPa) in the ATLA FNS compared to the AMC tunnel (5.9×10^4), noting that the initial increase was not observed in the AMC cavitation tunnel under similar operating conditions. Alternatively, the behaviour may be related to the test facility or CSM circuit.

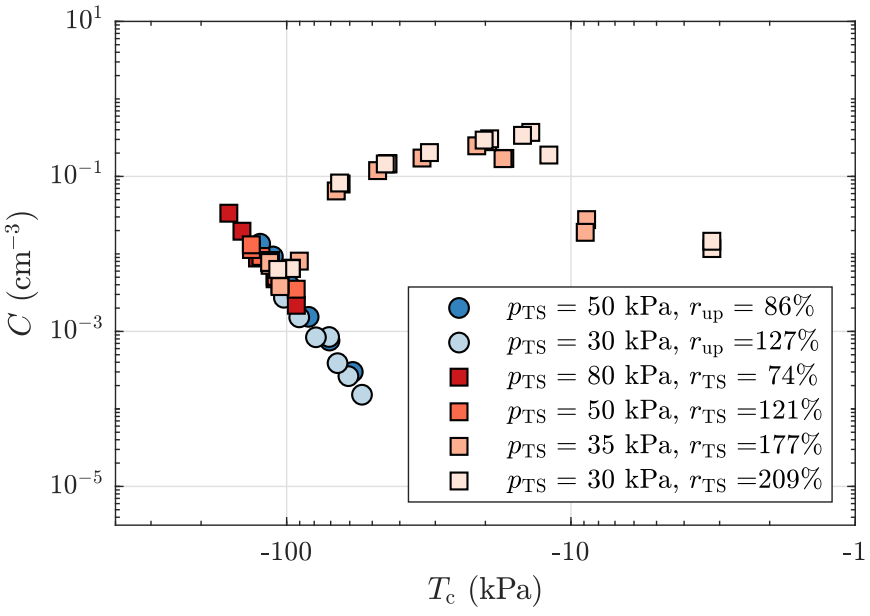

Figure 2.18: Anomalous behaviour in the measured distribution was observed at the ATLA FNS (squares, at test-section pressures of $p_{TS} = 30$ kPa & 35 kPa) but not at the AMC cavitation tunnel (circles). The relative saturation levels of oxygen in the test section, r_{TS}, and the plenum, r_{up}, are provided for each tunnel respectively. Tunnel conditions were $U_{TS} = 4$ m/s and $\gamma = 50$–58%.

For the ATLA FNS, the natural nuclei population appears to be controlled by the test-section relative saturation conditions, rather than the plenum. The variation of natural nuclei population with plenum static pressure and water saturation pressure is shown in Fig. 2.19, similar to the results presented in Fig. 2.15 for the AMC tunnel. The red dashed line represents where the plenum pressure equals the equilibrium saturation pressure (i.e. $p_{\mathrm{up}} = p_{\mathrm{sat}}$). The water in the plenum is undersaturated for points above this line and oversaturated for points below. Some of the solid points are located above this line which suggests that the saturation condition in the plenum at the ATLA FNS is not a suitable indicator of the natural nuclei population as it is for the AMC tunnel.

If the data presented in Fig. 2.19 are replotted to consider how the nuclei population varies with test-section static pressure instead of plenum static pressure, then all solid symbols now remain below the red line as shown in Fig. 2.20. The natural nuclei population was observed to increase only for oversaturated conditions in the test section at this test facility. This suggests that the saturation condition in the test section is a more accurate indicator of the threshold for natural nuclei population variation in the ATLA FNS than the plenum conditions. This may be due to the water spending longer time in the FNS test section exposed to oversaturated conditions ($\mathcal{O}(1)$ s) than the AMC test section ($\mathcal{O}(100)$ ms), as discussed earlier. Furthermore, nuclei recirculation in the ATLA FNS, which has a lower limb with resorbing capability but not a downstream tank, unlike the AMC tunnel, could potentially add to the complexity of the observed behaviour. An investigation of the effectiveness of free gas removal in the ATLA FNS, similar to that shown in Sect. 2.4.2 for the AMC tunnel, is warranted. Some of the baseline distributions appear in the oversaturated region, as was observed for the AMC cavitation tunnel data in Fig. 2.15. It should also be noted that the ATLA FNS datasets with 'local peak' behaviour shown in Fig. 2.18 are categorised as being above the baseline, although they appear to return to the baseline level at more negative tensions. Therefore, Fig. 2.20 should be interpreted with caution until the 'local peak' behaviour is better understood.

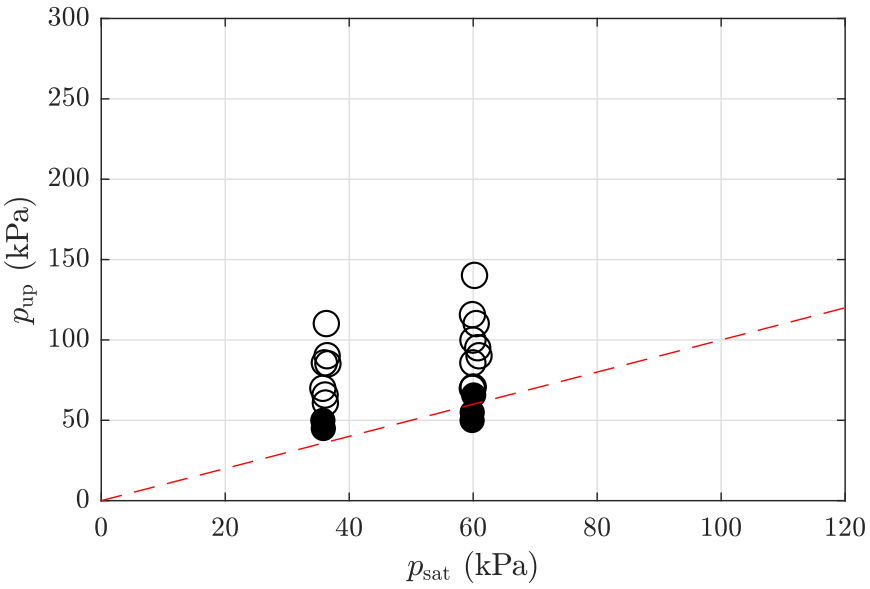

Figure 2.19: Parameter map of all nuclei distributions measured at the ATLA FNS presented as upstream pressure (in the plenum), p_{up}, against saturation pressure, p_{sat}. The red line represents when these pressures are equal ($r_{up} = 100\%$). Nuclei distributions at the baseline (hollow) and above the baseline (solid) are differentiated, but for this facility, the criterion $r_{up} < 100\%$ (as applicable to the AMC tunnel, see Fig. 2.15) is not a suitable measure of whether the population departs from the baseline.

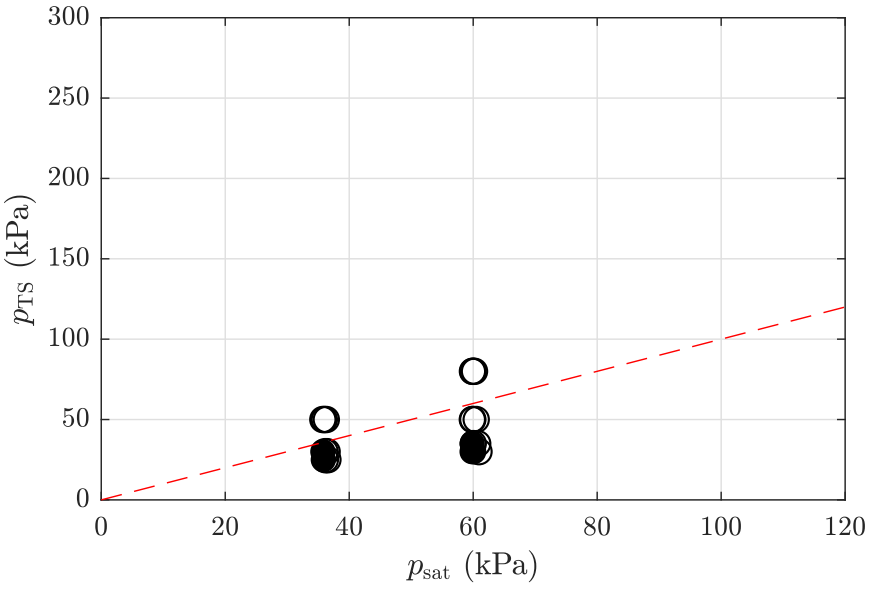

Figure 2.20: Baseline natural nuclei populations (hollow) and distributions above the baseline (solid) measured at the ATLA FNS presented as a function of test-section pressure, p_{TS}, and saturation pressure of the water, p_{sat}. The red line represents when these pressures are equal ($r_{TS} = 100\%$) and provides a conservative delineation above which (i.e. if $r_{TS} > 100\%$) the population no longer remains at the baseline.

2.4.7 Comparisons with other test facilities

Given the similarity between nuclei populations measured in the AMC and ATLA tunnels, albeit with the same device, it raises the obvious question of how much similarity there is between facilities generally. A comparison of natural populations measured using a CSM in several cavitation tunnels all with water DO contents of about 30% is shown Fig. 2.21. A baseline natural nuclei population in the AMC cavitation tunnel is compared with the FNS in Japan (measured using the ATLA CSM) (Nagaya et al., 2011; Takahashi et al., 2019), Grand Tunnel Hydrodynamique (GTH) in France (Gindroz, 1995), CEIMM cavitation tunnel in Italy (Gindroz, 1995) and the University of Michigan (UM) 9-inch water tunnel in the USA (Chang et al., 2009). With the exception of the Japanese data for which the same CSM device was used, each distribution was measured using a different CSM device and associated signal processing procedure. While the flow rate calibration of each venturi (and hence the pressure calibration of each venturi throat) is thought to be reliable, there are potential differences between discriminator algorithms employed with each device. Validation of CSM discriminators is a challenging task, which is reflected by the paucity of information in the open literature. These data show variations in concentration over some two orders of magnitude, however this is not a definitive comparison as many factors relating to CSM setup and operation, as well as facility operating history, are unknown. However, these data do show global similarity in terms of the power-law index and concentrations are generally within the range of variation observed over the longer term in the AMC tunnel, as discussed further below. On this basis, these results suggest a universal character of natural nuclei populations in conditioned cavitation tunnel water. To eliminate the differences in CSM setups, a standard device, and discriminator could be used to test natural nuclei populations in different facilities. This would allow comparisons to be made with greater confidence, at least in relative terms. Ultimately an optical device that counts every activation and eliminates any potential acoustic discriminator ambiguities or errors could be developed.

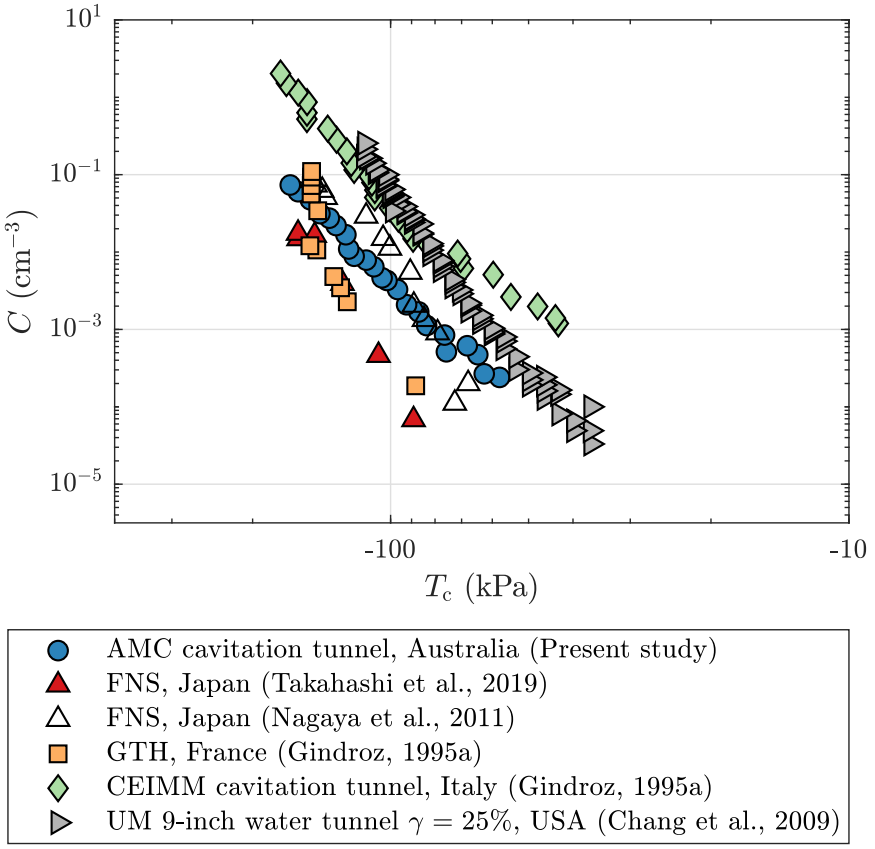

Figure 2.21: Baseline natural nuclei population comparison for a range of test facilities as measured using different CSM devices. The data show quite reasonable agreement between the different facilities noting the substantial variation in architecture and dimensions of the circuits and possible variation in the CSM design and/or signal processing techniques used. The dissolved oxygen content is nominally 30% of saturation at atmospheric pressure ($\gamma \sim 30\%$), unless otherwise specified.

2.4.8 Comparisons with CSM measurements in environmental waters

Given the similarities between natural nuclei populations in different cavitation tunnels, it is of interest to also compare these with populations measured in environmental waters generally using a CSM. A comparison of the baseline population in the AMC tunnel with two measurements at two depths, taken in the Iroise Sea (Gindroz et al., 1995) and in Lake Pend Oreille (Gowing and Shen, 2001), are shown in Fig. 2.22. For both these studies measurements were taken at a range of depths showing increasing critical tension with increasing depth. Two sample depths that bracket the range are shown in Fig. 2.22 to demonstrate the trend. Whilst the shallow depth measurements show some similarity in absolute terms, they have significantly different slopes. The populations at deeper depths differ significantly with the ocean data at 60 m depth (Gindroz et al., 1995) spanning more negative tensions than the lake data at 50 m depth (Gowing and Shen, 2001) (not shown) which sits between the 10 and 100 m datasets shown in Fig. 2.22. The deep measurements in the lake show close comparison with the AMC tunnel baseline measurement. The measurements taken in the ocean at both depths show a much greater slope than the lake and AMC baseline measurements implying a narrow range of nuclei critical tensions.

The ocean measurements by Gindroz et al. (1995) are taken with a similar experimental setup as used for the natural population taken in the French GTH shown in Fig. 2.21 which also shows a greater slope which could indicate device-specific results. Although the data are not plotted together, the GTH natural population does not compare well with the deep population measured in the Iroise Sea. Given the limited data available from CSM measurements, and differences in devices, in environmental waters it is difficult to comment on how well these populations compare with those measured in test facilities other than to conclude that they are of similar orders of magnitude in terms of critical tensions and concentrations. As with the comparison of measurements in facilities, measurements using a definitive technique or at least a consistent technique are required to gain greater insight.

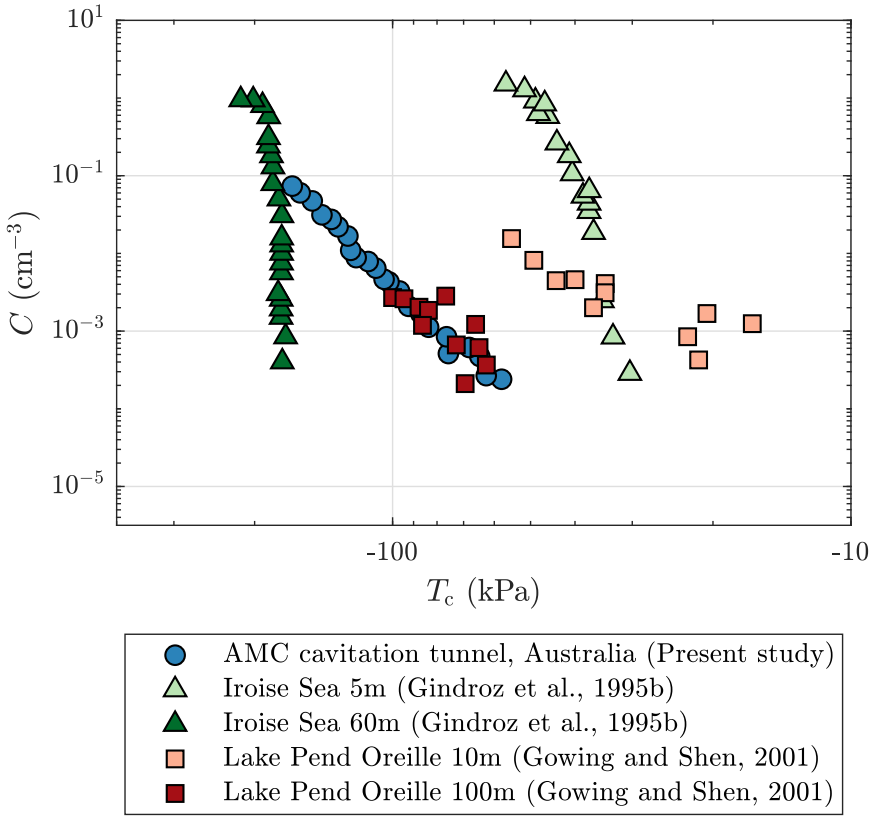

Figure 2.22: Comparison of nuclei distributions in a laboratory and in environmental waters of varying depth as measured using CSM devices. The AMC tunnel data compare closely to the lake measurement at a depth of 100 m.

2.4.9 Quantitative variations in measured populations and comparison with other experiments and theories

Extensive measurements of nuclei and microbubble populations in laboratory water, and environmental waters, have been made using a range of optical and acoustic techniques and it is of interest to compare these with the AMC tunnel natural population. A comparison of baseline AMC tunnel populations taken over two years and a single long sample taken over 40 hours (Venning et al., 2018b) are compared with a diversity of measurements using several techniques, as shown in Fig. 2.23. One population measured using a Coulter counter (an electromagnetic technique) is also included for comparison. It should be noted that microbubble or nuclei distributions can be represented in four ways, either as cumulative or non-cumulative concentration and either as a function of critical tension (or critical diameter) or equivalent bubble diameter at a particular reference pressure, p_∞. All AMC populations measured using the CSM presented in Fig. 2.23 have been converted to non-cumulative concentration as a function of equivalent bubble diameter, d, at ambient pressure, p_∞. This diameter can be calculated numerically from the critical pressure by rearranging Eq. 2.1 as:

$$(p_\infty - p_\mathrm{v}) \left(\frac{d}{4S}\right)^3 + \left(\frac{d}{4S}\right)^2 = \frac{4}{27(p_\mathrm{v} - p_\mathrm{c})^2} \tag{2.6}$$

where $p_\infty = p_\mathrm{TS}$ for AMC tunnel measurements. For the purposes of quantitative comparison all distributions can be represented as a power law:

$$\frac{\partial C}{\partial d} = A d^n \tag{2.7}$$

where A is the constant of proportionality and n is the power-law index.

All AMC baseline natural nuclei measurements show a concentration variation of between one and two orders of magnitude for a fixed diameter or less than one order of magnitude in diameter for a fixed concentration. Least-squares regression analysis of the two years of population measurements reveal n, the index of the power law, to average about -6.2 with high probability but to vary overall between -3.4 and -12.9. The multiplier A similarly averages about 9.8×10^8 with high probability but varies between 4.6×10^7 to 4.3×10^9. Within the spread of these parameters there is no clear correlation with any tunnel operating parameters (DO, velocity or pressure) nor any long-term temporal fluctuations. The long data measurement by Venning et al. (2018b) lies at about the mean of this range. Whilst this variation in global terms may be considered to be relatively small, for precise measurements of cavitation inception this range may be considered large necessitating regular measurement. Although the results presented do suggest that only one point may need to be measured to establish the entire distribution if it is assumed that the power-law index remains nominally unchanged for undersaturated conditions as defined above.

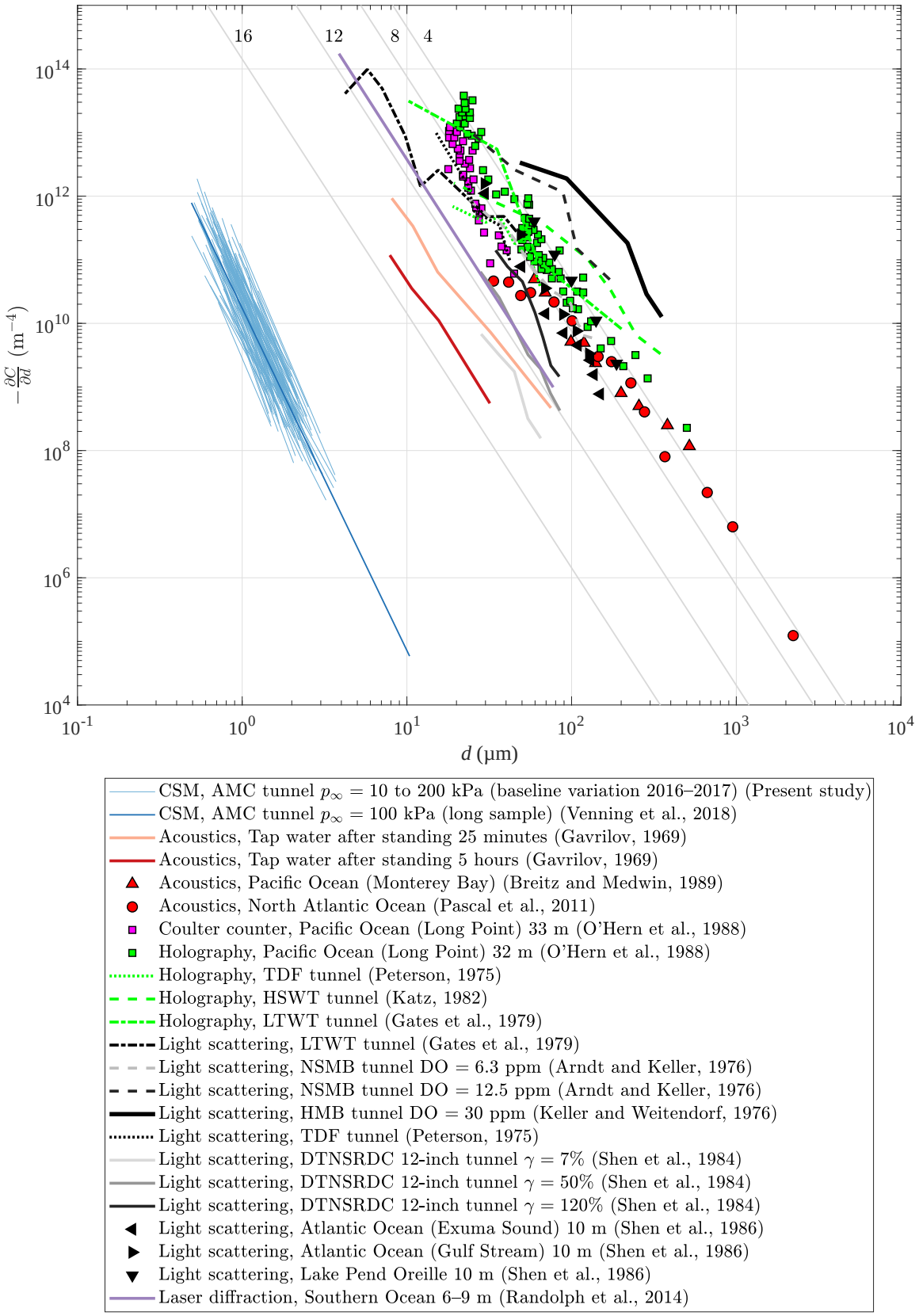

Figure 2.23: Comparison of nuclei distribution histograms from laboratory and environmental waters for a variety of measurement techniques. $-\frac{\partial C}{\partial d}$ is the derivative of the cumulative histogram and is equivalent to the number density distribution function in Katz (1982); Gates et al. (1979). d is the nucleus diameter at ambient pressure, p_∞. The solid, thin, grey lines come from the phenomenological model of Franklin (1992), with the numbers at the top of the figure representing the minimum number of molecules required to form the smallest sustainable cluster of free gas. The AMC data series are based on fits to cumulative histogram CSM data. Note that the holographic and light scattering methods may detect solid, non-cavitating particles, which may result in the overestimation of nuclei concentrations.

The populations measured using optical or acoustic techniques show some overlap in size with the AMC CSM populations but are generally two to three orders of magnitude greater in size but comparable in concentration range. Most of the populations are within the 10 to 100 µm size range which is typically the range for modelling nucleation in relatively high cavitation number flows, as noted in the introduction. There are several factors that should be noted. Most of the measurements made with optical or acoustic techniques are in water nominally saturated with air at atmospheric pressure although there are some tunnel populations where the water is degassed. The optical techniques could register not only bubbles but also impurities potentially artificially increasing concentrations. On the other hand, acoustic techniques should only respond to bubble dynamics. It can also be observed in Fig. 2.23 that the older ocean nuclei measurements are comparable with more recent laser diffraction measurements by Randolph et al. (2014). They also observed that the power-law index shows little variation over short time scales, but varies significantly between days, i.e. about -4.2 on one day and -6.0 on another. Overall, most of the populations measured using optical and acoustic techniques in facility and environmental waters compare reasonably closely implying universal behaviour.

Of all the populations measured using these techniques, it is only those by Shen et al. (1984) and in particular by Gavrilov (1969) that show reduced concentrations/sizes demonstrating the effects of degassing and standing over long periods respectively. Other populations measured by Arndt and Keller (1976) and Keller and Weitendorf (1976) show similar trends with reducing dissolved gas content but with initially higher concentrations and larger sizes. These differences could be attributable to factors such as residence and circuit pressure history, which are influenced by the tunnel architecture, that affect the life and existence of entrained bubbles. The data overall tend to follow a power law with an index of about -4 as can be seen from the solid, thin, grey lines with this slope shown on Fig. 2.23, which come from the phenomenological model of Franklin (1992) discussed below.

Finally, as noted above, only limited information can be gained on the nature of natural nuclei populations from these results. However, comparisons with other results and theories can perhaps provide some additional insight into such complex and apparently unpredictable phenomena. Apart from the long sample AMC tunnel natural population from Venning et al. (2018b), all baseline data lie within the size range decade of 0.5 to 5 µm equivalent bubble diameter. This size range corresponds with stabilised microbubble sizes in seawater found by Johnson and Cooke (1981). They report that 40 to 100 µm diameter microbubbles generated in slightly degassed seawater under controlled conditions would either quickly completely dissolve while others would reduce to finite sizes apparently stabilised by films compressed during dissolution. These stabilised bubbles ranged in sizes between 1 and 13 µm diameter. They also report that application of pressure reduction would grow some bubbles and that they would return to original sizes if the initial pressure was restored, or that with extended pressure increase some would dissolve completely. This behaviour could explain the variation in tunnel natural nuclei popula-

tions after tunnel operations involving large populations of bubbles such as filling and emptying, or degassing, as well as the effects of time, pressure and dissolved gas content.

Beyond possible explanations for microbubble evolution from large sizes there is also the possibility of growth from small sizes or homogeneous nucleation. As noted earlier, Franklin (1992, 1994) proposed a power-law model based on arguments of self similarity and that the population could be limited to a finite minimum size attributable to homogeneous nucleation based on dissolved gas content. Franklin argued how the effect of dissolved gas and standing time may affect the minimum number of molecules (numbered at the top of Fig. 2.23) required to form the smallest sustainable cluster of free gas. This model is shown for comparison in Fig. 2.23, where the dissolved air concentration is calculated assuming saturation at atmospheric conditions for each of the distributions shown. Ward et al. (1970) showed how dissolved gas affected the minimum sustainable nucleus size and how this was smaller for higher gas contents. That is, fewer molecules are required to form a nucleus for higher dissolved gas contents. This work on the effects of dissolved gas on homogeneous nucleation theory has been extended by Kwak and Oh (2004) and Němec (2016). Unfortunately this theory has not been extended to more practical liquids and to nuclei size distributions but may provide potential guidance in developing future investigations.

At this point, a word of caution should be noted with regard to comparing nuclei measurements between facilities as well as environmental waters. Although the DO levels, γ, may be similar, they are defined relative to atmospheric pressure and variations in temperature between measurements could lead to differences in the relative saturation level of oxygen in water, r. This in turn affects nucleus resorption and growth rates, as derived by Epstein and Plesset (1950) and discussed by Franc and Michel (2006). Therefore, a constant r may be preferred across different test locations and campaigns for comparative purposes, but this has its own challenges. The location in the tunnel which most influences the nuclei population (and thus where r is defined) can differ between test facilities, and it is impractical to control temperature and dissolved air content in environmental waters.

These challenges mean that nuclei population comparisons between test facilities and environmental waters should be made with care. For the latter, additional factors such as weather, sea state and biological activity exist, further complicating comparisons. The candidate has attempted to address the issue of nuclei population variability by providing a range of distributions measured over two years in Fig. 2.23. Note that this may also capture the effects of a range of factors such as temperature, saturation condition, biological activity and tunnel operation. Perhaps this approach is the most practical way to make comparisons.

2.5 Conclusions

The natural nuclei population dynamics within the cavitation tunnel at the Australian Maritime College (AMC) Cavitation Research Laboratory have been characterised using a Cavitation Susceptibility Meter (CSM). This population follows a power law and remains invariant at a baseline level over short time scales. That is, provided the water remains undersaturated in the low pressure part of the tunnel circuit upstream of the test section (plenum). For this undersaturated condition, the population also remains invariant throughout the tunnel circuit such that it can be measured from any location. However, at extreme operating conditions, the population can increase when the water is oversaturated. This indicates that this condition should be avoided unless direct measurements are concurrently made. Although little information is available on the nature of this population, it exhibits similar behaviour to microbubbles, suggesting gaseous diffusion plays a role in the population dynamics. The population was observed to decrease by approximately an order or magnitude during a week-long test campaign and to fluctuate by a similar amount over longer time scales. These historical trends necessitate regular monitoring of the population when investigating low cavitation number flows in which natural nuclei are active.

Natural nuclei populations were also measured in the Japanese Acquisition, Technology & Logistics Agency (ATLA) Flow Noise Simulator (FNS) using the AMC CSM. Measured populations were found to compare closely for undersaturated conditions suggesting a universal characteristic. However, the reference location in the ATLA FNS at which the pressure may be used to threshold whether the water is under or oversaturated was not found to be the plenum, unlike for the AMC tunnel. The pressure in the FNS test section, in which high flow velocity occurs, appears to be a more suitable indicator. While the AMC tunnel features a downstream tank (and large resorber) for free gas removal, such a tank is not part of the ATLA FNS architecture, which may lead to the recirculation of nuclei. The differences in natural nuclei population dynamics observed between the two facilities may, at least partially, be attributed to differences in tunnel design.

Measurements of natural populations in several tunnels of varying circuit architecture and volume using different CSMs show similar behaviour further suggesting the possibility of a universal characteristic. To confirm this possibility, at least in a relative sense, measurements would need to be taken in different facilities with the same CSM. Alternatively, newer technology such as an optical-based CSM that would eliminate acoustic ambiguities (yet still allow small nuclei to be measured) needs to be developed.

Comparison of CSM measurements, using different devices in test facilities and environmental waters show similar populations in a general sense. However, this observation is based on few measurements demonstrating the need for more data to be acquired and preferably, as noted above, with newer CSM technologies.

Microbubble or nuclei measurements in environmental waters using optical or acoustic techniques show populations in the 10 to 100 µm diameter range, as typically modelled for cavitation nucleation. However, CSM data show that smaller size populations, in the 0.5 to 5 µm equivalent bubble diameter range, as measured in facilities are also present in the these waters.

To gain further insight into the nature of these nuclei populations, including whether they can form from stabilisation of dissolving larger bubbles or from smaller homogeneous nuclei, simpler experiments eliminating many of the variables that apparently affect the populations in practical water volumes are required.

2.6 Acknowledgements

The authors acknowledge the support of the University of Tasmania, the Defence Science and Technology Group and the Acquisition, Technology & Logistics Agency. The authors thank AMC technical officers, Mr Robert Wrigley and Mr Steven Kent, and ATLA technical officer, Mr Kenji Naganuma, for providing technical assistance with test facility configuration and operation as well as CSM hardware configuration.

Chapter 3

Statistical aspects of tip vortex cavitation inception and desinence in a nuclei deplete flow

A detailed understanding of natural nuclei population dynamics in the cavitation tunnel at the Australian Maritime College Cavitation Research Laboratory was developed in Chapter 2. These results make it possible to investigate TVC inception in unseeded flows with greater confidence about the water quality and its behaviour during experiments. In this chapter, the probabilistic nature of TVC inception about an elliptical hydrofoil in nuclei deplete flows is characterised. A large sample of TVC inception events is achieved through the use of automated cavity detection. Comparisons are drawn with TVC desinence behaviour to reveal the statistical nature of TVC and the role of natural nuclei populations.

This chapter is a post-peer-review, pre-copyedit version of an article published in *Experiments in Fluids*, modified following thesis examiners' feedback. The final authenticated version is available online at:

`https://doi.org/10.1007/s00348-020-02967-x`.

The citation for the paper is:

M. Khoo, J. Venning, B. Pearce, and P. Brandner. Statistical aspects of tip vortex cavitation inception and desinence in a nuclei deplete flow. Exp. Fluids, 61(6):145, 2020.

3.1 Abstract

Tip vortex cavitation (TVC) inception and desinence behaviour of a NACA 0012 cross-section, elliptical hydrofoil is investigated from a statistical perspective in a cavitation tunnel. Measurements were made for incidences from 4° to 16° and Reynolds numbers from 1.0×10^6 to 2.1×10^6. The statistics of TVC inception were quantified by taking repeated measurements of the time until the appearance of a tip vortex cavity for a range of fixed incidences. In other experiments, the angle of attack was continuously increased until inception then decreased until desinence for a range of fixed cavitation numbers. The data were primarily acquired via an automated process using a laser and photodiode to detect the presence of a cavity. Measurements show that TVC inception in a nuclei deplete flow is a probabilistic process for which a large dataset is required for accurate characterisation. The probability of ingesting and activating a nucleus increases with time at a given test condition due to the increased volume of water exposed to low pressures. TVC desinence exhibits far less statistical variation than inception and is largely independent of the natural nuclei population. It does, however, exhibit hysteresis which is dependent on the topology of the cavitating flow. For the desinence of unattached cavitation, there is a small hysteresis between the inception and desinence indices. However, desinence is delayed for attached cavitation.

3.2 Introduction

Trailing vortices are inherently generated from the tips of three-dimensional lifting surfaces. Low pressures exist in these regions of concentrated vorticity (Fig. 3.1), making the flow susceptible to tip vortex cavitation (TVC) once the pressure reduces below vapour pressure. However, water is capable of withstanding high tensions (Blake Jr, 1949), such that cavitation does not incept at vapour pressure. The effective strength of the water is dependent on the size, concentration and spatial distribution of nuclei, such as microbubbles, in the volume. The size of these inhomogeneities, their distance from the vortex, and the flow field pressure gradients determine which nuclei are ingested into a vortex and how quickly. If a nucleus is drawn towards the low-pressure vortex core (Fig. 3.1) and exposed to its size-dependent critical pressure, its equilibrium becomes unstable and it grows rapidly, filling with vapour. The tension in the vortex varies in the streamwise direction, decreasing as the vortex diffuses downstream of the lifting surface. As the pressure increases, the cavity can no longer be sustained and it collapses. TVC is generally undesirable as it can be detrimental to the hydrodynamic, acoustic and structural performance of marine propellers and control surfaces, as well as turbomachinery.

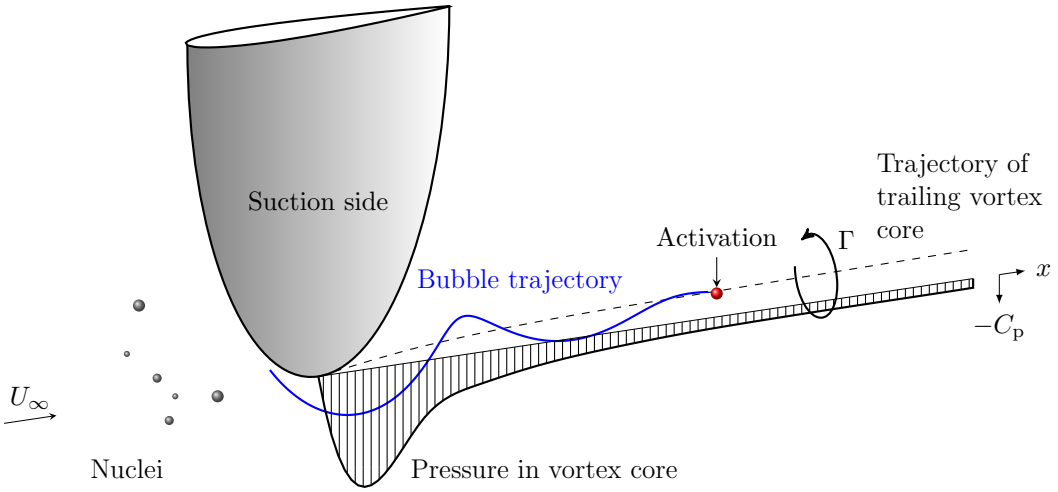

Figure 3.1: Notional capture of a nucleus (red sphere) into the trailing vortex of a lifting surface. The blue line denotes the nucleus trajectory. The freestream velocity is U_∞ and the circulation is Γ. The generic variation of the core pressure coefficient, C_p, with streamwise location, x, is also shown with the minimum pressure occurring close to the tip and pressure recovery downstream as the vortex diffuses.

Numerous TVC studies have been carried out in test facilities since the mid-twentieth century. In a seminal study by McCormick (1962), the critical cavitation index for desinence (the disappearance of cavitation) about a hydrofoil was found to depend on Reynolds number and incidence. A power-law fit applied to these data yields a Reynolds number power index of about 0.4, which can also be derived from boundary layer and airfoil theory (Billet and Holl, 1979; Franc and Michel, 2006). This index has been widely used for TVC scaling studies (Arndt and Dugue, 1992; Fruman and Dugue, 1994; Briançon-Marjollet and Merle, 1996). However, upon closer inspection of McCormick's data, the index decreases with increasing incidence (0.4 for 4°, 0.3 for 8°) for a rectangular-planform hydrofoil. Changes in incidence alter flow topology, in particular the boundary layer condition, which will in turn affect the vortex core size and minimum pressure. Therefore, the scaling of cavitation behaviour from model to full-scale is presumably only accurate for the flow topology studied and is not universally applicable. Moreover, several studies have indicated that the index varies with Reynolds number (Amromin, 2006; Shen et al., 2009), which suggests that further work is required to understand viscous effects on TVC.

In addition to flow topology, water quality, i.e. free and dissolved gas content, has also been shown to influence cavitation inception behaviour. McCormick (1962) measured the effect of dissolved air content on the critical cavitation index and deduced that undissolved gas influences TVC desinence behaviour. This has been confirmed in subsequent studies, in which the cavitation inception indices of propellers and hydrofoils were observed to scale or increase with injected nuclei populations (Briançon-Marjollet and Merle, 1996; Gindroz and Billet, 1998; Song et al., 2017). McCormick (1962) also noted the lower repeatability of cavitation inception measurements compared to desinence, and attributed this to the random distribution of nuclei in the flow which plays a role in the inception process. While this makes desinence behaviour easier to study scientifically, inception is likely to be of more interest for practical applications.

Extensive measurements of nuclei in facility and environmental waters have been carried out since the mid-twentieth century using optical, acoustic and hydrodynamic techniques (Gavrilov, 1969; O'Hern et al., 1988; Shen et al., 1984; Gindroz, 1995; Randolph et al., 2014). Hydrodynamic measurements typically report lower populations, partly because optical techniques may also detect non-cavitating particles and also due to the quality of the water itself. However, the power-law trends observed across all measurements are generally comparable (Khoo et al., 2020c) with a phenomenological model proposed by Franklin (1992) which describes the relationship between nuclei size and concentration as a power law with an index of -4. While this indicates a universal characteristic of water, Khoo et al. (2020c) noted temporal variations in the nuclei population which naturally occurs in a cavitation tunnel, also known as the natural nuclei population, which may be described as a nuclei deplete population. This is in contrast to those populations found in cavitating wakes or flows deliberately injected with microbubbles, whose nuclei concentrations are several orders of magnitude higher, as discussed by Brandner (2018) and Khoo et al. (2020c). Temporal variations in natural nuclei populations in cavitation tunnels highlight the importance of understanding nuclei population dynamics and of monitoring. This is a necessary consideration for TVC experiments in nuclei deplete flows.

Water tensile strength describes the ability of a body of water to withstand pressures below vapour pressure without cavitating. Venning et al. (2018b) showed that for 'infinite' sampling times, water has no strength due to the presence of large nuclei, albeit in low concentrations. However, for finite durations, there is general agreement that water tensile strength is statistical in nature due to the spatial distribution and temporal variation of nuclei in the flow (Arndt and Keller, 1992; Briançon-Marjollet and Merle, 1996; Mørch, 2000). Different definitions of water tensile strength can be found in TVC inception studies, with some using an event rate approach to account for the randomness of the nuclei distribution (Gindroz, 1995; Briançon-Marjollet and Merle, 1996), and others making multiple water tensile strength measurements at each test condition and considering the strength of the weakest nuclei found to be representative of the strength of the water (Arndt and Keller, 1992). Arndt and Maines (1994) extrapolated the relationship between test section pressure and velocity at inception to zero velocity to determine a critical pressure at inception. These definitions of tension have been applied to TVC inception scaling laws to account for nuclei effects, providing reasonable correlations (Arndt and Dugue, 1992; Arndt and Maines, 1994; Briançon-Marjollet and Merle, 1996). Given these considerations, TVC inception should be studied from a statistical perspective, with previous studies having done this with varying degrees of fidelity.

TVC inception is influenced not only by the random distribution of nuclei in the flow, but also by nuclei or bubble dynamics, which determine their motion and growth in a pressure field. A bubble typically follows a spiral trajectory as it is drawn towards the vortex core by the radial pressure gradient. Drag, lift and added mass forces serve to retard the motion of the bubble, affecting the number of orbits the bubble performs prior

to capture in the core (Oweis et al., 2005). It has been found that larger bubbles have shorter capture times in vortical flows as the force induced by the radial pressure gradient increases with R^3, where R is the bubble radius (Oweis et al., 2005). Zhang et al. (2017) suggested that a critical nucleus size for inception exists, defined as the largest bubble with a capture time less than a critical capture time (dependent on hydrofoil size and flow velocity). Therefore, larger, weaker bubbles may be present in the flow but will not be activated if they are in sufficiently low concentrations, passing the location of minimum pressure without ingestion into the vortex core. This work has provided the basis for the development of a TVC prediction model (Chen et al., 2019). In addition, pressure fluctuations in the vortex (Green, 1991; Arndt and Maines, 1994; Sinding et al., 2018) and vortex core wandering (Baker et al., 1974; Pennings et al., 2015b) are statistical in nature and further complicate the process of nuclei capture and activation. It is evident that bubble dynamics and behaviour of the vortical flow play an important role in TVC inception.

Only a limited number of TVC inception studies have been conducted in a statistical manner. Statistical models have been used to characterise nuclei distributions (Messino et al., 1963) which were coupled with computational fluid dynamics and bubble dynamics models to predict TVC event rates for hydrofoils and propellers (Hsiao and Chahine, 2005, 2008). The majority of TVC inception studies are based on small sample sizes, and hence do not adequately address the statistical nature of inception. Six or more TVC inception and water tensile strength measurements were made at each test condition by Arndt and Keller (1992), but this is a relatively small sample size in the context of statistical investigations. Several studies on travelling bubble cavitation about headforms using an event rate approach have been carried out. Schiebe (1969) calculated a probable cavitation occurrence rate based on measured nuclei distributions and compared it with experimental measurements of cavitation event rates with mixed success, citing a lack of accuracy in the nuclei measurement and recommending the use of larger statistical samples. Meyer et al. (1992) used Monte Carlo simulations to model the random processes in an experiment and while there was good agreement with experimental results, the lack of a quantitative definition of inception made it difficult to be sure about the validity of the results. Ceccio and Brennen (1991) measured several thousand cavitation events about headforms and successfully correlated these with measured nuclei distributions. While some statistical studies of cavitation inception exist, they are concerned with other types of cavitation than TVC and have produced mixed results.

TVC inception is an inherently statistical process for which the availability of detailed statistical studies is limited. The present work seeks to gain insight into the probabilistic nature of TVC inception by using larger datasets to more accurately characterise the phenomenon compared to event rate approaches used in past studies. This will contribute to the improvement of TVC prediction and management capabilities for practical applications.

3.3 Experimental overview

3.3.1 Test facility

Hydrofoil TVC measurements were made in the cavitation tunnel at the Australian Maritime College Cavitation Research Laboratory (AMC CRL). A schematic of the tunnel is shown in Fig. 3.2. The variable-pressure, closed-circuit water tunnel has a volume of 365 m^3. The test section has a 0.6 m $\times$ 0.6 m cross section and is 2.6 m in length. The working fluid is demineralised water. The test section centreline pressure can be varied between 4–400 kPa and the nominal flow velocity range is 2–12 m/s.

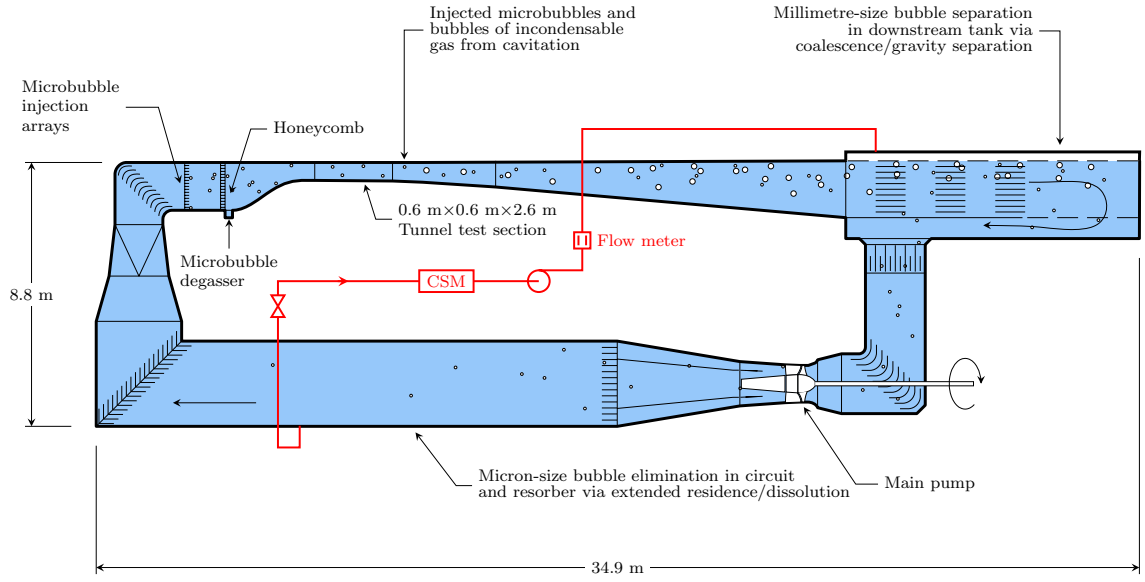

Figure 3.2: Schematic of the AMC cavitation tunnel. The circuit architecture allows for continuous removal of microbubbles or large volumes of injected incondensable gas. Ancillaries for microbubble seeding and for degassing of water are shown. Microbubbles may be either injected for modelling cavitation nucleation or generated by the cavitation itself. For the present study, water was sampled from the lower-limb resorber through the cavitation susceptibility meter (CSM) for natural nuclei population measurements.

The nuclei (free gas) and dissolved gas contents in the working fluid can be controlled in the tunnel. This enables reliable and repeatable cavitation experiments to be performed. A large downstream tank allows bubbles to be removed from the bulk flow via gravity separation. The resorber in the lower limb of the tunnel circuit promotes bubble dissolution by means of long exposure to high static pressure. A microbubble degassing system is used to lower the dissolved oxygen content of the water via the injection of bubbles into the test section at low pressures and velocities. Dissolved gas molecules are drawn out of solution, resulting in the growth of the injected bubbles which are removed in the downstream tank. A microbubble injection system enables the free gas content to be controlled during cavitation studies. An ever-present natural nuclei population has been shown to exist in the tunnel water, regardless of whether microbubble injection is used (Khoo et al., 2020c). Further details on this test facility can be found in Brandner et al. (2007).

3.3.2 Nuclei and dissolved gas contents

The natural nuclei population in the tunnel water was used for this study. No additional nuclei were injected into the flow. The population was monitored using a cavitation susceptibility meter (CSM). This is a hydrodynamic measurement technique whereby water is sampled from the circuit and passed through a centrebody venturi. The water is subjected to a tension in the venturi and a nucleus will cavitate if exposed to a tension which exceeds its size-dependent critical pressure, p_c. Cavitation events are counted using a piezoceramic sensor and an event rate is determined. A nuclei distribution can be characterised by conducting a tension sweep, where each tension has a corresponding cumulative nuclei concentration. Further details on the CSM operation can be found in Khoo et al. (2016).

A typical natural nuclei distribution in the AMC cavitation tunnel is provided in Fig. 3.3. The cumulative concentration increases as the tension applied to the water in the venturi increases (i.e. with increasing magnitude of tension, $T_c = p_c - p_v$, where p_v is vapour pressure). The cumulative distribution in Fig. 3.3 is consistent with previous measurements for which a power-law trend was observed (Venning et al., 2018b; Khoo et al., 2020c).

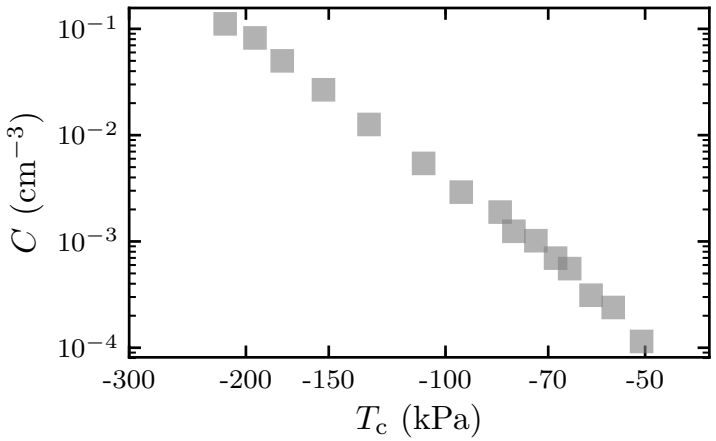

Figure 3.3: A typical natural nuclei population in the AMC cavitation tunnel measured using a cavitation susceptibility meter. Nuclei concentration, C, is plotted against the critical pressure of a nucleus, T_c. The distribution follows a power-law trend.

The dissolved oxygen content was maintained between 2.6 and 5.0 mg/L (i.e. 28%–61% relative to saturation at atmospheric pressure) throughout the experiment. The relative saturation level of dissolved oxygen in the water, r_{up}, using the plenum upstream of the test section as the reference location, was maintained between 12%–83% during the present study which ensured that the natural nuclei population remained at the baseline, as described in Khoo et al. (2020c). The definition of this relative saturation parameter and rationale for its use are provided in Khoo et al. (2020c).

3.3.3 Experimental setup

A schematic of the experimental setup is given in Fig. 3.4. A stainless steel, elliptical planform, NACA 0012 hydrofoil with a 150 mm root chord length and an aspect ratio of 1.5 was used for this study. It was mounted to a force balance with integrated angular encoder and stepper motor, allowing for computer-controlled angular positioning and a rate of change of about 0.14°/s. The assembly was installed at the test section mid-span in the ceiling. The mid-chord of the hydrofoil was 1.3 m from the test section entrance and was also the axis of rotation.

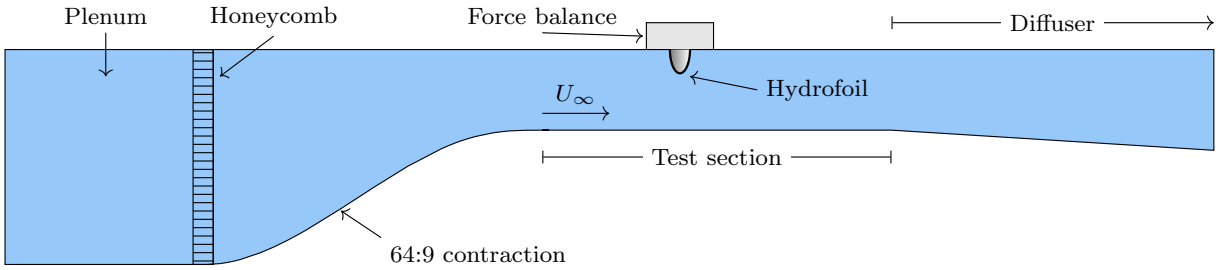

Figure 3.4: Schematic of the experimental setup in the upper limb of the AMC cavitation tunnel, showing the hydrofoil located within the test section. The force balance allows for angular positioning of the hydrofoil. The test section velocity is U_∞.

A laser and photodiode setup similar to that used by Yakushiji (2009) was the primary method for the detection of the presence of a tip vortex cavity. The laser was located on one side of the test section and aimed about $0.15c$ downstream of the hydrofoil tip, where c is the root chord length. This position was determined in part by prior observations of the inception location, and in part by optical access constraints. The photodiode was positioned on the opposite side of the test section. The appearance of a tip vortex cavity in the laser beam scatters the light and reduces the intensity detected by the photodiode. TVC inception and desinence were indicated by a decrease and increase in the diode output voltage, respectively. Note that this method cannot be used to detect cavities downstream of the laser beam. Arndt and Maines (2000) commented that inception can occur further downstream from the tip in 'strong' water (nuclei deplete flows). Several requirements need to be satisfied for this to occur, including a sufficiently low local cavitation number such that the vortex is under tension at this location, and the arrival of a sufficiently weak nucleus at the downstream location before cavitation occurs near the tip. Given that pressures are much lower near the tip, a far higher number of sufficiently weak nuclei are available to incept here in a nuclei deplete flow, which makes inception further downstream unlikely. In consideration of this, the present study is concerned with cavitation inception behaviour in the tip region.

High resolution photographs were taken of different cavity topologies in the vicinity of the hydrofoil tip using a digital single-lens reflex camera and stroboscopic lighting.

Two main methodologies were used to investigate TVC behaviour. Either the incidence or the cavitation number was varied. The Reynolds number ($Re = \frac{U_\infty c}{\nu}$, where ν is the fluid kinematic viscosity) and cavitation number ($\sigma = \frac{p_\infty - p_v}{\frac{1}{2}\rho {U_\infty}^2}$, where p_∞ is the freestream pressure in the test section at the same height as the hydrofoil tip and ρ is the fluid density) were maintained as constant where possible. The water temperature remained between 17.4°C and 28.2°C for the data presented in this paper. This is due to data acquisition at different times of the year. Since temperature changes minimally from day to day, there will be minimal changes in water properties and air solubility and thus cavitation inception behaviour for data acquired within the same day (i.e. data with each figure in the results). However, between figures, there may be a slight offset as higher tensions or incidence would be required to activate a nucleus of a given size at lower temperatures. It should be noted that the main intention of this paper is to demonstrate the trends in cavitation inception behaviour within the data presented in each figure rather than to assure identical test conditions across all data in all figures.

3.4 Results and discussion

A series of different experiments were performed to investigate different aspects of tip vortex cavitation inception in nuclei deplete flows. As such, the definition of cavitation inception varied slightly with test methodology. The definition associated with each dataset is provided in the following discussion.

3.4.1 Statistics of cavitation inception and desinence

The variation of time until inception for a range of incidences at fixed Reynolds and cavitation numbers is shown in Fig. 3.5. The incidence was continuously increased from a non-cavitating condition at 5.0° to a prescribed incidence between 5.5° to 6.2°, at which point timing began. The time until TVC inception, as detected by the photodiode, was recorded and the test was repeated 25 times across the range of incidences. A time of zero was recorded if inception occurred prior to reaching the prescribed incidence. Measurements were repeated at 6.0°, producing a large data set of 455 points from which the statistical distribution of TVC inception can be quantified. Time has been non-dimensionalised by the time scale U_∞/c, which enables comparisons with flows at different scales. If the nuclei population is appropriately scaled, then for the same dimensionless time, the rate of nuclei capture and activation is equivalent regardless of model size, flow velocity and pressure field (Lecoffre, 1999).

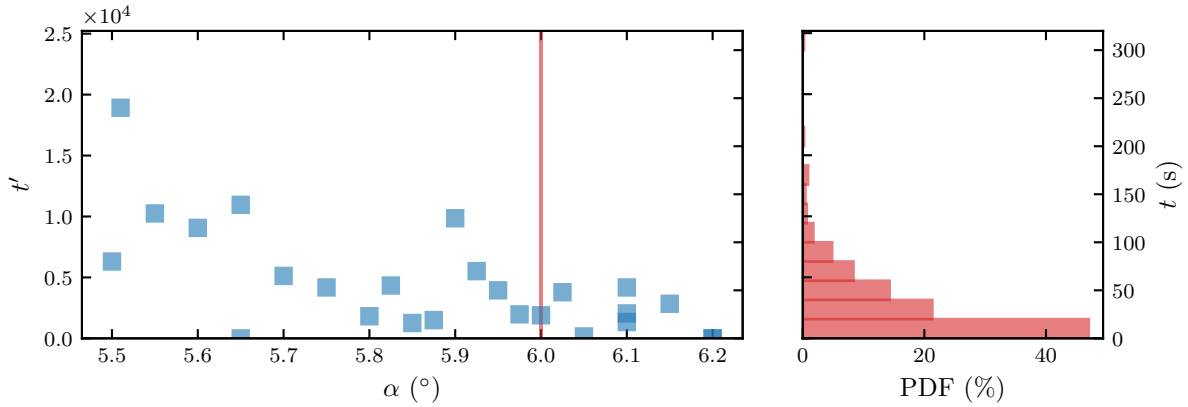

Figure 3.5: Variation of time until inception across a range of incidences, α (blue squares, left). Dimensional, t, and non-dimensional, $t' = tU_\infty/c$, time are shown, where U_∞ is the flow velocity and c is the maximum chord length. Inception is detected when a cavity breaks a laser beam about $0.15c$ downstream of the tip. Hydrofoil incidence was changed from 5.0° (non-cavitating state) to the prescribed value, at which point timing began. The vertical scatter represents the random nature of nuclei ingestion. The cavity generally incepted sooner at higher incidences. The vertical, red line denotes the incidence (6.0°) at which 455 repeated measurements were made. The corresponding probability distribution function (PDF) (right) shows that the probability of inception increases with decreasing time spent at each test condition. Measurements were taken at constant tunnel operating conditions ($Re = 2.1 \times 10^6$ and $\sigma = 0.87$).

The time until inception tends to decrease with increasing incidence. This is not unexpected given that the minimum vortex pressure decreases with increasing incidence, and more nuclei become susceptible to cavitation. Of greater interest is the high degree of scatter, particularly for incidences of 5.9° and smaller. This is most likely due to the spatial and size distributions of the nuclei, rather than pressure fluctuations in the vortex core. The concentration of susceptible nuclei decreases with decreasing incidence, as less tension is applied in the vortex core. This results in less frequent cavitation events, resulting in greater scatter in the inception data. Unsteady pressure fluctuations in the vortex core are not expected to vary significantly across pre-stall incidences and therefore do not appear to contribute as much to the observed scatter.

Vortex strength decreases with decreasing incidence, leaving only weaker nuclei susceptible to cavitation, which are present in lower concentrations and thus sparsely distributed in the flow. The probability of capture and activation of a susceptible nucleus is reduced, resulting in times until inception of up to 240 s (at 5.51°). It should be noted that a threshold incidence exists, below which inception is not physically possible as the vortex does not have sufficient strength to activate even the weakest nucleus. This presumably occurs when the minimum pressure in the vortex core, $p_{\min}$, is higher than the vapour pressure.

A probability density function (PDF) is also provided in Fig. 3.5 for the time until inception at 6.0°. Measurements were repeated 455 times at this condition to quantify the probabilistic nature of TVC inception. Inception is most likely to occur within 0–20 s than in any other time interval. However, times until inception of over 300 s were also observed. These occurrences were rare, but are again indicative of the probabilistic nature of the tensile strength of a body of water and its effect on TVC behaviour.

Some consideration should be given as to how these results would differ for a nuclei abundant flow. With higher concentrations of susceptible nuclei, the time until inception is expected to approach zero across all incidences at and above the threshold incidence ($p_{\min} < p_{\mathrm{v}}$), as opportunities for capture and activation become more frequent. The scatter in the data would disappear as a consequence. In this way, smaller sample sizes would be required to accurately characterise TVC inception behaviour as the concentration of susceptible nuclei increases.

Likewise at higher Reynolds numbers, the time until inception is also expected to approach zero across all incidences at and above the threshold incidence. A thinner boundary layer results in a smaller vortex core radius and hence lower minimum pressure for a constant circulation (McCormick, 1962; Franc and Michel, 2006). This results in a higher concentration of susceptible nuclei in the flow, a higher probability of capture and thus shorter times until inception.

The dependence of the incipient cavitation number on the spatial distribution of susceptible nuclei was not limited to the test approach, inception definition and operating conditions presented in Fig. 3.5. The incipient and desinent incidences are given in Fig. 3.6 for 58 different cavitation numbers. The effects of Reynolds number and relative saturation level of dissolved oxygen in the plenum are also provided. The incidence was continuously increased until TVC inception was detected, then continuously decreased until TVC desinence occurred. Inception is defined here as when a persistent cavity overlaps with the hydrofoil planform, when viewed from the side of the test section. Desinence is defined by the disappearance of the cavity from the test section.

The inception and desinence numbers trend with incidence due to pressure reduction in the vortex as the lift increases. The inception results exhibit similar scatter as presented earlier in Fig. 3.5, again due to variations in the time until inception of a susceptible nucleus. Meanwhile, the desinence data exhibit less variability and a linear trend can be observed between the desinent cavitation number and incidence for cavitation indices less than three. The lower scatter suggests that the random spatial distribution of the natural nuclei population does not play a significant role in TVC desinence. The pressure in the vortex core relative to vapour pressure is likely to control the disappearance of a tip vortex cavity, and the desinence data appear to represent the conditions at which the minimum vortex core pressure increases above vapour pressure. Experimental measurements or numerical simulations of the vortex core pressure at these conditions may be used to confirm this hypothesis.

Supplementary tests were performed by measuring the inception angle and spending 60 s at each 0.1° interval (triangles in Fig. 3.6). This enabled an assessment of how the inception angle is affected by exposure of a larger volume of water to the low-pressure vortex core. In general, smaller inception angles were measured, approaching the previously measured desinence angles. This is not surprising, as a larger volume of water passes through the streamtube of opportunity (i.e. the low pressure volume in which nucleus activation is possible), which increases the probability of nuclei capture and activation. The scatter in the inception data decreases for the longer time spent at each test condition, indicating that the incipient cavitation number, when determined in this manner, is less sensitive to the random spatial distribution of nuclei in the flow. Given the results in Fig. 3.5, which show that cavitation inception may not occur for over 300 s, a further increase in the time spent at each test condition should reduce the inception angles further.

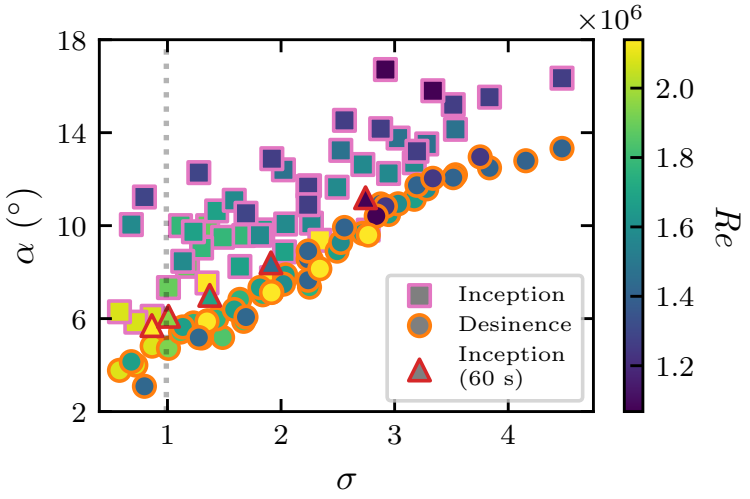

(a) Effect of Reynolds number, Re

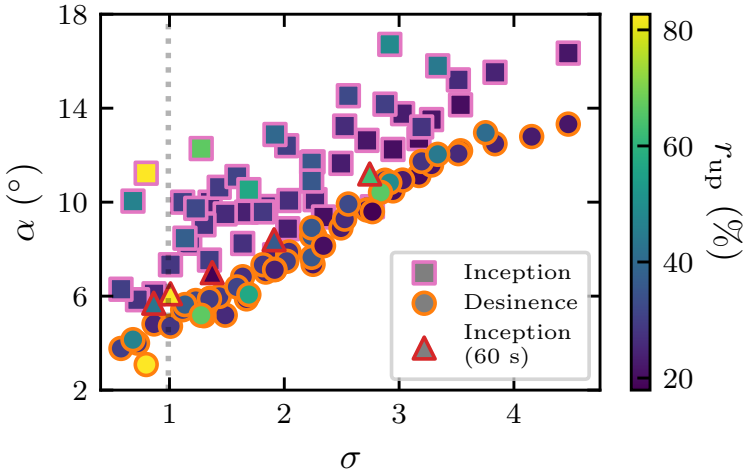

(b) Effect of relative saturation of dissolved oxygen in the plenum, r_{up}

Figure 3.6: Variation of inception and desinence angles, α, with cavitation number, σ. Inception is defined as when a persistent cavity overlaps with the hydrofoil planform. Greater variability is observed in the measured inception angles than the desinence. This suggests that the randomness of natural nuclei capture in vortical flows plays a greater role in the inception process. By spending 60 s at each test condition, lower inception angles were generally measured for a given cavitation number. Reynolds numbers at the upper end of the range tested (1.1×10^6–2.1×10^6) tend to correspond to lower cavitation numbers. The relative saturation of dissolved oxygen does not significantly affect the results across the range tested, however, additional data are required to confirm this. The vertical line corresponds to the conditions of Fig. 3.7.

Regardless of the time spent at each test condition, the desinence angles provide a lower bound on the inception angles, i.e. a desinence angle is always smaller than its corresponding inception angle. These angles would be expected to be the same if vapour pressure was the only controlling factor. This hysteretical nature has been recently investigated by Amini et al. (2019). An increase in the desinent cavitation index was observed with increasing dissolved gas content, due to diffusion of gas into the cavity in the presence of a laminar separation bubble which protects the vortex core. Arndt et al. (1991) attributed gaseous diffusion into the laminar separation zone to long residence times, while Green (1988) proposed three possible explanations for the hysteretical behaviour:

1. the recirculation of nuclei generated during the cavitation process,
2. the propagation of pressure waves from collapsing bubbles resulting in the activation of unstable nuclei, and
3. the effect of strong cavitation on the underlying single phase flow which could increase the chances of further cavitation.

It may also be due to differences in the energy required to move from one state to another (i.e. condensation during the desinence process as opposed to vaporisation during inception). The observation of this lower bound may also have implications for the cavitation characterisation of components from a practical perspective. That is, the desinence values could be used as a conservative predictor of the inception threshold, as noted by Chang et al. (2009).

The data in Fig. 3.6 were taken across a range of Reynolds numbers. It is shown in Fig. 3.6(a) that higher Reynolds numbers tend to correspond to lower cavitation numbers, as the two non-dimensional parameters vary inversely with flow velocity. As explained earlier, tip vortex strength is expected to increase with increasing Reynolds number, resulting in cavitation inception at lower incidences or higher cavitation numbers. This is indeed the case for the 'Inception' data. Furthermore, an increase in flow velocity increases the rate of nuclei capture by the tip vortex, which could also result in lower inception incidences or higher inception indices.

In Fig. 3.6(b), inception data appear to be unaffected by the relative saturation of dissolved oxygen in the plenum, which would suggest that the nuclei population did not change, as found by Khoo et al. (2020c). While dissolved gas and diffusion effects are known to influence desinent (Amini et al., 2019) and general (Holl, 1960; Arndt et al., 1991) cavitation behaviour, this was not the primary focus of the present study and there are limited data points upon which to draw conclusions. This area warrants further research.

A histogram of inception and desinence angle measurements, as detected by the photodiode, repeated 72 times at constant Reynolds and cavitation numbers is provided in Fig. 3.7. The incidence was continuously increased until TVC inception was detected, then continuously decreased until TVC desinence occurred. This is equivalent to repeated measurements at $\sigma = 0.99$ in Fig. 3.6, at a fixed Reynolds number.

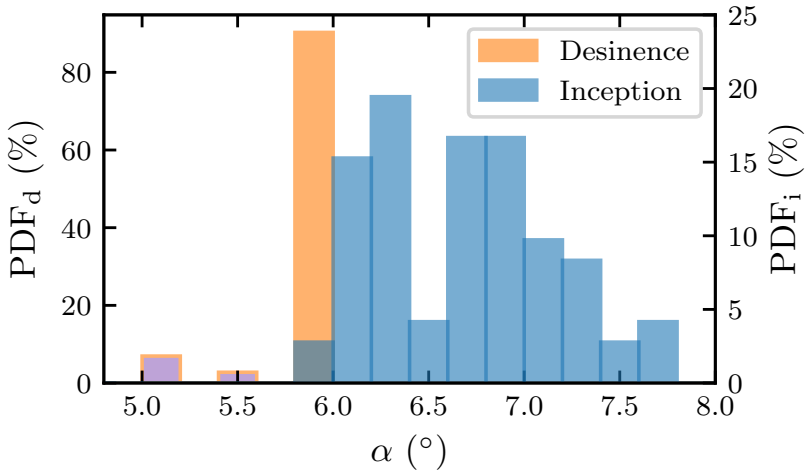

Figure 3.7: Histograms of desinent (orange, left axis) and incipient (blue, right axis) cavitation angles. Inception is detected when a cavity breaks a laser beam about 0.15 chord lengths downstream of the tip. Hydrofoil incidence, α, was continuously increased from 5.0° until inception, then continuously decreased until desinence. The measured inception angles exhibit greater variability than desinence angles, for which several outliers can be observed at lower incidences (purple). Measurements were taken at constant tunnel operating conditions ($Re = 1.7 \times 10^6$ and $\sigma = 0.99$), which corresponds to the vertical line in Fig. 3.6.

The lower scatter in the desinence data relative to the inception data is consistent with observations in Fig. 3.6. All of the desinence data lie within the 5.8°–6.0° interval with the exception of several outliers at lower incidences, where cavities sustained even with weaker tip vortices. This behaviour is considered in further detail in Sect. 3.4.2.

The distribution of the inception data does not yet appear converged. This indicates that a larger sample size (e.g. $\mathcal{O}(100 - 1000)$) is required to fully describe the statistical distribution of the inception angle in a nuclei deplete flow. Alternatively, an idea of the spread of the distribution could be found with as few as ten observations.

It is commonly known that Reynolds number and lift coefficient affect vortex strength and thus tip vortex cavitation inception behaviour. Furthermore, the tensile strength of a body of water determines how much tension the liquid can sustain prior to rupture. The results presented thus far demonstrate that the effective tensile strength is probabilistic in nature, and is influenced by test methodology which controls the volume of water, and hence number of nuclei, exposed to low pressures. This volume changes with not only the freestream velocity and the model scale, but also the time spent at each test condition and the increments in the variables of interest. This in turn affects the measured incipient cavitation number. When conducting TVC inception measurements for practical applications, consideration should be given to the relevant time scales and suitable waiting

times should be employed. The observation that the inception angle tends to increase with decreasing exposure time may have implications for cavitation inception management for practical applications.

3.4.2 Cavitation desinence hysteresis

In order to explain the existence of the outlying desinence data in Fig. 3.7, the same data set was plotted as desinence angle, α_d, against inception angle, α_i (Fig. 3.8). Two main modes of behaviour are evident. One colour represents desinence angles that remain relatively constant when the inception angle is 7.3° or smaller. For the other, smaller desinence angles are observed when the inception angle is 7.4° or larger. The data corresponding to the latter mode comprise the outliers in Fig. 3.7. A transition region lies between 7.3°–7.4° where both behaviours are observed.

The differences between the two modes were investigated by taking photographs of cavity topologies at varying stages of development, as shown in Fig. 3.9. The cavity topology can appear as an unattached tip vortex cavity at smaller incidences, or a cavity attached to the hydrofoil tip at larger incidences. It is evident that topological differences prior to desinence are responsible for the existence of two desinence modes. Similar observations were made in qualitative terms by Green (1988), who stated that the attachment of a trailing vortex cavity to the hydrofoil tip significantly influences the flow field. As a result, a higher cavitation number, sometimes higher than the incipient cavitation number, is required to detach the cavity from the hydrofoil.

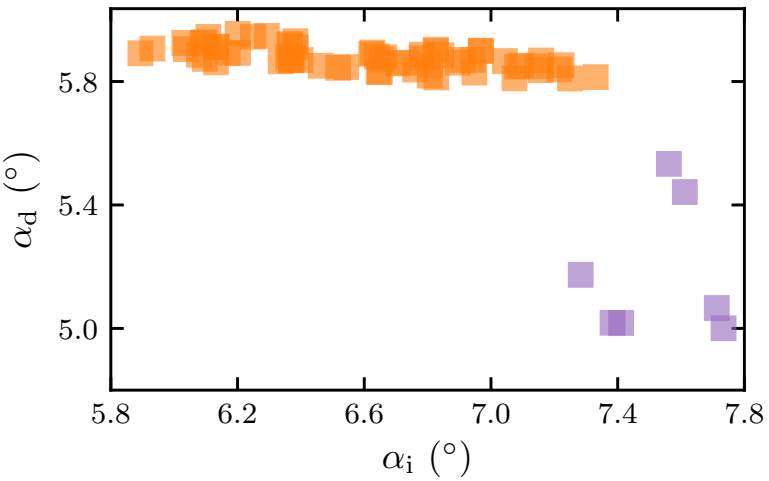

Figure 3.8: Desinence angle, α_d, as a function of inception angle, α_i, using the same data as in Fig. 3.7. Two modes are evident: large desinence angles correspond to smaller inception angles (orange), while small desinence angles occur for large inception angles (purple). The data points for the latter mode correspond to the outliers in Fig. 3.7. Measurements were taken at constant tunnel operating conditions ($Re = 1.7 \times 10^6$ and $\sigma = 0.99$).

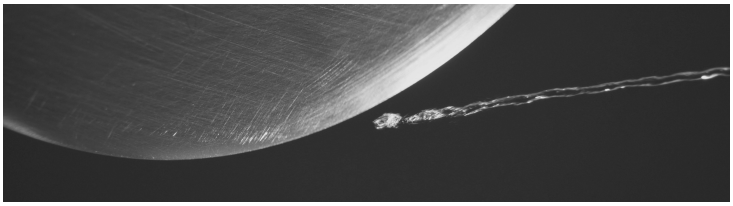

(a) $\alpha = 6.8°$, Unattached TVC

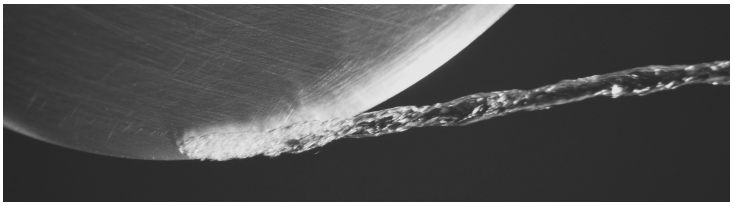

(b) $\alpha = 7.9°$, Attached TVC

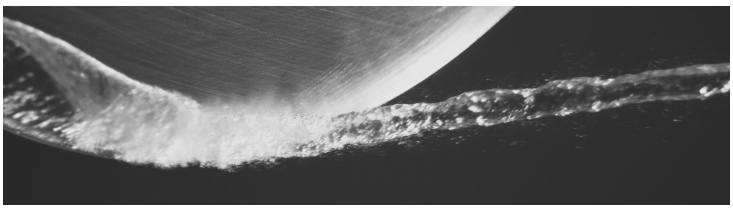

(c) $\alpha = 8.1°$, Attached TVC (with sheet cavitation)

Figure 3.9: Photographs of different stages of tip vortex cavitation (TVC) development. The flow is from left to right. The cavity is sometimes unattached (a) and sometimes attached (b, c). With more tension, leading-edge sheet cavitation appears simultaneously with TVC (c). The change in cavity topology is responsible for the lower desinence angles observed in Figs. 3.7 and 3.8 (purple data). Test conditions were $Re = 1.9 \times 10^6$ and $\sigma = 1.4$.

A photographic comparison was also conducted for the changing cavitation number approach, as presented in Fig. 3.10. Two inception-desinence runs are shown. For the first, the cavitation number was lowered well below the incipient value to a minimum value of $\sigma_{\min} = 1.31$, with the appearance of simultaneous leading-edge sheet and tip vortex cavitation. The consequent desinent cavitation number of 2.32 for the desinence of attached cavitation is significantly higher than the 1.94 observed for the second run (i.e. desinence of unattached cavitation) where only an unattached tip vortex cavity was observed at the minimum cavitation number of 1.85. This hysteretical observation further supports the theory that cavity topology at the minimum cavitation number affects TVC desinence behaviour. Gaseous diffusion is known to delay the disappearance of tip vortex cavities at higher cavitation numbers (Amini et al., 2019). Multiple observations of a tip vortex cavity in the 'attached' state without a sheet cavity (Fig. 3.9(b)), prior to desinence, suggest that cavity attachment affects or controls desinence behaviour.

Stable, attached cavities are often associated with laminar separation bubbles which can stabilise the local flow and shelter the tip vortex core (Amini et al., 2019). Experimentally-measured lift and drag curves have been plotted for a range of Reynolds numbers in Fig. 3.11. Laminar separation appears to influence the measured lift and drag force at about 8°. This influence decreases with increasing Reynolds number. Furthermore, the local Reynolds number at the tip is relatively low and therefore laminar flow and separation can be expected even at higher Reynolds numbers that are based on the root chord length. In fact, the observed attached cavities can occur due to the sheltering effect of a separated laminar boundary layer, whereas an attached turbulent boundary layer would sweep cavities downstream and prevent them from attaching to the foil (Franc and Michel, 2006). Laberteaux and Ceccio (2001) observed the steady closure of a vapour-filled cavity due to an oblique re-entrant jet. Adhesive forces due to interfacial phenomena at the gas-solid-liquid interface may also play a role in desinence hysteresis behaviour (Danov et al., 2016). This raises an interesting question about the influence of material and surface finish on cavity detachment behaviour. Alternatively, this phenomenon may be related to the supply of water vapour from the leading-edge cavity into the vortex.

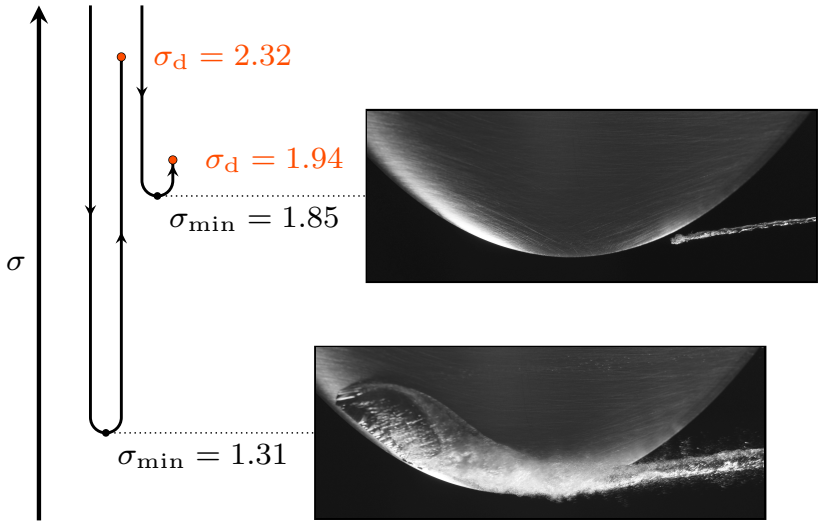

Figure 3.10: Schematic of different cavitation desinence tests for identical tunnel conditions ($\alpha = 8.0°$ and $Re = 1.7 \times 10^6$). Different topologies (as shown in photographs) were generated by reducing the cavitation number to two different minimum values (σ_{min}). The desinent cavitation number, σ_d, is dependent on the cavity topology.

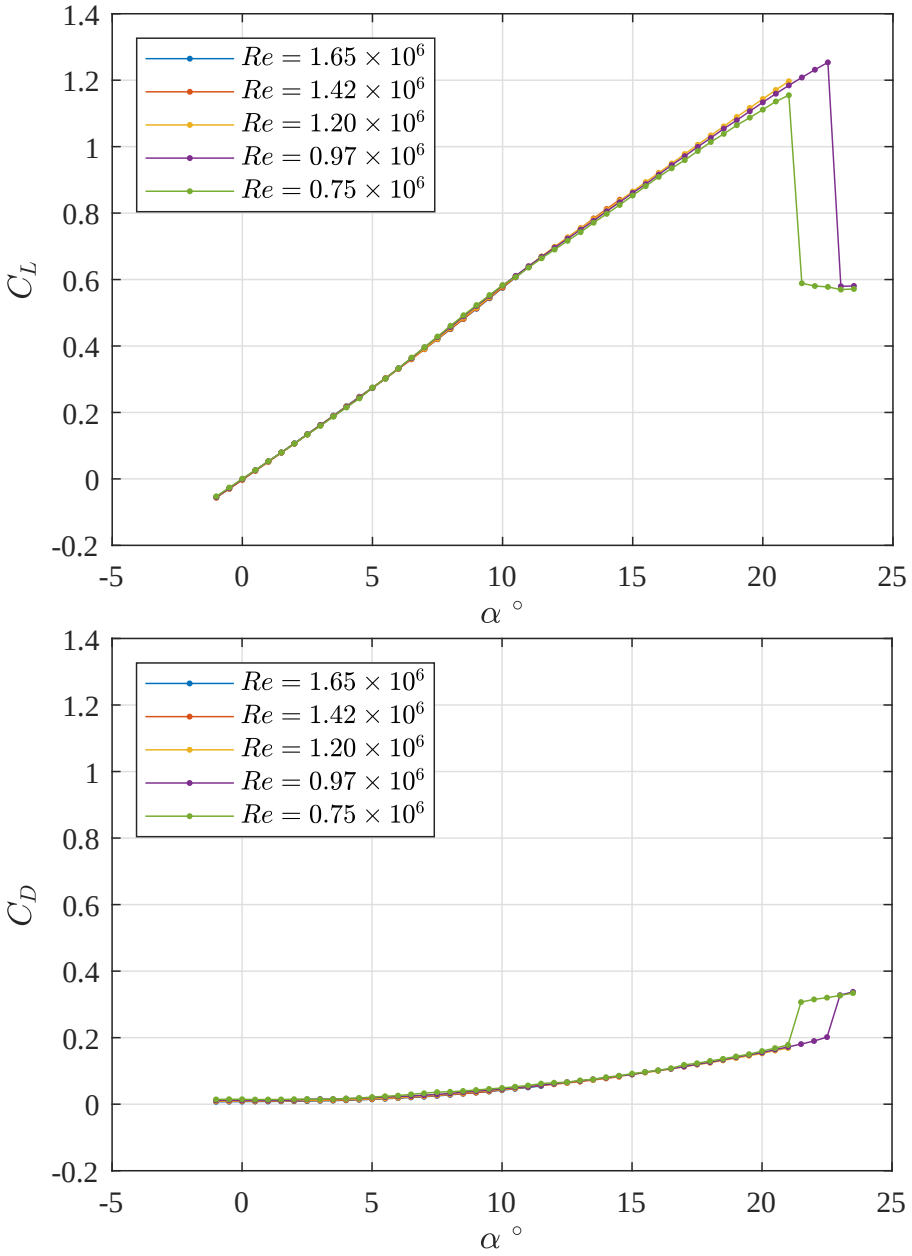

Figure 3.11: Hydrofoil lift (top) and drag (bottom) curves over a range of Reynolds numbers.

The effect of the different cavity topologies at the minimum cavitation number on the relationship between desinent cavitation number and incidence was investigated by varying the cavitation number at fixed incidences for a constant Reynolds number (Fig. 3.12). The test section pressure was reduced in 5 kPa steps from a non-cavitating condition, with 60 s spent at each test condition to monitor for inception. This was repeated until TVC inception was detected visually, then either:

1. the test section pressure was continuously increased until TVC desinence occurred, or
2. the test section pressure was decreased further until a leading-edge sheet cavity appeared then continually increased until desinence.

The minimum cavitation numbers reached during the tests are indicated by the circles, and the colour corresponds to the cavity state at this minimum cavitation number. The 'attached' condition required a lower cavitation number. A total of 38 tests were carried out, at 21 unique incidences between 3.5° and 10.0°.

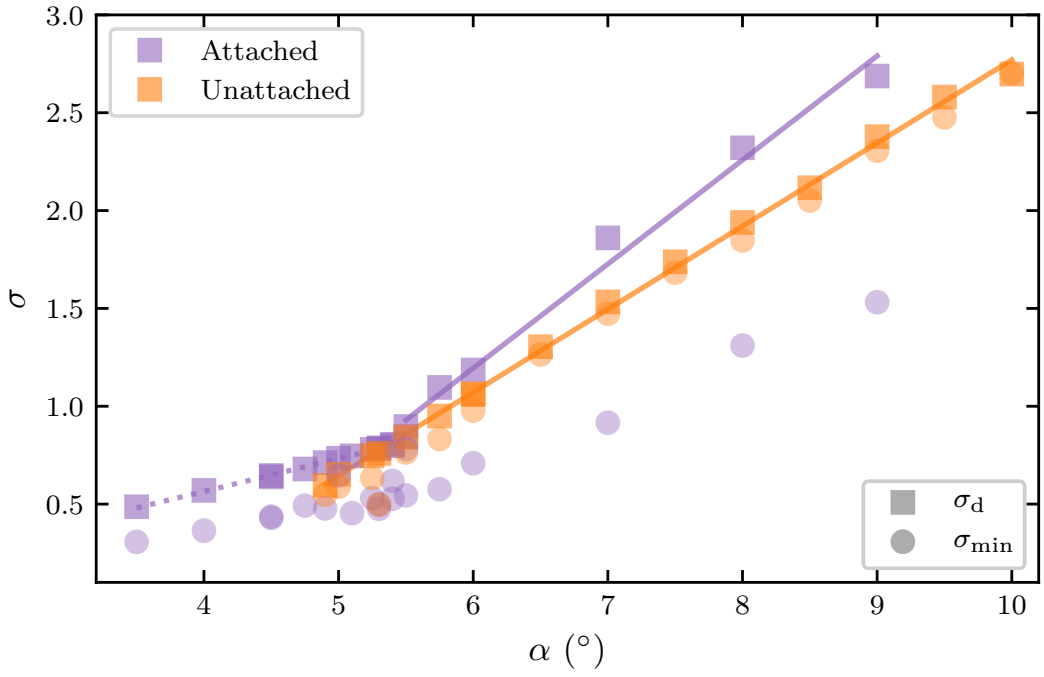

Figure 3.12: Variation of desinent cavitation number, σ_d in squares, with incidence, α, and cavity state (attached in purple and unattached in orange). Above 5.5°, two distinct desinence modes exist according to the topology. The mode with higher σ_d values corresponds to the attached cavity state. Below 5.5°, the influence of the leading-edge pressure distribution is indicated by the change in slope of the data. The minimum cavitation numbers, σ_{min}, for the tests are shown as circles and determine whether the cavity attaches to the hydrofoil. The Reynolds number was 1.8×10^6.

Below 4.9°, the cavity always manifests as simultaneous leading-edge sheet and tip vortex cavitation, i.e. an isolated tip vortex cavity is not observed. The desinent cavitation number is linearly dependent on the incidence, with a slope of 0.17/°, and is indicated by the dotted line. In this regime, the minimum pressure in the flow is at the leading-edge of the hydrofoil.

For $\alpha \geq 4.9°$, different desinence modes are again evident. The unattached mode, shown in orange, is linear across the range of incidences with a slope of 0.42/°. The minimum cavitation numbers required to induce this mode are close to the desinent values. That is, only a small hysteresis exists between the incipient and desinent cavitation numbers for the desinence of unattached cavitation. This may be because the cavity is not sheltered by the stabilised flow about the tip, or no additional energy is required to detach the cavity from the hydrofoil to overcome interfacial phenomena. The mode with higher desinent cavitation numbers, which corresponds to cavity attachment, has a steeper slope of 0.53/° for $\alpha \geq 5.5°$. The cavitation number hysteresis is much larger for the desinence of attached cavitation, as observed in Fig. 3.12. Below $\alpha = 5.5°$, the attached mode manifests with a lower slope, which appears to be an extension of the regime for which simultaneous leading-edge sheet and tip vortex cavitation occur at inception (dotted line). This suggests that desinence values here may correspond to vapour pressure at the leading edge.

The desinent cavitation numbers for the unattached regime show excellent linearity ($R^2 = 0.999$) with incidence. This supports the findings of Fruman and Dugue (1994), but others have observed different relationships (e.g. 'nearly linearly' by McCormick (1962), lift coefficient exponents of 1.4 and 2 by Arndt and Keller (1992)). The desinence data series for the attached regime may be interpreted as a polynomial with an index higher than 1 due to the 'kink' at 5.5°, which could explain the higher indices noted in other work. Additionally, if a set of desinence values from mixed cavitation modes was used, a non-linear relationship may be found.

Finally, the close agreement observed between the desinence data in Figs. 3.6 and 3.12 suggests that the test methodology (i.e. changing incidence or cavitation number) has no significant effect.

3.5 Conclusions

Tip Vortex Cavitation (TVC) behaviour about an elliptical planform hydrofoil has been studied in a nuclei deplete flow. Significant scatter in the inception data indicates that the tensile strength of a body of water is not constant, but rather varies throughout and is thus probabilistic in nature. At a given test condition, a cavity may not incept for a long time if the water is sufficiently deplete of nuclei. However, the volume of water exposed to low pressures in the vortical flow increases with time spent at each test condition, thereby increasing the probability of nuclei capture and activation. For nuclei deplete flows in particular, multiple measurements (e.g. $\mathcal{O}(100 - 1000)$) are required to accurately quantify the probabilistic nature of TVC inception. It can be reasoned that a smaller sample size will be required for nuclei abundant flows due to the higher nuclei flux through the low pressure region and increased probability of inception. To confirm this, further tests are required using flows injected with higher concentrations of larger microbubbles compared to the population studied here.

Different TVC desinence behaviours are observed, dependent on the topology of the cavitating flow. For the desinence of attached cavitation, the desinent cavitation number is higher and larger hysteresis is observed compared to the desinence of unattached cavitation. A number of possible reasons for this are proposed, including stabilisation of the cavity flow by a laminar separation bubble, and adhesive forces present at the gas-liquid-solid interface due to interfacial phenomena. Desinence measurements are not affected by nuclei, resulting in lower scatter in the observed cavitation numbers. While the repeatability of desinence simplifies cavitation measurements, inception is often of greater practical interest.

Further work is required to correlate vortex pressure and the tensile strength of a body of water, taking into account factors such as bubble dynamics during capture and unsteady pressure fluctuations in the vortex core. This would assist in the development of a TVC inception prediction model which takes a known nuclei population and pressure field, and computes the probability of inception for a given operating condition.

3.6 Acknowledgements

The authors acknowledge the support of the University of Tasmania and the Defence Science and Technology Group. The authors thank AMC technical officers, Mr Robert Wrigley and Mr Steven Kent for providing technical assistance with test facility configuration and operation.

Chapter 4

Nucleation effects on hydrofoil tip vortex cavitation

In this chapter, a nuclei abundant flow is introduced to assess the effect of two vastly different nuclei populations on TVC inception behaviour. This injected, polydisperse nuclei population is measured using an optical technique termed Mie scattering imaging (Russell et al., 2020b,a). The natural nuclei population is measured using a CSM. The appearance and noise emission of tip vortex cavities about an elliptical hydrofoil are compared for the two nuclei populations. The high resolution photography and acoustic measurements taken in this study are used in a related study to quantify the effect of hydrofoil incidence, and thus vortex strength, on cavity diameter and acoustic spectral content in flows deplete of nuclei (Venning et al. (2019) in Appendix D).

This chapter is an author accepted manuscript of an article published in the proceedings of the *21st Australasian Fluid Mechanics Conference*, modified following thesis examiners' feedback. The final authenticated version is available online at:

`http://www.afms.org.au/proceedings/21/Khoo_et_al_2018.pdf`.

The citation for the paper is:

M. Khoo, J. Venning, B. Pearce, and P. Brandner. Nucleation effects on hydrofoil tip vortex cavitation. In Proc. 21st Australasian Fluid Mech. Conf., 2018.

4.1 Abstract

Tip vortex cavitation inception about an elliptical planform, NACA 0012 hydrofoil is investigated in cavitation tunnel flows in which cavitation nuclei are deplete and abundant. Tests were conducted at fixed Reynolds and cavitation numbers. The onset, or inception, of cavitation was induced by increasing the angle of incidence and behaviour was recorded photographically and acoustically. Cavitation inception occurred at a higher incidence in the deplete case compared with the abundant due to fewer weaker nuclei. It also occurred within a small incidence change for the deplete case, with the appearance of a continuous, cavitating vortical flow structure. Whereas for the abundant case, inception was intermittent, occurring across a larger incidence range. This was associated with individual nuclei activation events increasing in frequency with increasing incidence. Sound pressure levels increased with inception and cavity development but reduced to a local minimum once the cavity attached to the hydrofoil, increasing thereafter with incidence. Overall sound levels were higher for the abundant case than for the deplete case.

4.2 Introduction

Cavitation occurs when a fluid changes from liquid to vapour phase due to pressure reduction. Tip Vortex Cavitation (TVC) is often the first form of cavitation to occur due to the low pressure generated in the vortex core (Brennen, 1995; Franc and Michel, 2006). A tip vortex is generated at the tip of a lifting surface operating at non-zero lift.

Microbubbles, and potentially gas-containing biological organisms or solid particles with trapped gas (Lecoffre, 1999), provide nuclei for cavitation inception. Nuclei are captured in vortical flows due to buoyancy created by the radial pressure gradient. A captured microbubble will trigger inception if the core pressure is below a size-dependent critical pressure less than vapour pressure. Microbubble equilibrium then becomes unstable—it will grow explosively and fill with vapour leading to macroscopic cavitation formation. TVC inception and development generates noise due to complex transients (Choi and Ceccio, 2007) and modes of oscillation (Pennings et al., 2015a).

Typically, practical flows contain a range of nuclei sizes at differing concentrations making TVC inception a complex probabilistic process. The nuclei deplete and abundant flows that are possible in the AMC cavitation tunnel allow the effects of nuclei content on TVC inception to be quantified, the results of which have implications for ship and submarine operations.

The definition of TVC inception is not entirely clear. The challenge of visually detecting inception is related to the difficulty of distinguishing a vaporous cavity from migration of nuclei into the vortex core with high nuclei concentration flows (Boulon et al., 1997). Two definitions of inception have been proposed: 1) the first appearance of a cavitation bubble and 2) the persistent attachment of a vapour core to the foil tip. Similar definitions were used for visual detection in Gowing et al. (1995), with the exception that a coalesced, persistent cavity within 0.2 chord lengths downstream of the hydrofoil tip was also considered to be 'attached'.

Criteria for TVC inception using acoustic measurements have also been proposed. An event rate threshold of one per second was used as an inception criterion in Briançon-Marjollet and Merle (1996), the results of which correlated well with those for visual detection using the same event rate threshold. In a separate study, a detection threshold of 3 dB above the background level was used for propeller cavitation inception (Gindroz and Billet, 1994). Using this approach, inception numbers from acoustic measurements were approximately 5–10% higher than for visual detection, regardless of nuclei population.

TVC behaviour at inception has also been documented in several studies (Boulon et al., 1997). Using visual observations and increasing the angle of incidence, the first appearance of a cavitation bubble occurred at lower incidence in a flow seeded with microbubbles compared with an unseeded flow. In contrast, permanent attachment of the vapour core to the foil tip occurred at practically the same incidence regardless of seeding conditions.

The sound level of propeller cavitation during cavity development was observed to increase monotonically with decreasing cavitation number (Gindroz and Billet, 1994). In contrast, a local peak was observed when cavitation desinence of a hydrofoil was studied by increasing the cavitation number (Song et al., 2017). It was also found that the maximum sound level increased with nuclei concentration.

A literature review reveals little published data on nucleation effects on hydrofoil TVC inception using correlated acoustic and visual measurements. To gain further insight into the effects of nuclei on TVC inception, flow physics and sound levels, experiments were carried out at the Australian Maritime College Cavitation Research Laboratory (AMC CRL) using an elliptical planform, NACA 0012 hydrofoil to address this gap. Only a limited number of cavitation test facilities currently exist which allow strict control over nuclei content in the water (Brandner et al., 2007; Lecoffre et al., 1988; Song et al., 2017). Two extreme cases of flows with a low concentration of small nuclei (referred to as 'deplete') and a high concentration of large nuclei ('abundant') were considered, with TVC inception behaviour measured both photographically and acoustically.

4.3 Experimental overview

TVC inception measurements were carried out in the cavitation tunnel at the AMC CRL. The test section is 0.6×0.6 m in cross section and 2.6 m long. The circuit volume is 365 m^3 and demineralised water is used as the working fluid. The absolute pressure at the centreline of the test section can be set between 4–400 kPa and the flow velocity can be varied between 2–12 m/s. The tunnel has ancilliaries for fast degassing and nuclei injection, and flow conditioning for continuous elimination of microbubbles enabling strict control of nuclei content. Further details on tunnel design and operation are described in (Brandner et al., 2007).

The model hydrofoil is of elliptical planform, NACA 0012 section profile, 150 mm base chord and aspect ratio of 1.5 (defined as $\mathit{AR} = b^2/A$, where b is the span and A is the planform area). It was ceiling-mounted nominally midway along the tunnel test section, as shown in figure 4.1. All experiments were conducted at a fixed Reynolds number, Re, of 2×10^6 (using base chord as the characteristic length) and cavitation number, σ of 1.0, where $Re = U_\infty c/\nu$ and $\sigma = (p_\infty - p_v)/q$, where U_∞ is the freestream velocity, c the base chord, ν the kinematic viscosity, p_∞ the freestream pressure, p_v the vapour pressure and q the dynamic pressure. The model incidence was set using an automated force balance via closed loop control.

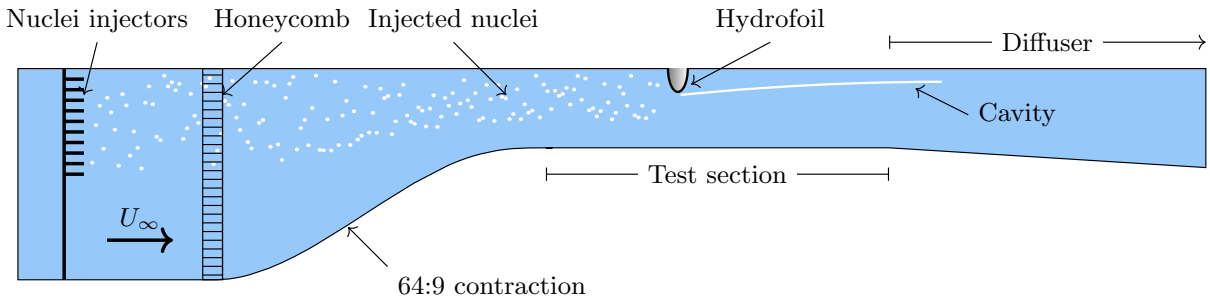

Figure 4.1: Schematic of the hydrofoil TVC experimental setup. Hydrophone and cameras are not shown. For the seeded case, microbubbles are injected from upstream of the test section through an array of injectors.

Cumulative histograms of nuclei concentration as a function of critical pressure relative to vapour pressure ($T_c = p_c - p_v$), for the nuclei deplete and abundant cases are shown in figure 4.2. The nuclei deplete case is the naturally occurring background population in the tunnel which is not active for many forms of cavitation (Venning et al., 2018b) but may be so for TVC given the high tensions developed in vortex cores. This background population is too sparse and small for practical measurement with optical techniques and have been measured with a Cavitation Susceptibility Meter (CSM) (Khoo et al., 2016). Water is sampled from the tunnel resorber and passed through a venturi at different throat pressures, resulting in a cumulative histogram of concentration against T_c. The abundant nuclei case is created using a 3 × 10 rectangular array of microbubble generators each

directly injecting about 10^6 bubbles per second. The array is located upstream of the contraction, as shown in figure 4.1. This population was measured in the test section upstream of the hydrofoil using Interferometric Mie Imaging (IMI) (Russell et al., 2018b). The CSM measurement produces a cumulative histogram whereas the IMI provides a histogram of concentration per unit size increment. These can be compared through numerical integration of the cumulative histogram:

$$C(T_\mathrm{c}) = \int_{T_{\mathrm{c}_\mathrm{min}}}^{T_\mathrm{c}} c(T_\mathrm{c}^*)\, dT_\mathrm{c}^* \tag{4.1}$$

where C is the concentration of all nuclei with critical tensions between the lowest critical tension of measured nuclei, $T_{\mathrm{c}_\mathrm{min}}$, and a given critical tension, T_c, and the concentration density, c, is a function of the critical tension, T_c^*. The initial bubble diameter, D_∞, corresponding to T_c can be found numerically from single bubble equilibrium theory (Franc and Michel, 2006):

$$\frac{4}{27{T_\mathrm{c}}^2} = \left(\frac{D_\infty}{4S}\right)^3 (p_\infty - p_\mathrm{v}) + \left(\frac{D_\infty}{4S}\right)^2 \tag{4.2}$$

where S is the surface tension.

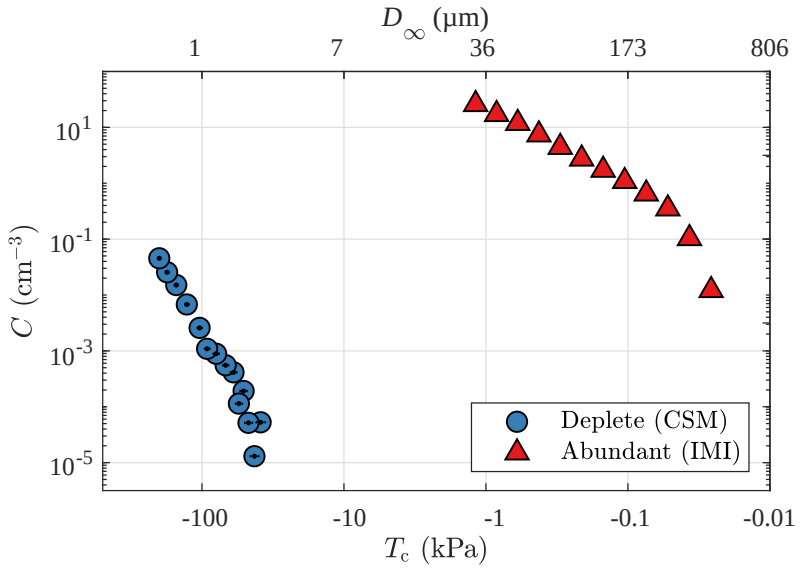

Figure 4.2: Deplete and abundant nuclei distributions measured using CSM and IMI methods respectively. For CSM measurements, water was sampled from the tunnel resorber. IMI measurements were taken in the test section.

Two approaches were used to detect TVC. Firstly, a digital single-lens reflex camera was used to take photographs near the hydrofoil tip at each test condition prior to and after inception. Acoustic measurements were taken for the corresponding test conditions using an in-ceiling hydrophone (Doolan et al., 2013) (Brüel&Kjær Type 8103, sample rate 204.8 kHz) located $2.5c$ downstream of the hydrofoil. The Sound Pressure Level (SPL) was calculated from the integral of the power spectral density (Hanning window in 1 s blocks, shifted by 1/8 s with one-third octave bands) across the range of measured frequencies (Glegg and Devenport, 2017). A lower cutoff frequency of 400 Hz was used to exclude frequencies not directly associated with the tip vortex cavity. The SPL is calculated by

$$\mathrm{SPL} = 10\log_{10}\left(\frac{1}{p_{\mathrm{ref}}^2}\int_{f_l^{(n)}}^{f_u^{(n)}} G_{pp}(f)\,df\right)\mathrm{dB\,re}\,p_{\mathrm{ref}} \tag{4.3}$$

where p_{ref} is the reference pressure (1 µPa), $f_l^{(n)}$ and $f_u^{(n)}$ are the lower and upper frequency of the nth band respectively, G_{pp} is the single-sided spectrum and f is the frequency.

The angle of incidence of the hydrofoil was increased while σ and Re were held constant. This enabled the injector settings to be maintained as constant. Starting from $\alpha = 0°$, preliminary runs were conducted by continuously increasing α to identify the approximate inception angles, α_{i}. Photographs and acoustic measurements were taken at $\alpha = 0°$, then α was increased with coarse resolution (0.5–1°). Finer resolution (0.1°) was used just prior to and just after α_{i}. The hydrofoil remained at each α for approximately 50 s, including 20 s of acoustic measurements.

4.4 Results

The changes in SPL with increasing α for the nuclei deplete and abundant cases are shown in figure 4.3. The red, dotted line represents a SPL of 3 dB above the background level measured at $\alpha = 0°$. TVC photographs are provided for α values corresponding to salient features on the SPL graph.

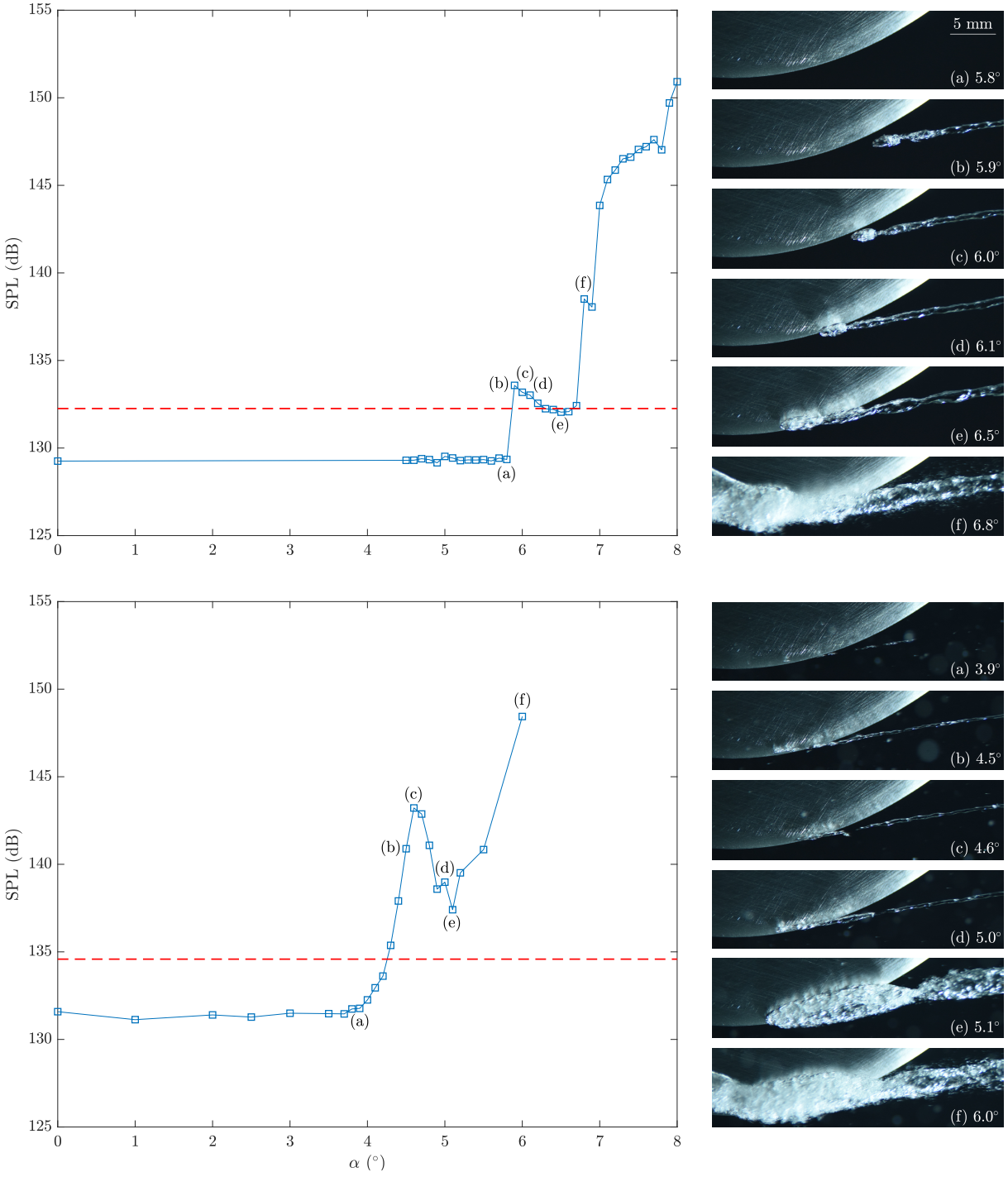

Figure 4.3: Change of Sound Pressure Level, SPL, with angle of incidence, α, without (top) and with (bottom) seeding for $\sigma = 1.0$ and $Re = 2 \times 10^6$. Red, dotted lines represent thresholds 3 dB above the background levels measured at $\alpha = 0°$. Photographs of the cavity are provided for angles of interest.

For the deplete case, inception occurs at $\alpha = 5.9°$ with the appearance of a continuous tip vortex cavity, the leading edge of which is just downstream of the hydrofoil tip. With inception, the SPL rises by about 5 dB. The cavity has a bulbous leading edge with a necked region immediately downstream suggesting the presence of re-entrant flow. Perturbations or waves can be seen on the cavity due to various cavity deformation modes (Pennings et al., 2015a). Both the re-entrant flow and cavity volumetric variations appear to be noise sources. The TVC moves upstream with increasing α accompanied by a decrease in SPL. The TVC reaches the hydrofoil outline by 6.1° and moves within the outline by 6.5°. At this α the leading edge flow appears suppressed which may be associated with the drop in SPL and the reduction of re-entrant flow noise. It is unlikely the SPL reduction is due to the change in cavity leading edge position as it only moved about 10 mm upstream and was measured with a hydrophone located at least 300 mm away. The SPL increases again with α, with a large increase occurring at 6.8° associated with TVC attachment and the formation of hydrofoil leading edge sheet cavitation. At this stage, the SPL remains significantly higher than the baseline non-cavitating noise. Possible noise sources include cavity volumetric variations and vapour packet shedding from the attached cavity. The SPL increases further with α due to sheet cavitation growth.

For the abundant case the pre-inception SPL is about 2 dB greater than the nuclei deplete case. This may be attributable to nuclei injector operation upstream, but perhaps more likely, excitation or deformation of nuclei in the flow. Inception in this case does not occur with a 0.1° change in α, as with the deplete case, but is a process that starts with intermittent nuclei capture and activation events which progress with increasing event rate to a sustained continuous cavity. This process starts at a much smaller α than for the deplete case due to the greater concentration of larger, weaker nuclei. Intermittent capture events are visible at about 2° but the SPL only begins to rise at about 3.9°. The cavity remains discontinuous with increasing α to 4.5° where it extends upstream to within the hydrofoil planform, and to 4.6° where the SPL reaches a local maximum. The extent of the intermittency decreases with increasing α and the cavity becomes continuous downstream of the hydrofoil planform at about $\alpha = 5.0°$ but is unsteady upstream of this point.

The increase in SPL with α up to 4.6° is presumably due to the increasing nuclei capture/activation rate and the local maximum is due to this rate also reaching a maximum. That is, for higher α this rate reduces with greater sustained cavity length, hence the reduction in SPL. The SPL reaches a local minimum at $\alpha = 5.1°$ where the cavity increases in diameter and becomes attached to the hydrofoil. For further α increase, the SPL increases with the formation of sheet cavitation as occurred for the nuclei deplete case.

The local SPL maximum that occurs after inception with TVC development is much higher for the abundant case than for the deplete case showing that intermittent nuclei activations generate higher SPL than local flow features or continuous cavity modes. The

cavity diameter during initial development is much less than for the deplete case which may be attributable to the lower incidence, and hence vortex strength, at inception, and possibly intermittency reducing the volume of dissolved gas diffusing from the liquid to the cavity. The latter is driven by the concentration gradient between the vapour/gaseous cavity and the liquid. This is evidenced by the similar cavity diameters and volumes that form once the cavity becomes persistent. Another possible reason for the smaller cavity diameter is reduced boundary layer thickness at lower α.

4.5 Conclusion

Tip vortex cavitation inception has been investigated about an elliptical hydrofoil in nuclei deplete and abundant flows using photographic and acoustic measurements. For the deplete case, inception occurred within a 0.1° angle of incidence change resulting in the sudden appearance of a continuous cavity and step change in sound pressure level. For the abundant case, inception occurred at lower incidence due to a higher concentration of weaker nuclei. For this case, inception involved intermittency associated with individual activation events increasing in frequency with incidence until a continuous cavity was sustained. This process occurred over a range of incidences and was accompanied by increasing sound levels to a local maximum possibly associated with a maximum cavitation rate.

Both cases exhibit local maxima in sound pressure level associated with inception or development although each appears associated with different cavity physics. Overall sound levels are much higher in the abundant case. These levels reached local minima with cavity hydrofoil attachment before increasing with incidence due to sheet cavity formation.

4.6 Acknowledgements

The authors acknowledge the support of the University of Tasmania and AMC technical officers Mr Robert Wrigley and Mr Steven Kent.

Chapter 5

Nucleation and cavitation number effects on tip vortex cavitation dynamics and noise

In Chapter 4, high resolution photography and acoustic measurements were used to examine the effects of nuclei content on TVC about an elliptical hydrofoil. In this chapter, high speed video and acoustic measurements of TVC behaviour about an elliptical hydrofoil with a higher aspect ratio are made synchronously. They reveal the effects of different injected nuclei populations on the location of TVC inception, as well as kinematics and acoustics along a range of streamwise locations. Large sample sizes of $\mathcal{O}(1000)$ are used to characterise the phenomenon. One population is monodisperse, which makes modelling and prediction easier as the flow is seeded with nuclei of nominally a single size. The other population is polydisperse, which is more representative of nuclei populations found in environmental waters, as seen in Chapter 2. Both populations are measured using Mie scattering imaging. The influence of cavitation number on the spatial and acoustic characteristics of tip vortex cavities is also investigated. Preliminary TVC inception location distributions published in Khoo et al. (2020b) (Appendix E) differ somewhat from those presented in this chapter, though some differences in the data acquisition approach and monodisperse nuclei size were noted.

This chapter is a post-peer-review, pre-copyedit version of an article published in *Experiments in Fluids*, modified following thesis examiners' feedback. The final authenticated version is available online at:

`https://doi.org/10.1007/s00348-021-03308-2`.

The citation for the paper is:
M. Khoo, J. Venning, B. Pearce, and P. Brandner. Nucleation and cavitation number effects on tip vortex cavitation dynamics and noise. Exp. Fluids, 62(10):216, 2021.

5.1 Abstract

The spatial and acoustic characteristics of tip vortex cavitation (TVC) inception were measured in a cavitation tunnel. Numerous cavitation events were recorded to reveal the influence of different nuclei populations and cavitation numbers on nuclei capture and activation physics, and the role of the streamwise pressure distribution in a vortex. Synchronised high speed video and hydrophone measurements of cavitation events were taken in the trailing vortex of an elliptical hydrofoil at an incidence of 6° and a Reynolds number of 1.5×10^6. The injected nuclei population in the tunnel test section was varied by using different microbubble generators mounted upstream of the test section. Both the nuclei population and cavitation number have a significant effect on the inception location distribution along the trailing vortex, and in particular, inception event rates. The cavitation number alters the flow volume subjected to tension, thereby also affecting the shape of the inception location distribution. Once the nuclei are activated, cavity kinematic and acoustic properties are influenced by the local pressure (i.e. inception location and cavitation number) more so than initial nucleus size, at least in the ∼50–100 µm diameter range considered in this study. Inception events that occur near the tip generate stronger acoustic pulses. At these inception locations, the frequency of the tonal peak associated with inception remains relatively constant for the two nuclei populations, but increases with cavitation number. This study provides insights into the roles of nucleation and cavitation number in TVC, and informs future measurements and predictions of TVC dynamics and noise.

5.2 Introduction

Cavitation inception in practical flows is typically heterogeneous in nature and occurs when a nucleus, such as a microbubble, is exposed to its size-dependent critical pressure, resulting in explosive growth. The vortex trailing from a three-dimensional lifting surface is characterised by a low-pressure core in which cavitation is most likely to appear (see Fig 5.1). Nuclei within its streamtube may be activated, as well as nuclei drawn into the vortex by its radial pressure gradient. This phenomenon is known as tip vortex cavitation (TVC). It is often the first type of cavitation to occur about marine propellers and is detrimental to acoustic stealth performance.

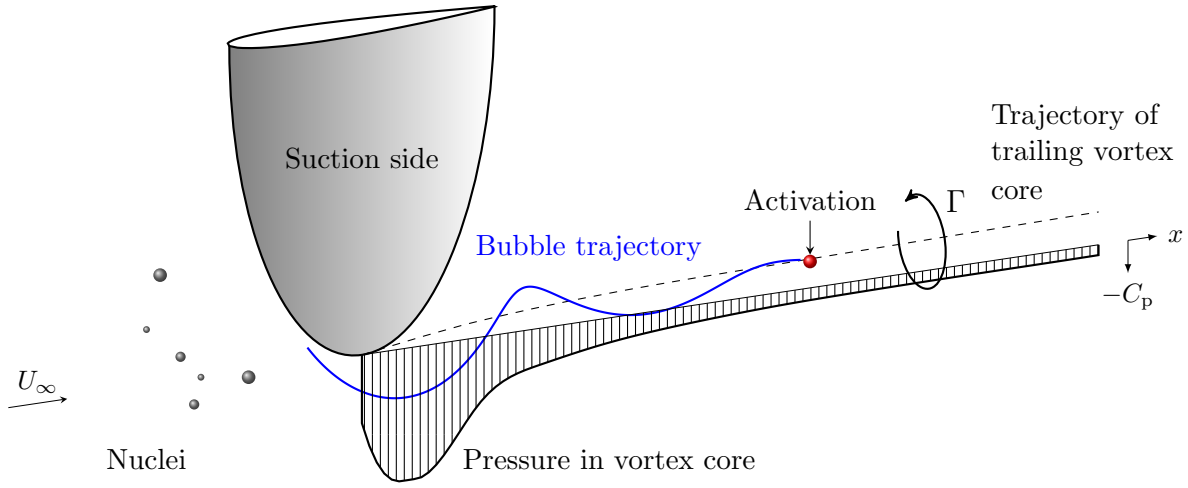

Figure 5.1: Notional capture of a nucleus (red sphere) into the vortex trailing from a lifting surface. The blue line denotes the nucleus trajectory. The freestream velocity is U_∞ and the circulation is Γ. The generic variation of the pressure coefficient, C_p, with streamwise location, x, similar to the trends observed for elliptical foils (Chen et al., 2019; Asnaghi et al., 2020), is also shown with the minimum pressure occurring close to the tip and pressure recovery downstream as the vortex diffuses.

Nuclei populations are known to vary within and between environmental and laboratory waters (Khoo et al., 2020c). They can influence TVC inception behaviour, with the earlier onset of cavitation measured in flows with higher concentrations of larger nuclei, also known as 'weak' water, as opposed to 'strong' water devoid of nuclei (Arndt and Keller, 1992; Gindroz and Billet, 1998; Khoo et al., 2018). Numerical simulations of TVC in flows with different nuclei populations have shown that fewer nuclei activations occur for populations with smaller nuclei (Hsiao and Chahine, 2005). In nature, these populations vary with location and depth (Gindroz et al., 1995; Gowing and Shen, 2001), as well as sea state (Johnson, 1986) and potentially biological activity (O'Hern et al., 1986). During experimental studies of TVC in cavitation tunnels, nuclei populations have been controlled by manipulation of the dissolved air content (Arndt and Maines, 2000; Chang et al., 2011) and by microbubble injection into the test flow (Briançon-Marjollet and Merle, 1996; Peng et al., 2017), the latter enabling more independent control over free and dissolved gas and thus their effects on cavitation behaviour. Nuclei populations have size and concentration distributions (Khoo et al., 2020c; Russell et al., 2020b), as well as spatial distributions. The arrival of a nucleus at a particular location, the low pressure vortex core in this case, is stochastic in nature. Therefore TVC inception is a stochastic process and large datasets may be required for accurate characterisation. For a flow deplete of nuclei, Khoo et al. (2020a) found that some hundreds of events are required to characterise the probability of TVC inception in a trailing vortex subjected to a given tension due to variability in the waiting time associated with nuclei capture. A flow abundant with nuclei is expected to require short waiting times with less variability.

The cavitation number is a non-dimensional quantity which controls the likelihood and scale of cavitation in a flow. In natural environments, it varies with the operational depth and velocity of the component, as well as the properties of the liquid. In cavitation

tunnels, it is typically set via tunnel pressure or flow velocity, or some combination of the pair. Maines and Arndt (1993) investigated TVC about an elliptical hydrofoil, and found that at higher cavitation numbers, TVC appears as unsteady, isolated events. A reduction in the cavitation number results in the development of a fully-cavitating vortex core with a characteristic bulbous head at the upstream extent of the cavity. This cavity moves upstream and attaches to the tip at even lower cavitation numbers. The appearance of TVC at inception is also dependent on the nuclei population. In strong water, TVC does not appear until high tensions are applied, in which case it manifests as a steady cavity, rather than isolated events (Khoo et al., 2018).

TVC inception location is of interest because the streamwise pressure distribution may affect tip vortex cavity dynamics and acoustics. The pressure distribution within a tip vortex, and hence the location of minimum pressure, close to the tip is dependent on hydrofoil planform, cross-section and tip geometry (Astolfi et al., 1999). The location of minimum pressure has been measured to be between 0.075 and 0.125 chord lengths downstream of the tip for elliptical hydrofoils in experimental (Fruman and Dugue, 1994) and numerical (Hsiao and Chahine, 2005; Asnaghi et al., 2020) studies. Cavitation inception may occur at streamwise locations along the vortex away from the location of minimum pressure, as long as the local pressure is sufficiently low to activate a captured nucleus. The capture of a nucleus is dependent on vortex strength, bubble size and its distance from the vortex (Ligneul and Latorre, 1989, 1993; Chen et al., 2019).

Quantitative data on TVC inception location is scarce. Anecdotal observations indicate that inception usually happens near the tip in weak water (Maines and Arndt, 1993; Arndt and Maines, 2000), but can occur between -0.05 and about 1.5 chord lengths downstream of the tip (Maines and Arndt, 1993; Higuchi et al., 1989). Arndt and Maines (2000) reported that in strong water, inception is equally likely between 0.05 and 1.0 chord length downstream of the tip, but quantitative distributions were not provided. In contrast, a more uniform distribution of inception locations was observed in a weaker flow seeded with larger monodisperse bubbles, compared to a stronger flow with a polydisperse distribution of smaller bubbles (Khoo et al., 2020b). In that study, the water quality was controlled by varying the free gas content (i.e. the nuclei population), rather than the dissolved or total gas content as done by Arndt and Maines (2000). More detailed studies are required to characterise nucleation and cavitation number effects on TVC inception location distribution, with a view to understanding cavity dynamics and acoustics.

A number of studies on TVC bubble dynamics can be found in the literature. Inception was observed to comprise of four phases by Maines and Arndt (1993):

1. Spherical nucleus entrainment.
2. Spheroidal bubble growth.
3. Transitional phase.
4. Cylindrical bubble growth.

Spheroidal growth is followed by axial stretching, with the cavity observed to initially elongate at a relatively constant rate. The elongation rate, which has been found to vary between one and almost five times the freestream velocity, is dependent on nucleus capture location and is higher when entrainment occurs closer to the tip (Arndt and Maines, 2000). For lower elongation rates, the cavity grows as it is advected downstream, but for higher elongation rates, the head of the cavity remains stationary as the tail extends downstream. The elongation rate decreases downstream in the pressure recovery region (Choi and Ceccio, 2007). A relationship between the elongation rate and theoretical vortex tension was proposed by Arndt and Maines (2000), but poor correlation was observed, suggesting the need for more detailed analytical models. High speed video measurements of TVC in a flow saturated with air showed that the maximum cavity elongation rate occurs when the bubble centre is between approximately 0.2 and 0.25 chord lengths downstream of the tip, although a significant degree of scatter was present in the dataset (Maines and Arndt, 1993). Based on the complexity of tip vortex cavity development from nucleus capture to cylindrical cavity elongation, Maines and Arndt (1993) concluded that spherical bubble dynamics do not adequately describe inception.

The theory of bubble acoustics has been studied in depth. The acoustic pressure generated by a bubble is dependent on its radius and the first and second time derivatives of the radius, and therefore its volumetric acceleration (Lamb, 1945; Fitzpatrick, 1958; Leighton, 2012). The natural frequency of spherical bubble oscillation was initially derived by Minnaert (1933), then extended by others, including Brennen (1995), to account for surface tension. Larger bubble radii and lower external pressures result in lower resonant frequencies. This is similar to the resonant frequencies of cylindrical cavities given by Neppiras (1980), for which longer cavities resonate at lower frequencies.

Some observations of water quality effects on tip vortex cavity dynamics and noise can be found in the literature. Higher cavity elongation rates have been observed in flows with stronger nuclei (Arndt and Maines, 2000), although these results may also be affected by the different tensions in the vortex required to activate nuclei with different critical pressures, which complicates the analysis. Choi et al. (2009) found numerically that larger nuclei with critical pressures close to vapour pressure grow in a quasi-steady manner subjected to slowly-applied tension, while nuclei under high tension grow explosively to a diameter larger than the equilibrium diameter before oscillating and generating noise. By varying the nuclei size distribution, Hsiao and Chahine (2005) observed fewer acoustic pressure pulses in flows with stronger, smaller nuclei. Although similar trends in acoustic magnitude were measured in strong and weak flows during the onset and development of TVC, higher sound pressure levels and different cavity appearances were observed for the latter (Khoo et al., 2018). The experiments of Higuchi et al. (1989) suggest that dissolved gas content does not influence TVC acoustics. Moreover, the cavitation number was found to have a moderate effect on simulated peak pressures of microbubbles during initial growth (Choi and Chahine, 2003). Depending on the bubble model employed, the highest acoustic pressures occurred during bubble collapse (spherical model) or splitting

(non-spherical model), rather than initial growth. Hsiao and Chahine (2005) showed numerically that bubble collapse noise increases in magnitude with decreasing cavitation number.

It is evident that the nuclei population, along with the pressure field, control TVC inception. While numerous studies have been carried out into TVC kinematics and acoustics, there is a lack of experimental studies on nucleation and cavitation number effects using strictly controlled nuclei populations. To quantify the influence of nucleation and cavitation number on TVC behaviour and its associated physics, the spatial and acoustic characteristics of hydrofoil TVC were studied in a cavitation tunnel, and related to inception locations along the vortex. Synchronised high speed video and acoustics measurements of $\mathcal{O}(1000)$ intermittent cavitation events were made. Nucleation effects were studied by varying the microbubble population in the tunnel test section. The influence of cavitation number was also investigated by changing the test section static pressure. This work provides greater insight into the effect of the vortex streamwise pressure distribution on nuclei capture and TVC development. Indeed for the monodisperse case discussed later, this pressure distribution can be inferred from the distribution of inception locations. Further insights are also gained into the importance of nuclei content and cavitation number for the measurement and prediction of TVC dynamics and noise.

5.3 Experimental overview

5.3.1 Test facility

The cavitation tunnel in the Australian Maritime College (AMC) Cavitation Research Laboratory is located in Launceston, Australia. It is a medium-sized, variable pressure water tunnel constructed of stainless steel (wetted areas). The tunnel volume is 365 m^3 and the working fluid is demineralised water. The test section cross section measures 0.6 m $\times$ 0.6 m, with a length of 2.6 m. The test section pressure, p_∞, can be varied between 4–400 kPa absolute, while the test section velocity, U_∞, range is nominally 2–12 m/s.

The tunnel design and ancillaries enable strict control over both free and dissolved gas contents. Millimetre-sized bubbles are removed in a large tank downstream of the test section via coalescence and gravity separation. Smaller bubbles dissolve in the lower segment resorber due to extended residence at high static pressure. This avoids the recirculation of free gas bubbles that are either injected or generated by cavitation about a test component. The tunnel also features a fast degassing facility, by which the dissolved gas content can be reduced. Further details on the facility are provided in Brandner et al. (2007).

5.3.2 Experimental setup

The stainless steel hydrofoil used for this study has an elliptical planform and a NACA 0012 cross section. The root chord length is 150 mm and the span is 300 mm. The hydrofoil was mounted to the test section ceiling, 1.45 m from the test section entrance, as shown in Fig. 5.2. The incidence was set to 6°.

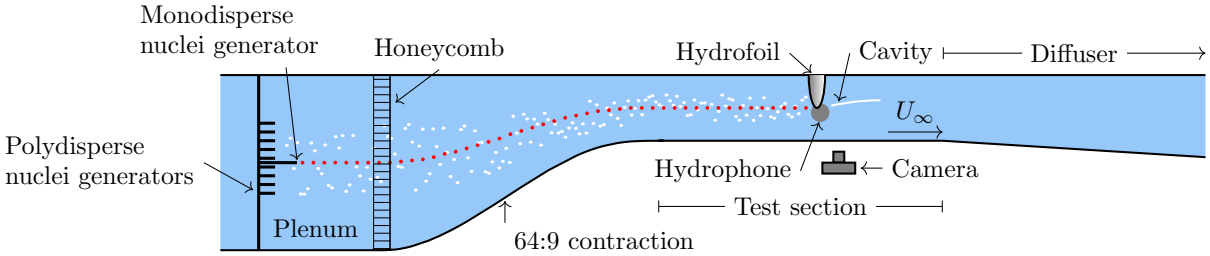

Figure 5.2: Schematic of the experimental setup in the upper segment of the cavitation tunnel, showing the hydrofoil located in the test section. The test section velocity is U_∞. Mono- and polydisperse nuclei populations were injected upstream of the test section for different test runs. They are shown as red and white dots, respectively. The locations of the high speed video camera and hydrophone used for TVC inception observations are also denoted.

Optical measurements were acquired with a Phantom v2640 high speed camera mounted beneath the test section. A 24 mm Nikkor lens was used, providing a magnification of 3.57 pixels/mm. Images were acquired at 2048×200 pixels (574×56 mm) at a frame rate of 16,000 fps. Constellation LED lights were used for illumination. Acoustic measurements were taken using a hydrophone (Brüel & Kjær Type 8103, sample rate 200 kHz) mounted in a side window at test section mid-height, 0.2 chord lengths downstream of the hydrofoil tip. Details of the hydrophone mounting arrangement can be found in Doolan et al. (2013). The hydrophone signal was conditioned using a Brüel & Kjær Type 2692-A charge amplifier and recorded using a 24-bit data acquisition card (National Instruments PXIe-4497).

Nucleation effects on TVC inception behaviour were investigated using two injected nuclei populations. An injected monodisperse microbubble population (hereinafter termed 'monodisperse') with a dominant bubble diameter of 91 µm in the test section was generated using a stainless steel 'T'-junction with 100 µm bore from Valco Instruments Co. Inc.. This is based on a device designed by YLec Consultants as described in Russell et al. (2018a). A single nuclei generator was mounted upstream of the contraction, at the mid-span and mid-height of the plenum, as shown in Fig. 5.2.

An injected polydisperse microbubble population (hereinafter termed 'polydisperse') featuring bubbles with a range of diameters was also used. These microbubbles are generated in devices via the depressurisation of supersaturated water (Giosio et al., 2016). An array of these devices is mounted in the plenum (Russell et al., 2020b). They are typically arranged in a triangular grid, 80 mm apart (an equivalent spacing of 30 mm in the test section), mounted across three columns of a supporting strut. In the present study, a lower concentration of polydisperse nuclei was generated by only using the two

outer columns. This results in spanwise and vertical spacing between generators of 139 and 80 mm, respectively.

The mono- and polydisperse nuclei generators each produce a plume with a diameter of about 80 mm in the test section. Each plume is presumed to have a spatial concentration profile that follows a Gaussian distribution due to turbulent mixing in the plenum. The monodisperse plume and the centre of four overlapping plumes generated by the polydisperse array were observed to be centred on the foil tip. The close spacing of the polydisperse generators relative to the plume size resulted in a near homogenous distribution within the nuclei capture streamtube which is $\mathcal{O}(10)$ mm in diameter.

An optical measurement technique called Mie scattering imaging (MSI) was used to quantify the injected nuclei populations within the test section (Russell et al., 2020a,b). Measurements were taken $2.2c$ upstream of the hydrofoil tip such that the measured populations were representative of those captured by the vortex. Microbubbles were illuminated with a 532 nm laser (Ekspla, Lithuania) and defocussed photographs were acquired using a 48 megapixel camera (IO Industries, Canada). Bubble diameters are calculated using the spatial frequency of the interference fringes in the defocussed images (Russell et al., 2020a,b).

5.3.3 Test conditions

Two types of tests were conducted. Firstly, a cavitation number, σ, of 1.6 was used to compare the effects of mono- and polydisperse nuclei populations on TVC inception dynamics and acoustics. The cavitation number is defined as $\sigma = \frac{p_\infty - p_\mathrm{v}}{q}$, where p_∞ is the freestream pressure upstream of the hydrofoil tip, p_v is the vapour pressure, $q = \frac{1}{2}\rho {U_\infty}^2$ is the freestream dynamic pressure and ρ is the fluid density. Secondly, cavitation number effects were studied by varying p_∞. A cavitation number range between 1.6 and 2.4 was investigated with the monodisperse population. For each type of test, synchronous optical and acoustic measurements were made in multiple 30.6 s blocks.

The Reynolds number, Re, was fixed at 1.5×10^6. It is defined as $Re = \frac{U_\infty c}{\nu}$, where c is the hydrofoil root chord length and ν is the kinematic viscosity of the water.

The polydisperse nuclei population was controlled by maintaining a constant generator cavitation number, σ_gen, of 0.7. This is defined as $\sigma_\mathrm{gen} = \frac{p_\mathrm{down} - p_\mathrm{v}}{p_\mathrm{up} - p_\mathrm{down}}$, where p_up is the pressure upstream of the generator orifice and p_down is the generator outlet pressure. The pressure upstream of the orifice was adjusted to maintain a constant generator cavitation number for the different test section conditions. For a cavitation number of 1.6, the monodisperse nuclei population was controlled by setting the inlet air and water pressures of the generator, as described in Russell et al. (2018a). For the study of cavitation number effects, the inlet pressures were adjusted to maintain a constant pressure difference between the supply pressures and the plenum pressure at the outlet of the generator.

The two injected microbubble populations are shown in Fig. 5.3. Both cumulative and non-cumulative forms are provided. Measurements were acquired at the same nominal test section operating conditions as those used to study nucleation effects. The monodisperse and polydisperse nuclei distributions are constructed from 271 and 15 bubble detections, respectively. Larger sample sizes would be preferred, especially for the polydisperse population. However, very long acquisition times are required to measure lower bubble concentrations due to the relatively small field of view for MSI measurements. In this instance, an extrapolation of the measured nuclei distributions in Russell et al. (2020b) to higher generator cavitation numbers indicates that the polydisperse population measured in this study is reasonable and the sample size used is adequate.

The monodisperse population has a dominant bubble diameter of 91 µm. The critical pressure, p_c, of such bubbles is effectively vapour pressure (Khoo et al., 2020c). The polydisperse nuclei distribution features bubbles with a range of smaller diameters, in concentrations lower than that of the peak concentration for the monodisperse case. The diameter of the largest bubble detected was 88 µm, with a concentration more than two orders of magnitude less than for the monodisperse population. The total measured concentrations are similar between the mono- and polydisperse populations, at 5×10^3 and 4×10^3 m^{-3}, respectively.

The dissolved oxygen content was maintained between 1.9 and 4.0 mg/L (i.e. 21–45% relative to saturation at atmospheric pressure) throughout the experiment. The relative saturation level of dissolved oxygen in the water, r_{up}, using the plenum upstream of the test section as the reference location, was maintained between 13 and 27% during the present study which ensured that the natural nuclei population (i.e. the existing nuclei in the tunnel water without nuclei injection) remained at the baseline, as described in Khoo et al. (2020c). In flows with injected nuclei, the total population comprises of both the natural and injected nuclei. As shown in Fig. 5.3(a), the natural nuclei population is much stronger than the injected populations, and can be shown to be inactive during these experiments.

5.3.4 Data processing

Optical and acoustic data corresponding to an example cavitation event are shown in Fig. 5.4. The composite photograph on the left shows the development of the cavity over time and is constructed from sections of multiple exposures stitched together.

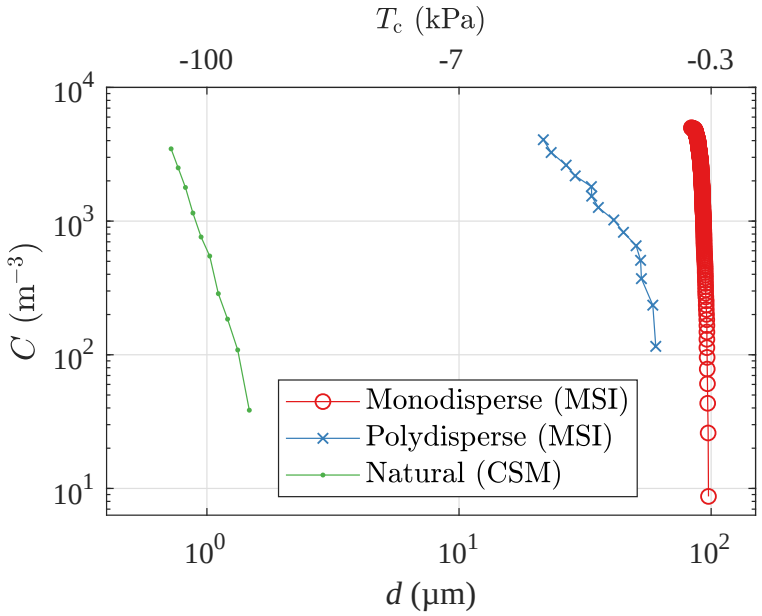

(a) Cumulative

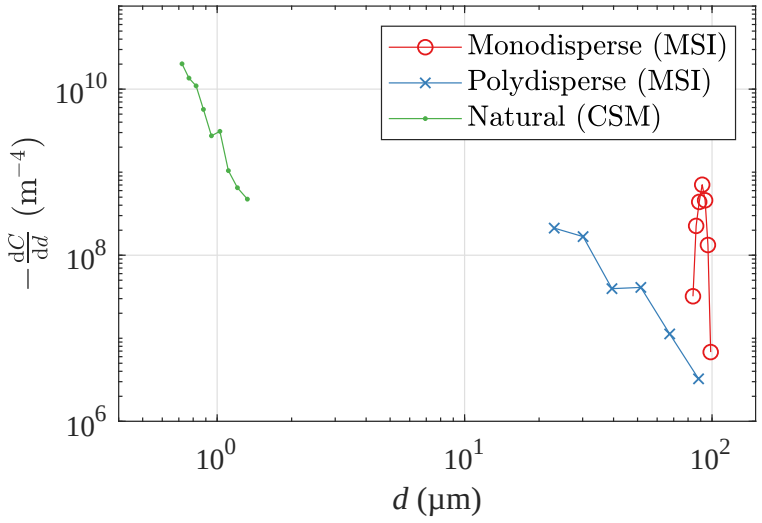

(b) Non-cumulative

Figure 5.3: Injected nuclei populations as measured using Mie scattering imaging (MSI). The natural, or pre-existing, nuclei distribution is also provided, as measured using a cavitation susceptibility meter (CSM). Both (a) cumulative and (b) non-cumulative forms are shown. In (a) the cumulative nuclei concentration, C, is plotted against the measured or equivalent bubble diameter, d, in the test section. The critical tension required to activate a nucleus, $T_c = p_c - p_v$, is also shown. In (b), the number density distribution function, $-\frac{dC}{dd}$, is plotted against bubble diameter. The monodisperse population has a dominant bubble diameter of 91 µm. The polydisperse population comprises of bubbles with a wider range of smaller diameters. Test section conditions were $\sigma = 1.6$ and $Re = 1.5 \times 10^6$.

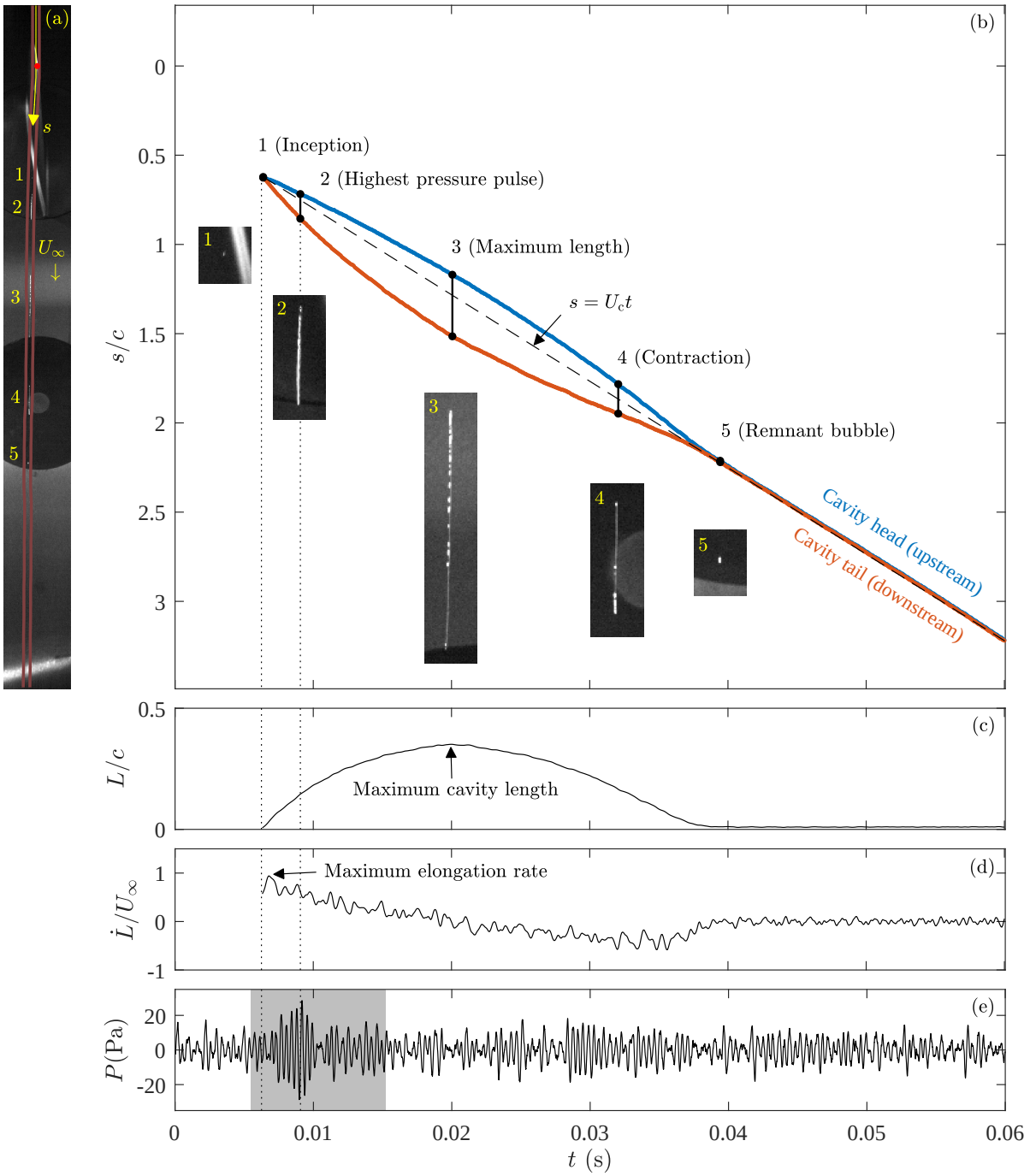

Figure 5.4: Spatial and acoustic measurements of a single cavitation event ($\sigma = 1.6$, monodisperse). The (a) multiple-exposure composite photograph shows different stages of cavity development: (1) inception, (2) highest pressure pulse, (3) maximum length, (4) contraction, and (5) remnant bubble. The red dot denotes the hydrofoil tip. Data were extracted from within the bounds denoted by the burgundy lines either side of the trajectory. The distance along the cavity trajectory, s, is plotted in the (b) space-time graph, which shows cavity development over time, t. The blue and orange lines denote the positions of the cavity head and tail, respectively. Inception occurs at $s_\mathrm{i}/c = 0.62$, where s_i is the distance along the cavity trajectory, downstream of the tip, that inception occurs. The cavity advection velocity, U_c, is the gradient of the dashed line. Enlarged images of the cavity at the different stages are inset. The evolution of the (c) cavity length, L, and (d) cavity elongation rate, $\dot{L}$, are provided. The (e) time series of the acoustic pressure measurement, P, is high-pass filtered with a cut-off frequency of 1 kHz. The grey region denotes the duration of hydrophone data used for acoustics processing. The left and right vertical dotted lines are drawn at the time of inception and the highest pressure pulse, respectively.

5.3.4.1 Optical data processing

Image processing was carried out using MATLAB software. The cavity trajectory was measured from a photograph of a developed tip vortex cavity. Bounds were set to ±10 pixels (i.e. ±2.8 mm) of the trajectory and are denoted by the burgundy lines on the composite photograph in Fig. 5.4a. The distance along the cavity trajectory downstream of the tip, s, is normalised by c in this analysis (i.e. s/c). The maximum pixel intensity within the bounds at each spanwise location along the vortex trajectory was extracted from each video frame, and used to construct space-time datasets that show cavity development. A binary image was generated using an intensity filter to distinguish bright pixels from the background (i.e. non-cavitating conditions). Pixel intensity distributions for non-cavitating conditions were used to set the intensity threshold. Morphological image processing was used to minimise noise in the image, then an area filter was applied to identify each cavity and exclude spurious detections. The locations of the upstream and downstream extents of the cavity were extracted and analysed to obtain the cavity kinematics. The cavity length, L, is the distance between these extents, while the elongation rate, $\dot{L}$, is the first time derivative of the length.

The temporal evolution of the cavity length and elongation rate are shown in Figs. 5.4c and 5.4d, respectively. The location of TVC inception downstream of the hydrofoil tip, s_i/c, was defined as the position of the cavity at its earliest appearance and is labelled '1' in Fig. 5.4b. In a check of 10% of the high speed video runs, 9 cavities were detected with lengths between 0.28 (the optical resolution) and 3.0 mm. Of these, two-thirds were categorised as other entities such as out-of-focus bubbles or solid particles. The few TVC events detected in this size range account for only a very small proportion of the $\mathcal{O}(1000)$ cavities longer than 3 mm detected across these runs. Therefore, only cavities which grow to a maximum length, L_max, of over $0.02c$ (3 mm) were used for the analysis. The maximum elongation rate, $\dot{L}_\mathrm{max}$, usually occurs within 1 ms of the optical detection of inception (i.e. 16 high speed video frames).

The cavity grows axially to a maximum length of about $0.4c$ at the point indicated '3' in Fig. 5.4b, when the cavity head, or upstream extent, is about one chord length downstream of the tip, before contracting axially to a remnant bubble that is transported downstream, annotated '5'. Dissolved air can diffuse into the cavity in the low pressure zone, and while vapour condenses in the pressure recovery region, the air may not dissolve, resulting in a remnant bubble (Brennen, 1995).

The cavity advection velocity, U_c, is the gradient of a line connecting the start and the end of the cavity in the space-time data, as shown in Fig. 5.4b with a black, dashed line. It represents the mean advection velocity of the cavity head. It will be shown later that the advection velocities of the main cavity and remnant bubble can differ.

The merging and splitting of isolated cavities is common at lower cavitation numbers. Cavity splitting during the later stages of cavity development has been studied (Choi

and Chahine, 2004), with the downstream segment travelling faster than the main cavity (Arndt and Maines, 2000). The cavity advection velocities presented in the results include cavities that split into multiple cavities downstream. In order to quantify the kinematic properties of isolated events, merged events are not included in the cavity kinematics results. Note that the maximum elongation rate is extracted from kinematic data prior to the merge or split, if either occurs.

5.3.4.2 Acoustic data processing

The pressure, P, time series measured using the hydrophone was high-pass filtered with a cut-off frequency of 1 kHz (to exclude tunnel-related noise) and is provided in Fig. 5.4e. The highest acoustic pressure pulse typically occurs within 5 ms of the optical detection, after the cavity has entered the cylindrical growth phase. As such, the acoustic properties of inception events were analysed using a slightly wider window of hydrophone data. The acoustic data comprised 9.8 ms (1950 samples), starting 0.8 ms prior to the optical detection of a cavity. The starting offset was corrected for the propagation delay based on the measured inception location and the sound speed. Power spectral densities (PSDs) were calculated by applying a single Hanning window to the unfiltered acoustic data for each inception event and normalising the signal power as described by Welch (1967). Non-cavitating noise was extracted from the same acquisition run using the same 9.8 ms window length and Hanning window. The PSDs of multiple sequences of non-cavitating noise data were averaged to generate representative spectra. The sound pressure levels (SPLs) of individual cavitation events were determined by integrating the PSD between 1 and 100 kHz, the Nyquist frequency. A reference pressure of 1 μPa was used to express the SPL in decibels.

The temporal separation between some cavities was so small that the acoustic pulses they generated could not be distinguished. For the monodisperse nuclei population, about 38% of cavitation events fell into this category at the lowest cavitation number of 1.6, decreasing to 5% at the highest cavitation number of 2.4. Acoustics data for such events have been omitted from the acoustic analysis.

5.4 Results and discussion

5.4.1 Optical measurements

5.4.1.1 Event rates and estimates of vortex properties

The number of cavitation events detected using high speed photography, and acquisition duration are provided in Table 5.1 for each test condition. For the nuclei population comparison at a cavitation number of 1.6, $\mathcal{O}(1000)$ events were recorded in multiple 30.6 s blocks of video data. Single 30.6 s blocks were used for each of the higher cavitation numbers for the cavitation number comparison, resulting in $\mathcal{O}(100)$ events being recorded at each of those test conditions. The cavitation event rate for each test condition is shown in Fig. 5.5. For the monodisperse case, the event rate increases with decreasing cavitation number. This is unsurprising as the cavitation number was lowered by reducing the test section pressure. This in turn lowered the vortex core pressure resulting in a longer streamwise length along which the pressure was below vapour pressure, as will be shown in Sect. 5.4.1.2. Extrapolation of these data suggests that the incipient cavitation number is at least 2.5. The minimum pressure coefficient in the vortex, $C_{\mathrm{p,min}}$, can be defined as

$$C_{\mathrm{p,min}} = \frac{p_{\mathrm{min}} - p_\infty}{q}, \tag{5.1}$$

where p_{min} is the minimum pressure in the vortex.

As the critical pressures of the monodisperse nuclei are essentially vapour pressure, then assuming the pressure in the core is vapour pressure (for the incipient case of $\sigma = 2.5$), a minimum pressure coefficient in the vortex core can be obtained by

$$\begin{aligned} C_{\mathrm{p,min}} &= \frac{p_{\mathrm{v}} - p_\infty}{q} \\ &= -\sigma \\ &= -2.5. \end{aligned} \tag{5.2}$$

For cavitation numbers less than 2.5, the highest tension, T, generated by the vortex may then be inferred as

$$\begin{aligned} T &= p_{\mathrm{min}} - p_{\mathrm{v}} \\ &= C_{\mathrm{p,min}} q + p_\infty - p_{\mathrm{v}}. \end{aligned} \tag{5.3}$$

And since

$$p_\infty = \sigma q + p_{\mathrm{v}}, \tag{5.4}$$

the tension is

$$\begin{aligned} T &= C_{\mathrm{p,min}} q + \sigma q + p_{\mathrm{v}} - p_{\mathrm{v}} \\ &= q\left(C_{\mathrm{p,min}} + \sigma\right), \end{aligned} \tag{5.5}$$

which, for the lowest freestream cavitation number presented in this paper, $\sigma = 1.6$, corresponds to $-0.9q$, or $-50\,\mathrm{kPa}$ (absolute).

With the estimated minimum vortex pressure of $p_{\mathrm{min}} = -48\,\mathrm{kPa}$ and the lift coefficient, $C_{\mathrm{L}} = 0.44$ from force measurements, it is possible to estimate the vortex core radius for $\sigma = 1.6$. Firstly, the mid-span bound circulation, Γ_0, is defined as

$$\Gamma_0 = \frac{1}{2} C_{\mathrm{L}} U_\infty c. \tag{5.6}$$

Assuming the circulation in the tip vortex flow, Γ_{tip}, is $0.3\Gamma_0$, and a Rankine vortex model (Franc and Michel, 2006), the core radius at the location of minimum pressure, a, is estimated to be 1.2 mm using

$$a = \frac{\Gamma_{\mathrm{tip}}}{2\pi\sqrt{\frac{p_\infty - p_{\mathrm{min}}}{\rho}}}. \tag{5.7}$$

The core diameter is then about 10–100 times larger than those of the injected nuclei. Two-dimensional simulations of a Rankine vortex using the approach of Paul et al. (2021) show the diameter of the streamtube of ingested nuclei to be $\mathcal{O}(10)$ mm, which is an order of magnitude larger than the core size.

The cumulative nuclei populations presented in Fig. 5.3(a) suggest there are as many nuclei in the polydisperse population compared to the monodisperse. However, Fig. 5.5 shows that the rate of nuclei activations are some eight times greater in the monodisperse case. This indicates that radial ingestion and activation of nuclei along the vortex is biased towards the larger bubbles. This filtering of the polydisperse bubble population is due to the increase in the radial ingestion force with the cube of the bubble radius (Oweis et al., 2005), such that the larger monodisperse microbubbles are more readily drawn into the vortex.

Table 5.1: Cavitation event count and acquisition duration for each test condition.

Nuclei population	σ	Event count	Duration (s)
Monodisperse	2.4	126	30.6
Monodisperse	2.2	233	30.6
Monodisperse	2.0	418	30.6
Monodisperse	1.8	614	30.6
Monodisperse	1.6	6621	275.4
Polydisperse	1.6	1662	550.8

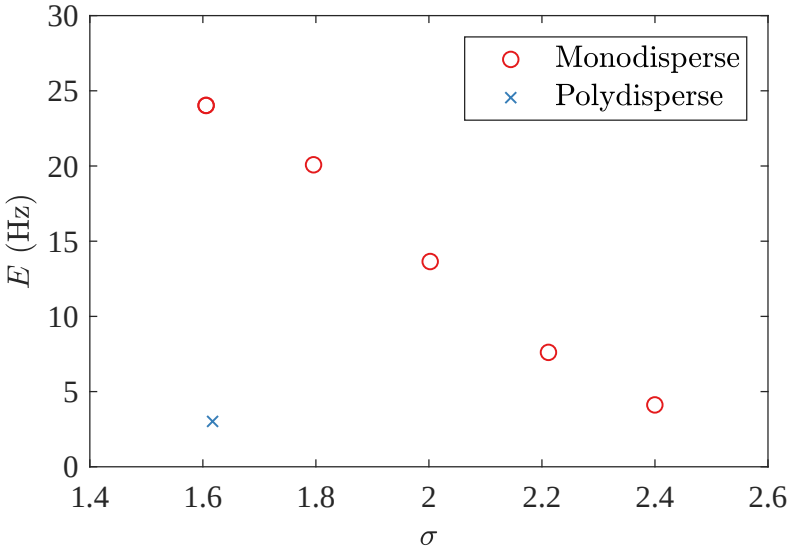

Figure 5.5: Effect of cavitation number, σ, and nuclei population on inception event rate, E, for test conditions investigated in this study. The event rate decreases with increasing cavitation number for the monodisperse nuclei population. The rate corresponding to the monodisperse case is eight times higher than that of the polydisperse for the same test section conditions.

5.4.1.2 Inception location

Spatial distributions of the event rate along the vortex trajectory are given in Fig. 5.6(a) for different nuclei populations. The event rates corresponding to the monodisperse population are higher than for the polydisperse case across the range of inception locations observed. This is attributed to the higher concentration of nuclei that are captured. The distributions trend similarly. The highest event rates occur between the tip and $0.2c$ downstream, which is consistent with the location of the minimum pressure, as discussed in Sect. 5.2. The event rate gradually decreases till about $1c$ downstream, from which point the rate decreases steeply. For both nuclei populations, the most upstream inception location was about $0.05c$ upstream of the tip. The most downstream inception locations were $2.4c$ and $3.1c$ downstream of the tip for the monodisperse and polydisperse populations, respectively. However, the four most downstream non-zero bins of each distribution represent only 12 out of the 8283 total recorded events, so the most downstream locations quoted are only indicative. Overall, 95% of all inception events occurred less than 1.04 and $0.96c$ downstream of the tip for the mono- and polydisperse cases, respectively.

Some notable differences were observed in the results when compared to those of a similar experiment conducted by Khoo et al. (2020b). In that study, the inception location histogram corresponding to the monodisperse population was relatively uniform between the tip and $0.6c$ downstream, while a prominent peak between the tip and $0.2c$ downstream was observed for the polydisperse case. For the current dataset, there is greater similarity between the shapes of the distributions. While there is no clear explanation for this, the earlier study differed with respect to a number of aspects. Although sample sizes were similar, the data acquisition method (image-based trigger instead of block recording) and monodisperse nuclei size (75 µm dominant bubble diameter instead of 91 µm) used, were not. It should also be noted that the image-based trigger used for the earlier investigation was positioned at $2.4c$, which precluded the detection of inception events further downstream.

The effect of cavitation number on inception location is illustrated in Fig. 5.6(b). The monodisperse population was used for this investigation and the cavitation number was changed via the test section pressure. Inception occurs further downstream with decreasing cavitation number, with an increasing length of vortex along which the local pressure is sufficiently low to activate captured nuclei. Meanwhile, the event rate near the tip remains relatively unchanged with cavitation number. These trends are shown with greater clarity in Fig. 5.7. This indicates that even at the highest cavitation number tested, the local pressure near the tip is sufficiently low to activate all monodisperse nuclei captured here. A reduction in the cavitation number does not lead to the cavitation of any additional nuclei at this location as all monodisperse nuclei were also activated at the highest cavitation number. It does, however, result in a longer portion of the trailing vortex being under tension, and thus additional activations occur downstream.

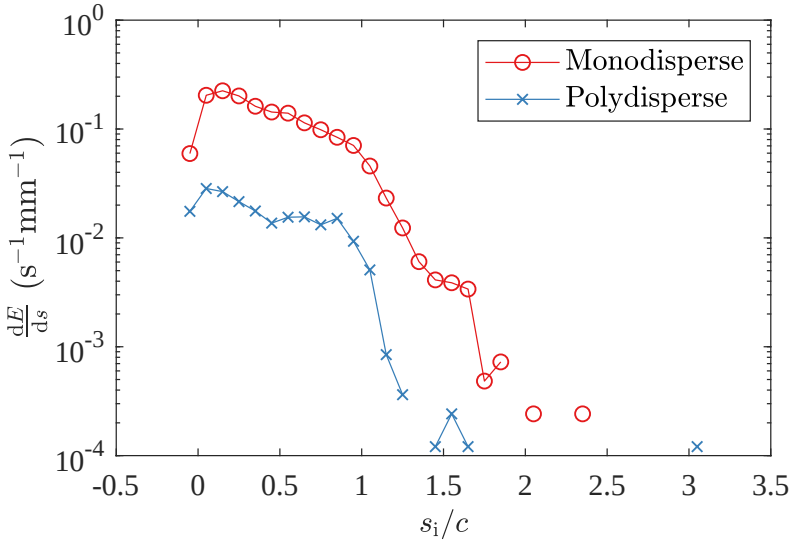

(a) Nuclei population effect, $\sigma = 1.6$

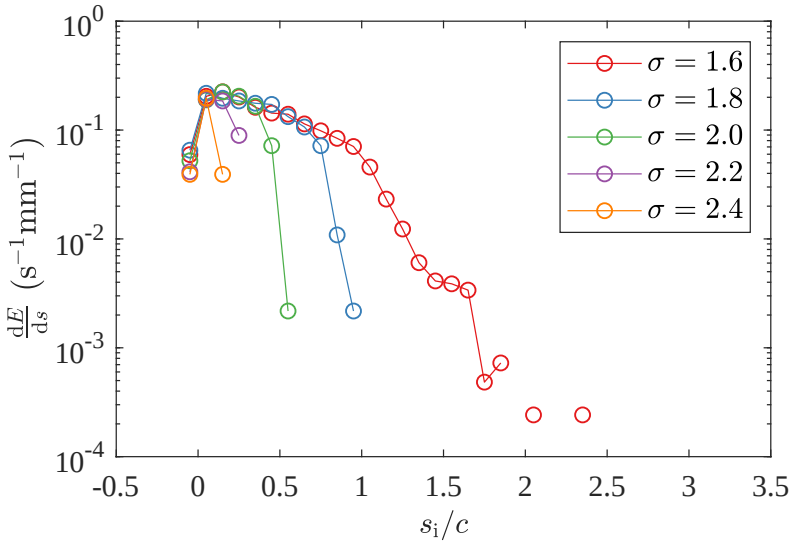

(b) Cavitation number, σ, effect (Monodisperse)

Figure 5.6: Effect of inception location, s_i/c, on inception event rate density, $\frac{dE}{ds}$, for different (a) nuclei populations and (b) cavitation numbers. A bin width of $0.1c$ is used to construct the histograms and markers are located at the middle of each non-zero bin. Higher event rates are observed for the monodisperse nuclei population compared to the polydisperse. In both cases, the event rate peaks just downstream of the hydrofoil tip and decreases with increasing inception distance from the tip. The range of locations downstream of the tip at which inception occurs increases with decreasing cavitation number. Inception happens most often just downstream of the tip for all cavitation numbers tested.

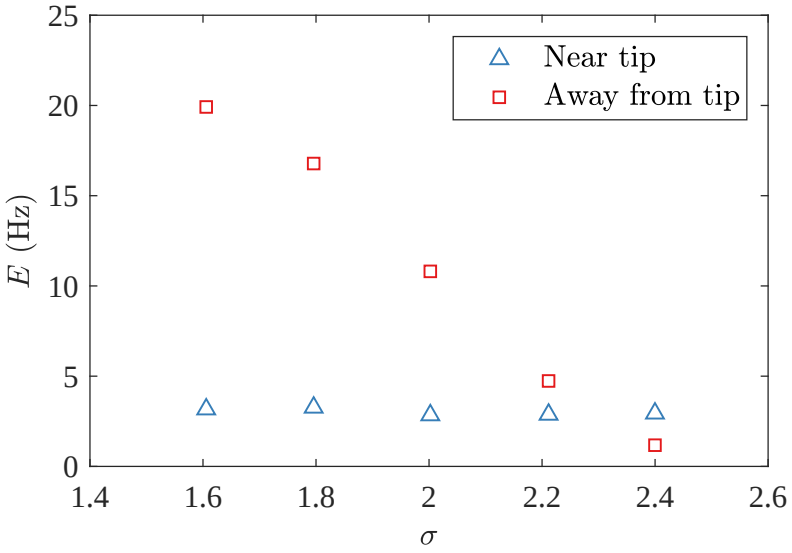

Figure 5.7: Effect of cavitation number, σ, on inception event rate, E, at different inception locations in a flow with an injected monodisperse nuclei population. The event rate between the tip and 0.1 chord lengths downstream is independent of cavitation number. Away from the tip, the rate decreases with increasing cavitation number.

5.4.1.3 Effect of inception location on maximum cavity length

The influence of inception location on maximum cavity length is shown for the two nuclei populations (see Fig. 5.8(a)). From Fig. 5.8, a bin width of $3.8 \times 10^{-3}c$, or 0.57 mm, is used for inception location data. Merged cavities form when two or more isolated cavities join, resulting in a longer cavity. Many were observed at the lowest cavitation number. However, only isolated cavities are included in Fig. 5.8. The highest maximum lengths ranging between 1 and $2c$ occur between $-0.05c$ and $0.28c$. The inclusion of merged cavities increases the peak by only 5%, which shows that the longest incipient cavity that can be sustained in the tip vortex is about $2c$ in length. The scatter in the maximum length data is highest near the location of the peak. The maximum length then decreases with increasing downstream distance. In general, the nuclei population does not affect the behaviour of the maximum cavity length. The mono- and polydisperse data sets exhibit similar degrees of scatter, noting that the sample size is about four times larger for the former.

In contrast, cavitation number has a significant effect on maximum cavity length (see Fig. 5.8(b)). The maximum length increases with decreasing cavitation number. For the cavitation numbers above 1.6, the peak maximum lengths occur across a smaller range of inception locations (i.e. between $-0.04c$ and the tip). The maximum length decreases with increasing inception distance downstream and at a higher rate at lower cavitation numbers. It is evident that the local pressure, rather than the initial bubble size, determines the maximum length of the cavity.

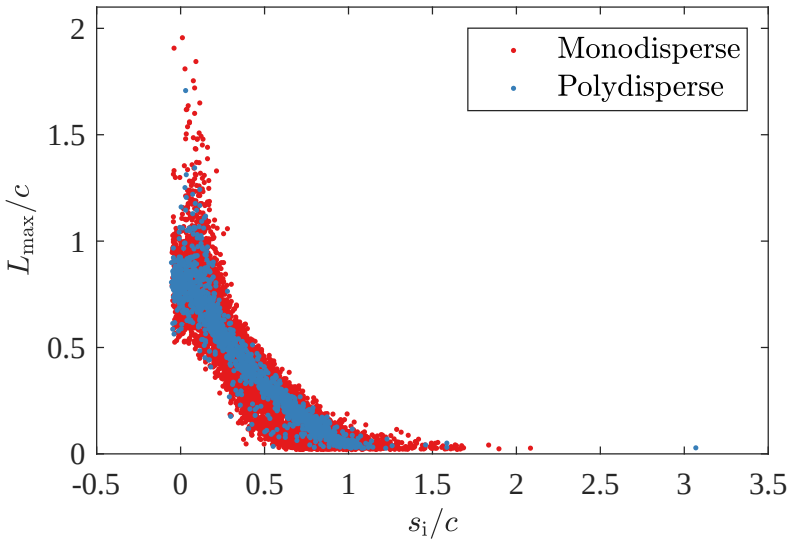

(a) Nuclei population effect, $\sigma = 1.6$

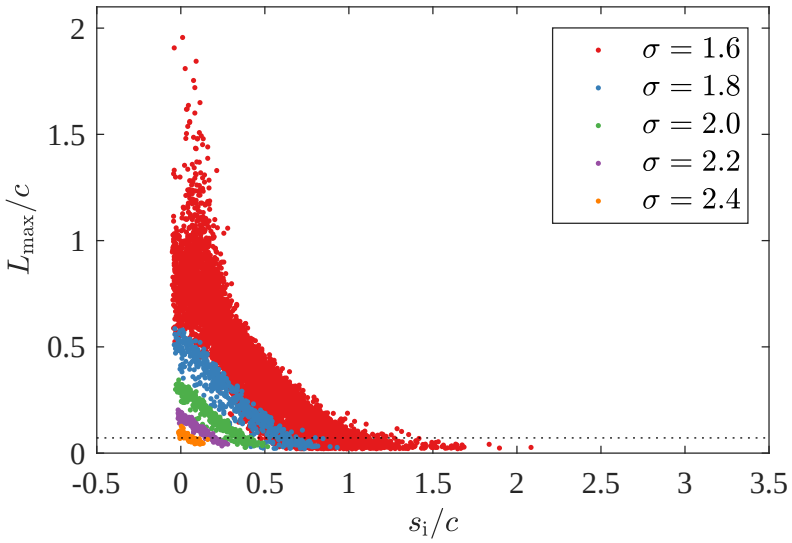

(b) Cavitation number, σ, effect (Monodisperse)

Figure 5.8: Effect of inception location, s_i/c, on maximum cavity length, L_{max}/c, for different (a) nuclei populations and (b) cavitation numbers. The maximum cavity length decreases with increasing inception distance downstream from the tip and increasing cavitation number. The trend is independent of nuclei population. The dotted line in (b) corresponds to the mean L_{max}/c for $\sigma = 2.4$ and is used to infer the streamwise pressure distribution in Fig. 5.10.

5.4.1.4 Effect of streamwise location on maximum cavity elongation rate

The effect of streamwise location on maximum cavity elongation rate is illustrated in Fig. 5.9(a) for different nuclei populations. The highest maximum elongation rates ranging from 2.4 to $2.6U_\infty$ occur between -0.01 and $0.1c$ downstream of the tip. It decreases linearly to about $1.2c$ and subsequently asymptotes to about $0.16U_\infty$. The rate tends to decrease upstream of $0.02c$.

There are a group of inception events with lower elongation rates labelled 'Data 1' in Fig. 5.9(a) that sit below the main band of data. Inspection of these outlying events reveals that they incept upstream of existing cavities and grow to a maximum length of about $0.4c$. This appears to be a consequence of cavity interaction effects and illustrates how existing cavities can suppress the elongation rate of new ones. The initial nucleus size has no significant effect on the maximum elongation rate.

The effect of cavitation number on maximum cavity elongation rate is shown in Fig. 5.9(b). Again, the cavitation number is shown to have a greater effect on cavity dynamics than the initial nucleus size. The maximum elongation rate increases with decreasing cavitation number. For all cavitation numbers, the maximum elongation rate tends to decrease with increasing distance downstream, reflecting the effect of the change of local pressure in the vortex on cavity dynamics. The slope of the reduction of the maximum elongation rate with increasing inception distance downstream of the tip increases with increasing cavitation number. This is in contrast with the maximum length data. For all cavitation numbers tested, the highest maximum elongation rate occurs between the tip and $0.04c$ downstream. The downstream asymptotic behaviour observed for the cavitation numbers of 1.6 and 1.8 cannot be observed for higher cavitation numbers of 2.0 and above.

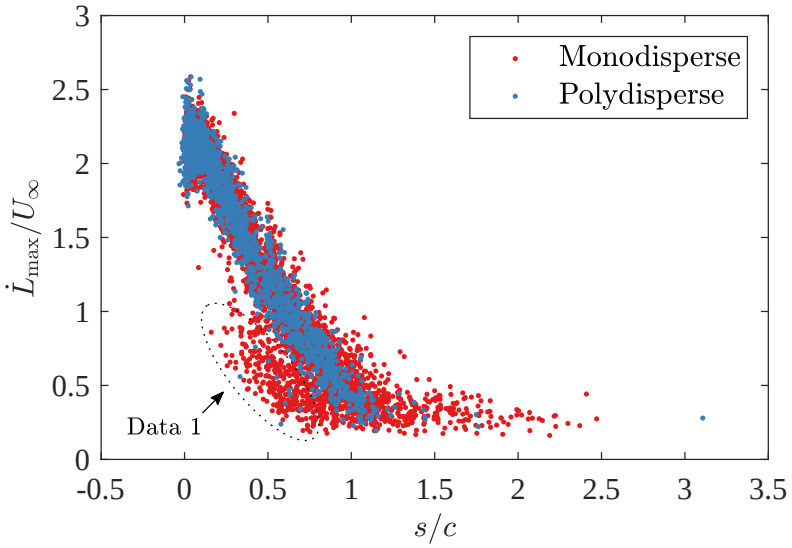

(a) Nuclei population effect, $\sigma = 1.6$

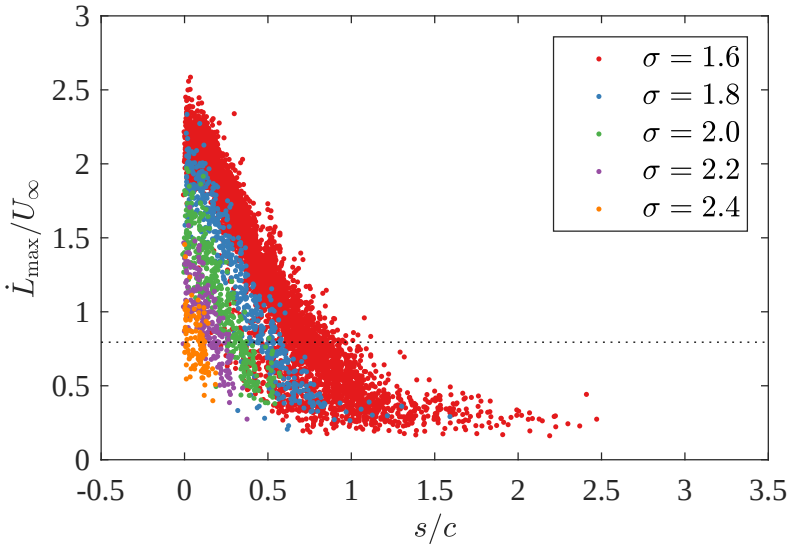

(b) Cavitation number, σ, effect (Monodisperse)

Figure 5.9: Effect of streamwise location, s/c, on maximum cavity elongation rate, $\dot{L}_{\max}/U_\infty$, for different (a) nuclei populations and (b) cavitation numbers. The highest maximum elongation rates occur near the tip. The rate decreases with increasing distance from the tip and increasing cavitation number. Nuclei population has no significant effect on the maximum elongation rate. The dotted line in (b) corresponds to the mean $\dot{L}_{\max}/U_\infty$ for $\sigma = 2.4$ and is used to infer the streamwise pressure distribution in Fig. 5.10. Data labelled 'Data 1' represent shorter cavities that incept upstream of existing cavities.

5.4.1.5 Streamwise pressure distribution

The streamwise pressure distribution was inferred from the maximum cavity length and elongation rate data (see Fig. 5.10). The average inception or streamwise location corresponding to the mean maximum length and elongation rate was determined for the $\sigma = 2.4$ data in Figs. 5.8(b) and 5.9(b). It is assumed that the local pressure here is vapour pressure, and is sufficient to activate the monodisperse nuclei population. Then the streamwise location corresponding to the same maximum length and elongation rate was identified for each of the lower cavitation numbers. The local pressures at these locations are also assumed to be vapour pressure. Therefore, the local pressure coefficient at each streamwise location is simply the negative of the corresponding cavitation number.

It was inferred from the event rate data in Fig. 5.5 that the minimum pressure coefficient is -2.5, and the streamwise pressure distribution in Fig. 5.10 shows that the minimum pressure coefficient occurs near the tip and recovers to -1.6 at about 0.8 chord lengths downstream. The rate of pressure recovery decreases with increasing distance downstream. The pressure distribution changes slightly depending on the kinematic property used, although the overall trends are similar and comparable to those observed in simulations (Chen et al., 2019; Asnaghi et al., 2020) and inferred from experimental measurements (Fruman and Dugue, 1994) of elliptical hydrofoils. Additional direct measurements of the vortex core pressure using an identical foil geometry and operating conditions would be useful to validate the inferred pressure distributions in Fig. 5.10.

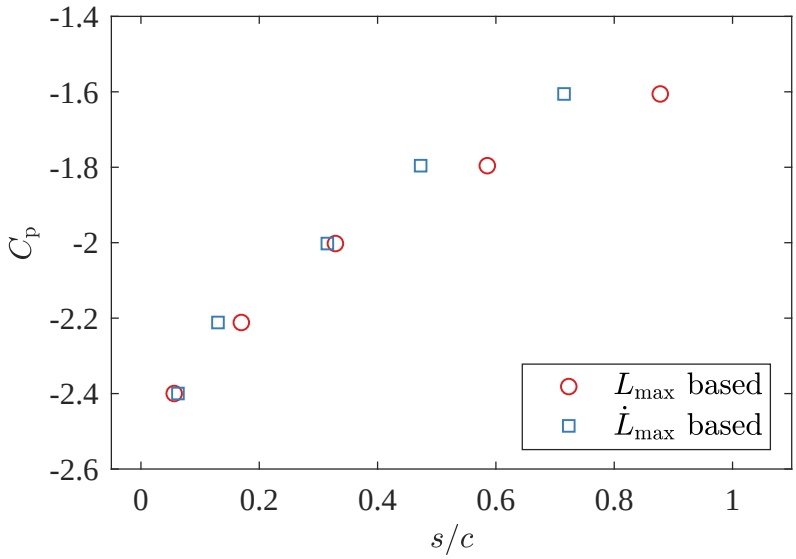

Figure 5.10: Pressure coefficient, C_p, as a function of location along the vortex, s/c, inferred from maximum cavity length, L_{max}, and maximum elongation rate, $\dot{L}_{max}$, data in Figs. 5.8(b) and 5.9(b), respectively. The pressure is lowest near the tip, and the rate of recovery decreases with distance downstream.

5.4.1.6 Effect of inception location on cavity advection velocity

The influence of inception location on cavity advection velocity is shown in Fig. 5.11. As described in Sect. 5.3.4.1, this parameter represents the mean advection velocity of the cavity head along the vortex trajectory. Nuclei population has no significant effect on cavity advection velocity. Tip vortex cavities tend to have higher advection velocities when inception occurs further downstream. The outliers with advection velocities between 0.8 and $1U_\infty$ and inception locations between 0.5 and $1c$ downstream of the tip, denoted 'Data 2', are mainly associated with relatively short cavities that incept downstream of existing longer cavities. This suggests that existing cavities alter the flow field such that new ones that incept downstream travel at higher advection velocities compared to isolated cavities. Inception events near the tip with advection velocities lower than $0.6U_\infty$, denoted 'Data 3', correspond to long, isolated cavities for which the cavity head initially migrates downstream at a much slower rate than the cavity tail.

The effect of cavitation number on the cavity advection velocity behaviour is shown in Fig. 5.11(b). Again, the cavitation number is found to influence the cavity dynamic properties more than the initial nucleus size. Higher advection velocities occur with increasing cavitation number and increasing inception distance downstream of the tip. For the highest cavitation number, the cavity advection velocity can exceed that of the freestream. It is deduced from Figs. 5.8(b) and 5.11(b) that the size or inertia of a smaller cavity allows it to travel at a higher velocity. Cavity length is determined by the local pressure which is controlled by the cavitation number and the streamwise position at inception, as demonstrated in Sect. 5.4.1.3.

Given that tip vortex cavity development is comprised of multiple stages, as demonstrated in Fig. 5.4, cavity advection velocity was investigated in additional detail. Rather than calculating the cavity advection velocity based on the entire cavity region identified in the space-time plot, two velocities were calculated for an event: one for the main body of the cavity comprising both growth and contraction phases, U_{c1}, and one for the remnant bubble, U_{c2}. The spatial histories of some example cavities are given in Fig. 5.12, showing typical cavities that incepted near the tip for each of the cavitation numbers, as well as two downstream inception events for a cavitation number of 1.6. Cavity regions for a number of example events are plotted, annotated with corresponding advection velocities. If the remnant bubble was not detected by the image processing method, its location was determined by inspection, and is shown by a dashed line drawn between it and the cavity.

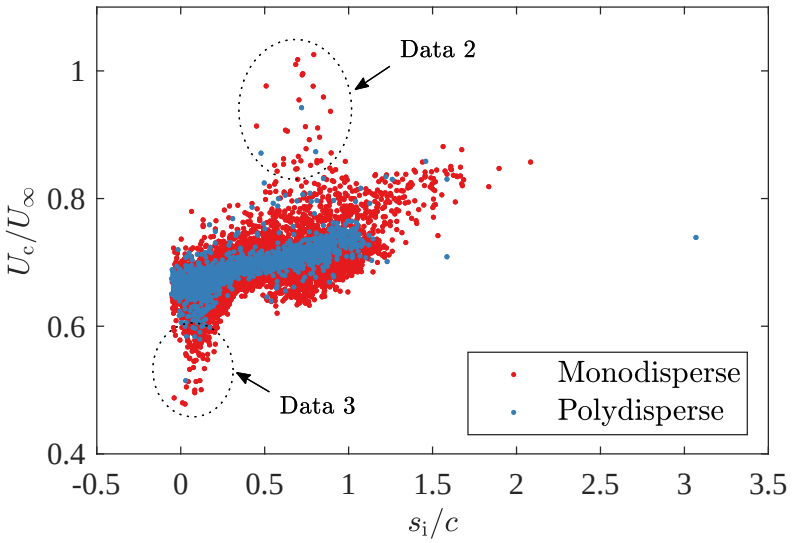

(a) Nuclei population effect, $\sigma = 1.6$

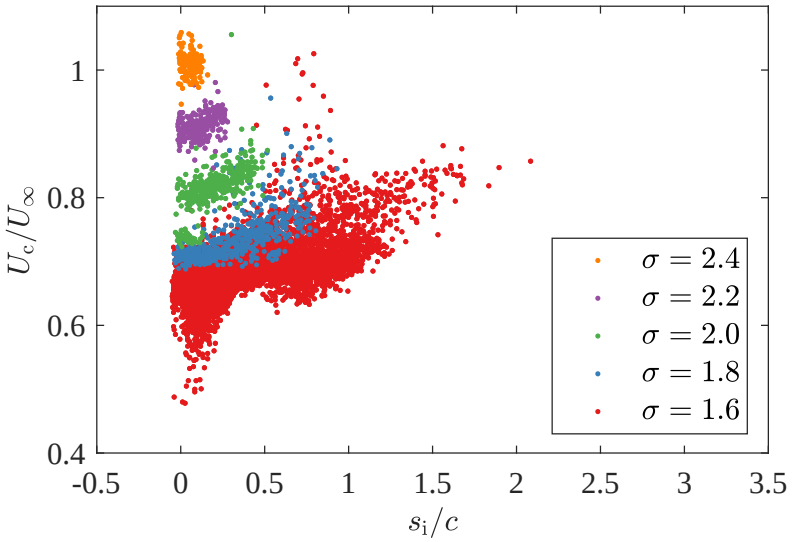

(b) Cavitation number, σ, effect (Monodisperse)

Figure 5.11: Effect of inception location, s_i/c, on cavity advection velocity, U_c/U_∞, for different (a) nuclei populations and (b) cavitation numbers. The advection velocity tends to increase with increasing inception distance from the tip and increasing cavitation number. The trend is generally independent of nuclei population. Data labelled 'Data 2' represent shorter cavities that incept downstream of existing longer cavities, and 'Data 3' denotes long cavities.

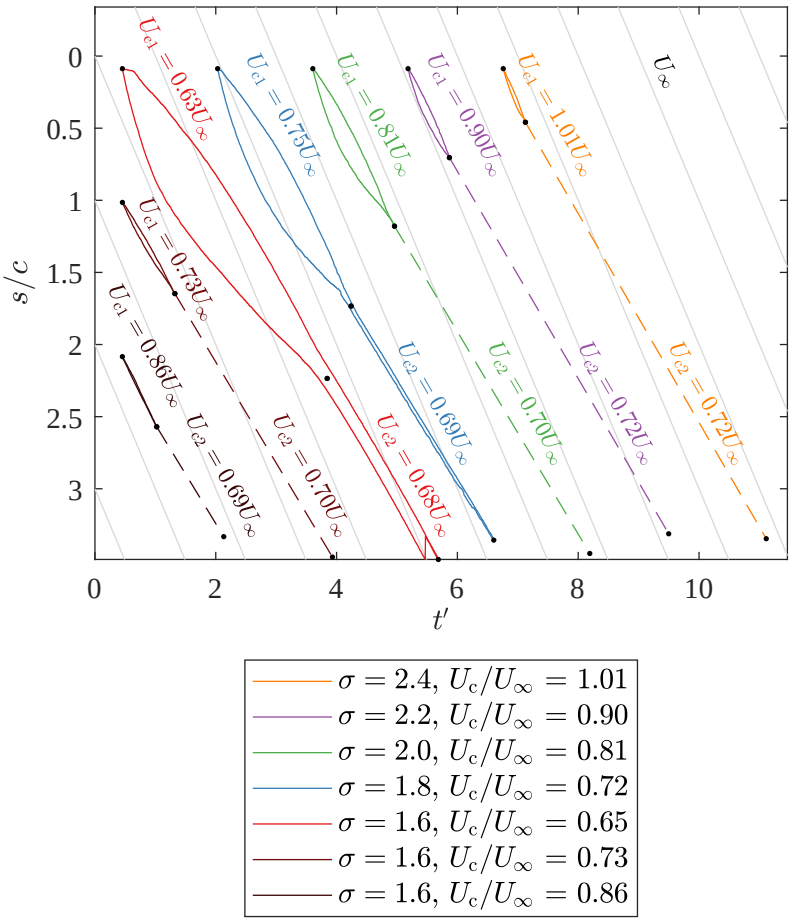

Figure 5.12: Space-time plot of example cavities showing the effects of cavitation number and inception location on the main cavity body advection velocity, U_{c1}, and remnant bubble advection velocity, U_{c2}. Cavity advection velocities, U_c, defined using the entire cavity region are also provided for each cavity. All velocities are expressed as a proportion of the freestream velocity, U_∞. Nondimensional time, $t' = t/U_\infty c$, is shown on the x-axis. The freestream velocity is represented by the solid, grey lines. The black dots are the coordinates used to derive the advection velocities, as explained in the text. The main body advection velocity increases with increasing cavitation number and increasing inception distance downstream of the tip, and thus decreasing maximum length. The remnant bubble advection velocity is about $0.7U_\infty$, independent of cavitation number and inception location.

The advection velocity of the main body trends in the same way with cavitation number and inception location as illustrated in Fig. 5.11(b). Higher main body advection velocities are found for cavities with shorter maximum lengths. These maximum lengths vary with cavitation number and inception location in the same manner as presented in Fig. 5.8(b). The advection velocity of the remnant bubble is about $0.7U_\infty$ and is independent of cavitation number and inception location, suggesting it is not cavitation-related. It may, however, indicate a constant axial velocity deficit in the vortex core, although the effect of the cavity on the axial velocity distribution in the vortex core has not been quantified.

5.4.2 Acoustic measurements

5.4.2.1 Sound pressure levels

The effect of inception location on the sound pressure level (SPL) of inception events is shown in Fig. 5.13(a) for different nuclei populations. The hydrophone was located $0.2c$ downstream of the tip and is marked with a vertical, dotted line in the figure. The nuclei population has no significant effect on the SPL behaviour. The highest pressure pulses occur when inception is near the tip and decrease in amplitude with increasing inception distance downstream. The maximum SPLs ranging from 152 to 153 dB occur when inception occurs between 0.05 and $0.14c$ downstream, which is similar to where the highest cavity elongation rates were observed in Sect. 5.4.1.4, albeit delayed by about $0.05c$. Given this similarity, the SPL and maximum elongation rate were plotted against each other to examine their relationship (see Fig. 5.13(b)). For maximum elongation rates up to about $1.7U_\infty$, the SPL increases with increasing maximum elongation rate. This is consistent with the theory that higher growth rates contribute to higher pressure pulse amplitudes (Lamb, 1945). Beyond $1.7U_\infty$, there is a higher degree of scatter. In this range, 90% of the events with lower SPL comprised of cavities that incept upstream of the tip, with the remainder incepting up to $0.25c$ downstream of the tip. Meanwhile, higher SPLs were measured for other cavities with similar maximum elongation rates that incept downstream of the tip. The lower SPLs might be explained in part by the relative positions of the hydrophone, hydrofoil and cavity. The hydrofoil may attenuate the acoustic pressure pulse generated for events that incept near the tip.

The effect of cavitation number on SPL is shown in Fig. 5.14(a). Inception events become quieter with increasing cavitation number and increasing distance downstream of the tip. The higher maximum elongation rates observed at lower cavitation numbers produce higher SPLs, as seen in Fig. 5.14(b). Only data for cavities with inception locations between the tip and $0.15c$ downstream are shown in this figure as it is a region of interest given the higher event rates, cavity elongation rates and SPLs associated with cavities that incept here. This indicates that SPL is controlled by the elongation rate, which is a function of the local pressure.

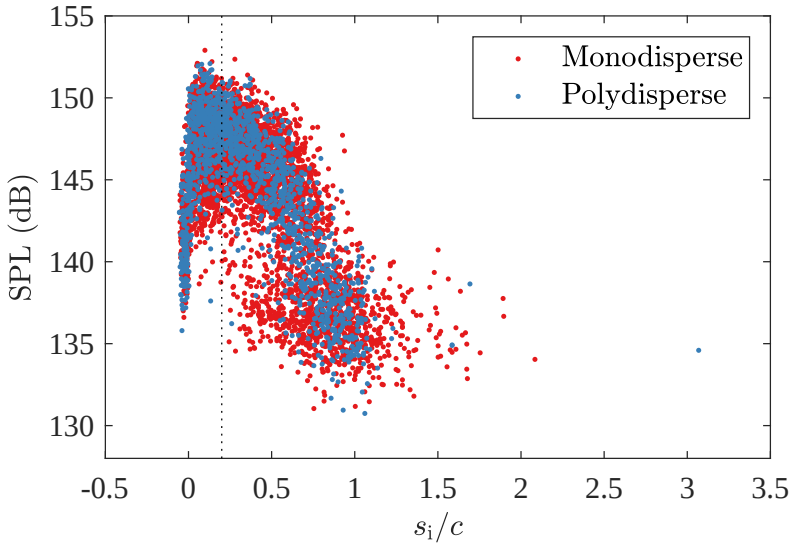

(a) Effect of inception location, s_i/c

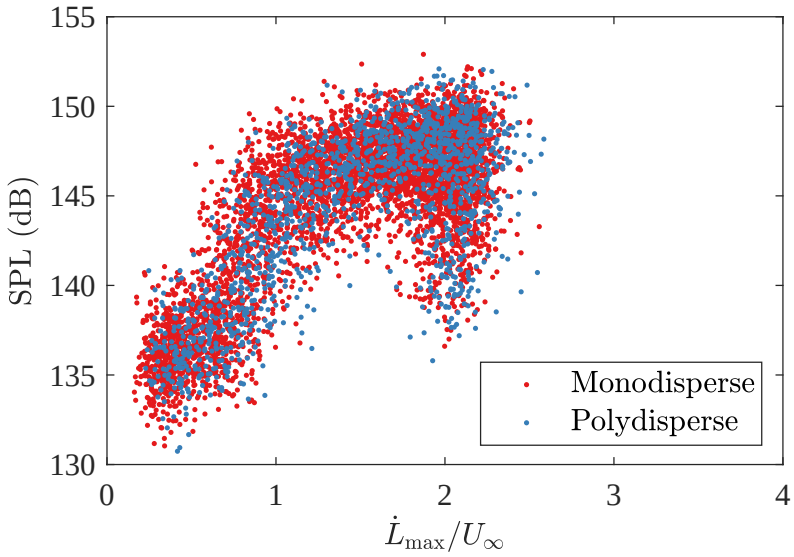

(b) Effect of maximum elongation rate, $\dot{L}_{max}/U_\infty$

Figure 5.13: Effect of (a) inception location and (b) maximum cavity elongation rate on the sound pressure level (SPL) of inception events ($\sigma = 1.6$). The SPL is calculated using the integral of the power spectral density between 1 and 100 kHz and includes background noise. The hydrophone location is 0.2 chord lengths downstream of the tip, and is denoted by the dotted line in (a). The maximum SPL occurs between 0.05 and $0.14c$ downstream of the tip, with a sharp reduction further upstream and gradual decrease with increasing inception distance downstream. Nuclei population has no significant effect on SPL.

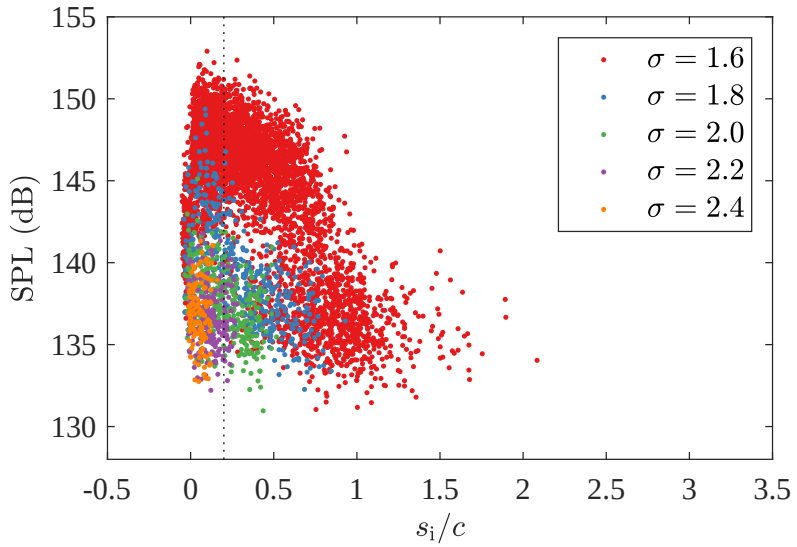

(a) Effect of inception location, s_i/c

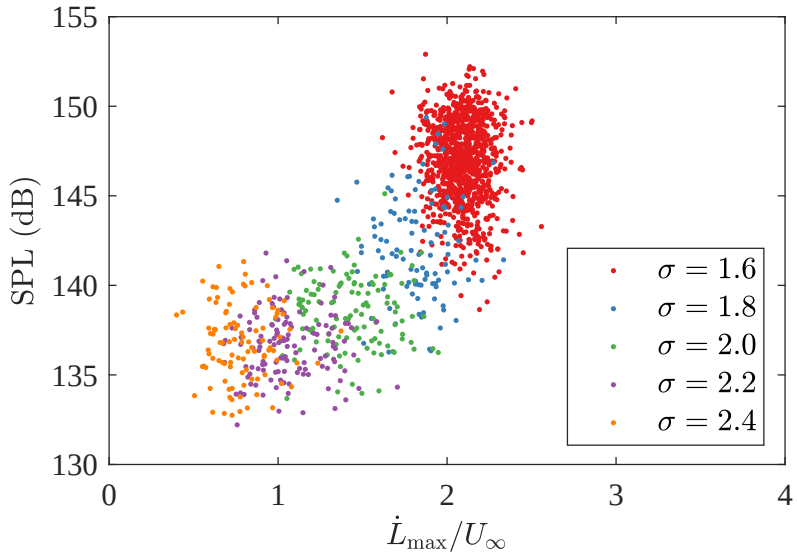

(b) Effect of maximum elongation rate, $\dot{L}_{max}/U_\infty$

Figure 5.14: Effect of (a) inception location and (b) maximum cavity elongation rate on the sound pressure level (SPL) of inception events (monodisperse). The SPL is calculated using the integral of the power spectral density between 1 and 100 kHz and includes background noise. The hydrophone location is 0.2 chord lengths downstream of the tip, and is denoted by the dotted line in (a). Only inception events that occur between the tip and 0.15 chord lengths downstream are shown in (b). The SPL is higher at lower cavitation numbers and for higher maximum elongation rates.

5.4.2.2 Acoustic frequency spectra

Power spectral densities of non-cavitating noise in flows with different nuclei populations are shown in Fig. 5.15. The polydisperse nuclei generators produce high frequency, broadband noise between 10 and 100 kHz, as well as some noise in the 5 to 6.5 kHz range.

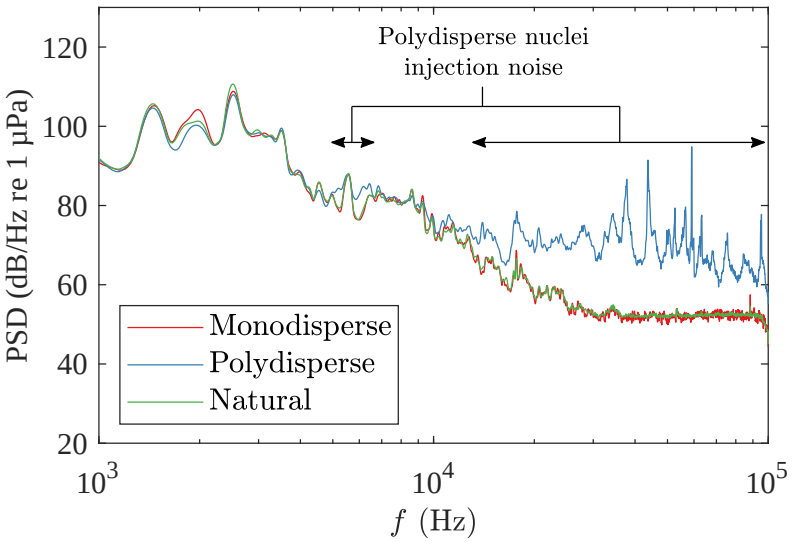

Figure 5.15: Single-phase noise for different nuclei populations ($\sigma = 1.6$). Broadband noise above 10 kHz, and between 5 and 6.5 kHz is present for the polydisperse case due to the operation of the polydisperse nuclei generators. Neither flows with monodisperse nor natural nuclei populations exhibit such noise.

The influence of inception location on TVC noise frequency spectra for the two nuclei populations is presented in Fig. 5.16. The difference between power spectral densities (PSDs) of cavitating and non-cavitating noise, ΔPSD, is shown to depict only the contribution from cavitation. As mentioned earlier, a bin width of $3.8 \times 10^{-3}c$, or 0.57 mm, is used, and data for cavities that incept in the same bin are averaged. Two strong narrowband peaks centred at 2.27 and 2.76 kHz can be observed when inception occurs near the tip, regardless of nuclei population. The lower-frequency peak is associated with cavitation inception, and weakens by $0.6c$. The peak also narrows downstream of $0.2c$ and its centre increases slightly to 2.36 kHz.

The peak centred at 2.76 kHz also narrows downstream of $0.6c$, with its frequency shifting slightly higher to 2.82 kHz. The signal power remains relatively constant from the tip until $0.8c$, at which point it decreases and disappears by $1c$. Based on the results presented later in Fig. 5.17, it is suggested that this is a tunnel-related resonant frequency excited by TVC inception events.

High frequency, broadband noise between 10 and 100 kHz can be observed for cavitation events that incept near the tip for the monodisperse case (see Fig. 5.16(a)). This noise subsides with increasing inception distance downstream and disappears at about $0.5c$. Such noise is difficult to distinguish for the polydisperse case in Fig. 5.16(b), being masked by the noise of the nuclei generators as seen in Fig. 5.15.

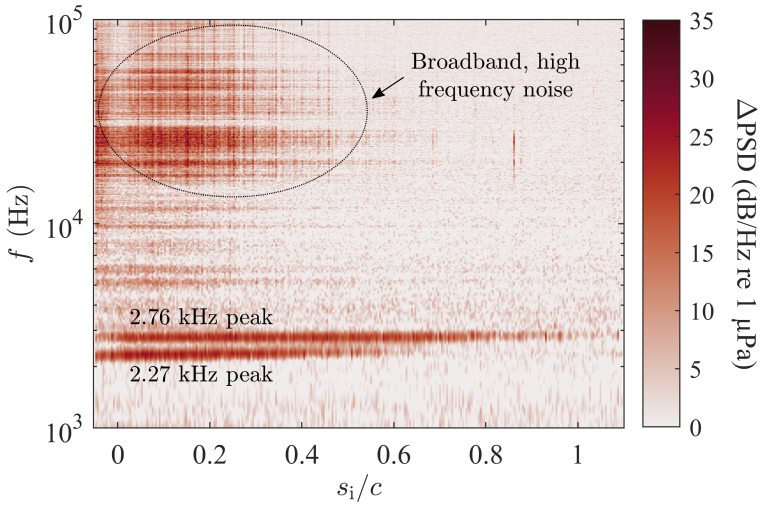

(a) Monodisperse

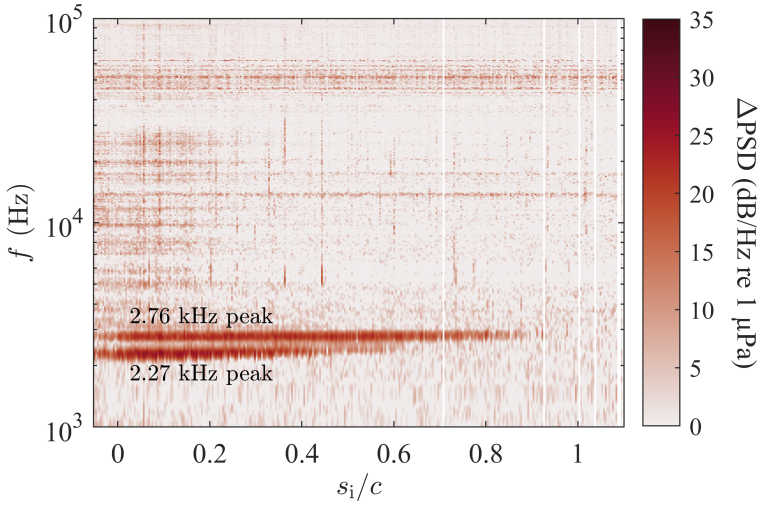

(b) Polydisperse

Figure 5.16: Effect of inception location, s_i/c, on power spectral densities (PSDs) of inception events ($\sigma = 1.6$), in flows with (a) monodisperse and (b) polydisperse nuclei populations. The difference of cavitating and non-cavitating PSDs, ΔPSD, is presented in order to isolate cavitation noise. Data for events incepting at the same streamwise location are averaged. Two narrow-band peaks are present between the tip and 0.6 chord lengths downstream, independent of nuclei population. The higher-frequency peak persists until $s_i/c = 1$. This peak may be a tunnel-related resonant frequency. Broadband noise above 10 kHz exists for the monodisperse case, decreasing with increasing inception distance downstream from the tip.

The effect of cavitation number on the PSDs of inception events for the monodisperse case is presented in Fig. 5.17. The mean ΔPSD of inception events occurring between the tip and 0.15c downstream is shown for each cavitation number. Similarly to Fig. 5.14(b), only upstream inception locations are considered for this comparison as this is a region of interest given the higher event rates, cavity elongation rates and SPLs discussed earlier.

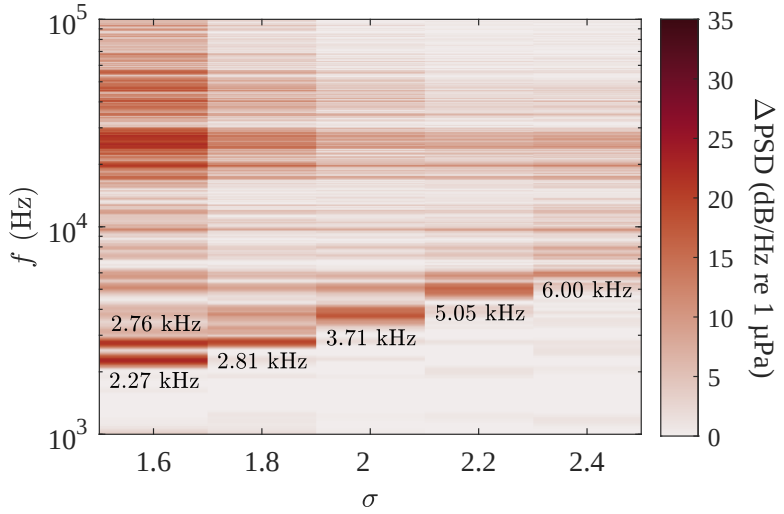

Figure 5.17: Effect of cavitation number, σ, on the mean power spectral densities (PSDs) of inception events that occur between the tip and 0.15 chord lengths downstream, in a flow with monodisperse nuclei. The difference of cavitating and non-cavitating PSDs, ΔPSD, is shown in order to isolate cavitation noise. The peak frequencies of narrow-band noise are annotated either above or below the corresponding spectral bands. The peak at 2.76 kHz may be tunnel-related. The peak frequency associated with cavitation noise increases with increasing cavitation number. The broadband noise between 10 and 100 kHz reduces with increasing cavitation number.

TVC acoustic characteristics are dependent on cavitation number. As discussed above, the peak at 2.76 kHz observed for a cavitation number of 1.6 may be tunnel-related. A peak at 2.81 kHz appears for a cavitation number of 1.8. This is difficult to distinguish from the potential tunnel-related peak. The peak frequency increases to 3.71, 5.05 and 6.00 kHz for cavitation numbers of 2.0, 2.2 and 2.4, respectively. The peak frequency trends with the square of the external pressure. Spherical and non-spherical bubble theory states the resonant frequency goes with the square root of the pressure (Brennen, 1995; Neppiras, 1980), however the squared relationship may be expected once bubble length, which is inversely proportional to external pressure, is taken into account. Additionally, high spatial and temporal resolution imaging of cavity surface deformations may extend existing knowledge on the relationship between cavity dynamics and acoustics. Such imaging could be used to assess the performance of cavity dynamic (Pennings et al., 2015a) and acoustic (Ffowcs Williams and Hawkings, 1969; Testa et al., 2018) models. Finally, the broadband noise between 10 and 100 kHz observed for a cavitation number of 1.6 decreases with increasing cavitation number. This behaviour is similar to that of the spectral peaks at frequencies lower than 10 kHz, as discussed above.

5.4.2.3 Summary of results

The results presented show that the tip region plays a dominant role with respect to TVC event rate, kinematics and acoustics. This is where the longest and loudest cavities incept, and also where the highest elongation rates occur. It is inferred that the minimum pressure is located here, causing more explosive cavity growth and higher noise emission compared to when inception occurs further downstream. Changes in local pressure due to cavitation number and with inception location influence tip vortex cavity kinematics and acoustics more than nuclei population and initial nucleus size, at least across the size ranges investigated in this study. While a clear difference between inception event rates for each population was observed, it is possible that the microbubbles activated in each population are so similar in size and critical pressure that the dynamic and acoustic characteristics of individual inception events are effectively invariant. Further insight into the effects of nucleation on TVC could be gained by studying two monodisperse nuclei populations, with different dominant bubble sizes and thus critical pressures. In this way, correlations of TVC inception number and nuclei population could be quantified using water tensile strength. Finally, it was assumed in this analysis that for the monodisperse case, TVC inception occurred at vapour pressure. In theory, this would be sufficient to activate the monodisperse microbubbles and produce vaporous cavitation. This could be confirmed via direct pressure measurements.

5.5 Conclusions

High speed video and synchronous hydrophone measurements allow the study of the spatial and acoustic characteristics of tip vortex cavitation inception. Quantitative insights were made into inception location, cavity dynamics and acoustic behaviour. Nuclei populations can substantially affect TVC inception behaviour, and were investigated using mono- and polydisperse nuclei populations, in addition to different cavitation numbers.

Nuclei population affects inception event rates due to differences in nuclei size distributions and therefore capture physics and activation rates. The shapes and ranges of the inception location distributions were observed to be similar for each nuclei population, with the highest event rate occurring near the tip. At lower cavitation numbers, the lower test section pressure results in lower vortex core pressure and a longer length of the vortex under tension, such that nuclei ingested downstream are also activated. This increases the length of the activation zone and the event rate. In a flow with relatively weak monodisperse nuclei, the event rate near the tip remains constant since all available nuclei captured in this region are also activated at higher cavitation numbers. The minimum pressure coefficient of about -2.5 occurs near the tip according to the streamwise vortex pressure distribution inferred from the cavity kinematic data. Based on the kinematic and acoustic measurements, it is concluded that the lower pressure in this region causes more explosive cavity growth and higher noise emissions.

Following activation, cavity kinematic properties are determined more by the local pressure than initial nucleus size, at least for the ∼50–100 µm diameter range considered in this study. Cavities that incept at higher tensions, whether at lower cavitation numbers or closer to the tip, grow into longer cavities. Such cavities have lower advection velocities, usually lower than the freestream velocity. Remnant bubbles are transported at about 70% of the freestream velocity independent of inception location and cavitation number.

Cavity acoustic properties are affected more by the local pressure than initial nucleus size. The sound pressure levels of inception events are highest when inception occurs near the tip and are higher at lower cavitation numbers. Further work is required to accurately measure volumetric changes during cavity growth to explain observed acoustic magnitudes.

Similar tonal peaks were measured in flows with mono- and polydisperse nuclei populations indicating the spectral content is independent of initial nucleus size. The frequency of the tonal peak increases with cavitation number. At a fixed cavitation number, the frequency remains relatively constant when inception occurs in the vicinity of the tip, but the peak decreases in power and disappears further downstream. Broadband spectral content at higher frequencies was measured for the monodisperse case when inception occurred near the tip. High spatial and temporal resolution imaging of cavity surface deformations could allow the performance of theoretical cavity dynamic and acoustic models to be assessed. It may also reveal the role of different deformation modes in tip vortex cavity noise generation.

Although the cavity kinematics and acoustics discussed above appear to be relatively independent of nuclei size, the results should be qualified by the fact that the critical pressures of bubbles in the diameter range 50–100 µm only differ by several hundred pascals. Furthermore, the two injected populations are not too dissimilar in a global sense when compared with the natural nuclei population, as shown in Fig. 5.3(a), which can withstand tensions beyond −100 kPa. Therefore, the similarities in the kinematic and acoustic characteristics of TVC for each nuclei population are perhaps not surprising. Further work is required to generate nuclei populations with higher tensile strengths between those of the 50–100 µm and the natural populations to better understand the influence of nuclei populations on TVC.

5.6 Acknowledgements

The authors acknowledge the support of the University of Tasmania and the Defence Science and Technology Group. The authors thank Dr Rhys Paul for assistance with data acquisition, and AMC technical officers, Mr Robert Wrigley and Mr Steven Kent for providing technical assistance with test facility configuration and operation.

Chapter 6

General discussion and conclusions

Nuclei population dynamics and nucleation effects on TVC inception and desinence were investigated through a series of experiments in cavitation test facilities. The effect of natural and injected nuclei populations on TVC behaviour about elliptical hydrofoils was studied using optical, spatial and acoustic measurements.

Natural nuclei population dynamics in different cavitation test facilities were characterised to improve understanding of water quality during TVC experiments in nuclei deplete flows. The natural nuclei population in the cavitation tunnel at the Australian Maritime College Cavitation Research Laboratory was measured using a cavitation susceptibility meter as optical measurements are impractical. The population exhibits similar behaviour to microbubbles, follows a power law and remains invariant at a baseline level over short timescales. The baseline was observed to decrease by an order of magnitude over a week-long test campaign, and to vary by a similar amount over longer timescales. These historical trends necessitate regular monitoring of the population when investigating flows in which natural nuclei are active. For undersaturated conditions, the natural nuclei population remains invariant around the tunnel circuit. Therefore, the population in the test section can be determined from measurements of water sampled from a different part of the circuit (e.g. the lower-segment resorber). This finding is useful as it enables both water quality and TVC measurements to be made without interference of the CSM sampling probe with the TVC experiment in the test section.

The baseline level of the natural nuclei population in the larger Japanese cavitation tunnel is similar to that of the Australian facility. This enables comparative TVC experiments to be conducted with minimal difference between the water quality used for each measurement. However, the pressure in the test section of the Japanese tunnel is a better indicator of whether the natural nuclei population has increased above the baseline, rather than the dissolved oxygen saturation condition in the plenum for the Australian tunnel. This is attributed to differences in the tunnel architecture. The test section of

the Japanese tunnel is much longer, resulting in higher residence times here compared to in the Australian facility. Furthermore, the Australian facility has a large tank downstream of the test section and a large resorber for free gas removal, neither of which feature in the Japanese tunnel design. This may lead to the recirculation of nuclei. A comparison of natural nuclei populations in different cavitation tunnels, measured using a range of CSMs, show similar populations, indicating a possible universal characteristic of natural nuclei populations in water. This is further supported by comparisons with nuclei population measurements made in environmental waters using optical and acoustic measurement techniques. Similar power law indices are observed for the distributions compared, although the concentrations can differ in magnitude. Larger size (10 to 100 µm diameter) populations were previously measured with optical and acoustic techniques in environmental waters. However, the CSM results demonstrate that smaller size populations (0.5 to 5 µm equivalent bubble diameter), as measured in test facilities, are also present in environmental waters.

An improved understanding of natural nuclei population dynamics in cavitation tunnels allows TVC experiments to be better-designed to account for these dynamics. This knowledge was applied to the design of experiments to study TVC inception and desinence about an elliptical hydrofoil in a nuclei deplete flow at the Australian test facility. Test conditions were chosen such that water in the plenum was undersaturated with dissolved oxygen, meaning the natural nuclei population remained at the baseline level for all tests. To avoid any interference effects of the CSM sampling probe with the flow about the test component, the nuclei population in the test section was measured by sampling water from the lower-segment resorber, as discussed earlier.

Incipient and desinent cavitation indices exhibit different characteristics in nuclei deplete flows. Significant scatter in the measured TVC inception indices reveals that the tensile strength of a nuclei deplete flow is stochastic in nature and can only be sufficiently characterised with a large number of measurements. The probability of inception at a given test condition increases with waiting time as the volume of water, and thus the number of nuclei exposed to low pressures, increases. Conversely, the desinent cavitation number exhibits higher repeatability and less scatter, indicating that desinence is less dependent on the nuclei population. Furthermore, different cavitating flow topologies result in different desinent behaviour. Desinence of an attached cavity features greater hysteresis effects compared to that of a cavity which has not attached to the tip. This may be due to factors such as stabilisation of the cavity flow by a laminar separation bubble, and adhesive forces present at the gas-liquid-solid interface due to interfacial phenomena.

Equipped with a deeper understanding of TVC behaviour in nuclei deplete flows, the study was extended to consider two vastly different nuclei populations and their effects on TVC behaviour. The appearance of TVC, particularly at inception, changes with nuclei population. For the deplete case, a continuous cavity appears suddenly with increasing hydrofoil incidence, accompanied by a step change in the sound pressure level. For the

abundant case, TVC appears at lower incidence due to the higher concentration of weaker nuclei in the flow. Intermittent cavities appear, increasing in frequency with incidence and eventually forming a continuous, attached cavity. TVC noise in the nuclei abundant flow is louder compared to that in the deplete flow. The sound pressure level increases gradually with incidence and thus vortex strength, reaching a local maximum possibly associated with the maximum activation rate. The sound pressure levels measured in the nuclei deplete flow also exhibit a local maximum, but due to different cavity physics. For both nuclei populations, the sound pressure level exhibits a local minimum with increasing incidence, as the cavity attaches to the hydrofoil tip. This may be due to suppression of the leading edge flow about the cavity, a reduction in the frequency of intermittent events (for the nuclei abundant case), or the presence of more stable cavities fixed in space.

The investigation of nucleation effects on TVC behaviour was extended to TVC kinematics and acoustics, using mono- and polydisperse nuclei populations. These artificially-generated populations are more comparable in size and concentration than those populations used in the previous set of experiments in nuclei deplete and abundant flows. The monodisperse nuclei had sufficiently large diameters to produce a weaker flow with effectively no tensile strength. Meanwhile, the polydisperse nuclei comprised bubbles with a range of smaller diameters in lower concentrations, resulting in a theoretically stronger flow. Cavity inception and development across a range of streamwise vortex locations were measured at a fixed incidence and Reynolds number for each of these nuclei populations.

The nuclei population influences the inception event rate due to differences in the availability of susceptible nuclei between the two populations. However, the shapes of the inception location distributions were observed to be similar between nuclei populations, with the highest event rate occurring near the tip. It is inferred that this is also the location of the minimum pressure in the vortex, given that the longest and loudest cavities incept here, and the highest cavity elongation rates occur here. As expected, the cavitation number influences TVC inception and development. For lower cavitation numbers, nuclei can be captured and activated across a longer streamwise length as more of the vortex is under tension. This also results in a higher event rate. For the monodisperse nuclei population, the event rate near the tip remains constant with decreasing cavitation number as all available nuclei captured here are also activated at higher cavitation numbers. After activation, cavity kinematics are determined more by the local pressure (i.e. cavitation number and streamwise location) than the initial nucleus size, at least for the $\sim$50–100 µm diameter range considered. The velocity of the upstream extent of the cavity is lower for longer cavities and is typically less than the freestream velocity. Meanwhile, the remnant bubble that appears after cavity contraction is transported at about 70% of the freestream velocity, independent of cavitation number and inception location.

Similarly, the acoustic emissions generated by tip vortex cavities are influenced more by the local pressure than initial nucleus size. As mentioned above, the loudest cavities incept near the tip, becoming louder with decreasing cavitation number. The tonal peaks

observed in frequency spectra for the different injected nuclei populations are similar. The peak frequency increases with cavitation number. For a given cavitation number, the frequency associated with TVC remains relatively constant with streamwise inception location, while the sound pressure level decreases downstream. Broadband, high frequency noise is also present in TVC acoustics for the monodisperse nuclei population, but is difficult to observe for the polydisperse population due to background noise from the nuclei generators. This highlights one of the challenges of measuring TVC acoustics in a complex laboratory environment.

While it is commonly known that TVC inception occurs earlier in flows with weaker nuclei populations, this research reveals more about other important aspects of nucleation effects on TVC. An improved understanding of nuclei population dynamics and nucleation effects on TVC inception, desinence, kinematics and noise has been achieved. Natural nuclei population dynamics in test facilities need to be taken into account when designing experiments in flows with low pressures. This knowledge was applied to the study of TVC in nuclei deplete flows, which demonstrated the stochastic nature of TVC inception and its dependence on the nuclei population, in contrast with desinence. Comparisons of TVC behaviour in flows with a range of natural and artificially-generated nuclei populations showed that nuclei content influences TVC behaviour to varying degrees, dependent on the variation in water quality. The appearance and noise emissions of TVC significantly differ between nuclei deplete and abundant flows, but the differences in these characteristics are less pronounced between flows with injected mono- and polydisperse nuclei populations which are more similar with respect to bubble size and concentration distributions. Nevertheless, variations in nuclei concentrations clearly affect inception event rates, even when both populations are artificially-seeded. This body of work lays the foundation for further studies discussed below. This will lead to an even deeper understanding of nucleation effects on TVC and the associated physics, as well as the improvement of TVC experimental design and TVC prediction capabilities.

6.1 Future work

1. Different-sized monodisperse nuclei populations

   (a) In Chapter 5, both mono- and polydisperse nuclei populations were used to study TVC spatial and acoustic characteristics. Both the nuclei size range and concentration were varied between the populations. It was also explained that the minimum size of the activated nuclei in the polydisperse flow can only be estimated due to the complex nature of the flow. The use of monodisperse populations with different dominant sizes would enable a more accurate assessment of the size of nuclei activated in the vortex, and thus a more detailed understanding of TVC physics.

   (b) Although the nuclei size range and concentration were varied between populations in Chapter 5, it was noted that they are not too dissimilar when compared to the natural nuclei population. This may explain similarities between the cavity kinematic and acoustic characteristics observed for the two nuclei populations. Further work is required on the generation of monodisperse nuclei populations with higher tensile strengths between those of the 50–100 µm and the natural populations to better understand the influence of nuclei populations on TVC.

2. Injected nuclei population control and dynamics in cavitation tunnels

   (a) While polydisperse nuclei population dynamics have been characterised by Russell et al. (2020b), a similar study is required for injected, monodisperse nuclei populations. This will provide a better understanding of how these populations vary with tunnel operating conditions and how they can be controlled in spite of changing tunnel operating conditions. This will lead to better-controlled TVC experiments.

3. Statistical behaviour of TVC inception in nuclei abundant flows

   (a) In Chapter 3, it was reasoned that fewer samples would be required to characterise TVC inception in nuclei abundant flows compared to deplete ones. Additional experiments are required to confirm this and to thus assess the repeatability of measurements in abundant flows. This would improve quantitative understanding about the characteristics of TVC inception in such flows and guide experimental design.

4. Direct measurements of tip vortex pressures

   (a) In Chapter 5, inferences about the local pressure in the tip vortex were made on the assumption that the large, monodisperse nuclei were activated at vapour pressure. Direct pressure measurements of the tip vortex would confirm whether this is the case and if the cavitation observed was vaporous in nature.

5. Validation of theoretical models using experimental measurements

   (a) Higher spatial and temporal resolution measurements of geometric changes during cavity growth, and corresponding acoustic magnitudes and frequencies could be used to validate theoretical cavity dynamic and acoustic models, leading to an improved prediction capability. They may also reveal the role of different deformation modes in tip vortex cavity noise generation.

   (b) A more detailed understanding of acoustic noise sources in cavitation test facilities is required to better design acoustic TVC experiments. This will help to avoid or minimise the overlap of tunnel-related resonances and TVC-related frequencies, and thus avoid unwanted excitations. Further consideration should also be given to the influence of nuclei generator noise and hydrophone positioning on TVC acoustic measurements.

6. Natural nuclei populations

   (a) The development of an optical-based CSM would eliminate acoustic ambiguities in the current design and allow for the measurement of higher nuclei concentrations with greater accuracy.

   (b) To better understand the nature of these nuclei populations, additional studies should be carried out using benchtop experiments rather than complex test facilities such as cavitation tunnels. These studies could provide insight into whether natural nuclei form from the stabilisation of dissolving larger bubbles, or from smaller, homogeneous nuclei.

7. Merged and split cavities

   (a) Both merged and split cavities were observed during the study of tip vortex cavity kinematics and acoustics but were not the focus of the investigation. Additional analysis could be carried out to understand and compare their kinematic and acoustic properties with isolated cavities. This would provide a broader understanding of the characteristics of different tip vortex cavity topologies that are possible.

Bibliography

E. Achenbach. Experiments on the flow past spheres at very high reynolds numbers. *J. Fluid Mech*, 54:565–575, 1972.

A. Amini, M. Reclari, T. Sano, M. Iino, M. Dreyer, and M. Farhat. On the physical mechanism of tip vortex cavitation hysteresis. *Exp. Fluids*, 60(7):118, 2019.

E. Amromin. Two-range scaling for tip vortex cavitation inception. *Ocean Eng.*, 33(3-4): 530–534, 2006.

R. Arndt and C. Dugue. Recent advances in tip vortex cavitation research. In *Proc. Int. Symp. Propulsors and Cavitation*, pages 142–149, 1992.

R. Arndt and A. Keller. Free gas content effects on cavitation inception and noise in a free shear flow. In *Two phase flow and cavitation in power generation systems. Grenoble, 30 March-2 April 1976*, 1976.

R. Arndt and B. Maines. Nucleation and bubble dynamics in vortical flows. *J. Fluids Eng, Trans ASME*, 122(3):488–493, 2000.

R. Arndt, V. Arakeri, and H. Higuchi. Some observations of tip-vortex cavitation. *J. Fluid Mech.*, 229:269–289, 1991.

R. E. Arndt. Cavitation in vortical flows. *Ann. Rev. Fluid Mech.*, 34(1):143–175, 2002.

R. E. Arndt and A. P. Keller. Water quality effects on cavitation inception in a trailing vortex. *J. Fluids Eng., Trans ASME*, 114(3):430–438, 1992.

R. E. Arndt and B. H. Maines. Further studies of tip vortex cavitation. In *Proc. 2nd Int. Symp. Cavitation, Tokyo*, 1994.

R. E. A. Arndt. Cavitation research from an international perspective. *IOP Conf. Ser. Earth Environ. Sci.*, 15(1):12002, 2012.

A. Asnaghi, U. Svennberg, and R. E. Bensow. Large eddy simulations of cavitating tip vortex flows. *Ocean Eng.*, 195:106703, 2020.

J.-A. Astolfi, D. Fruman, and J.-Y. Billard. A model for tip vortex roll-up in the near field region of three-dimensional foils and the prediction of cavitation onset. *Eur. J. Mech. B Fluids*, 18(4):757–775, 1999.

M. Atlar. The specialist committee on water quality and cavitation - final report. *Proc. 23rd ITTC*, 2, 2002.

M. Atlar and M. Billet. Proceedings of the 23rd ITTC – Volume II, The specialist committee on water quality and cavitation. 2000.

G. Baker, S. Barker, K. Bofah, and P. Saffman. Laser anemometer measurements of trailing vortices in water. *J. Fluid Mech.*, 65(2):325–336, 1974.

M. Billet. Cavitation nuclei measurements. In *Proc. ASME Int. Symp. Cavitation Inception, New Orleans, LA*, 1984.

M. Billet and J. Holl. Scale effects on viscous types of limited cavitation. In *Proc. Int. Symp. Cavitation Inception*, pages 2–7, 1979.

M. L. Billet. Cavitation nuclei measurements-a review. In *Proc. Cavitation and Multiphase Flow Forum*, 1985.

F. Blake Jr. The tensile strength of liquids: A review of the literature. Technical memo no. 9. Technical report, Acoustic Research Lab., Harvard Univ., 1949.

O. Boulon, J.-P. Franc, and J.-M. Michel. Tip vortex cavitation on an oscillating hydrofoil. *J. Fluids Eng.*, 119(4):752–758, 1997.

P. Brandner. Microbubbles and cavitation: Microscales to macroscales. In *Proc. 10th Int. Cavitation Symp. (CAV2018)*, 2018.

P. Brandner, Y. Lecoffre, and G. Walker. Design considerations in the development of a modern cavitation tunnel. In *Proc. 16th Australasian Fluid Mech. Conf.*, 2007.

P. Brandner, G. Wright, B. Pearce, L. Goldsworthy, and G. Walker. An experimental investigation of microbubble generation in a confined turbulent jet. In *Proc. 17th Australasian Fluid Mech.Conf.*, 2010.

P. A. Brandner, J. A. Venning, and B. W. Pearce. Wavelet analysis techniques in cavitating flows. *Philos. Trans. R. Soc. A*, 376(2126):20170242, 2018.

N. Breitz and H. Medwin. Instrumentation for insitu acoustical measurements of bubble spectra under breaking waves. *J. Acoust. Soc. Am.*, 86(2):739–743, 1989.

C. E. Brennen. Observations of cavitating flow. In *Proc. 20th Symp. Naval Hydrodynamics*. National Academy Press, 1994.

C. E. Brennen. *Cavitation and Bubble Dynamics*. Cambridge University Press, 1995.

C. E. Brennen. *Cavitation and Bubble Dynamics*. Cambridge University Press, 2014.

L. Briançon-Marjollet and L. Merle. Inception, development and noise of a tip vortex cavitation. In *21st Symp. Naval Hydrodynamics*, pages 851–864, 1996.

S. L. Ceccio and C. E. Brennen. Observations of the dynamics and acoustics of travelling bubble cavitation. *J. Fluid Mech.*, 233:633–660, 1991.

G. Chahine and Y. Shen. Bubble dynamics and cavitation inception in cavitation susceptibility meters. *J. Fluids Eng.*, 108(4):444–452, 1986.

N. Chang, R. Yakushiji, H. Ganesh, and S. Ceccio. Mechanism and scalability of tip vortex cavitation suppression by water and polymer injection. In *Proc. 7th Int. Symp. Cavitation*, 2009.

N. Chang, H. Ganesh, R. Yakushiji, and S. L. Ceccio. Tip vortex cavitation suppression

by active mass injection. *J. Fluids Eng.*, 133(11):111301, 2011.

L. Chen, L. Zhang, X. Peng, and X. Shao. Influence of water quality on the tip vortex cavitation inception. *Phys. Fluids*, 31(2):023303, 2019.

J. Choi and S. L. Ceccio. Dynamics and noise emission of vortex cavitation bubbles. *J. Fluid Mech.*, 575:1–26, 2007.

J. Choi, C.-T. Hsiao, G. Chahine, and S. Ceccio. Growth, oscillation and collapse of vortex cavitation bubbles. *J. Fluid Mech.*, 624:255–279, 2009.

J.-K. Choi and G. L. Chahine. A numerical study on the bubble noise and the tip vortex cavitation inception. *J. Ship and Ocean Tech.*, 7(3):13–33, 2003.

J.-K. Choi and G. L. Chahine. Noise due to extreme bubble deformation near inception of tip vortex cavitation. *Phys. Fluids*, 16(7):2411–2418, 2004.

H. W. Coleman and W. G. Steele. Engineering application of experimental uncertainty analysis. *AIAA Journal*, 33(10):1888–1896, 1995.

L. d'Agostino and A. Acosta. Separation and surface nuclei effects in a cavitation susceptibility meter. *J. Fluids Eng.*, 113(4):695–698, 1991a.

L. d'Agostino and A. Acosta. A cavitation susceptibility meter with optical cavitation monitoring part two: experimental apparatus and results. *J. Fluids Eng.*, 113(2):270–277, 1991b.

K. D. Danov, R. D. Stanimirova, P. A. Kralchevsky, K. G. Marinova, S. D. Stoyanov, T. B. Blijdenstein, A. R. Cox, and E. G. Pelan. Adhesion of bubbles and drops to solid surfaces, and anisotropic surface tensions studied by capillary meniscus dynamometry. *Adv. Colloid Interface Sci.*, 233:223–239, 2016.

K. de Graaf, B. Pearce, and P. Brandner. The influence of nucleation on cloud cavitation about a sphere. In *Proc. 16th Int. Symp. Transport Phenomena and Dynamics of Rotating Machinery (ISROMAC 2016)*, 2016.

G. B. Deane and M. D. Stokes. Scale dependence of bubble creation mechanisms in breaking waves. *Nature*, 418(6900):839, 2002.

C. Doolan, P. Brandner, D. Butler, B. Pearce, D. Moreau, and L. Brooks. Hydroacoustic characterisation of the AMC cavitation tunnel. In *Proc. Acoustics 2013 Victor Harbor: Science, Technology and Amenity*, pages 1–7, 2013.

Endress+Hauser. *Operating Instructions Oxymax W COS41 Dissolved oxygen sensor*. Endress+Hauser, April 2004. BA284C/07/en/04.04, 51506691.

P. S. Epstein and M. S. Plesset. On the stability of gas bubbles in liquid-gas solutions. *The Journal of Chemical Physics*, 18(11):1505–1509, 1950.

J. Ffowcs Williams and D. L. Hawkings. Sound generation by turbulence and surfaces in arbitrary motion. *Philos. Trans. R. Soc. Lond. Ser. A Math. Phys. Sci.*, 264:321–342, 1969.

H. M. Fitzpatrick. Cavitation noise. In *Proc. 2nd Symp. Naval Hydrodynamics, Washington*, 1958.

F. E. Fox and K. F. Herzfeld. Gas bubbles with organic skin as cavitation nuclei. *J.*

Acoust. Soc. Am., 26(6):984–989, 1954.

J.-P. Franc and J.-M. Michel. *Fundamentals of Cavitation*, volume 76. Springer Science & Business Media, 2006.

R. Franklin. A note on the radius distribution function for microbubbles of gas in water. In *Proc. ASME Cavitation and Multiphase Flow Forum*, volume 135, pages 77–85, 1992.

R. Franklin. The cavitating submerged jet. Technical report, American Society of Mechanical Engineers, New York, NY (United States), 1994.

D. Fruman and C. Dugue. Tip vortex roll-up and cavitation. In *Proc. 19th Symp. Naval Hydrodynamics*, pages 633–654, 1994.

C. Garrett, M. Li, and D. Farmer. The connection between bubble size spectra and energy dissipation rates in the upper ocean. *J. Phys. Oceanogr.*, 30(9):2163–2171, 2000.

E. Gates, M. Billet, J. Katz, K. Ooi, and J. Holl. Cavitation inception and nuclei distributions joint ARL/CIT experiments. Technical report, Pennsylvania Stat. Univ. University Park Applied Research Lab, 1979.

L. Gavrilov. On the size distribution of gas bubbles in water. *Sov. Phys. - Acoustics*, 15 (1):22–24, 1969.

B. Gindroz. Propeller cavitation characteristics: The practical interest of nuclei measurements in test facilities and at sea. In *Proc. ASME FED Symp. Cavitation*, 1995.

B. Gindroz and M. Billet. Influence of the nuclei on the cavitation inception for different types of cavitation on ship propellers. *J. Fluids Eng.*, 120(1):171–178, 1998.

B. Gindroz and M. L. Billet. Nuclei and propeller cavitation inception. In *FED Cavitation and Gas-Liquid Flow in Fluid Machinery Devices*, volume 190, pages 251–260, 1994.

B. Gindroz, J.-Y. Billard, and P. Geistdoerfer. Cavitation nuclei measurements at sea. *ASME-PUBLICATIONS-HTD*, 321:497–504, 1995.

B. Gindroz, G. Bailo, F. Matera, and M. Elefante. Influence of the cavitation nuclei on the cavitation bucket when predicting the full-scale behavior of a marine propeller. In *Proc. 21st Symp. Naval Hydrodynamics*, pages 839–850, 1997.

D. Giosio, B. Pearce, and P. Brandner. Influence of pressure on microbubble production rate in a confined turbulent jet. In *Proc. 20th Australasian Fluid Mech. Conf.*, 2016.

S. Glegg and W. Devenport. *Aeroacoustics of Low Mach Number Flows: Fundamentals, Analysis, and Measurement*. Academic Press, 2017.

S. Gowing. Comparison of a centerbody and a standard cavitation susceptibility meter. In *Proc. ASME/JSME Joint Fluids Eng. Conf., San Francisco, California*, 1999.

S. Gowing and Y. T. Shen. Nuclei effects on tip vortex cavitation scaling. In *Proc. 4th Int. Symp. Cavitation, California*, 2001.

S. Gowing, C. Vikram, and S. Burton. Comparison of holographic, light scattering and venturi techniques for bubble measurements in a water tunnel. In *Proc. ASME Cavitation and Multiphase Flow Forum*, pages 25–28, 1988.

S. Gowing, L. Briançon-Marjollet, D. Frechou, and V. Godeffroy. Dissolved gas and nuclei effects on tip vortex cavitation inception and cavitating core size. In *Proc. 5th*

Int. Symp. Cavitation, pages 173–180, 1995.

S. Green. *Tip vortices: Single phase and cavitating flow phenomena*. PhD thesis, California Institute of Technology, 1988.

S. Green. Correlating single phase flow measurements with observations of trailing vortex cavitation. *J. Fluids Eng.*, 113(1):125–129, 1991.

E. N. Harvey, D. Barnes, W. D. McElroy, A. Whiteley, D. Pease, and K. Cooper. Bubble formation in animals. i. physical factors. *J. Cell. Physiol.*, 24(1):1–22, 1944.

H. Higuchi, R. Arndt, and M. Rogers. Characteristics of tip vortex cavitation noise. *J. Fluids Eng.*, 111:495–501, 1989.

J. Holl. An effect of air content on the occurrence of cavitation. *J. Basic Eng.*, pages 941–946, 1960.

C. Hsiao and G. Chahine. Scaling of tip vortex cavitation inception for a marine open propeller. In *Proc. 27th Symp. Naval Hydrodynamics, Seoul, Korea*, pages 5–10, 2008.

C.-T. Hsiao and G. L. Chahine. Scaling of tip vortex cavitation inception noise with a bubble dynamics model accounting for nuclei size distribution. *J. Fluids Eng.*, 127(1): 55–65, 2005.

B. D. Johnson. Bubble populations: background and breaking waves. In *Oceanic Whitecaps*, pages 69–73. Springer, 1986.

B. D. Johnson and R. C. Cooke. Generation of stabilized microbubbles in seawater. *Science*, 213(4504):209–211, 1981.

J. Katz. *Cavitation inception in separated flows*. PhD thesis, California Institute of Technology, 1982.

A. Keller and E. Weitendorf. Influence of undissolved air content on cavitation phenomena at the propeller blades and on induced hull pressure amplitudes. In *Proc. lAHR Symp. Two Phase Flow and Cavitation in Power Generation System*, pages 65–76, 1976.

M. Khoo, J. Venning, B. Pearce, P. Brandner, and Y. Lecoffre. Development of a cavitation susceptibility meter for nuclei size distribution measurements. In *Proc. 20th Australasian Fluid Mech. Conf.*, 2016.

M. Khoo, J. Venning, K. Takahashi, J. Arai, T. Mori, B. Pearce, P. Brandner, and D. Ranmuthugala. Joint research between Australia and Japan on the cavitation inception of marine propellers and control surfaces. In *MAST Asia 2017*, pages 1–6, 2017.

M. Khoo, J. Venning, B. Pearce, and P. Brandner. Nucleation effects on hydrofoil tip vortex cavitation. In *Proc. 21st Australasian Fluid Mech. Conf.*, 2018.

M. Khoo, J. Venning, B. Pearce, and P. Brandner. Statistical aspects of tip vortex cavitation inception and desinence in a nuclei deplete flow. *Exp. Fluids*, 61(6):145, 2020a.

M. Khoo, J. Venning, B. Pearce, and P. Brandner. Nucleation effects on tip vortex cavitation inception location. In *Proc. 22nd Australasian Fluid Mech. Conf.* The University of Queensland, 2020b.

M. Khoo, J. Venning, B. Pearce, K. Takahashi, T. Mori, and P. Brandner. Natural nuclei

population dynamics in cavitation tunnels. *Exp. Fluids*, 61(2):34, 2020c.

H.-Y. Kwak and S.-D. Oh. Gas-vapor bubble nucleation—a unified approach. *J. Colloid Interface Sci.*, 278(2):436–446, 2004.

K. Laberteaux and S. Ceccio. Partial cavity flows. part 2. cavities forming on test objects with spanwise variation. *J. Fluid Mech.*, 431:43–63, 2001.

H. Lamb. *Hydrodynamics*. Dover Publications, 1945.

Y. Lecoffre. *Cavitation Bubble Trackers*. A. A. Balkema, 1999.

Y. Lecoffre, P. Chantrel, and J. Teiller. Le grand tunnel hydrodynamique (GTH). *La Houille Blanche*, (7-8):585–592, 1988.

T. Leighton. *The Acoustic Bubble*. Academic press, 2012.

P. Ligneul and R. Latorre. Study on the capture and noise of spherical nuclei in the presence of the tip vortex of hydrofoils and propellers. *Acta Acustica united with Acustica*, 68(1):1–14, 1989.

P. Ligneul and R. Latorre. Study of nuclei distribution and vortex diffusion influence on nuclei capture by a tip vortex and nuclei capture noise. *J. Fluids Eng.*, 115(3):504–507, 1993.

Z. Liu, K. Sato, and C. E. Brennen. Cavitation nuclei population dynamics in a water tunnel. In *FED-Vol. 153, Cavitation and Multiphase Flow*, number 153, pages 119–124. American Society of Mechanical Engineers, 1993.

B. Maines and R. Arndt. Bubble dynamics of cavitation inception in a wing tip vortex. In *Proc. ASME Cavitation and Multiphase Flow Forum, FED, 1993*, volume 153, pages 93–97, 1993.

B. McCormick. On cavitation produced by a vortex trailing from a lifting surface. *J. Basic Eng.*, 84(3):369–378, 1962.

L. Mées, D. Lebrun, D. Allano, F. Walle, Y. Lecoffre, R. Boucheron, and D. Fréchou. Development of interferometric techniques for nuclei size measurement in cavitation tunnel. In *Proc. 28th Symp. Naval Hydrodynamics, Pasadena, California*, 2010.

D. Messino, D. Sette, and F. Wanderlingh. Statistical approach to ultrasonic cavitation. *J. Acoust. Soc. Am.*, 35(10):1575–1583, 1963.

R. Meyer, M. Billet, and J. Holl. Freestream nuclei and traveling-bubble cavitation. *J. Fluids Eng.*, 114(4):672–679, 1992.

M. Minnaert. XVI. On musical air-bubbles and the sounds of running water. *Lond. Edinb. Dubl. Phil. Mag.*, 16(104):235–248, 1933.

K. A. Mørch. Cavitation nuclei and bubble formation—a dynamic liquid-solid interface problem. *J. Fluids Eng.*, 122(3):494–498, 2000.

K. A. Mørch. Reflections on cavitation nuclei in water. *Phys. Fluids*, 19(7):1–7, 2007.

T. Mori, K. Naganuma, R. Kimoto, R. Yakushiji, and S. Nagaya. Hydrodynamic and hydroacoustic characteristics of the Flow Noise Simulator. In *Proc. 5th ASME-JSME Joint Fluids Eng. Conf., FEDSM2007-37531*, 2007.

S. Nagaya, R. Kimoto, K. Naganuma, and T. Mori. Observation and scaling of tip vortex cavitation on elliptical hydrofoils. In *Proc. ASME-JSME-KSME 2011 Joint Fluids Eng. Conf.*, pages 225–230. American Society of Mechanical Engineers, 2011.

T. Němec. Homogeneous bubble nucleation in binary systems of liquid solvent and dissolved gas. *J. Chem. Phys.*, 467:26–37, 2016.

E. A. Neppiras. Acoustic cavitation. *Phys. Rep.*, 61(3):159–251, 1980.

S. J. Norris, I. Brooks, G. de Leeuw, A. Sirevaag, C. Leck, B. Brooks, C. Birch, and M. Tjernstrom. Measurements of bubble size spectra within leads in the arctic summer pack ice. *Ocean Sci.*, 2011.

T. O'Hern, S. Green, and E. Morss. Measurements of oceanic nuclei distributions. In *Proc. ASME Cavitation and Multiphase Flow Forum*, pages 23–26, 1986.

T. O'Hern, L. d'Agostino, and A. Acosta. Comparison of holographic and Coulter counter measurements of cavitation nuclei in the ocean. *J. Fluids Eng.*, 110(2):200–207, 1988.

T. J. O'Hern. *Cavitation inception scale effects: Nuclei distributions in natural waters, Cavitation inception in a turbulent shear flow.* PhD thesis, Caltech, 1987.

D. Oldenziel. A new instrument in cavitation research: the cavitation susceptibility meter. *J. Fluids Eng.*, 104(2):136–141, 1982.

G. Oweis, I. van der Hout, C. Iyer, G. Tryggvason, and S. Ceccio. Capture and inception of bubbles near line vortices. *Phys. Fluids*, 17(2):022105, 2005.

G. F. Oweis, J. Choi, and S. L. Ceccio. Dynamics and noise emission of laser induced cavitation bubbles in a vortical flow field. *J. Acoust. Soc. Am.*, 115(3):1049–1058, 2004.

R. W. Pascal, M. J. Yelland, M. A. Srokosz, B. I. Moat, E. M. Waugh, D. H. Comben, A. G. Cansdale, M. C. Hartman, D. G. Coles, and P. Chang Hsueh. A spar buoy for high-frequency wave measurements and detection of wave breaking in the open ocean. *J. Atmos. Ocean. Technol.*, 28(4):590–605, 2011.

R. Paul, J. Venning, B. Pearce, and P. Brandner. Nuclei transport about a sphere. In *11th Int Symp on Cavitation (CAV2021), Daejon, Korea*, 2021.

X. Peng, L. Xu, and Y. Cao. The study of tip vortex flow and cavitation inception on an elliptical hydrofoil. In *Proc. 5th Int. Symp. Marine Propulsion, Espoo, Finland*, 2017.

P. Pennings, J. Bosschers, J. Westerweel, and T. Van Terwisga. Dynamics of isolated vortex cavitation. *J. Fluid Mech.*, 778:288–313, 2015a.

P. Pennings, J. Westerweel, and T. Van Terwisga. Flow field measurement around vortex cavitation. *Exp. Fluids*, 56(11):206, 2015b.

F. Peterson, F. Danel, A. Keller, and Y. Lecoffre. Comparative measurements of bubble and particulate spectra by three optical methods. *Report of Cavitation Committee, 14th ITTC*, 1975.

T. Pham, J. Michel, and Y. Lecoffre. Dynamical nuclei measurement: On the development and the performance evaluation of an optimized center-body meter. *J. Fluids Eng.*, 119 (4):744–751, 1997.

K. Randolph, H. M. Dierssen, M. Twardowski, A. Cifuentes-Lorenzen, and C. J. Zappa.

Optical measurements of small deeply penetrating bubble populations generated by breaking waves in the Southern Ocean. *J. Geophys. Res. Oceans*, 119(2):757–776, 2014.

P. Russell, D. Giosio, J. Venning, B. Pearce, P. Brandner, and S. Ceccio. Microbubble generation from condensation and turbulent breakup of sheet cavitation. In *Proc. 31st Symp. Naval Hydrodynamics, Monterey, California*, 2016.

P. Russell, D. Giosio, J. Venning, B. Pearce, P. Brandner, V. Aumelas, and G. Maj. Towards real-time optical measurement of microbubble content in hydrodynamic test facilities. In *Proc. 10th Int. Symp. Cavitation (CAV2018)*, pages 1056–1061, 2018a.

P. Russell, D. Giosio, J. Venning, B. Pearce, P. Brandner, and S. Ceccio. Microbubble disperse flow about a lifting surface. In *Proc. 32nd Symp. Naval Hydrodynamics, Hamburg, Germany*, 2018b.

P. Russell, J. Venning, B. Pearce, and P. Brandner. Calibration of Mie Scattering Imaging for microbubble measurement in hydrodynamic test facilities. *Exp. Fluids*, 61(4):93, 2020a.

P. S. Russell, L. Barbaca, J. A. Venning, B. W. Pearce, and P. A. Brandner. Measurement of nuclei seeding in hydrodynamic test facilities. *Exp. Fluids*, 61(3):79, 2020b.

F. R. Schiebe. The influence of gas nuclei size distribution on transient cavitation near inception. Technical report, St. Anthony Falls Laboratory, 1969.

Y. Shen and S. Gowing. Cavitation susceptibility of ocean and laboratory waters. In *Proc. 21st American Towing Tank Conf., Washington, DC*, 1986.

Y. Shen, S. Gowing, and R. Pierce. Cavitation susceptibility measurements by a venturi. In *Proc. ASME Int. Symp. Cavitation Inception, New Orleans, LA*, 1984.

Y. Shen, G. Chahine, C.-T. Hsiao, and S. Jessup. Effects of model size and free stream nuclei on tip vortex cavitation inception scaling. In *Proc. 4th Int. Symp. Cavitation, California*, 2001.

Y. T. Shen, S. Gowing, and B. Eckstein. Cavitation susceptibility measurements of ocean lake and laboratory waters. Technical report, David W Taylor Naval Ship Research and Development Center Bethesda MD, 1986.

Y. T. Shen, S. Jessup, and S. Gowing. Tip vortex cavitation inception scaling for high reynolds number application. In *Proc. ASME/JSME 2003 4th Joint Fluids Eng. Summer Conf.*, pages 233–239. American Society of Mechanical Engineers Digital Collection, 2009.

K. M. Sinding, D. R. Hanson, M. H. Krane, and J. Koncoski. Insight into tip vortex cavitation using velocity field measurements. In *Proc. 10th Int. Symp. Cavitation*. ASME Press, 2018.

M. Song, L. Xu, X. Peng, and D. Tang. An acoustic approach to determine tip vortex cavitation inception for an elliptical hydrofoil considering nuclei-seeding. *Int. J. Multiph. Flow*, 90:79–87, 2017.

D. Stramski, E. Boss, D. Bogucki, and K. J. Voss. The role of seawater constituents in light backscattering in the ocean. *Prog. Oceanogr.*, 61(1):27–56, 2004.

K. Takahashi. Personal communication, September 2021.

K. Takahashi, J. Arai, and T. Mori. Nuclei population dynamics in NSRC/ATLA Flow Noise Simulator. Technical report, Acquisition, Technology & Logistics Agency, Japan, 2019.

C. Testa, S. Ianniello, and F. Salvatore. A Ffowcs Williams and Hawkings formulation for hydroacoustic analysis of propeller sheet cavitation. *J. Sound Vib.*, 413:421–441, 2018.

J. Venning, D. Giosio, S. Smith, B. Pearce, and P. Brandner. The influence of nucleation on the spectral content of cloud cavitation about a hydrofoil. In *Proc. 10th Int. Symp. Cavitation (CAV2018)*, pages 1015–1030, 2018a.

J. Venning, M. Khoo, B. Pearce, and P. Brandner. Background nuclei measurements and implications for cavitation inception in hydrodynamic test facilities. *Exp. Fluids*, 59(4): 71, 2018b.

J. Venning, M. Khoo, B. Pearce, and P. Brandner. Observations on a cavitating trailing vortex behind a control surface. In *MAST Asia 2019*, pages 1–9, 2019.

J. A. Venning, S. D. Vincentis, B. W. Pearce, and P. A. Brandner. Microbubble generation for PIV seeding. In *Proc. 20th Australasian Fluid Mech. Conf.*, 2016.

C. Ward, A. Balakrishnan, and F. Hooper. On the thermodynamics of nucleation in weak gas-liquid solutions. *J. Basic Eng.*, 92(4):695–701, 1970.

P. Warneck and J. Williams. *The atmospheric chemist's companion: Numerical data for use in the atmospheric sciences*. Springer Science & Business Media, 2012.

P. Welch. The use of fast fourier transform for the estimation of power spectra: a method based on time averaging over short, modified periodograms. *IEEE Trans. Audio and Electroacoustics*, 15(2):70–73, 1967.

E. Worch. *Hydrochemistry: Basic Concepts and Exercises*. Walter de Gruyter GmbH & Co KG, 2015.

R. Yakushiji. *Mechanism of Tip Vortex Cavitation Suppression by Polymer and Water Injection*. PhD thesis, The University of Michigan, 2009.

L.-X. Zhang, L.-Y. Chen, X.-X. Peng, and X.-M. Shao. The effect of water quality on tip vortex cavitation inception. *J. Hydrodynamics*, 29(6):954–961, 2017.

X. Zhang. *Influence of bubbles on the water-leaving reflectance*. PhD thesis, Dalhousie University, 2001.

Appendices

Appendix A

Development of a cavitation susceptibility meter for nuclei size distribution measurements

This appendix is an author accepted manuscript of an article published in the proceedings of the 20th Australasian Fluid Mechanics Conference, Perth, Australia, 5–8 December 2016, modified following thesis examiners' feedback. The final authenticated version is available online at:

`http://www.afms.org.au/proceedings/20/Khoo_et_al_2016.pdf`.

The citation for the paper is:

M. Khoo, J. Venning, B. Pearce, P. Brandner, and Y. Lecoffre. Development of a cavitation susceptibility meter for nuclei size distribution measurements. In Proc. 20th Australasian Fluid Mech. Conf., 2016.

A.1 Abstract

Cavitation inception in practical flows is invariably heterogeneous as nucleation sites are provided by microbubble populations. Microbubbles grow explosively, filling with vapour, when exposed to a critical pressure which is size dependent. The detection of physical bubble activations in a known pressure field can therefore be used to measure bubble size distributions. The nuclei population within a test flow can be measured using a venturi and by counting the number of activations or events using the acoustic emission from each bubble collapse in the downstream pressure recovery region. Such devices are known as Cavitation Susceptibility Meters (CSMs).

The development, calibration and operation of a CSM for use in the cavitation tunnel at the Australian Maritime College is described. The minimum pressure in the CSM is reduced in steps by increasing the flow rate or decreasing tunnel static pressure to activate increasing numbers of smaller nuclei in order to provide a cumulative size distribution. Simultaneous flow rate measurement permits nuclei volumetric concentration as well as venturi throat pressure to be determined.

The concentration measurement is shown to have an uncertainty of less than 0.5%, while the critical pressure has an uncertainty of approximately 5%. The volume measurement and timing uncertainties for flow rate calibration are found to account for 81% of this uncertainty. Sample nuclei distribution measurements are presented, showing critical pressures as low as 100 kPa below vapour pressure, corresponding to an equivalent bubble diameter of 1 μm in the test section.

A.2 Introduction

The presence of microbubbles, or nuclei, in water is known to control the inception and dynamic behaviour of cavitation about marine propulsors (Atlar and Billet, 2000; Gindroz and Billet, 1998; Shen et al., 2001). The equilibrium of a microbubble at external pressures below a critical value becomes unstable such that it will grow explosively. By this mechanism, they provide heterogeneous cavitation nucleation sites. The dynamic behaviour of microbubbles is described by the Rayleigh-Plesset equation (Franc and Michel, 2006). Knowledge of nuclei content in cavitation tunnel water is essential to accurately assess the cavitation performance of test components.

Optical and hydrodynamic techniques are generally used to measure nuclei distributions in water. Optical techniques include holography (Mées et al., 2010), Interferometric Laser Imaging (Mées et al., 2010), shadowgraphy (Russell et al., 2016; Venning et al., 2016) and Phase Doppler Analysis (Gindroz and Billet, 1998). These techniques enable direct measurements of nuclei size and concentration. However, they may falsely identify contaminant particles as microbubbles and have a minimum detectable size due to opti-

cal diffraction limits. Depending on the implementation, these methods possess varying degrees of temporal and spatial resolution. A Cavitation Susceptibility Meter (CSM) is a hydrodynamic device that uses a venturi to induce cavitation inception and therefore measure the critical pressure of microbubbles and other active nuclei. It allows nuclei smaller than 1 μm in diameter to be measured. Bubble size can be derived from the measured critical pressure using the equations for a bubble in equilibrium (Franc and Michel, 2006). As the test flow must be sampled, this method lacks spatial and temporal resolution and is effective for flows with homogeneous nuclei distributions. It has been used in laboratory (Chahine and Shen, 1986; d'Agostino and Acosta, 1991b; Gowing, 1999; Mées et al., 2010; Oldenziel, 1982; Pham et al., 1997) and real-world environments (Shen and Gowing, 1986).

A CSM developed by YLec Consultants, also known as the 'Venturix' (Pham et al., 1997), was implemented to measure the nuclei size distribution in the water tunnel at the Australian Maritime College's Cavitation Research Laboratory. The variable-pressure, closed-circuit cavitation tunnel has a volume of 365 m^3 (demineralised water). The test section has a 0.6×0.6 m cross section and is 2.6 m long. It has ancilliaries for fast degassing and nuclei injection that enable strict control of the nuclei content. A schematic of the tunnel is shown in figure A.1. Further details regarding the tunnel design and operation are described in Brandner et al. (2007).

Implementation of both a CSM and a nuclei injection system enables rigorous experimental modelling of cavitation inception and dynamic behaviour of marine propulsors to be conducted.

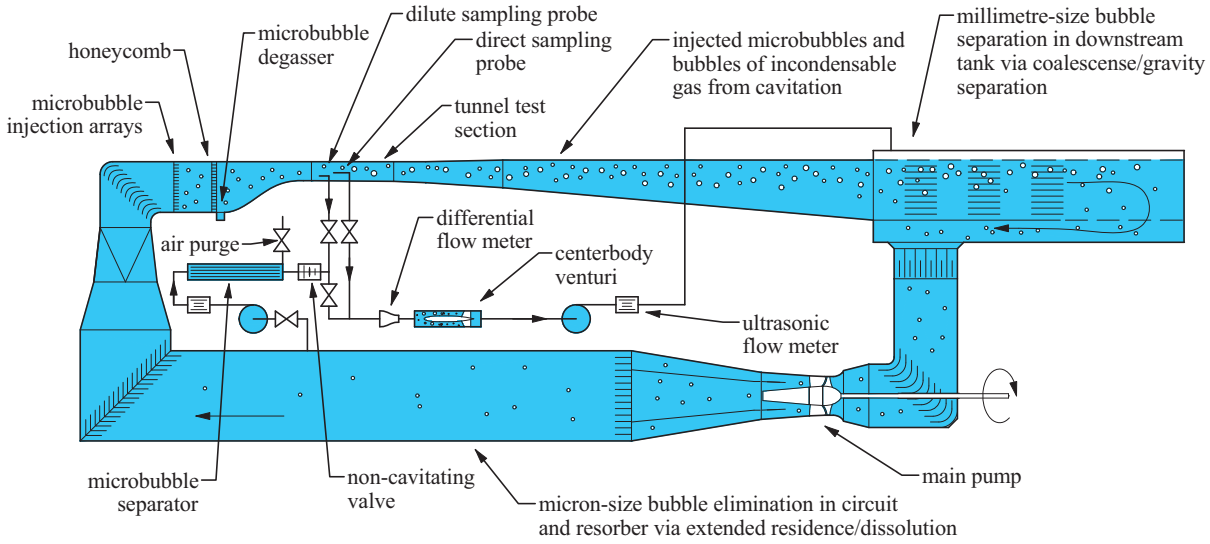

Figure A.1: Schematic of the cavitation tunnel and CSM circuit.

A.3 CSM Design and Operating Principle

Water is continuously sampled from the tunnel test section and passed through a contraction, or throat, in the venturi which is formed by the annular gap between a centrebody and an external sleeve (figure A.2). This design is simpler to manufacture than conventional venturis and allows alternate external sleeves to be fitted for various diagnostics (eg. imaging and pressure characterisation). Boundary layer tripping devices are used to generate turbulent flow around the centrebody, thus delaying boundary layer separation in the downstream diffuser which gives rise to undesirable sheet cavitation.

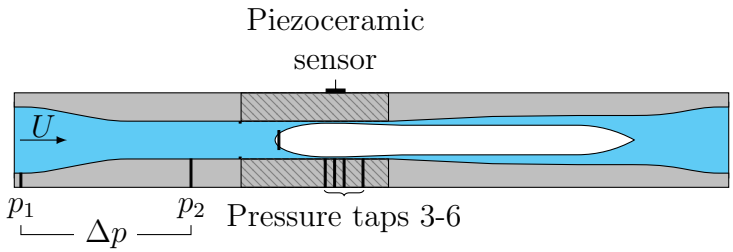

Figure A.2: Schematic showing venturi arrangement, including the interchangable outer sleeve (shaded area) with pressure taps and piezoceramic sensor.

As the tunnel static pressure is reduced or dynamic pressure in the venturi throat increased, the throat static pressure (p_{VT}) reduces below vapour pressure (p_v). Larger free gas bubbles (in the order of 100 μm) collapse at or above this pressure. However, smaller nuclei sustain larger negative pressures prior to reaching their critical pressure (p_c), at which point they become unstable and grow explosively. With the onset of cavitation, the minimum venturi throat pressure is equal to the critical pressure of the smallest nuclei being activated. Using the formulas for spherical bubble equilibrium (Franc and Michel, 2006), the following polynomial is derived, which is solved numerically to give the equivalent initial bubble diameter (D_0),

$$\frac{4}{27\left(p_v - p_c\right)^2} = \left(\frac{D_0}{4S}\right)^3 \left(p_0 - p_v\right) + \left(\frac{D_0}{4S}\right)^2 \tag{A.1}$$

where S is the surface tension and p_0 is the initial pressure.

Once nuclei are activated and grow in the venturi throat, they are advected downstream into a high pressure region in the diffuser where they collapse. The collapse of the vapour-filled bubble generates a shockwave, the propagation of which excites a structural response in the venturi outer sleeve that is measured by a piezoceramic sensor. Each event is counted using signal processing. The nuclei event rate and concentration (C) is then calculated for the sampled water by,

$$C = \frac{N}{\Delta t Q} \tag{A.2}$$

where N is the number of activations counted over time Δt, and Q is the volumetric flow rate. The critical pressures of the activated nuclei are determined using the minimum pressure coefficient in the venturi throat which is measured under non-cavitating conditions. Direct measurement of the minimum throat pressure in real time is not possible due to destabilisation of the pressure field during cavitation events and undesirable cavitation at the pressure taps.

A.4 Differential Flow Meter Calibration

The volumetric flow rate can be measured using ultrasonic flow meters, although for redundancy and field use, a differential flow meter can be useful. In this case, the volumetric flow rate is determined using the measured differential pressure, $\Delta p = p_1 - p_2$, across a contraction located upstream of the centrebody venturi. The Bernoulli equation for incompressible flow across the contraction is modified to incorporate a flow coefficient (C_Q) which characterises the viscous losses and geometric parameters of the contraction. The flow coefficient is given by,

$$C_Q = \frac{Q}{A_2\sqrt{2\Delta p/\rho}} \tag{A.3}$$

where A_2 is the contraction outlet area and ρ is fluid density. C_Q was determined from calibration. A differential pressure sensor (Siemens P500, span: 0–31.25 kPa, model: 7MF5403-1EA10-Z) was used to measure the contraction pressure difference while tunnel water was pumped through it and collected in a tank. The flow rate was calculated by dividing the measured volume by the water discharge time. The flow coefficient was measured for a range of Reynolds numbers based on the contraction outlet diameter. A power law trendline was fitted to the data,

$$C_Q = a_1 \times Re^{b_1} \tag{A.4}$$

where $a_1 = 0.826$ and $b_1 = 0.0186$. The Reynolds number is defined as $Re = {}^{U_2 D_2}/_{\nu}$, where U_2 is the mean flow velocity at the outlet of the contraction, D_2 is the contraction outlet diameter and ν is the fluid kinematic viscosity. The measured C_Q data and corresponding trendline are shown in figure A.3.

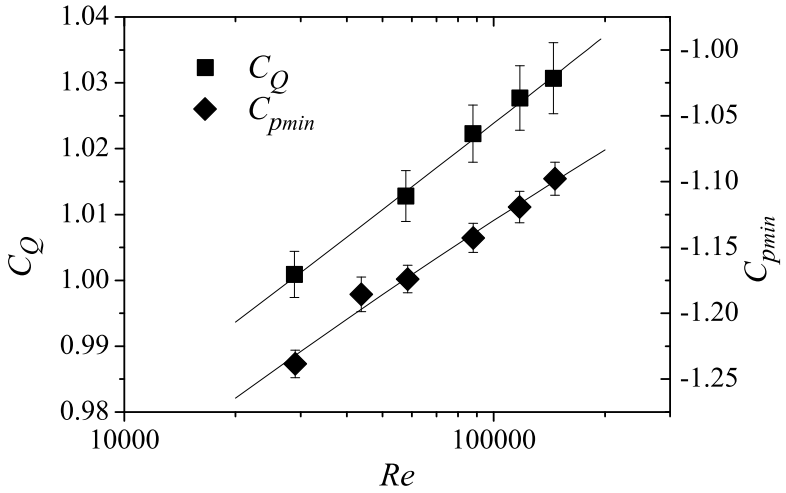

Figure A.3: Flow coefficient (C_Q) for the contraction and minimum pressure coefficient ($C_{p_{min}}$) in the venturi throat as functions of Reynolds number.

The flow velocity at the outlet of the contraction, U_2, is then,

$$U_2 = \left[a_1 \left(\frac{D_2}{\nu} \right)^{b_1} \left(\frac{2\Delta p}{\rho} \right)^{0.5} \right]^{\frac{1}{1-b_1}} \tag{A.5}$$

This allows the volumetric flow rate to be determined, then used in equation A.2 to calculate the nuclei concentration. The flow velocity is also used together with the venturi throat calibration parameters to determine the venturi throat pressure.

A.5 Venturi Throat Calibration

In order to determine the minimum throat pressure, the pressure coefficient (C_p) along the throat was measured as a function of Re under non-cavitating conditions. A sleeve with pressure taps at four locations along the venturi throat and pre-diffuser was installed (figure A.2). Two of the upstream locations each had two opposing taps (not shown), allowing the alignment of the centrebody within the sleeve to be assessed. The pressure coefficient at each pressure tap is defined as,

$$C_p = \frac{p_x - p_1}{\frac{1}{2}\rho U_{VT}^2} \tag{A.6}$$

where p_x is the pressure at location x in the throat, p_1 is the pressure at a reference location upstream of the venturi measured using high and low range absolute pressure sensors (Siemens DSIII, span: 0–500 kPa, model: 7MF4333-1GA02-2AB1 and Siemens DSIII, span: 0–130 kPa, model: 7MF4333-1FA02-2AB1, respectively) and U_{VT} is the mean flow velocity in the venturi throat, determined using either the ultrasonic flow meters (as shown in this paper), or the differential flow meter. Both methods were calibrated simultaneously. The differential pressure, $p_x - p_1$, was measured using a high range differential pressure transducer (Siemens SITRANS P500, span: 0–16 bar, model:

7MF5403-1GA10-Z). The absolute pressures to which the sensor was exposed were made less severe by conducting the calibration at high test section pressure (400 kPa). The sensors were mounted on a frame located a short distance (i.e. <0.5 m) from the venturi centrebody. A handheld pressure calibrator was used to verify the factory calibration of the pressure sensors. The streamwise variation of C_p is shown in figure A.4 for a range of Re.

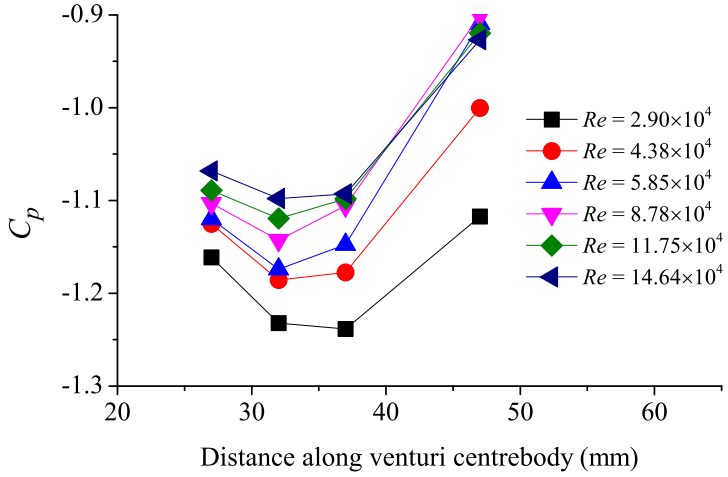

Figure A.4: Variation of pressure coefficient along venturi centrebody for a range of Reynolds numbers. The throat is located between 27 and 37 mm. A pressure tap located downstream of the throat at 47 mm was also used.

The magnitude of C_p in the venturi throat decreases with increasing Re value. The minimum pressure coefficient ($C_{p_{min}}$) occurs at one streamwise location for all but the lowest Re value. Due to boundary layer growth, the location of the minimum pressure is downstream of the minimum geometrical throat area for all Re. A power law trendline was fitted to the $C_{p_{min}}$ values as a function of Re to give,

$$C_{p_{min}} = a_2 \times Re^{b_2} \tag{A.7}$$

where $a_2 = -2.53$ and $b_2 = -0.0701$. The measured $C_{p_{min}}$ data and corresponding trendline are shown in figure A.3.

The minimum venturi throat pressure (p_{min}) is determined from,

$$p_{min} = p_1 + \frac{1}{2}\rho a_2 \left(\frac{D_2}{\nu}\right)^{b_2} \left(\frac{A_2}{A_{VT}}\right)^2 U_2^{(b_2+2)} \tag{A.8}$$

This corresponds to the critical pressure (p_c) of the smallest activated nuclei.

Since the pressure taps in the sleeve surrounding the venturi centrebody are potential cavitation sites, this calibration sleeve was replaced with a sleeve without pressure taps for nuclei measurements.

A.6 Signal Processing Technique

Cavitation bubble collapse events are counted using the measured voltage (V_P) across a piezoceramic sensor (STEMiNC, 1 MHz resonant frequency, model: SMD15T21R111WL). The signal is measured at a sampling frequency of 2 MHz. Four stages of signal processing are used to shape each bubble collapse signal into an individual peak:

1. High-pass filter (to remove low frequency structural resonance and shorten event duration)
2. Rectification (to enable smoothing of data)
3. Low-pass filter (to smooth data into single peaks)
4. Log function (to homogenise nuclei event signal amplitudes, improving the effectiveness of peak counting)

Peak counting is used to count the number of maxima in the processed signal above a threshold level. The nuclei event and volumetric flow rates are used to calculate the nuclei concentration as per equation A.2. Samples of the raw and processed signal from the piezoceramic sensor are provided in figure A.5. The effect of the threshold level on the total nuclei count (for the complete dataset from which figure A.5 data was extracted) is provided in figure A.6. If the threshold is set too high, nuclei events are missed. Conversely, if the threshold level is set too low, additional peaks due to unfiltered structural resonance are counted, resulting in a higher nuclei concentration. The threshold level is currently set based on correlation of aurally-detected events and signal peaks. Further investigation of the acoustic emissions from bubble collapses is required to quantify the counting accuracy and to improve its performance.

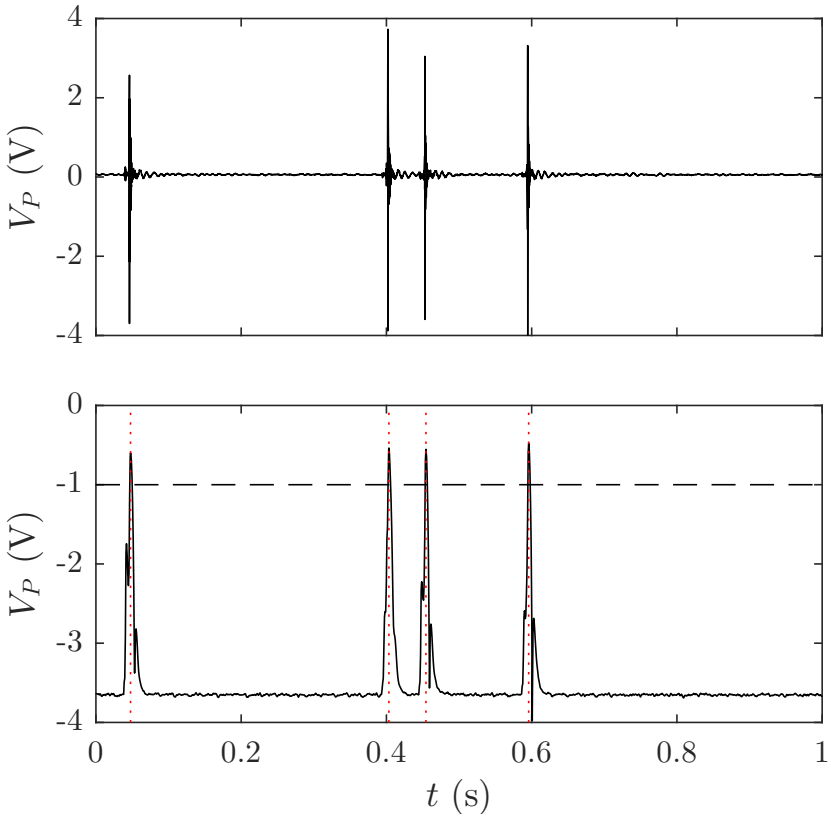

Figure A.5: Piezoceramic sensor signal: raw (top) and processed (bottom). A threshold level of -1 (horizontal, dashed line) gives a count of 4. Vertical, dotted lines indicate detections.

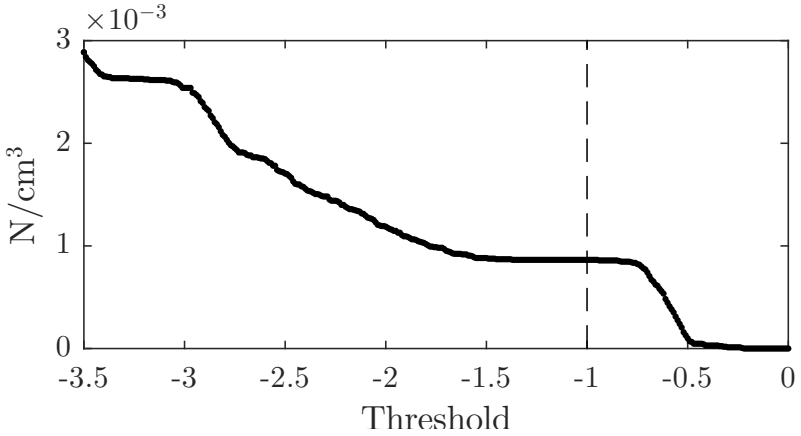

Figure A.6: Effect of threshold setting on nuclei concentration.

A.7 Nuclei Distribution Measurement

A cumulative background nuclei distribution for the cavitation tunnel is shown in figure A.7. Nuclei concentrations were measured at a range of throat pressures by increasing the venturi flow rate. The measurement method is cumulative, with a larger number of cavitation events occurring with decreasing pressure as all nuclei with a critical pressure greater than or equal to the throat pressure are activated. The results show that a nucleus with an equivalent bubble diameter in the test section less than 1.78 μm can sustain a pressure in the venturi throat of 49.1 kPa below vapour pressure before activation while a nucleus with an equivalent diameter less than 1.01 μm can sustain −95.2 kPa. The measured background nuclei concentrations in the order of 10^{-4} N/cm^3 are relatively low compared to the maximum anticipated concentrations in the laboratory environments in the order of 10 N/cm^3. Nuclei generators can be used to control the concentration of artificially-seeded nuclei in the test section (Brandner et al., 2010; Lecoffre, 1999).

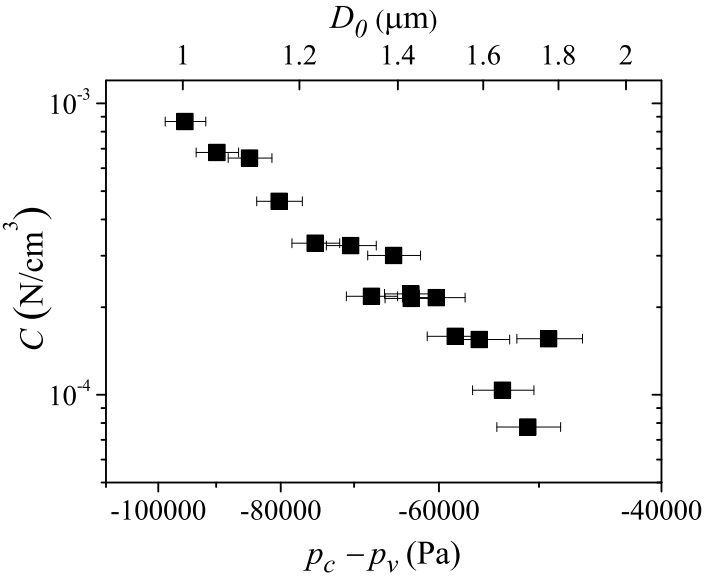

Figure A.7: Cavitation tunnel cumulative background nuclei distribution. D_0 is the equivalent bubble diameter in the test section with static pressure 105 kPa and dissolved O_2 content 3 mg/L.

A.8 Uncertainty Analysis

An uncertainty analysis summary is provided in table A.1. Bias errors were propagated for each of the measured quantities used to calculate the variables of interest, as described in Coleman and Steele (1995). For the nuclei concentration, the uncertainty in the activation count was assumed to be zero as validation of the event counting method has not been carried out. Further investigation of acoustic emissions from bubble collapses is required to quantify the counting accuracy. This will directly influence the nuclei concentration uncertainty. The main sources of uncertainty in the venturi throat pressure measurement were the C_p and U_2 measurements, both of which stem from the uncertainties in the tank volume and timing measurements. These two parameters account for 81% of the $p_c - p_v$ uncertainty, implying that it could be reduced with a more accurate direct flow rate calibration.

f	Ref. value	$\%\epsilon_f$	Major contributors
C_Q	1.02	0.424	Vol (64%), Δt (35%)
U_2	4.21 m/s	0.435	C_Q (99%)
Q_{UT}	0.00123 m^3/s	0.465	Vol (53%), Δt (29%)
C_p	−1.14	0.970	Q_{UT} (92%)
Re	8.79×10^4	1.19	ν (85%), Q_{UT} (15%)
p_{VT}	−60,600 Pa	5.12	C_p (54%), U_2 (41%)
$C^\dagger$	0.000271 N/cm^3	0.436	U_2 (100%)
$p_c - p_v$	−63,100 Pa	4.92	C_p (54%), U_2 (41%)

Table A.1: Uncertainties for a flow rate of 1.2 l/s at 25°C. ϵ_f is the total uncertainty in f, the variable of interest and Vol is the tank volume for flow meter calibration. † denotes that the error in activation count, N, was assumed to be zero.

A.9 Conclusions

The calibration and operation of a Cavitation Susceptibility Meter for use in the cavitation tunnel at the Australian Maritime College was presented. The flow and minimum pressure coefficients were calibrated experimentally for a range of Reynolds numbers. The sensitivity of the nuclei concentration measurement to threshold level setting was illustrated, highlighting the requirement for further investigation of acoustic emissions from bubble collapses to quantify the counting accuracy. The concentration measurement was shown to have an uncertainty of less than 0.5%, while the critical pressure had an uncertainty of approximately 5%. The volume measurement and timing uncertainties for flow rate calibration accounted for 81% of this uncertainty. Sample nuclei distribution measurements showed nuclei with critical pressures of up to 95.2 kPa below vapour pressure, corresponding to an equivalent bubble diameter of 1.01 μm in the test section.

Appendix B

Joint research between Australia and Japan on the cavitation inception of marine propellers and control surfaces

This appendix is an author accepted manuscript of an article presented at the MAST (Maritime/Air Systems and Technology) Asia Conference, Chiba, Japan, 12–14 June 2017. The final authenticated version is available online at:

`https://mastconfex.com/asia2017/`.

The citation for the paper is:

M. Khoo, J. Venning, K. Takahashi, J. Arai, T. Mori, B. Pearce, P. Brandner, and D. Ranmuthugala. Joint research between Australia and Japan on the cavitation inception of marine propellers and control surfaces. In MAST Asia 2017, pages 1–6, 2017.

Appendix B has been removed for copyright reasons

Appendix C

Background nuclei measurements and implications for cavitation inception in hydrodynamic test facilities

This appendix is a post-peer-review, pre-copyedit version of an article published in *Experiments in Fluids*. The final authenticated version is available online at:

`https://doi.org/10.1007/s00348-018-2520-5`.

The citation for the paper is:

J. Venning, M. Khoo, B. Pearce, and P. Brandner. Background nuclei measurements and implications for cavitation inception in hydrodynamic test facilities. Exp. Fluids, 59(4):71, 2018.

C.1 Abstract

Water susceptibility and background nuclei content in a water tunnel are investigated using a Cavitation Susceptibility Meter. The measured cumulative histogram of nuclei concentration against critical pressure shows a power law dependence over a large range of concentrations and pressures. These results show that the water strength is not characterised by a single tension but is susceptible to 'all' tensions depending on the relevant time scale. This background nuclei population is invariant of tunnel conditions showing that they are stabilised against dissolution. Consideration of a practical cavitating flow about a sphere shows that although background nuclei may be activated, their numbers are so few compared with other sources that they are insignificant for this case.

C.2 Introduction

Inception of hydrodynamic cavitation in practical flows is invariably due to heterogeneous nucleation. These discrete sites of weakness, termed nuclei, are typically microbubbles either free in the liquid volume or volumes of gas trapped in or on adjacent surfaces. Depending on nuclei strength, water can sustain tensions well below the saturated vapour pressure before vapourisation occurs. Nuclei have been shown to control not only inception but also the dynamics of cavitation. Although nuclei may typically be microbubbles they may also be gas volumes associated with solid particles (Mørch, 2007) or potentially biological entities (O'Hern, 1987).

One method for measuring the nuclei concentration is by direct imaging. This may, however, be problematic for several reasons. Firstly, often concentrations can be so low as to make optical measurement times impractically long. Secondly, nuclei can be so small, of the order of 0.1 µm, such that imaging with visible light wavelengths is beyond diffraction limits. Thirdly, for the case of solid contaminants, imaging would only reveal the size of the particle itself, not the volume of the trapped gas, which is the governing parameter for cavitation inception.

To overcome these limitations, measurements may be taken with a Cavitation Susceptibility Meter (CSM). These devices have been in use since the 1970s to directly measure the nuclei distribution in water. The operating principle involves passing sampled water through a venturi exposing it to reduced pressure, thus activating all nuclei with critical pressures greater than, or equal to, the throat pressure. Nuclei activations are counted by analysing the output signal from a high-frequency piezoceramic sensor, which measures the structural response of the venturi due to nuclei collapse. By varying the flow rate, and hence the throat pressure, a cumulative histogram of nuclei concentration as a function of critical pressure can be measured.

The quantification of the 'susceptibility' of a liquid to cavitation occurrence (i.e. its 'strength'), inherent in the name of the device described above, is a topic where a consensus has yet to be reached. Franc and Michel (2006) suggest that the susceptibility of a liquid is the critical pressure associated with the activation of the largest nuclei present (based on a complete nuclei histogram obtained using a CSM in a time period of about 10 minutes). A number of authors, (e.g. Chahine and Shen, 1986; Arndt, 2012) have followed this approach and reported specific values of susceptibility for particular volumes of water. Alternatively, Gindroz and Billet (1994) suggest a practical definition of susceptibility as the tension when the microbubble population corresponds to 10^{-4} cm^{-3}. This second definition is somewhat arbitrary and may not be generally applicable. Both of these definitions have stemmed from nuclei measurements obtained using a CSM technique.

Susceptibility is of particular interest in test facilities where conditions can be controlled to a greater degree than in real flows. Nuclei populations are dependent on the dissolved gas content, levels of contaminants, artificial seeding of microbubbles and flow conditions about a model and around the test facility circuit. The cavitation tunnel at the Australian Maritime College (AMC) has the capability to continuously remove microbubbles generated either by cavitation or injected for the purposes of modelling nucleation. Microbubbles larger than about 100 µm are removed in a large settling chamber via coalescence and gravity separation and those remaining are dissolved in a resorber through extended residence at high pressure. The test fluid is demineralised water filtered to 1 µm. Despite these measures there exists a background nuclei population of unknown nature, for which there may be limited control, that is not amenable to measurement via optical techniques. This population may however be characterised using a CSM which is the subject of the present work. A canonical flow about a sphere is also considered in this paper to demonstrate what role these nuclei may play regarding susceptibility, as well as the inception and dynamic behaviour of cavitation.

C.3 Susceptibility measurements

For this experiment, the tunnel water was degassed to 30% of saturation at atmospheric pressure, which is typical for cavitation testing to ensure all introduced microbubbles are dissolved in the resorber. The tunnel static pressure was controlled at 100 kPa and the water was not recirculated but maintained as a quiescent volume. Water was sampled from the resorber and passed through the CSM and returned to the tunnel via the settling chamber to avoid returned water being re-sampled within the duration of the measurement. The CSM developed at the AMC uses a centrebody type venturi based on a design by YLec Consultants (Grenoble, France) as reported by Pham et al. (1997).

The measured cumulative histogram of nuclei concentration with critical pressure is shown in figure C.1, with uncertainties as discussed in Khoo et al. (2016). This measurement commenced with the lowest tension and greatest activation rate, and the CSM flow rate was progressively decreased to reduce tension, such that the lowest concentrations and longest measurements were made last. The flow rate was progressed when the first of two conditions were met, either the nuclei count exceeded 100 after recording for at least 30 s, or the time-out of 10^4 s. The long acquisition time was necessary because event rates become very low as the tension is reduced. At the tension of -5 kPa, only one event was recorded in over two hours. This means that the uncertainty of the concentration at low tensions is higher than desired, but practical considerations prevent the acquisition of extremely long time series. The estimated time required to achieve 100 nuclei activations would be approximately 280 hours. Tensions lower than -5 kPa were tested but no activations were recorded within the measurement duration.

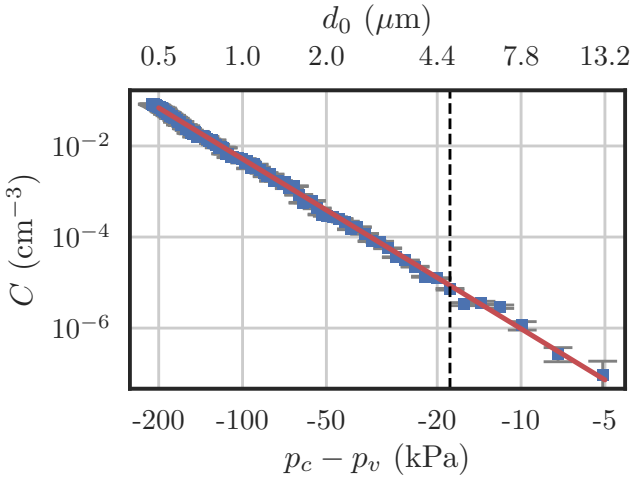

Figure C.1: Cumulative background nuclei distribution in the AMC cavitation tunnel. The trend line is a power fit and the dashed line corresponds to the minimum pressure on the surface of a sphere, as discussed in section C.4.

The secondary horizontal axis shown in figure C.1 represents the equivalent initial bubble diameter in the tunnel test section (d_0 at $p = p_0$), which can be calculated numerically as:

$$\frac{4}{27(p_v - p_c)^2} = \left(\frac{d_0}{4S}\right)^3 (p_0 - p_v) + \left(\frac{d_0}{4S}\right)^2, \tag{C.1}$$

where p_c is the critical pressure, p_v is the vapour pressure and S is the surface tension.

The data measured follows a power law, where the concentrations are in cm^{-3} and tensions are in kPa:

$$C = 1.8 \times 10^{-10}(p_v - p_c)^{3.73} \tag{C.2}$$

These results show that the water may not be characterised by a particular tension but rather is susceptible to 'all' tensions depending on the relevant time scale. This time scale will, in-turn, depend on relevant length and velocity scales. Equivalent bubbles diameters in the test section are less than 13 µm, which is below typical sizes measured by various means in laboratory studies or in the ocean, making comparisons with other data difficult. As these sizes are at or below limits of optical measurement techniques it is also difficult to assess the nature of these nuclei. Due to the low concentrations involved it is also difficult to use microscopy techniques with high magnifications as the volumes required are impractically large. Additional tests have shown that the measured population is independent of the direction of flow rate progression. Furthermore, the population is invariant for all tunnel operating conditions. This shows that unlike microbubbles, either created by cavitation or injected as nuclei, these background nuclei are stabilised against dissolution.

C.4 An example flow, cavitation about a sphere

To analyse implications of these results, the example of cavitating flow around a sphere is considered. This flow is examined for the cases with only background nuclei present and where the oncoming flow is artificially seeded with nuclei, as considered by de Graaf et al. (2016). The principal parameter characterising the flow is the cavitation number:

$$\sigma = \frac{p_0 - p_v}{\frac{1}{2}\rho U_\infty^2} \tag{C.3}$$

For this example the sphere diameter is 0.15 m, the freestream velocity is 10.6 m/s, the freestream pressure is 43.7 kPa, the dynamic pressure is 56 kPa and $\sigma = 0.75$. At this cavitation number, the flow undergoes energetic shedding with frequent large scale cavity extinction and re-nucleation providing insight into nucleation physics. Two sets of four still images for the unseeded and seeded cases, selected to depict a cycle of cavity nucleation, growth and collapse are shown in figure C.2.

Single-phase pressure measurements by Achenbach (1972) have shown the minimum pressure coefficient, $C_{p,min} \approx -1.1$ at this Reynolds number of 1.5×10^6. Thus, for this experiment the minimum pressure in the flow field can be estimated as −18 kPa. This pressure is indicated by the dashed line in figure C.1 indicating that only large nuclei (> 5 µm), which have low concentration, will be activated. The number of activated nuclei can be conservatively estimated by considering potential flow about the sphere, the streamwise distance over which nuclei are activated and the local concentration of activated nuclei from equation C.2. The total expected number of activated nuclei on the imaged half of the sphere can then be determined from integrating the local population over all radii with pressure less than vapour pressure. Assuming nuclei are activated over $0.2D$ gives an estimated number of activated nuclei per image of about 6×10^{-4}, or some 1580 photographs to image a single activation.

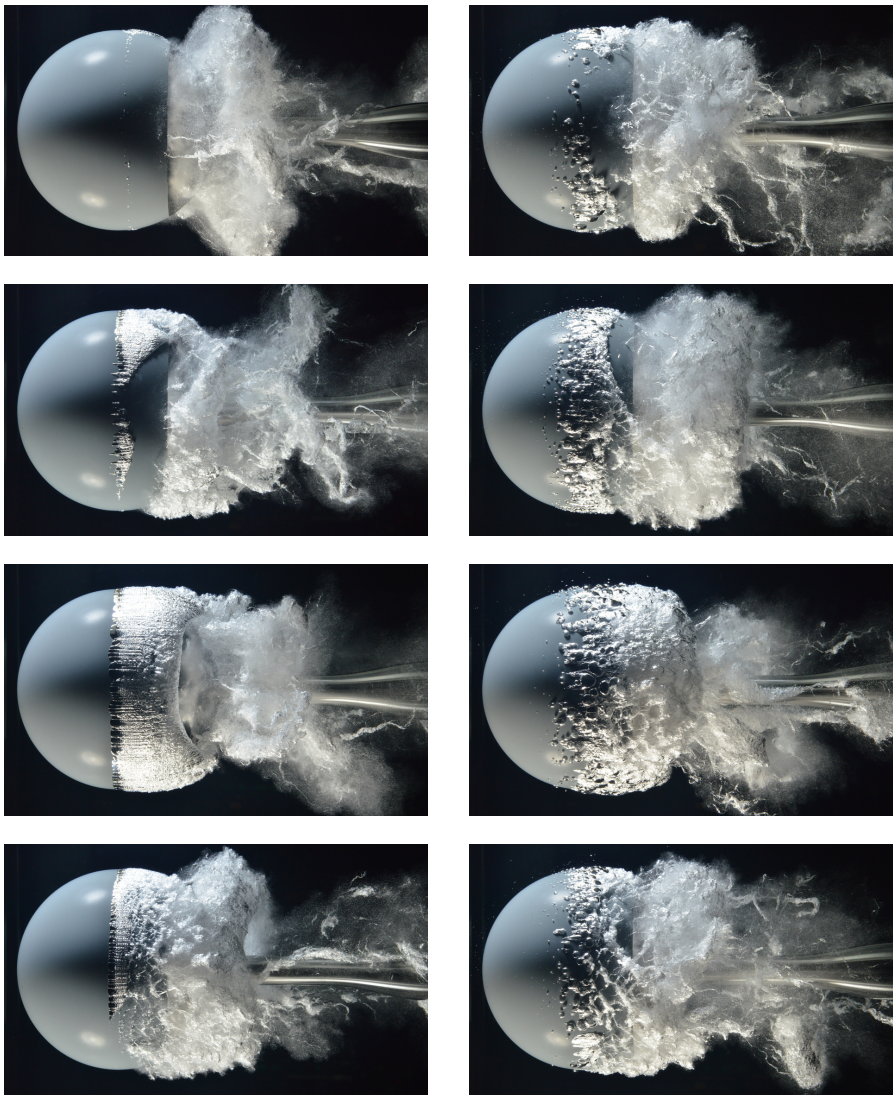

Figure C.2: Two sets of still images selected to depict shedding cycles of cavitation around a sphere for cases where the freestream was unseeded (left) and seeded with nuclei (right). The top row represents the nucleation of the cavity, the middle rows are the growth phase and the bottom row is the cavity collapse. The photographs were taken with a Nikon D800E digital camera with two synchronised stroboscopic light sources.

The top two images of figure C.2 for the unseeded case, depicting the typical nucleation phase of a shedding cycle, show large numbers of activated nuclei. Since the concentrations of background nuclei are low, this clearly demonstrates that these cannot be due to the background population. Therefore, these nuclei must be from the surface and/or provided by the previously shed cavity. For the seeded case, all images show a large number of activated nuclei continuously supplied from the freestream regardless of the stage of shedding. That is, while background nuclei may be activated, their numbers are so small in comparison with other nucleation mechanisms that they are insignificant.

C.5 Conclusions

Results of a detailed study into the susceptibility of water in the AMC cavitation tunnel are provided. The concentration of nuclei in the water is shown to follow a power law and is invariant of tunnel conditions and as such are stabilised against dissolution. Further, it is shown that the water is susceptible to all applied tensions, depending on the relevant time scale in order to activate weaker nuclei. This implies that the length and velocity scales of the flow in question are important in determining the required time-scale for inception. Although ever present, the background population does not have any practical effect on the example flow about a sphere, as the number of activated nuclei are so few compared with other nucleation sources.

C.6 Acknowledgements

The authors acknowledge the support of the Australian Defence Science and Technology Group.

Appendix D

Observations on a cavitating trailing vortex behind a control surface

This appendix is an author accepted manuscript of an article presented at the MAST (Maritime/Air Systems and Technology) Asia Conference, Chiba, Japan, 17–19 June 2019. The final authenticated version is available online at:

`https://mastconfex.com/asia2019/`.

The citation for the paper is:

J. Venning, M. Khoo, B. Pearce, and P. Brandner. Observations on a cavitating trailing vortex behind a control surface. In MAST Asia 2019, pages 1–9, 2019.

Appendix D has been removed for copyright reasons

Appendix E

Nucleation effects on tip vortex cavitation inception location

This appendix is an author accepted manuscript of an article published in the proceedings of the 22nd Australasian Fluid Mechanics Conference, Brisbane, Australia, 7–10 December 2020. The final authenticated version is available online at:

https://doi.org/10.14264/015283f.

The citation for the paper is:

M. Khoo, J. Venning, B. Pearce, and P. Brandner. Nucleation effects on tip vortex cavitation inception location. In Proc. 22nd Australasian Fluid Mech. Conf. The University of Queensland, 2020.

E.1 Abstract

Nuclei, or microbubble, populations are inextricably linked to tip vortex cavitation (TVC) inception and dynamics. In order to gain a better quantitative understanding of this relationship, high-speed video measurements were taken in a cavitation tunnel of TVC inception locations about an elliptical hydrofoil in flows with mono- and polydisperse injected nuclei populations. Sample sizes of $\mathcal{O}(1000)$ were acquired. For both populations, inception occurred between 0.02 chord lengths upstream of the hydrofoil tip and about 2.1 chord lengths downstream along the cavity trajectory. However, inception location distribution varied significantly with nuclei population. This is explained by the higher concentrations of weaker nuclei in the monodisperse case, which increases the distance along the vortex within which nuclei are susceptible to cavitation. These results provide the foundation for studies on TVC dynamics and acoustics.

E.2 Introduction

Cavitation inception in practical flows is invariably heterogeneous where nuclei, typically microbubbles, are exposed to a size-dependent critical pressure, resulting in explosive cavity growth. For all but the largest nuclei, critical pressures are well below vapour pressure, or absolute zero, such that liquids typically sustain tensile stresses prior to nuclei activation. A trailing vortex has low pressures in its core, which is the likely location for inception. Nuclei are drawn into the vortex core due to the radial pressure gradient. This phenomenon is known as tip vortex cavitation (TVC), see figure E.1. It is often the first type of cavitation to occur about marine propellers and is detrimental to acoustic stealth performance. TVC has been studied extensively (Arndt, 2002). Scale effects due to Reynolds number (McCormick, 1962; Shen et al., 2009) and nuclei (Arndt and Keller, 1992; Gindroz and Billet, 1998) have been the focus of many investigations, with the aim to extrapolate model-scale results to full scale.

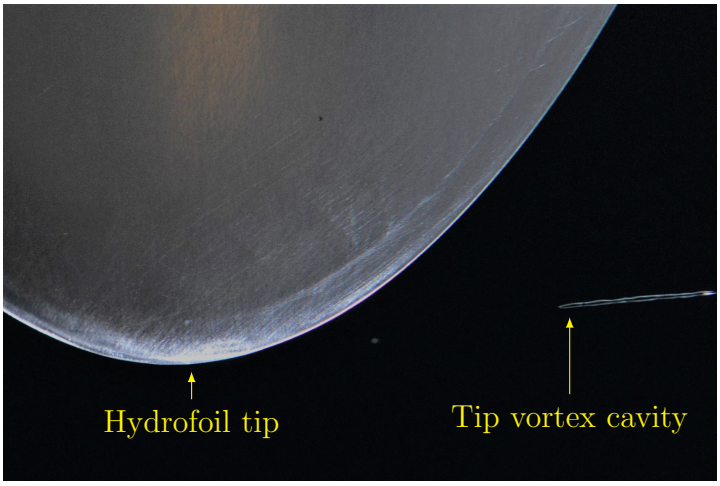

Figure E.1: Photograph showing an example of tip vortex cavitation downstream of an elliptical hydrofoil. The flow direction is left to right.

Nuclei populations can vary within and between environmental and laboratory waters (Khoo et al., 2020c). They are known to influence TVC behaviour, with earlier onset of cavitation measured in flows with higher concentrations of larger nuclei, also known as 'weak' water (Arndt and Keller, 1992; Gindroz and Billet, 1998; Khoo et al., 2018). While numerous studies of nucleation effects on cavitation have been carried out, only limited observations have been made of their effects on inception location. Such observations have the potential to offer insights into TVC dynamics and acoustics.

The influence of TVC inception location on cavity dynamics and acoustics is of interest as the streamwise variation of the vortex core pressure affects TVC behaviour. The minimum pressure occurs approximately $0.125c$ downstream of the tip for elliptical hydrofoils, where c is the chord length (Fruman and Dugue, 1994; Asnaghi et al., 2020). However, since inception could potentially occur at any location in the flow where the pressure is below vapour pressure, the location of inception has been reported anywhere from $0.05c$ upstream to $2c$ downstream of elliptical hydrofoil tips (Higuchi et al., 1989; Maines and Arndt, 1993; Arndt and Maines, 2000).

While it is convenient to describe water as either 'weak' or 'strong', as done by Arndt and Maines (2000), nuclei populations have size, concentration and spatial distributions and are therefore statistical in nature (Venning et al., 2018b). This means TVC inception is also statistical and requires large numbers of repeated measurements for accurate characterisation, particularly in nuclei deplete flows (Khoo et al., 2020a). Previous studies using large numbers of cavitation events either span a range of test conditions (Arndt and Maines (2000): 500 events) or are used for averaging (Oweis et al. (2004): 1000 events, Choi and Ceccio (2007): 100 events), and are not used to quantify TVC inception statistics. While it was found that $\mathcal{O}(100)$–$\mathcal{O}(1000)$ samples are required to describe the statistics of TVC inception in nuclei deplete flows, it was suggested that fewer samples may be required for flows with higher nuclei populations (Khoo et al., 2020a). A clearer understanding of sample size selection is required to inform the design of TVC inception experiments.

Nuclei populations in cavitation test facilities have been varied by manipulation of the dissolved air content (Arndt and Maines, 2000; Chang et al., 2011) and by microbubble injection (Briançon-Marjollet and Merle, 1996), the latter enabling more independent control over free and dissolved gases and thus their effects on cavitation behaviour. Even stricter nuclei control and measurement is required to isolate nuclei size and concentration, and to quantify their individual effects on TVC inception location.

In this paper, the effects of two nuclei populations on TVC inception location are presented using large datasets. This provides the basis for studies into TVC dynamics and acoustics, and how they relate to nuclei content and inception location.

E.3 Experimental overview

Hydrofoil tip vortex cavitation inception locations were measured in a cavitation tunnel using a high-speed video camera. Two injected nuclei populations were studied at a fixed Reynolds number and incidence. The experimental setup is shown in figure E.2 and further details are provided below.

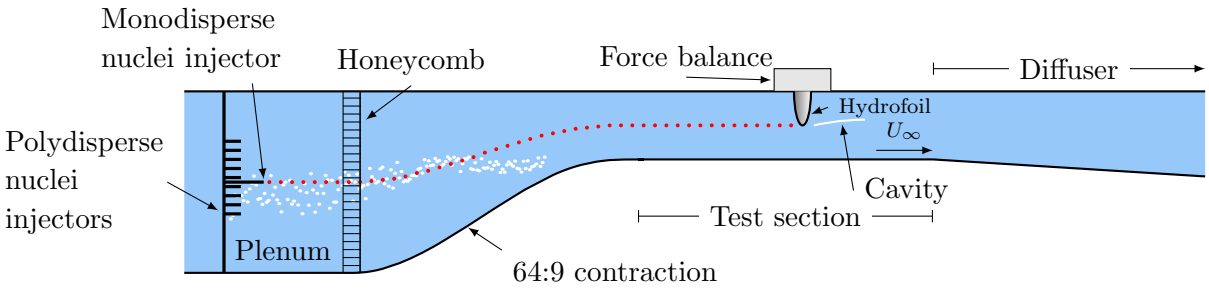

Figure E.2: Schematic of the experimental setup in the upper segment of the AMC cavitation tunnel, showing the hydrofoil located in the test section. The force balance allows for angular positioning of the hydrofoil. The test section velocity is U_∞. Mono- and polydisperse nuclei populations were injected upstream of the test section for different test runs. They are shown as red and white dots, respectively.

E.3.1 Test facility

The cavitation tunnel in the Australian Maritime College (AMC) Cavitation Research Laboratory is a medium-sized, variable-pressure water tunnel located in Launceston, Australia. It is constructed of stainless steel (wetted areas) and has a volume of 365 m^3. The working fluid is demineralised water. The test section cross section is 0.6 m $\times$ 0.6 m, with a length of 2.6 m. The test section pressure, p_∞, can be varied between 4–400 kPa, while the test section velocity, U_∞, range is nominally 2–12 m/s.

The tunnel design and ancillaries allow for strict control of free and dissolved gas contents. The test flow can be seeded with microbubbles, or nuclei, using injectors mounted in the plenum upstream of the test section. Bubbles are removed downstream of the test section in a large downstream tank (via coalescence and gravity separation) and a lower segment resorber (via extended residence and dissolution). The tunnel features a fast degassing facility, which allows the dissolved gas content to be reduced as required. Further details are provided in Brandner et al. (2007).

E.3.2 Free and dissolved gas content

Two injected nuclei populations were used for this study. An injected monodisperse microbubble population (hereinafter termed 'monodisperse') with a nominal dominant bubble diameter of 100 µm was generated using a stainless steel 'T'-junction with 100 µm bore from Valco Instruments Co. Inc. This injector was mounted upstream of the contraction, at the mid-span and mid-height of the plenum, see figure E.2.

An injected polydisperse microbubble population (hereinafter termed 'polydisperse') with a range of bubble diameters was generated using the cavitation of supersaturated water fed through an array of injectors mounted in the plenum (Giosio et al., 2016; Russell et al., 2020b). They are typically arranged in a triangular grid, 80 mm apart (an equivalent spacing of 30 mm in the test section), mounted across three columns of a supporting strut. For this study, only the two outer columns were used to produce a low concentration of polydisperse nuclei, resulting in a spanwise and vertical spacing between injectors of 139 and 80 mm, respectively. This corresponds to 52 and 30 mm in the test section, respectively.

The injected nuclei populations were measured using Mie Scattering Imaging (MSI) (Russell et al., 2020b,a). They are presented as histograms of nuclei concentration against bubble diameter in figure E.3. The Reynolds number is $Re = \frac{U_\infty c}{\nu}$, where U_∞ is the test section velocity, c is the hydrofoil root chord length and ν is the fluid kinematic viscosity. It was fixed at $Re = 1.5 \times 10^6$ for this study. The cavitation number is $\sigma = \frac{p_\infty - p_v}{\frac{1}{2}\rho {U_\infty}^2}$, where p_∞ is the freestream pressure in the test section at the same height as the hydrofoil tip, p_v is the vapour pressure and ρ is the fluid density. It was fixed at $\sigma = 1.6$ for this study.

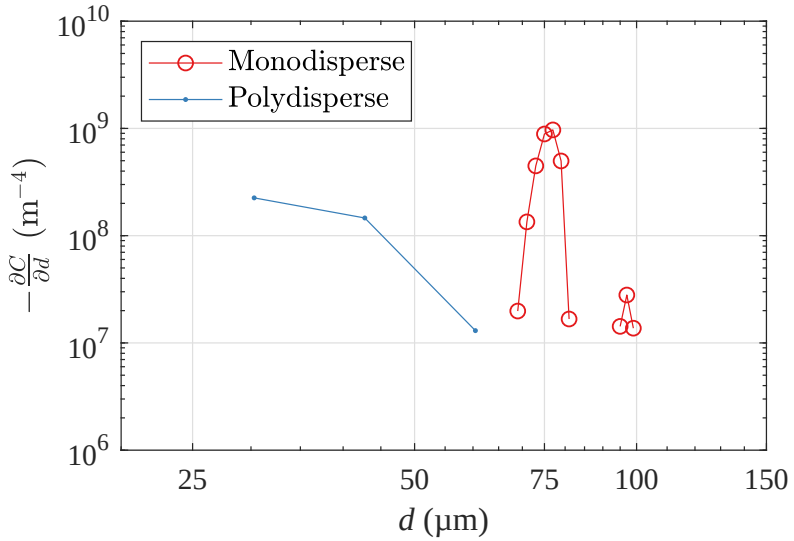

Figure E.3: Comparison of nuclei distribution histograms measured using Mie Scattering Imaging ($Re = 1.5 \times 10^6$, $\sigma = 1.6$). The nuclei density distribution, $-\frac{\partial C}{\partial d}$, is plotted against nucleus diameter, d. The monodisperse nuclei distribution features a prominent peak at $d = 77$ µm and a smaller one at $d = 97$ µm. The polydisperse nuclei distribution has a lower concentration of bubbles across a range of smaller sizes.

The monodisperse and polydisperse nuclei distributions are constructed from 170 and 15 bubble detections, respectively. While larger sample sizes are preferred, there are sufficient detections to identify the characteristics of each distribution. The monodisperse nuclei distribution exhibits a peak concentration at $d = 77$ µm. A smaller peak at $d = 97$ µm, based on 4 bubble detections, also exists. It is possible that ~ 97 µm diameter bubbles were injected but broke up into ~ 77 µm diameter bubbles. The critical pressure of bubbles in this size range is effectively vapour pressure, which results in weak water.

The polydisperse nuclei distribution comprises a lower concentration of bubbles across a range of smaller diameters. It is stronger than the monodisperse nuclei distribution, as no bubbles larger than about 60 µm in diameter were detected.

The dissolved oxygen content was maintained between 2.6 and 3.7 mg/L (i.e. 29–41% relative to saturation at atmospheric pressure) throughout the experiment.

E.3.3 Cavitation inception location measurement & processing

A stainless steel hydrofoil with an elliptical planform and NACA 0012 cross section was studied. It has a root chord length of 150 mm and a span of 300 mm. It was mounted to a six-component force balance with a stepper motor and encoder for angular positioning. This unit was installed 1.45 m from the test section entrance, as shown in figure E.2. The hydrofoil incidence, α, was fixed at 6° throughout this study.

Visual measurements were taken using a high-speed camera (Phantom v2640 with Nikon 24 mm focal length lens, frame rate 16 kHz). It was mounted beneath the test section. LED lighting was used to illuminate the cavities. Recordings were triggered using an image-based trigger.

Visual measurements of a single cavitation event in a flow injected with monodisperse bubbles are shown in figure E.4. Image processing was carried out using MATLAB software. The composite photograph (left) shows the different stages of development of a single cavity. Boundaries of the cavity trajectory were identified using an image of a steady cavity attached to the hydrofoil tip. The distance along the cavity trajectory downstream of the hydrofoil tip, s, is normalised by the hydrofoil root chord length, c, in this analysis (i.e. s/c). Note that the image-based trigger used for video acquisition was located at $s/c \approx 2.4$.

Pixels with the maximum intensity within the trajectory bounds at each s/c location were extracted from each video frame. Space-time plots were constructed which quantify cavity development. Intensity and area filters were applied to identify tip vortex cavities. Cavitation inception was defined as the elongation of a captured nucleus, so the filter was tuned to only pass such cavities. The downstream distance along the cavity trajectory corresponding to the earliest appearance of the cavity (i.e. the top of the leftmost point of the shaded region in figure E.4) was defined as the inception location, s_i/c.

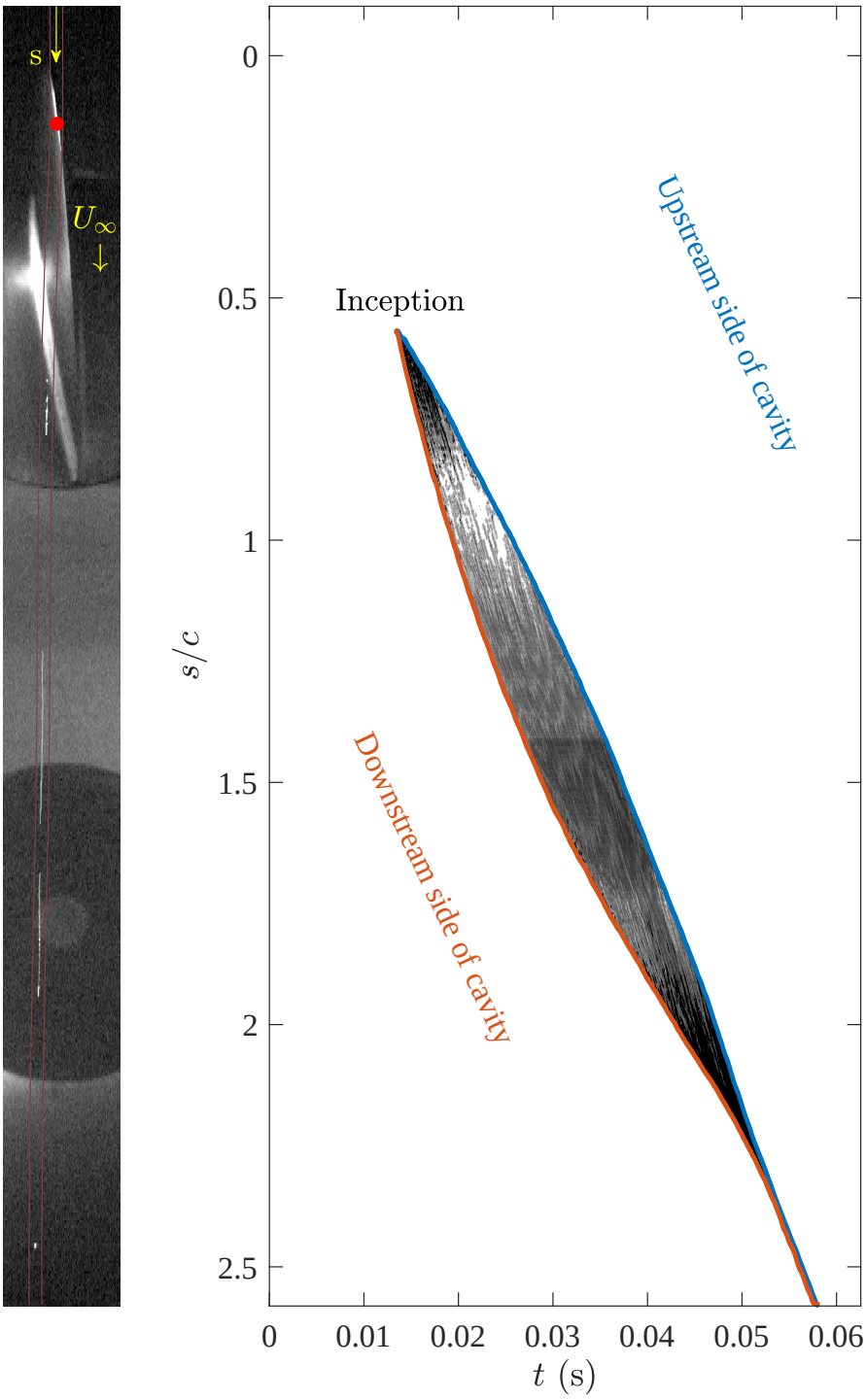

Figure E.4: Visual measurements of a single cavitation event in a flow injected with monodisperse bubbles ($Re = 1.5 \times 10^6$, $\sigma = 1.6$, $\alpha = 6°$). The composite photograph (left) shows different stages of cavity development, with the flow direction top to bottom. The hydrofoil tip is marked with a red circle. The distance along the cavity trajectory (bounded by the dark red lines) downstream of the tip, s, normalised by the root chord length, c, is plotted against time, t, in the space-time graph (right). The shaded region corresponds to a cavity identified using intensity and area filters. The inception location is at $s_\mathrm{i}/c = 0.58$.

E.4 Results and Discussion

Histograms of inception location are provided in figure E.5. A total of 4023 events were captured for the monodisperse case and 1405 for the polydisperse. Although $\mathcal{O}(1000)$ events were recorded in each case, the inception location distributions converge to that of the final dataset within $\mathcal{O}(100)$ events.

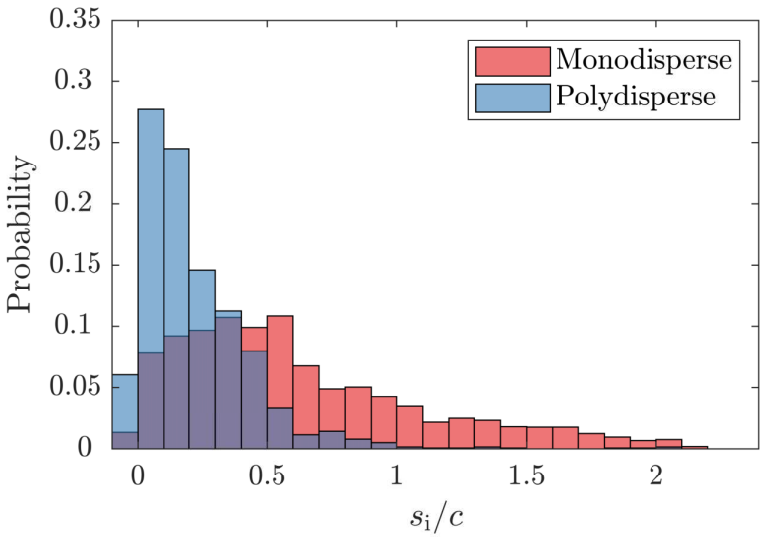

Figure E.5: Histograms of inception location, s_i/c, for different nuclei populations ($Re = 1.5 \times 10^6$, $\sigma = 1.6$ and $\alpha = 6°$). The hydrofoil tip corresponds to $s_i/c = 0$. The distribution is more uniform for the monodisperse case, especially between $s_i/c = 0$ and 0.6. Inception is most likely just downstream of the tip for the polydisperse case. Inception events were observed between $s_i/c = -0.02$ and about 2.1 for both cases.

The inception location distributions differ significantly. In the monodisperse case, a greater proportion of inception events occur at downstream locations. The higher concentration of weaker nuclei in the monodisperse case increases the distance along the vortex within which nuclei are susceptible to cavitation. The distribution is relatively uniform between $s_i/c = 0$ and 0.6. This could be associated with a stronger radial pressure gradient across this range, which draws larger bubbles into low pressure regions faster than smaller ones. It may be that $p \ll p_v$ in this region, but such inferences are made with caution as vaporous and gaseous cavitation have not been distinguished in this study. The former occurs when the equilibrium of a nucleus becomes unstable when exposed to its critical pressure, resulting in explosive growth as the cavity fills with vapour. The latter occurs when a larger bubble grows due to pressure reduction and gaseous diffusion at a pressure higher than vapour pressure. Measurement or simulation of the pressure field could assist with understanding the physics of nuclei capture and type of cavitation that occurs.

For the polydisperse case, inception events most commonly occur just downstream of the tip, tending to decrease in probability with increasing downstream distance. The 'window of opportunity' for inception for this case is smaller due the presence of stronger nuclei that require higher tensions to activate, hence a greater clustering of data points about what is presumably the location of minimum vortex pressure. The location of the peak shows agreement with the location of minimum pressure in the tip vortex of an elliptical hydrofoil, which has been found to be $0.125c$ downstream of the tip (Fruman and Dugue, 1994; Asnaghi et al., 2020).

For both nuclei populations, inception events were detected up to $0.02c$ upstream of the tip. This is indicative of the start of tip vortex development in this region. Inception events were also detected up to $s_\mathrm{i}/c \approx 2.1$ for both cases. These results are in agreement with Maines and Arndt (1993) and Higuchi et al. (1989) who observed inception between $0.05c$ upstream and $2c$ downstream of the tip (in the streamwise direction), respectively. In the present study, some inception events exhibited only minimal elongation. This occurred at $s_\mathrm{i}/c \gtrsim 1.2$ for the monodisperse case and $s_\mathrm{i}/c \gtrsim 1.8$ for the polydisperse. This indicates weakening of the vortex, but it is unclear whether these inception events constitute vaporous or gaseous cavitation.

E.5 Conclusions

Nucleation effects on tip vortex cavitation inception location about an elliptical hydrofoil have been studied in a cavitation tunnel using high-speed video measurements. Sample sizes of $\mathcal{O}(1000)$ were acquired. The nuclei population was found to influence inception location distributions significantly. In the monodisperse case, a greater proportion of events occurred at downstream locations. This was attributed to the higher concentration of weaker nuclei in this flow, which increased the distance along the vortex within which nuclei could cavitate. For both nuclei populations, inception was detected between 0.02 chord lengths upstream of the hydrofoil tip and about 2.1 chord lengths downstream of the tip along the cavity trajectory. Some of the inception events exhibited only minimal elongation. The distinction between vaporous and gaseous cavitation should be given further consideration as it would enable the local pressure to be inferred with greater confidence. This study provides the foundation for investigations into TVC acoustics and its dependence on TVC dynamics using cavity properties determined from high-speed video measurements.

E.6 Acknowledgements

The authors acknowledge the support of the University of Tasmania and the Defence Science and Technology Group. The authors thank AMC technical officers, Mr Robert Wrigley and Mr Steven Kent for providing technical assistance with test facility configuration and operation.